Development of Motion Control Systems for Hydraulically Actuated Cranes with Hanging Loads

Konrad Johan Jensen

UiA University of Agder

Doctoral Dissertations at the University of Agder 394

Konrad Johan Jensen

Development of Motion Control Systems for Hydraulically Actuated Cranes with Hanging Loads

Doctoral Dissertation for the Degree *Philosophiae Doctor (PhD)* at
the Faculty of Engineering and Science, Specialisation in Mechatronics

University of Agder
Faculty of Engineering and Science
2023

Doctoral Dissertations at the University of Agder 394
ISSN: 1504-9272
ISBN: 978-82-8427-107-1

© Konrad Johan Jensen, 2023

Printed by Aksell, Kristiansand

Preface

This project has been carried out between February 2016 and September 2022. The work towards this doctoral thesis has been carried out at the University of Agder, campus Grimstad, and the project is funded by the Ministry of Education in Norway, project number 155597. Associate Professor Morten Kjeld Ebbesen has been the main supervisor and Professor Michael Rygaard Hansen has been the co-supervisor, both from the University of Agder.

Acknowledgments

First of all I want to thank my supervisor, Associate Professor Morten Kjeld Ebbesen, for his guidance and support during this project. He has always shown interest in this project and given me valuable insight and knowledge. I would also like to thank my co-supervisor Professor Michael Rygaard Hansen for his industrial know-how and expertise.

Thank you to my colleagues and the faculty staff for making the University a great place to work.

Experimental work has been a large part of this project, and I would like to thank the lab staff at the Mechatronics lab for giving me the help and opportunity to conduct my experiments.

A big thank you to my fiancée June for always supporting me and showing interest in my work, and enduring my late nights. She has been with me in sickness and in health, and has given me the fervor to pursue my academic goals. A special thanks to my daughters Mara Emilie and Luna Johanne for always putting a smile on my face!

Konrad Johan Jensen
Grimstad, Norway
2023

Abstract

Automation has been used in industrial processes for several decades to increase efficiency and safety. Tasks that are either dull, dangerous, or dirty can often be performed by machines in a reliable manner. This may provide a reduced risk to human life, and will typically give a lower economic cost. Industrial robots are a prime example of this, and have seen extensive use in the automotive industry and manufacturing plants. While these machines have been employed in a wide variety of industries, heavy duty lifting and handling equipment such as hydraulic cranes have typically been manually operated. This provides an opportunity to investigate and develop control systems to push lifting equipment towards the same level of automation found in the aforementioned industries. The use of winches and hanging loads on cranes give a set of challenges not typically found on robots, which requires careful consideration of both the safety aspect and precision of the pendulum-like motion. Another difference from industrial robots is the type of actuation systems used. While robots use electric motors, the cranes discussed in this thesis use hydraulic cylinders. As such, the dynamics of the machines and the control system design may differ significantly. In addition, hydraulic cranes may experience significant deflection when lifting heavy loads, arising from both structural flexibility and the compressibility of the hydraulic fluid.

The work presented in this thesis focuses on motion control of hydraulically actuated cranes. Motion control is an important topic when developing automation systems, as moving from one position to another is a common requirement for automated lifting operations. A novel path controller operating in actuator space is developed, which takes advantage of the load-independent flow control valves typically found on hydraulically actuated cranes. By operating in actuator space the motion of each cylinder is inherently minimized. To counteract the pendulum-like motion of the hanging payload, a novel anti-swing controller is developed and experimentally verified. The anti-swing controller is able to suppress the motion from the hanging load to increase safety and precision. To tackle the challenges associated with the flexibility of the crane, a deflection compensator is developed and experimentally verified. The deflection compensator is able to counteract both the static deflection due to gravity and dynamic deflection due to motion. Further, the topic of adaptive feedforward control of pressure compensated cylinders has been investigated. A novel adaptive differential controller has been developed and experimentally verified, which adapts to system uncertainties in both directions of motion. Finally, the use of electro-hydrostatic actuators for motion control of cranes has been investigated using numerical time domain simulations. A novel concept is proposed and investigated using simulations.

The appended papers at the end of this thesis present the developed methods which have been investigated and experimentally verified using a hydraulic loader crane located at the University of Agder, Grimstad, Norway.

Sammendrag

Automasjon har blitt brukt i industrielle prosesser i flere tiår for å øke effektivitet og sikkerhet. Oppgaver som er enten kjedelige, farlige, eller skitne kan ofte bli pålitelig utført av maskiner. Dette kan redusere risikoen for tap av menneskeliv, og vil typisk gi en lavere økonomisk kostnad. Industrielle roboter er et prakteksempel på dette, og de har blitt mye brukt i bilbransjen og i fabrikker. Selv om disse maskinene har blitt brukt i mange forskjellige industrier, så har større og tyngre lasthåndteringsutstyr typisk vært manuelt operert. Dette gir en mulighet til å undersøke og utvikle kontrollsystemer som kan løfte lasthåndteringsutstyr opp mot det samme automasjonsnivået som i de tidligere nevnte industriene. Bruk av vinsjer og hengende laster på kraner gir et sett med utfordringer man typisk ikke vil finne på roboter, noe som vil kreve omtanke både med hensyn til sikkerhet og presisjon for den svingende lasten. En annen forskjell fra industrielle roboter er aktueringssystemene som brukes. Mens roboter bruker elektriske motorer, så bruker kranene som diskuteres i denne avhandlingen hydrauliske sylindere. Av den grunn så vil dynamikken til maskinene og designet av kontrollsystemene variere kraftig. I tillegg så kan hydrauliske kraner oppleve markant utbøying når de løfter tunge laster, som kommer av strukturell fleksibilitet og kompressibiliteten til hydraulikkvæsken.

Arbeidet som presenteres i denne avhandlingen fokuserer på bevegelsesstyring av hydraulisk aktuerte kraner. Bevegelsesstyring er et viktig tema når man utvikler automasjonssystemer, for det å bevege seg fra en position til en annen er et vanlig krav for automatiserte løfteoperasjoner. En ny banekontroller som opererer i aktuatorrommet er utviklet, som utnytter de lastuavhengige proposjonalventilene som typisk er å finne på hydraulisk aktuerte kraner. Ved å bruke aktuatorrommet så vil bevegelsen til hver sylinder bli redusert. For å motvirke svingbevegelsene til den hengende laster så er en ny anti-sving kontroller utviklet og eksperimentelt verifisert. Anti-sving kontrolleren klarer å dempe bevegelsen til den hengende laster for å øke både sikkerhet og presisjon. For å håndtere utfordringene med kranens fleksibilitet så har en utbøyningskompensator blitt utviklet og eksperimentelt verifisert. Utbøyningskompensatoren klarer å motvirke både den statiske utbøyningen grunnet gravitasjon og den dynamiske utbøyningen grunnet bevegelse. I tillegg så har temaet om adaptiv fremoverkobling av trykkompenserte sylindere blitt undersøkt. En ny adaptiv differensiell kontroller har blitt utviklet og eksperimentelt verifisert, som klarer å tilpasse seg usikkerhet i begge bevegelsesretningene til sylinderen. Og til slutt så har bruken av elektrohydrostatiske aktuatorer for bevegelsesstyring av kraner har blitt undersøkt ved hjelp av numeriske simuleringer. Et nytt konsept er foreslått og undersøkt via simulering.

De vedlagte artiklene på slutten av denne avhandlingen presenterer de utviklede meto-

dene som har blitt undersøkt og eksperimentelt verifisert på en hydraulisk lastebilkran lokalisert på Universitetet i Agder, Grimstad, Norge.

Publications

Six scientific articles are appended to this dissertation and will be referred to by their character. The papers have been published in peer-reviewed journals and are printed in their original state:

Paper A Jensen, K.J.; Kjeld Ebbesen, M.; Rygaard Hansen, M. Development of Point-to-Point Path Control in Actuator Space for Hydraulic Knuckle Boom Crane. *Actuators* **2020**, *9(2)*, 27. doi:10.3390/act9020027

Paper B Jensen, K.J.; Ebbesen, M.K.; Hansen, M.R. Adaptive Feedforward Control of a Pressure Compensated Differential Cylinder. *Appl. Sci.* **2020**, *10(21)*, 7847. doi:10.3390/app10217847

Paper C Jensen, K.J.; Kjeld Ebbesen, M.; Rygaard Hansen, M. Anti-swing control of a hydraulic loader crane with a hanging load. *Mechatronics* **2021**, 77, 102599. doi:10.1016/j.mechatronics.2021.102599

Paper D Jensen, K.J.; Kjeld Ebbesen, M.; Rygaard Hansen, M. Novel Concept for Electro-Hydrostatic Actuators for Motion Control of Hydraulic Manipulators. *Energies* **2021**, *14(20)*, 6566. doi:10.3390/en14206566

Paper E Jensen, K.J.; Kjeld Ebbesen, M.; Rygaard Hansen, M. Development of 3D Anti-Swing Control for Hydraulic Knuckle Boom Crane. *Modeling, Identification and Control* 42(3):113–129, 2021. doi:10.4173/mic.2021.3.2

Paper F Jensen, K.J.; Kjeld Ebbesen, M.; Rygaard Hansen, M. Online Deflection Compensation of a Flexible Hydraulic Loader Crane Using Neural Networks and Pressure Feedback. *Robotics* **2022**, *11(2)*, 34. doi:10.3390/robotics11020034

Contents

List of Figures

List of Tables

Abbreviations

CBV Counter Balance Valve.

DCV Directional Control Valve.

DOF Degrees of Freedom.

EHA Electro-Hydrostatic Actuator.

PMSM Permanent Magnet Synchronous Motor.

POCV Pilot-operated Check Valve.

SVM Space Vector Modulation.

Chapter 1

Introduction

1.1 Motivation and Problem Statement

Lifting equipment has been used for hundreds of years, and today cranes are used in a wide variety of applications both offshore and onshore. Various lifting operations on ships, ports, trucks, and warehouses around the world rely on cranes for material handling and efficient logistics operation. Today most cranes are manually operated, typically using some kind of joystick. Therefore, cranes have a large potential for automation, which can increase time efficiency, precision, and safety for lifting operations. This can in some ways be similar to modern manufacturing plants where industrial robots are used for lifting light loads and other applications such as welding. By increasing the level of automation for lifting and handling using large manipulators such as cranes, new technologies can be developed which may outperform the manual operation used today. This can be boiled down to a desire to reach the same level of automation as with industrial robots, but with much larger lifting capacity.

Many lifting operations with cranes are done using winches, typically with steel wire ropes. This results in a hanging load with up to several uncontrolled degrees of freedom. While winches provide several advantages, a set of challenges also appears. The task of motion control is now extended to controlling both the crane tip position and the hanging load position. A hanging payload may also be susceptible to wind loads, which increases the difficulty of control. In addition, large weight-optimized cranes may experience significant deflection when lifting heavy payloads due to their flexibility. This deflection introduces a potential source of error for the calculated payload position, which could become a safety hazard when performing autonomous lifting.

Most of the focus in this thesis is directed at hydraulically actuated cranes, such as knuckle boom cranes and loader cranes. While these cranes appear different from for example electric gantry cranes, most of the research and development done are designed to be compatible with different crane types. Figure 1.1 shows a typical offshore knuckle boom crane, which is mounted on an offshore vessel and is used for lifting heavy loads both above and below the water line.

Figure 1.1: Typical offshore knuckle boom crane shown in resting position, manufactured by National Oilwell Varco [1]. Taken from Paper A.

The main motivation for this project comes from the potential for automation using cranes and a desire to solve the challenges associated with lifting operations using cranes with hanging loads. For the load handling industry, achieving a similar level of automation as in the automotive or manufacturing industries will be a major technological lift. In the future, load handling operations may even be fully automated. This, in addition to the development of autonomous ships at sea and autonomous trucks at land, may be the most disruptive technological advancement for offshore and onshore lifting operations the load handling industry has seen. Tho achieve this level of autonomy, several challenges related to the safe, precise and efficient handling of large payloads must be investigated.

This project aims to handle these challenges using a combination of modeling, simulations, and experiments. As such, three research questions have been formulated:

- How can a path control algorithm be developed to control both the crane tip position and payload position?

- During operation, how can the pendulum motion in the payload hanging from the winch be suppressed?

- When the crane is operated with heavy loads, how can the deflection due to gravity and the mass of the payload be counteracted?

1.2 Thesis Outline

This thesis is divided into four chapters, which are followed by the appended papers listed in the beginning. The content of each chapter is summarized below:

Chapter 1 - Introduction

This chapter presents the problem to be investigated and the motivation for this project, and an outline of the thesis (this part) aimed at providing an overview of the content to the reader. This is followed by a description of the considered system which has been used as a basis for simulations and experiments in this project. A review of the current state of the art is given, with a focus on motion control, anti-swing control, and deflection compensation. At the end of the introduction, a summary of the appended papers and their contributions is given.

Chapter 2 - Background Theory, Modeling and Control

This chapter presents more general topics such as modeling of components, motion control, and kinematics. These topics have been developed during this project, but are not limited to hydraulic cranes and can be used for a wide variety of systems. They also form a basis from which more advanced control systems can be designed, as discussed in the following chapter.

Chapter 3 - Research Method and Results

This chapter presents the research conducted during the time of this project. It contains the novel methods developed, as well as simulation and experimental results. This chapter is considered the core scientific contribution of this project, and aims at showcasing the solutions to the challenges presented.

Chapter 4 - Concluding Remarks

At the end of the thesis, the outcome of this project is discussed. Some concluding remarks about the research done during the time of this project are given. Finally, some comments about the future work is made and possible improvements are discussed.

Appended Papers

All the previously listed papers are included at the end of this thesis. These papers provide the details and contributions to several of the topics in the preceding chapters. The reader is encouraged to study the papers to gain more detailed and in-depth knowledge of the selected topics for motion control of hydraulic cranes.

1.3 Considered System

During this project an HMF 2020K4 loader crane has been used for experiments and to test the developed control systems. The crane is located in the Mechatronics lab at Campus Grimstad, as seen in Figure 1.2. An illustration of the crane and its components is shown in Figure 1.3. The crane has a total of five actuators; slew cylinder, main cylinder, knuckle cylinder, telescopic system, and a winch. The slew cylinder is connected to a rack

and pinion at the base of the crane, and rotates the crane. The main cylinder and knuckle cylinder are connected to each of the booms via linkage systems. These linkages optimizes the effective torque arm of the joint. The telescopic system consists of four booms packed inside each other, with four cylinders connected at the top.

Figure 1.2: The HMF 2020K4 crane in the laboratory with the telescopic booms extended.

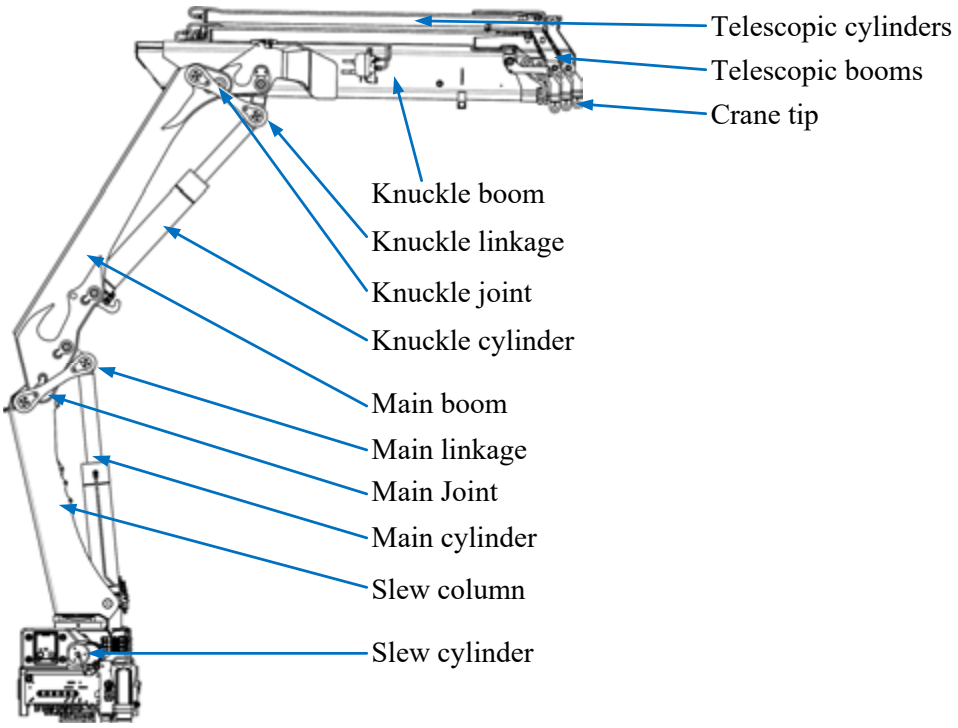

Figure 1.3: Overview of the HMF 2020K4.

Every cylinder is driven by a pressure compensated directional control valve (DCV), which is connected to a central pump. In the laboratory the pump is driven by a constant speed induction motor. Counterbalance valves (CBVs) are used for load holding, assisting

in lowering load, and protection against pressure surges. An illustration of the simplified hydraulic circuit for the knuckle cylinder is shown in Figure 1.4.

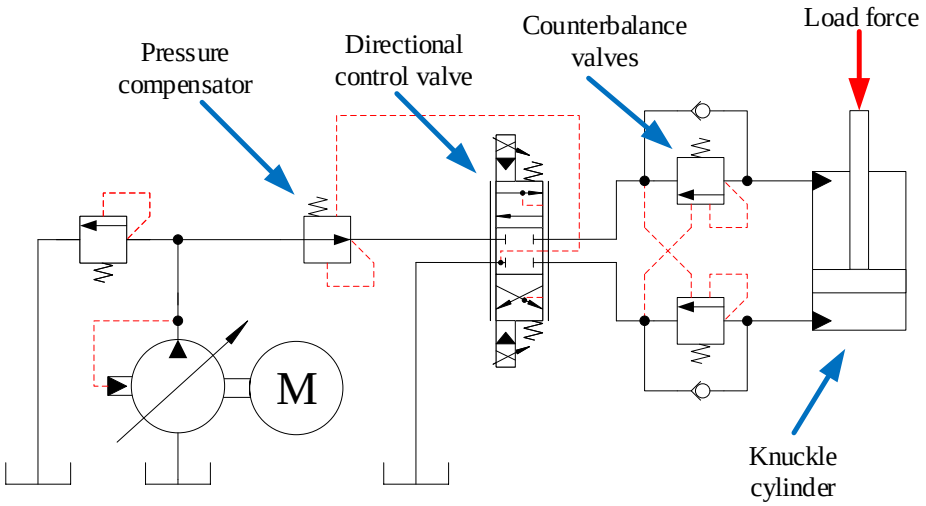

Figure 1.4: A simplified version of the hydraulic circuit for the knuckle cylinder. Taken from Paper B.

The control system for the crane is implemented on a CompactRIO from National Instruments. The CompactRIO sends the control signal to the valves, and reads the various sensors mounted on the crane. Programming of the CompactRIO is done in LabVIEW. An illustration of the connections between the CompactRIO and the crane are shown in Figure 1.5.

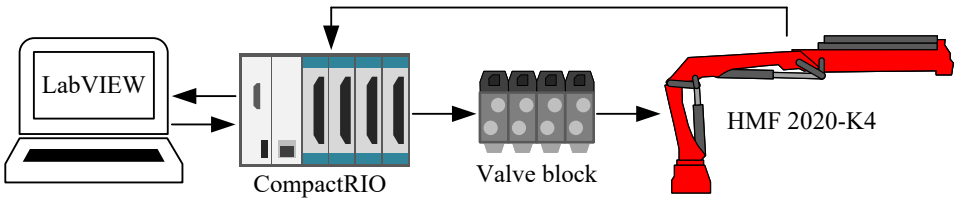

Figure 1.5: Connections between the CompactRIO and the crane. Taken from Paper B.

1.4 State of the Art

This section presents some of the current state-of-the-art topics and applications related to motion control of cranes and hydraulic manipulators. Some of the topics presented originate from robotics, and can be adapted to hydraulic cranes as a means to increase the level of automation for heavy duty lifting equipment. Due to the high-level nature of these topics they can be implemented both on robots and cranes. The topics presented are relevant to the control systems that have been developed during this project. This

section describes four of the most relevant topics for motion control of hydraulically actuated cranes, namely feedforward control, path control, anti-swing control, and deflection compensation.

1.4.1 Feedforward Control

Feedforward control is a technique which, unlike feedback control, does not rely on the measured system output or an error signal to generate a control signal. Instead, knowledge of the system parameters is used to generate the control signal based on an input signal. In essence, there exist two types of feedforward control. The first type is a disturbance controller, which uses the measured (or observed) disturbance to generate a control signal which will cancel the effect from the disturbance on the system. The second type utilizes the setpoint or reference signal to generate an output. In this case the feedforward controller uses the inverse of either the system dynamics or steady state gain. For both feedforward types a potential output error can be eliminated before it appears. This is in contrast to feedback control where an error must occur before the feedback controller kicks in. In practice, an additional feedback controller is used to compensate for the system dynamics and any steady state error in case of modeling errors or uncertainty. An example of a position control system using feedforward is shown in Figure 1.6.

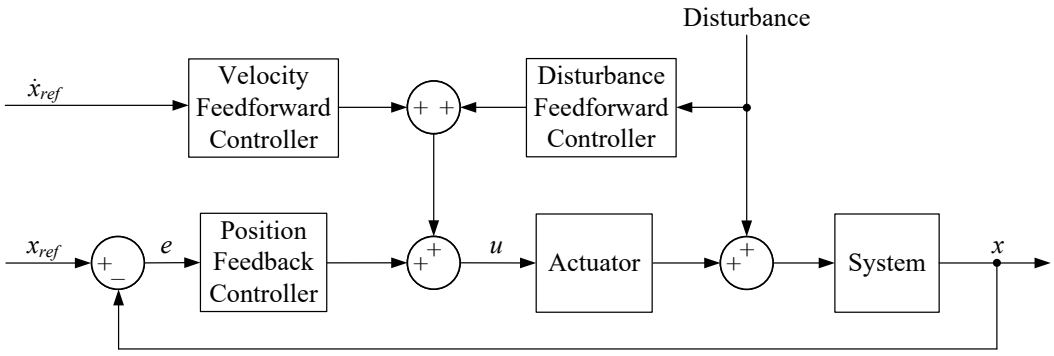

Figure 1.6: Example of a position control system using feedforward for both the velocity reference and measured disturbance in addition to position feedback control.

Feedforward control has been used in a wide variety of systems and control topologies. A classic application is position and velocity control where the inverse of a system or its steady state gain can be used. Applications include feedforward in combination with feedback control [2], feedforward pressure control [3, 4], control of piezo actuators [5], and nanopositioning systems [6].

Disturbance rejection is another topic for which feedforward is effective. Measurable disturbances from for example wind speed, gravity, and vibrations are used to compensate for the effects they exert on the system. Feedforward disturbance rejection has been used for suppression of vibrations in [7, 8, 9]. Disturbance compensation of systems with dead-time has been investigated in [10], where a novel feedforward controller with matching dead time was used. In [11] control of an underwater lifting body was developed. The controller was designed as a cascaded PID controller with feedforward based on the

estimated load. Feedforward is also a popular method to control systems with a lot of friction, which most of the times will be nonlinear. Typically, parameters are identified experimentally and a model of the friction is used for compensation inside the motion controller, see [12, 13, 14].

1.4.2 Path Control

Path control is a type of motion control where a manipulator is moved in space, typically between a set of given points. For some control systems, the motion can be split into three parts, an acceleration phase, a constant speed phase, and a deceleration phase. Also, synchronization of the motion between each actuator is often done to ensure all actuators have the same cycle time. Path control is commonly used for industrial robots, and point-to-point control of robotic systems can be found in literature in [15, 16, 17].

Regarding motion control of hydraulic cranes, different methods can be used. In general, either the position, velocity, or the force of the hydraulic actuator is controlled, or a combination of these. Various methods are found in literature, such as feed forward control [2], vector control [18], pressure control [3, 4], and force control [19, 20].

Tool-point control refers to a type of path control where the position of the tip of the manipulator is controlled. For manipulators without kinematic redundancy, tool point control is typically done using inverse kinematics, see [21, 22, 23]. For a given tool-point position, the corresponding joints angles of the manipulator can be calculated and used in the controller. Tool-point control has also been implemented on hydraulically actuated systems. This includes control of offshore cranes [24, 25, 26], control of a telescopic handler [27], tool-point velocity control of flexible loader cranes [28, 29, 30], and trajectory planning for a loader crane [31].

Various methods for more advanced motion control have been investigated in literature. Tool-point control for a loader crane with kinematic redundancy can be found in [32], and for a hydraulic manipulator in [33, 34]. In these cases the redundancy was solved using the pseudo-inverse Jacobian method. In [35], trajectory planning was developed and implemented on a forestry crane. The motion task was described in 3D Cartesian space, while the crane was controlled in 6 Degrees of Freedom (DOF) joint space. The transformation between joint space and Cartesian space imposes highly non-linear velocity constraints for the joints. A motion control system which included tool-point control, velocity control, configuration control, and flow sharing was developed for a loader crane in [36].

1.4.3 Anti-swing Control

Hanging loads are susceptible to pendulum-like motion and oscillations when moved by lifting equipment. Anti-swing control refers to the task of reducing or removing these oscillations. This is an extensively studied topic, and typical applications include cranes and lifting equipment in manufacturing plants, ports, and warehouses etc.

A hanging load which experiences this pendulum-like motion can increase operation time, reduce efficiency, and in the worst case lead to safety hazards and accidents. Dif-

ferent techniques have been tested to suppress this load swing. Anti-swing control is a difficult task, as systems with hanging loads are underactuated, meaning the degrees of freedom are greater than the number of controlled actuators.

Typically the anti-swing controllers are implemented on electric overhead cranes, where one or several servomotors control the translational motion of the crane. An illustration of an overhead crane with a hanging load is shown in Figure 1.7. The anti-swing control system is typically in parallel with the position control system for the crane. The anti-swing controller uses feedback from the swing angle to give an input to the servomotor. Early work on anti-swing control of overhead cranes includes [37, 38, 39, 40], where linearized models are utilized.

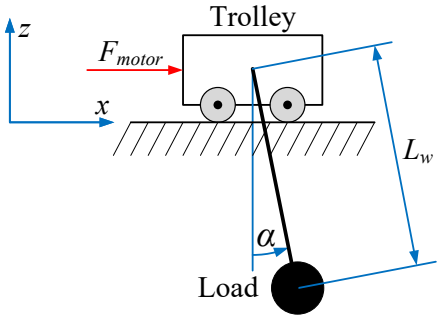

Figure 1.7: Illustration of an overhead crane with a hanging load, showing the payload angle α, wire length L_w, and translational force from the motor F_{motor}.

More advanced anti-swing control often uses a nonlinear model of the crane and hanging payload. These control systems include feedback linearization [41], optimal control [42], and Lyapunov-based control [43, 44]. Other types of nonlinear control have also been applied to anti-swing control, for example fuzzy logic control [45, 46, 46], sliding mode control [47, 48], and robust control [49]. In addition, active control of the wire length using a winch has also been investigated in [50, 51].

Input shaping is a method that can be used both for anti-swing and to suppress vibrations in flexible systems. This is a model based approach and is typically based on system dynamics, for example bandwidth and damping ratio. The input signal to the crane is designed to be self-canceling to suppress the oscillations [52, 53, 54].

Another method found in literature is called delayed reference control. In this case the position reference generator inside the control system is time-shifted based on feedback from the payload angle. This time-shift contributes to a motion in the opposing direction, and thereby the controller can suppress the oscillations in the hanging load [55, 56].

Anti-swing control for hydraulic cranes is not an extensively studied area, but reference includes [57] which investigates tool-point control and anti-swing for a planar hydraulic crane with a single degree of freedom for the hanging load.

1.4.4 Deflection Compensation

Some types of cranes and other manipulators may be considered flexible, and this flexibility will lead to deflections and oscillations of the mechanical structure. While flexible

manipulators can have some advantages over rigid structures, such as lower mass and inertia, higher payload-to-mass ratio, lower energy consumption and smaller actuators, the structural flexibility must be considered when used for precision motion control. This is where deflection compensation comes into play. Suppressing both the static deflection (due to gravity), and dynamic deflection (due to motion) have received research attention over the years.

The goal of the deflection compensator is to dampen oscillations and counteract static deflection in the flexible manipulator. Typically, this has been divided into two groups, model-based control and model-free control. Model-based control requires accurate models of the complex flexible system and various methods have been studied. These include assumed modes [58, 59, 60], Lagrangian formulation [61, 62], lumped parameter [63, 64, 65], and neural networks [66]. Model-based controllers can be implemented using feedforward, and include linear models [67], nonlinear inverse dynamics [68], and input shaping [69]. Model-free control utilizes feedback from the flexible system, and includes robust control and sliding mode control [70, 71, 72].

The use of neural networks for deflection compensation has also received interest. They can be used both in a feedforward and feedback topology, see [73]. Some neural network controllers are combined with sliding mode control, to provide stabilization and robust control of nonlinear systems [74, 75, 76].

1.5 Contributions

This thesis is based on six papers that have been published during the project period. They address the shortcomings in the current state of the art. There is a lack of developed and experimentally implemented methods for path control of hydraulic loader cranes and similar hydraulic manipulators with nonlinear kinematics and pressure compensated control valves. For this wide range of applications there is no path control based on actuator space taking into account both hanging loads and deflection of the structure. This is reflected in the research questions and the work done during this project. It is also recognized as the main topics of the published papers. The first milestone of this project is presented in Paper A, which is path control in actuator space. This path controller is used in all the following papers.

Paper A: Development of Point-to-Point Path Control in Actuator Space for Hydraulic Knuckle Boom Crane

Summary: This paper presents a novel method for point-to-point path control in actuator space. The path controller is implemented on a hydraulic loader crane. The developed path controller operates in actuator space of the crane, in contrast to joint space or Cartesian space. By utilizing the actuator space, most of the parameters and constraints of the system become either linear or constant. As such, the control system design in greatly simplified. In addition, the motion for each actuator is minimized compared to other methods, and it avoids change in direction of motion between two points. This significantly reduces jerky motion, fatigue, and energy consumption. However, unlike other

methods the tool-point does not move in a straight line from start to end. The use of actuator space is well suited for hydraulic cranes with pressure compensated DCVs, as the relationship between control signal and actuator velocity is linear. Therefore, system linearization or feedback linearization is not needed. In addition, optimization is used to minimize oscillations during motion. The novel method has been tested both in simulations and experiments, and shows good setpoint tracking and minimal oscillations.

Contributions: The developed path controller uses the concept of actuator space. It represents the first step towards automating motion control of the hydraulic crane, and is particularly suited for hydraulic machines with pressure compensated DCVs. The inherent minimization of the actuator motion is a major advantage of this type of path control. The path controller has been used in the five following papers in this thesis to test new control systems, showing its immediate usefulness.

Published as: Jensen, K.J.; Kjeld Ebbesen, M.; Rygaard Hansen, M. Development of Point-to-Point Path Control in Actuator Space for Hydraulic Knuckle Boom Crane. *Actuators* **2020**, *9(2)*, 27. doi:10.3390/act9020027

Paper B: Adaptive Feedforward Control of a Pressure Compensated Differential Cylinder

Summary: This paper presents an adaptive feedforward controller applied to a hydraulically actuated crane. The crane uses a pressure compensated DCV and differential cylinder as the actuator. The adaptive feedforward controller showcases the novelty of using two independent feedforward states, one for each direction of motion. Implemented for the motion control system, simulation results show the feasibility of the adaptive controller with a reduction in cylinder position error compared to an ideal fixed gain feedforward controller. From the experimental results the performance increase is even more pronounced, with an 80 % reduction in RMS position error. These results showcase that the novel controller with two separate feedforward states is able to adapt to model uncertainties in both directions of motion.

Contributions: A novel approach for adaptive feedforward control for hydraulic machines is developed, which is especially useful for systems with pressure compensated DCVs. These types of valves are frequently used in industry and this controller can be implemented for a wide variety of machines.

Published as: Jensen, K.J.; Ebbesen, M.K.; Hansen, M.R. Adaptive Feedforward Control of a Pressure Compensated Differential Cylinder. *Appl. Sci.* **2020**, *10(21)*, 7847. doi:10.3390/app10217847

Paper C: Anti-swing control of a hydraulic loader crane with a hanging load

Summary: This paper presents a solution to the challenges associated with hanging loads, and investigates anti-swing control for a hydraulic loader crane. A planar 2-DOF case is considered, and both the hanging load dynamics and rigid-body kinematics are derived to create an anti-swing controller. The anti-swing controller operates in parallel to the position controller, and generates a set of tool-point velocities to cancel the pendulum-like motion of the hanging payload. A simulation is conducted while running path control in actuator space, and the results show a significant reduction in the load swing during motion. In addition, experiments are conducted to verify the performance of the controller in a real-world scenario. Experimental results also show a large reduction in the load swing.

Contributions: A new method for anti-swing control for hydraulic cranes is developed, where the control system is utilizing the properties of the pressure compensated DCVs. This paper shows the feasibility of anti-swing control for large and slow(er) hydraulic cranes. Applications include hydraulic cranes both offshore and onshore. These control systems have previously been limited to electric cranes with high-bandwidth servo-drives.

Published as: Jensen, K.J.; Kjeld Ebbesen, M.; Rygaard Hansen, M. Anti-swing control of a hydraulic loader crane with a hanging load. *Mechatronics* **2021**, 77, 102599. doi:10.1016/j.mechatronics.2021.102599

Paper D: Novel Concept for Electro-Hydrostatic Actuators for Motion Control of Hydraulic Manipulators

Summary: This paper investigates the design and application of an EHA for motion control of hydraulic cranes as an alternative to valve-controlled systems. A novel concept is proposed which complies with requirements such as overload handling, flow compensation, regeneration capability, and passive load holding. An analysis of four quadrant operation is conducted which shows high energy efficiency and closed loop performance. A numerical simulation is conducted which compares the novel concept with a traditional valve-controlled system. The simulation uses path control and anti-swing control of a hydraulic crane as a load case. The comparative results show a significant reduction in energy consumption with similar position tracking performance.

Contributions: Design and investigation of the feasibility and improved efficiency of EHAs for hydraulic cranes. This paper shows the development of actuation systems for the next generation of hydraulic manipulators. The novel concept is able to regenerate energy, and the elimination of throttling valves significantly reduces energy consumption compared to a conventional hydraulic system.

Published as: Jensen, K.J.; Kjeld Ebbesen, M.; Rygaard Hansen, M. Novel Concept for Electro-Hydrostatic Actuators for Motion Control of Hydraulic Manipulators.

Energies **2021**, *14(20)*, 6566. doi:10.3390/en14206566

Paper E: Development of 3D Anti-Swing Control for Hydraulic Knuckle Boom Crane

Summary: This paper presents anti-swing control in three dimensions applied to a hydraulic loader crane. The handing load dynamics and rigid-body kinematics are derived and used to design the anti-swing controller. The controller generates a set of tool-point velocities based on the measured payload angles, and the kinematic functions are used to transform the control signal into actuator space. A simulation is conducted which identifies the challenge with using the slewing motion. Therefore, pressure feedback is implemented and simulation results show a significant reduction in the payload angles during motion. Experiments confirm the challenges with the slewing motion, but the developed pressure feedback controller is able to stabilize the system. The experimental results show that the anti-swing controller yields good suppression of the payload angles in practice.

Contributions: An extension of paper C featuring a fully developed anti-swing control system in three dimensions using rigid-body kinematics and pressure feedback to successfully dampen oscillations in both the crane motion and hanging load. As most cranes operate in three dimensions this paper is of significant relevance for a wide variety of hydraulic cranes.

Published as: Jensen, K.J.; Kjeld Ebbesen, M.; Rygaard Hansen, M. Development of 3D Anti-Swing Control for Hydraulic Knuckle Boom Crane. *Modeling, Identification and Control* 42(3):113–129, 2021. doi:10.4173/mic.2021.3.2

Paper F: Online Deflection Compensation of a Flexible Hydraulic Loader Crane Using Neural Networks and Pressure Feedback

Summary: This paper presents the development of a deflection compensator implemented on a hydraulic loader crane. A neural network deflection estimator is trained based on measurements from the laboratory, and kinematic functions are derived to transform the estimated static deflection into actuator space. The static deflection compensator is used in a feedforward topology, while a dynamic deflection compensator is developed and used in a feedback topology. The dynamic compensator uses pressure feedback and an adaptive bandpass filter to counteract the oscillations in the flexible crane. Simulation results showcase the feasibility of the proposed controllers. Experiments are also conducted while running path control, and the results showcase the effectiveness of the static and dynamic compensators. The experimental results show a 90 % decrease in tool point deviation.

Contributions: This paper shows the development of both static and dynamic deflection compensation of large and flexible manipulators, specifically hydraulic cranes for lifting and load handling. The designed control system is able to solve one of the challenges with

flexible cranes, and successfully counteracts the deflections arising when lifting heavy payloads.

Published as: Jensen, K.J.; Kjeld Ebbesen, M.; Rygaard Hansen, M. Online Deflection Compensation of a Flexible Hydraulic Loader Crane Using Neural Networks and Pressure Feedback. *Robotics* **2022**, *11(2)*, 34. doi:10.3390/robotics11020034

Chapter 2

Background Theory and Modeling

This chapter presents various topics which are more general in nature, and will serve as background theory for this thesis. The topics presented have all been used in the published papers and cover a wide range of fields related to engineering. This includes modeling of hydraulic components, electric motors, and kinematics of mechanical systems. In addition, optimization and some machine learning is presented. These topics can be applied in the context of model based design and virtual prototyping, in order to develop a complex mechatronic system.

2.1 Hydraulic Modeling

When developing hydraulic systems, methods like modeling and simulation play an important role in the design process. Deriving accurate models of critical hydraulic components is vital for simulation of complex multi-domain systems such as hydraulic cranes. Focus has been directed towards the modeling of pressure compensated DCVs and CBVs, as these are used in many modern hydraulic machines as well as the HMF 2020K4 crane used in this project. For this reason models of these valves are included in the simulations for all six papers in this project. An example of a state-of-the-art load sensing circuit for a hydraulic crane using these components is shown in Figure 2.1.

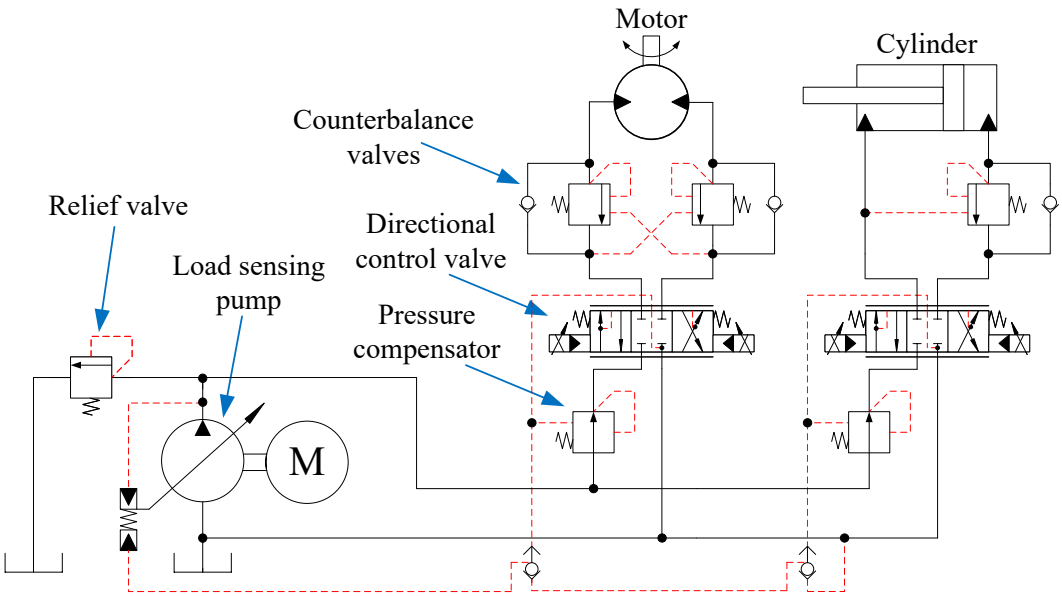

Figure 2.1: Hydraulic circuit for a crane with two actuators using load sensing.

2.1.1 Pressure Compensated Directional Control Valves

In many state-of-the-art hydraulic systems the pressure compensated DCV is used as it provides load independent flow control. They are often used in combination with load sensing pumps, which increases system efficiency since only the required pressure is generated. An illustration of a pressure compensated DCV is shown in Figure 2.2.

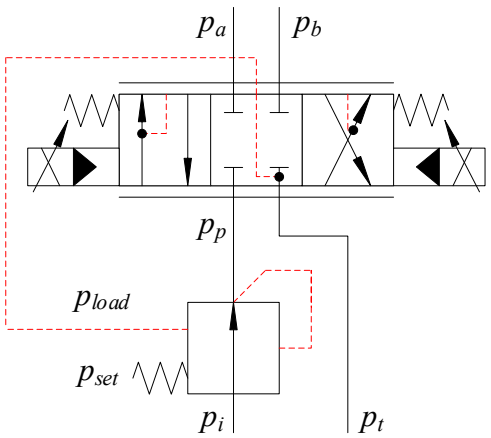

Figure 2.2: Pressure compensated DCV. Taken from Paper B.

The pressure compensator senses the load pressure and throttles the flow to keep the pressure drop over the DCV constant. This ensures that the flow is only dependent on the spool position. The governing equations for the pressure compensator are given in Equations (2.1)-(2.3).

$$u_{PC} = \frac{p_{set} + p_{load} - p_p}{\Delta p_{PC}} \tag{2.1}$$

$$p_{load} = \begin{cases} p_a & \text{if } u_{spool} \geq 0 \\ p_b & \text{otherwise} \end{cases} \tag{2.2}$$

$$Q_{PC} = k_{PC} \cdot u_{PC} \cdot \sqrt{p_i - p_p} \tag{2.3}$$

where

u_{PC}	=	opening of compensator, $0 \leq u_{PC} \leq 1$
p_p	=	compensated pressure at port p
Δp_{PC}	=	pressure difference when fully opened
p_a	=	pressure at port a
p_b	=	pressure at port b
p_t	=	tank pressure
p_{set}	=	spring pressure setting
p_{load}	=	load pressure
u_{spool}	=	main spool position, $-1 \leq u_{spool} \leq 1$
Q_{PC}	=	flow through pressure compensator
k_{PC}	=	flow gain of compensator
p_i	=	compensator inlet pressure

When the pressure compensator is throttling the flow, the steady state value of p_p is then given by Equation (2.4).

$$p_p = p_{load} + p_{set} \tag{2.4}$$

The sensing of the load pressures p_a and p_b ensures a constant pressure drop over the DCV, equal to p_{set}. This yields a load independent flow and is shown in Equation (2.5).

$$\begin{aligned} Q_{DCV} &= k_{DCV} \cdot u_{spool} \cdot \sqrt{p_p - p_{load}} \\ &= k_{DCV} \cdot u_{spool} \cdot \sqrt{p_{set}} \\ &= Q_{DCV,max} \cdot u_{spool} \end{aligned} \tag{2.5}$$

where

k_{DCV}	=	flow gain of the DCV
$Q_{DCV,max}$	=	maximum valve flow for the DCV

The model of the DCV is now only dependent on the rated flow and the control signal sent to the valve.

2.1.2 Counterbalance Valves

The CBV is a core component in many hydraulic systems, as it adds various safety features to the system. This includes load holding, safe lowering of loads, and protection against over pressure and burst pressure. If mounted directly on a hydraulic actuator it will also protect against overrunning loads in case of hose rupture. Figure 2.3 shows an example of double CBVs.

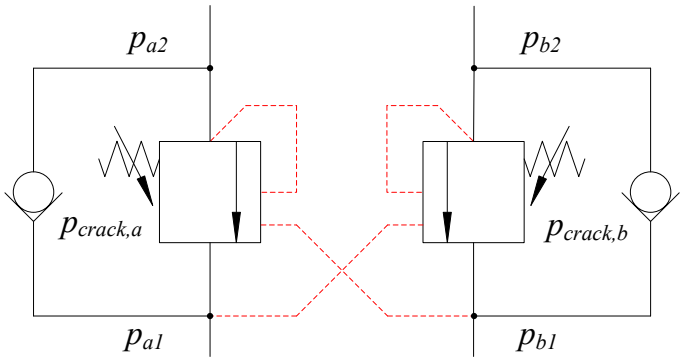

Figure 2.3: Double CBVs.

The CBV can be modeled as a variable orifice based on the static equilibrium for the internal poppet. For valve a in Figure 2.3 the spring force tries to keep the valve closed, while the backpressure p_{a2} and opposing pressure p_{b2} tries to open the valve. The opposing pressure usually acts on a larger area than the backpressure, and the ratio between these two areas is typically denoted ψ. The unitless opening for the CBV can be calculated as shown in Equations (2.6) and (2.7).

$$u_a = \frac{p_{a2} + \psi \cdot p_{b1} - p_{crack,a}}{\Delta p_{CBV}} \tag{2.6}$$

$$u_b = \frac{p_{b2} + \psi \cdot p_{a1} - p_{crack,b}}{\Delta p_{CBV}} \tag{2.7}$$

where

u_a	=	opening of valve a, $0 \leq u_a \leq 1$
u_b	=	opening of valve b, $0 \leq u_b \leq 1$
p_{a1}	=	pressure at valve a input side
p_{a2}	=	pressure at valve a actuator side
p_{b1}	=	pressure at valve b input side
p_{b2}	=	pressure at valve b actuator side
$p_{crack,a}$	=	crack pressure of valve a
$p_{crack,b}$	=	crack pressure of valve b
ψ	=	pilot area ratio
Δp_{CBV}	=	pressure difference when fully opened

The openings u_a and u_b can be used in combination with the rated flow and pressure drop of the CBV to model the variable orifice.

The hydraulic modeling has ensured that the dynamics of the hydraulic system is included in the simulations in the papers, while keeping the computational costs and modeling complexity at a minimum.

2.2 Electric Modeling

This section covers the modeling of electric motors, both synchronous and asynchronous. Electric motors are often used as prime movers for hydraulic systems, in addition to

countless applications in various industries. While the asynchronous induction motor has been an industry work horse for decades, synchronous motors such as the permanent magnet synchronous motors (PMSM) are becoming increasingly popular. For instance, electrification is pushing the use of large PMSMs in electric vehicles, while smaller PMSMs are being used in servo positioning systems, often replacing DC-motors or even hydraulic systems.

2.2.1 Servomotor and Servodrive

The servomotor is used as an actuator in many mechatronic systems due to its precise position control, high torque density, and low inertia. In paper D a servomotor is used as the prime mover for an electro-hydrostatic actuator (EHA). Most servomotors are three-phase PMSMs, and modeling of both the servomotor and the servodrive is typically done in the *dq*-frame, also called the rotating reference frame. Transforming the three-phase voltages into the *dq*-frame is done using the Park transformation, defined in Equations (2.8) and (2.9). The governing equations for the PMSM in the *dq*-frame are given in Equations (2.10)-(2.12).

$$\begin{bmatrix} u_d \\ u_q \end{bmatrix} = \mathbf{P} \cdot \begin{bmatrix} u_a \\ u_b \\ u_c \end{bmatrix} \tag{2.8}$$

$$\mathbf{P} = \frac{2}{3} \cdot \begin{bmatrix} \cos(\theta_e) & \cos(\theta_e - \frac{2\pi}{3}) & \cos(\theta_e + \frac{2\pi}{3}) \\ -\sin(\theta_e) & -\sin(\theta_e - \frac{2\pi}{3}) & -\sin(\theta_e + \frac{2\pi}{3}) \end{bmatrix} \tag{2.9}$$

where

u_d	=	d-axis voltage
u_q	=	q-axis voltage
u_a	=	a-phase voltage
u_b	=	b-phase voltage
u_c	=	c-phase voltage
θ_e	=	electrical rotor angle

$$u_d = R_s \cdot i_d + L_d \cdot \frac{di_d}{dt} - N_p \cdot \omega \cdot i_q \cdot L_q \tag{2.10}$$

$$u_q = R_s \cdot i_q + L_q \cdot \frac{di_q}{dt} + N_p \cdot \omega \cdot (i_d \cdot L_d + \lambda_m) \tag{2.11}$$

$$T_m = \frac{3}{2} \cdot N_p \cdot (i_q \cdot (i_d \cdot L_d + \lambda_m) - i_d \cdot i_q \cdot L_q) \tag{2.12}$$

where

R_s	=	stator resistance
L_d	=	d-axis inductance
L_q	=	q-axis inductance
i_d	=	d-axis current
i_q	=	q-axis current
N_p	=	number of pole pairs
ω	=	motor speed
λ_m	=	permanent magnet flux linkage
T_m	=	motor torque

A servodrive typically consists of current controllers for both the d-axis and q-axis currents, along with a speed controller. Since the current i_d is the flux-producing component, the current reference $i_{d,ref}$ is typically set to zero since the permanent magnet provides the necessary flux. In cases where field-weakening is used $i_{d,ref}$ will become negative. An illustration of a servodrive is shown in Figure 2.4. An encoder is used to measure the rotor angle and speed, while space vector modulation (SVM) is used to generate the signals for the inverter.

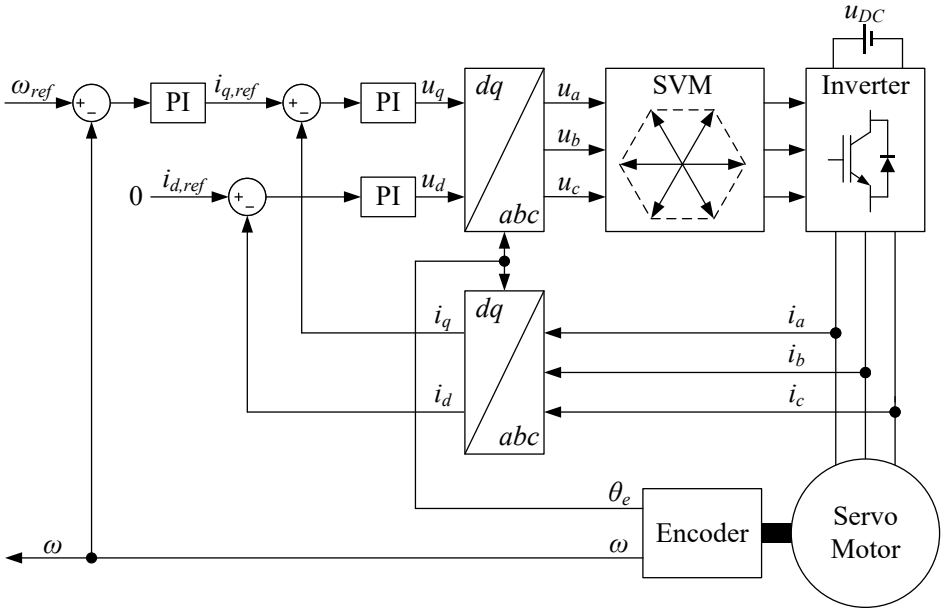

Figure 2.4: Servodrive the dq-frame with a PMSM.

2.2.2 Induction Motor

In many industrial hydraulic systems an induction motor is used as the prime mover for the hydraulic pump. The induction motor offers many advantages, such as low cost, high reliability, and self-starting capability. The induction motor is also used in other applications such as fans, water pumps, and drive trains. Due to its widespread use, modeling and simulation of an induction motor is of interest for many industries. A model of an induction motor was used in Paper D as the prime mover for a hydraulic load sensing system.

A common model for the induction motor is the T model, often used in steady state analysis and for parameter estimation. This is shown in Figure 2.5. Another model which is common in vector control applications is the inverse-Γ model, shown in Figure 2.6.

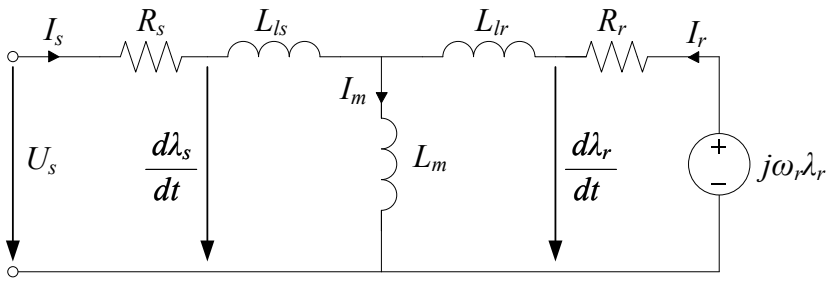

Figure 2.5: Dynamic T model of an induction motor.

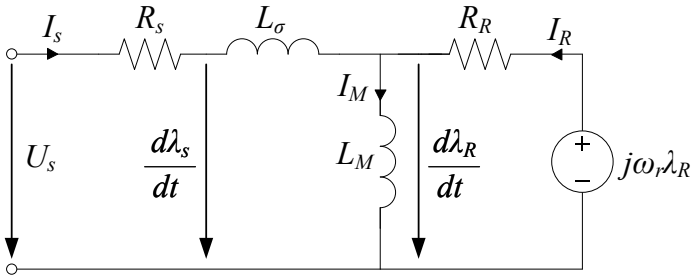

Figure 2.6: Dynamic inverse-Γ model of an induction motor.

In both models the $\alpha\beta$-frame is used, i.e. the two-axis stationary reference frame. Transforming the three-phase voltages into the $\alpha\beta$-frame is done using the Clarke transformation, shown in Equations (2.13) and (2.14).

$$\mathbf{U}_s = \begin{bmatrix} u_\alpha \\ u_\beta \end{bmatrix} = \mathbf{C} \cdot \begin{bmatrix} u_a \\ u_b \\ u_c \end{bmatrix} \tag{2.13}$$

$$\mathbf{C} = \frac{2}{3} \cdot \begin{bmatrix} 1 & -\frac{1}{2} & -\frac{1}{2} \\ 0 & \frac{\sqrt{3}}{2} & -\frac{\sqrt{3}}{2} \end{bmatrix} \tag{2.14}$$

where

U_s = stator voltage vector
u_α = α-axis voltage
u_β = β-axis voltage

Transforming the motor parameters from the T model to the inverse-Γ model is done according to Equations (2.15)-(2.19). Note that the stator resistance R_s is the same for

both models.

$$L_s = L_{ls} + L_m \tag{2.15}$$
$$L_r = L_{lr} + L_m \tag{2.16}$$
$$L_M = \frac{L_m^2}{L_r} \tag{2.17}$$
$$L_\sigma = L_s - L_M \tag{2.18}$$
$$R_R = \left(\frac{L_m}{L_r}\right)^2 \cdot R_r \tag{2.19}$$

where

L_s	=	stator inductance
L_r	=	rotor inductance
L_{ls}	=	stator leakage inductance
L_{lr}	=	rotor leakage inductance
L_m	=	magnetizing inductance
L_M	=	inverse-Γ magnetizing inductance
L_σ	=	inverse-Γ leakage inductance
R_r	=	rotor resistance
R_R	=	inverse-Γ rotor resistance

The governing equations for the inverse-Γ model is shown in Equations (2.20)-(2.25). Note that λ_R^* is the complex conjugate of λ_R.

$$U_s = R_s \cdot I_s + \frac{d\lambda_s}{dt} \tag{2.20}$$
$$0 = R_R \cdot I_R + \frac{d\lambda_R}{dt} - j \cdot \omega_r \cdot \lambda_R \tag{2.21}$$
$$I_M = I_s + I_R \tag{2.22}$$
$$\lambda_s = L_\sigma \cdot I_s + L_M \cdot I_M \tag{2.23}$$
$$\lambda_R = L_M \cdot I_M \tag{2.24}$$
$$T_m = \frac{3}{2} \cdot N_p \cdot \mathrm{Im}\{\lambda_R^* \cdot I_s\} \tag{2.25}$$

where

I_s	=	stator current
I_R	=	rotor current
I_M	=	magnetizing current current
λ_s	=	stator flux
λ_R	=	rotor flux
ω_r	=	rotor speed

2.3 Rigid-body Kinematics

Kinematics describe the motion of bodies in a system without considering the forces involved. Kinematic analysis of rigid multi-body systems such as cranes or robots is

typically conducted based on the geometry of the system and the types of joints involved. This section provides details of the kinematics of the hydraulic loader crane used in this project.

2.3.1 Forward Kinematics

Forward kinematics refers to the transformation between joint space and Cartesian space. The forward kinematics are derived based on the Denavit-Hartenberg parameters for the system. Figure 2.7 shows the joint angles, telescopic length, lifting radius, and tip position of the HMF 2020K4 crane. Figure 2.8 shows the geometry when both booms are horizontal. The dimensions of the booms are shown in Table 2.1. The Denavit-Hartenberg parameters for this configuration are shown in Table 2.2. **R** and **T** are rotational and translational matrices, and the angles θ_m and θ_k denote the rotation about the main joint and knuckle joint, respectively.

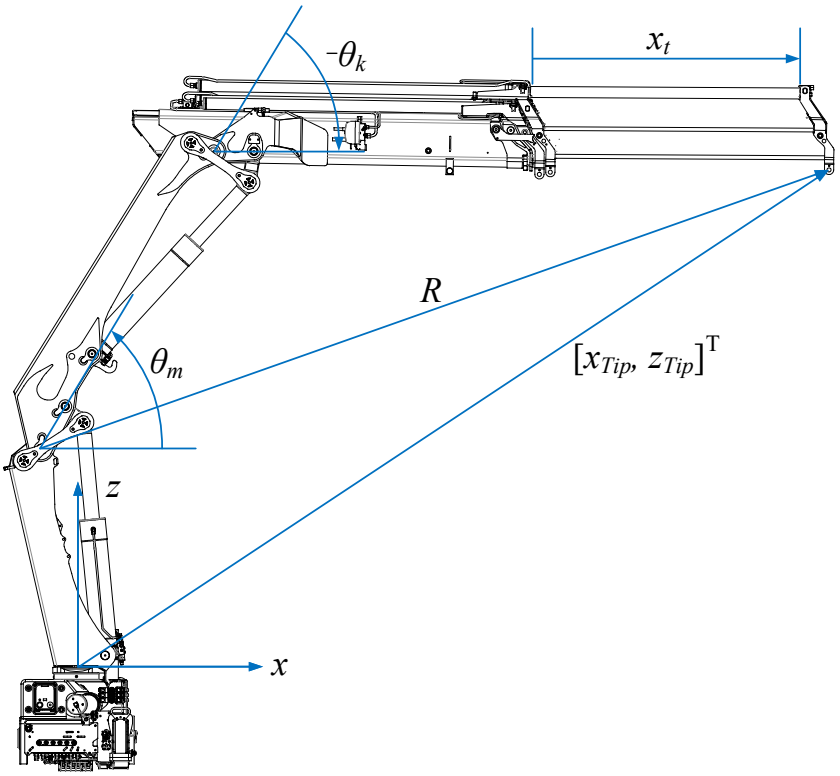

Figure 2.7: Crane geometry showing the joint angles θ_m and θ_k, lifting radius R, telescopic length x_t, and crane tip positions x_{Tip} and z_{Tip}. Taken from Paper F.

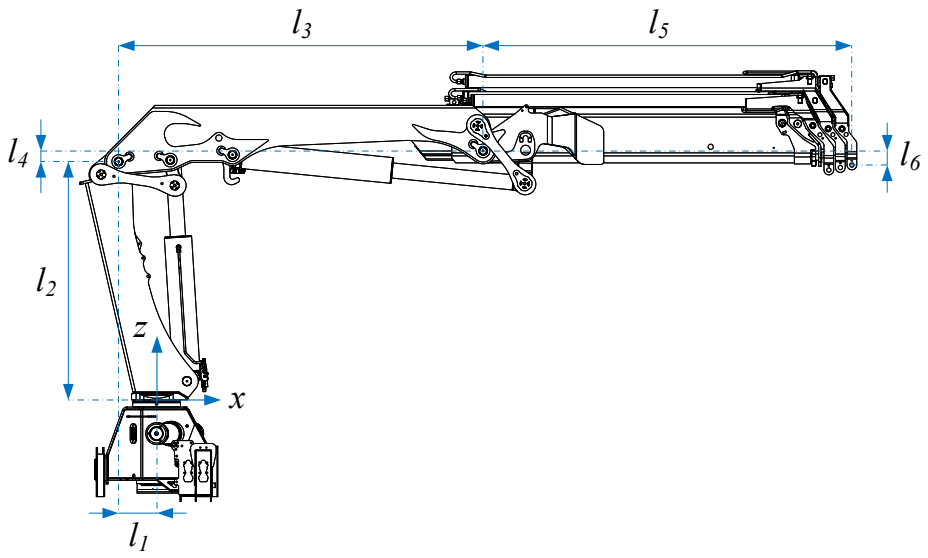

Figure 2.8: Crane geometry used with Denavit-Hartenberg parameters. Taken from Paper F.

Table 2.1: Dimensions shown in Figure 2.8.

Name	Length [m]
l_1	0.250
l_2	1.569
l_3	2.400
l_4	0.070
l_5	2.429
l_6	0.093

Table 2.2: Denavit-Hartenberg parameters using the main cylinder, knuckle cylinder, and telescopic cylinder.

$\mathbf{R}_z$	$\mathbf{T}_z$	$\mathbf{T}_x$	$\mathbf{R}_x$
0	l_2	$-l_1$	90°
θ_m	0	0	−90°
0	l_4	l_3	90°
θ_k	0	0	−90°
0	$-l_6$	l_5	0
0	0	x_t	0

For the following equations the notation $c_{\theta_m} = \cos(\theta_m)$ and $s_{\theta_m} = \sin(\theta_m)$ is used. Given a set of Denavit-Hartenberg parameters, a transformation matrix $\mathbf{A}_{DH}$ of the for-

ward kinematics can be calculated, given as:

$$\begin{aligned}\mathbf{A}_{DH} &= \mathbf{T}_z(l_2)\cdot\mathbf{T}_x(-l_1)\cdot\mathbf{R}_x(90^\circ)\cdot\mathbf{R}_z(\theta_m)\cdot\mathbf{R}_x(-90^\circ)\cdot\mathbf{T}_z(l_4)\cdot\mathbf{T}_x(l_3)\cdot\mathbf{R}_x(90^\circ) \\ &\quad\cdot\mathbf{R}_z(\theta_k)\cdot\mathbf{R}_x(-90^\circ)\cdot\mathbf{T}_z(-l_6)\cdot\mathbf{T}_x(l_5)\cdot\mathbf{T}_x(x_t) \qquad (2.26)\\ &= \begin{bmatrix} c_{\theta_m+\theta_k} & 0 & -s_{\theta_m+\theta_k} & x_{Tip} \\ 0 & 1 & 0 & 0 \\ s_{\theta_m+\theta_k} & 0 & c_{\theta_m+\theta_k} & z_{Tip} \\ 0 & 0 & 0 & 1 \end{bmatrix} \qquad (2.27)\end{aligned}$$

The crane tip positions x_{Tip} and z_{Tip} are given in Equations (2.28) and (2.29).

$$x_{Tip} = -l_1 + l_3\cdot c_{\theta_m} - l_4\cdot s_{\theta_m} + l_5\cdot c_{\theta_m+\theta_k} + l_6\cdot s_{\theta_m+\theta_k} + x_t\cdot c_{\theta_m+\theta_k} \qquad (2.28)$$

$$z_{Tip} = l_2 + l_3\cdot s_{\theta_m} + l_4\cdot c_{\theta_m} + l_5\cdot s_{\theta_m+\theta_k} - l_6\cdot c_{\theta_m+\theta_k} + x_t\cdot s_{\theta_m+\theta_k} \qquad (2.29)$$

2.3.2 Inverse Kinematics

Inverse kinematics describes the relation between Cartesian space and joint space and has been implemented in paper F. In this paper only the motion in the xz-plane is considered, using the main cylinder, knuckle cylinder, and telescopic cylinder. This gives the crane kinematic redundancy, which was removed by keeping the telescopic actuator length x_t fixed and solving for the main joint angle θ_m and knuckle joint angle θ_k.

The calculations are based on the lifting radius R, defined as the distance from the main joint to the crane tip. The squared lifting radius R^2 is shown in Equation 2.30.

$$R^2 = (x_{Tip} + l_1)^2 + (z_{Tip} - l_2)^2 \qquad (2.30)$$

First, an expression for the knuckle boom angle θ_k is derived. Inserting Equations (2.28) and (2.29) into (2.30) yields

$$\begin{aligned}R^2 &= (l_3\cdot c_{\theta_m} - l_4\cdot s_{\theta_m} + l_5\cdot c_{\theta_m+\theta_k} + l_6\cdot s_{\theta_m+\theta_k} + x_t\cdot c_{\theta_m+\theta_k})^2 \\ &\quad + (l_3\cdot s_{\theta_m} + l_4\cdot c_{\theta_m} + l_5\cdot s_{\theta_m+\theta_k} - l_6\cdot c_{\theta_m+\theta_k} + x_t\cdot s_{\theta_m+\theta_k})^2 \\ &= 2\cdot(l_3\cdot l_5 - l_4\cdot l_6 + l_3\cdot x_t)\cdot c_{\theta_k} + 2\cdot(l_3\cdot l_6 + l_4\cdot l_5 + l_4\cdot x_t)\cdot s_{\theta_k} \qquad (2.31)\\ &\quad + l_3^2 + l_4^2 + l_5^2 + l_6^2 + 2\cdot l_5\cdot x_t + x_t^2\end{aligned}$$

The equations can be presented in a more compact form, given below:

$$R^2 = A\cdot c_{\theta_k} + B\cdot s_{\theta_k} + C \qquad (2.32)$$

$$A = 2\cdot(l_3\cdot l_5 - l_4\cdot l_6 + l_3\cdot x_t) \qquad (2.33)$$

$$B = 2\cdot(l_3\cdot l_6 + l_4\cdot l_5 + l_4\cdot x_t) \qquad (2.34)$$

$$C = l_3^2 + l_4^2 + l_5^2 + l_6^2 + 2\cdot l_5\cdot x_t + x_t^2 \qquad (2.35)$$

Solving Equation (2.32) yields two solutions, and by taking the minimum angle the crane will be in the desired elbow-up configuration. The calculation of θ_k is shown below:

$$\theta_k^* = 2\cdot\tan^{-1}\left(\frac{B \pm \sqrt{A^2 + B^2 - C^2 + 2\cdot C\cdot R^2 - R^4}}{A - C + R^2}\right) \qquad (2.36)$$

$$\theta_k = \min(\theta_k^*) \qquad (2.37)$$

The next step is to calculate θ_m. Expanding and factorizing Equations (2.28) and (2.29) yields:

$$x_{Tip} = (l_5 \cdot c_{\theta_k} + l_6 \cdot s_{\theta_k} + x_t \cdot c_{\theta_k} + l_3) \cdot c_{\theta_m} - (l_5 \cdot s_{\theta_k} - l_6 \cdot c_{\theta_k} + x_t \cdot s_{\theta_k} + l_4) \cdot s_{\theta_m} - l_1 \quad (2.38)$$

$$z_{Tip} = (l_5 \cdot s_{\theta_k} - l_6 \cdot c_{\theta_k} + x_t \cdot s_{\theta_k} + l_4) \cdot c_{\theta_m} + (l_5 \cdot c_{\theta_k} + l_6 \cdot s_{\theta_k} + x_t \cdot c_{\theta_k} + l_3) \cdot s_{\theta_m} + l_2 \quad (2.39)$$

Rearranging gives a more compact form, yielding two equations with two unknowns, namely $\cos(\theta_m)$ and $\sin(\theta_m)$.

$$x_{Tip} = E \cdot c_{\theta_m} - D \cdot s_{\theta_m} - l_1 \quad (2.40)$$

$$z_{Tip} = D \cdot c_{\theta_m} + E \cdot s_{\theta_m} + l_2 \quad (2.41)$$

$$D = l_5 \cdot s_{\theta_k} - l_6 \cdot c_{\theta_k} + x_t \cdot s_{\theta_k} + l_4 \quad (2.42)$$

$$E = l_5 \cdot c_{\theta_k} + l_6 \cdot s_{\theta_k} + x_t \cdot c_{\theta_k} + l_3 \quad (2.43)$$

These two equations can then be solved to find θ_m.

$$c_{\theta_m} = \frac{D \cdot z_{Tip} - D \cdot l_2 + E \cdot x_{Tip} + E \cdot l_1}{D^2 + E^2} \quad (2.44)$$

$$s_{\theta_m} = \frac{E \cdot z_{Tip} - E \cdot l_2 - D \cdot x_{Tip} - D \cdot l_1}{D^2 + E^2} \quad (2.45)$$

$$\theta_m = \tan^{-1}\left(\frac{s_{\theta_m}}{c_{\theta_m}}\right) \quad (2.46)$$

2.3.3 Actuator Kinematics

Actuator kinematics describe the relation between actuator space and joint space, namely the joint angles as functions of the cylinder lengths, $\theta_m(x_m)$ and $\theta_k(x_k)$. An illustration of the main joint linkage is shown in Figure 2.9. The associated lengths are given in Table 2.3. The coordinate x_m is the length of the hydraulic cylinder, and the length l_e is an intermediate length used to apply the law of cosines for the calculations.

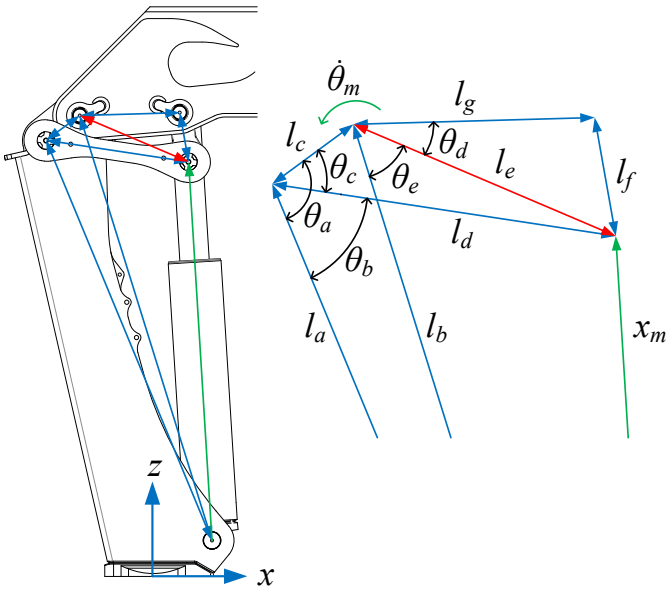

Figure 2.9: Illustration of the main joint actuator kinematics.

Table 2.3: Lengths of the parts in the main linkage.

Name	Length [m]
l_a	1.473
l_b	1.514
l_c	0.143
l_d	0.490
l_f	0.170
l_g	0.340

The calculation of the main joint angle $\theta_m = \theta_m(x_m)$ is given in Equations (2.47)-(2.53). An offset angle $\tilde{\theta}_m = 1.3$ rad is subtracted from $\theta_d + \theta_e$ to ensure that the main boom is horizontal when $\theta_m = 0$.

$$\theta_a = \cos^{-1}\left(\frac{l_a^2 + l_c^2 - l_b^2}{2 \cdot l_a \cdot l_c}\right) \tag{2.47}$$

$$\theta_b = \cos^{-1}\left(\frac{l_a^2 + l_d^2 - x_m^2}{2 \cdot l_a \cdot l_d}\right) \tag{2.48}$$

$$\theta_c = \theta_a - \theta_b \tag{2.49}$$

$$l_e = \sqrt{l_c^2 + l_d^2 - 2 \cdot l_c \cdot l_d \cdot \cos(\theta_c)} \tag{2.50}$$

$$\theta_d = \cos^{-1}\left(\frac{l_e^2 + l_g^2 - l_f^2}{2 \cdot l_e \cdot l_g}\right) \tag{2.51}$$

$$\theta_e = \cos^{-1}\left(\frac{l_b^2 + l_e^2 - x_m^2}{2 \cdot l_b \cdot l_e}\right) \tag{2.52}$$

$$\theta_m = \theta_d + \theta_e - \tilde{\theta}_m \tag{2.53}$$

To calculate the actuator space kinematics for the knuckle joint, the same procedure is followed as with the main joint. The geometry for the knuckle linkage is shown in Figure 2.10. The coordinate x_k is the length of the hydraulic cylinder, and the length l_l is the intermediate length. The lengths of the knuckle linkage system are shown in Table 2.4.

Table 2.4: Lengths of the knuckle linkage.

Name	Length [m]
l_h	1.626
l_i	1.650
l_j	0.168
l_k	0.490
l_m	0.220
l_n	0.280

As with the main joint, an offset angle $\tilde{\theta}_k = 3.1086$ rad is used to ensure that the knuckle boom is horizontal when $\theta_m + \theta_k = 0$. The calculations for the knuckle joint angle

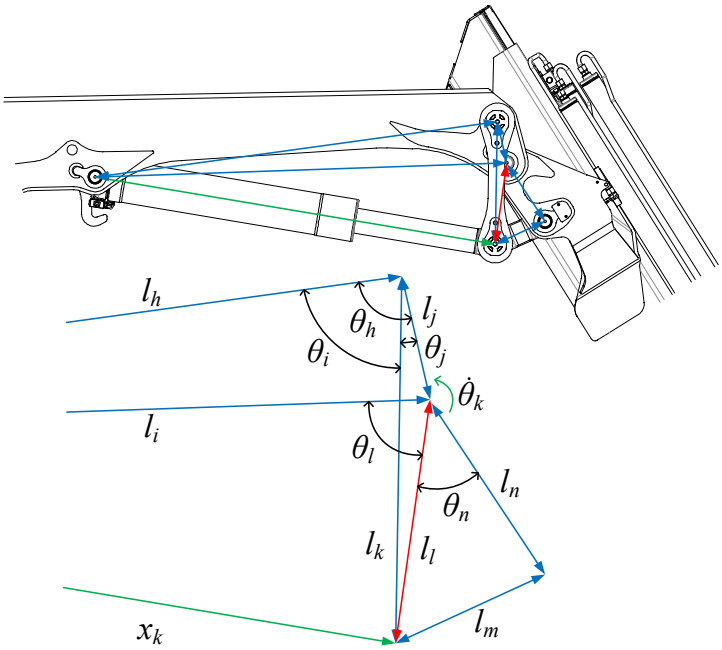

Figure 2.10: Geometry of the linkage system for the knuckle joint.

$\theta_k = \theta_k(x_k)$ are shown in Equations (2.54)-(2.60).

$$\theta_h = \cos^{-1}\left(\frac{l_h^2 + l_j^2 - l_i^2}{2 \cdot l_h \cdot l_j}\right) \tag{2.54}$$

$$\theta_i = \cos^{-1}\left(\frac{l_h^2 + l_k^2 - x_k^2}{2 \cdot l_h \cdot l_k}\right) \tag{2.55}$$

$$\theta_j = \theta_h - \theta_i \tag{2.56}$$

$$l_l = \sqrt{l_j^2 + l_k^2 - 2 \cdot l_j \cdot l_k \cdot \cos(\theta_j)} \tag{2.57}$$

$$\theta_n = \cos^{-1}\left(\frac{l_l^2 + l_n^2 - l_m^2}{2 \cdot l_l \cdot l_n}\right) \tag{2.58}$$

$$\theta_l = \cos^{-1}\left(\frac{l_i^2 + l_l^2 - x_k^2}{2 \cdot l_i \cdot l_l}\right) \tag{2.59}$$

$$\theta_k = \theta_n + \theta_l - \tilde{\theta}_k \tag{2.60}$$

2.3.4 Inverse Actuator Kinematics

Inverse actuator kinematics is the transformation from joint space to actuator space given by the functions $x_m = x_m(\theta_m)$ and $x_k = x_k(\theta_k)$. Curve fitting is used instead of the analytical inverse since Equations (2.53) and (2.60) are such complex expressions. Curve fitting is done with 9^{th} order polynomials, given as:

$$x = p_9 \cdot \theta^9 + p_8 \cdot \theta^8 + p_7 \cdot \theta^7 + p_6 \cdot \theta^6 + p_5 \cdot \theta^5 + p_4 \cdot \theta^4 + p_3 \cdot \theta^3 + p_2 \cdot \theta^2 + p_1 \cdot \theta + p_0 \tag{2.61}$$

Generating the inverse actuator kinematics is done numerically by calculating $\theta_m = \theta_m(x_m)$ and then inverting the axes. This gives a solution on which the curve is fitted. The coefficients for the main cylinder and knuckle cylinder are given in Table 2.5 and

plots of the curve fits are shown in Figure 2.11. The curve fit overlaps with the data points and yields a close match to the numerical inverse.

Table 2.5: Curve fitting coefficients for inverse actuator kinematics.

Coefficient	Main	Knuckle
p_9	$-8.324 \cdot 10^{-5}$	$-2.044 \cdot 10^{-5}$
p_8	$4.068 \cdot 10^{-4}$	$-2.996 \cdot 10^{-4}$
p_7	$-4.087 \cdot 10^{-4}$	$-1.571 \cdot 10^{-3}$
p_6	$-1.797 \cdot 10^{-3}$	$-4.609 \cdot 10^{-3}$
p_5	$2.914 \cdot 10^{-3}$	$-1.045 \cdot 10^{-2}$
p_4	$1.293 \cdot 10^{-2}$	$-1.135 \cdot 10^{-2}$
p_3	$-4.794 \cdot 10^{-2}$	$3.451 \cdot 10^{-3}$
p_2	$2.438 \cdot 10^{-2}$	$1.153 \cdot 10^{-2}$
p_1	$3.471 \cdot 10^{-1}$	$3.042 \cdot 10^{-1}$
p_0	1.291	1.923

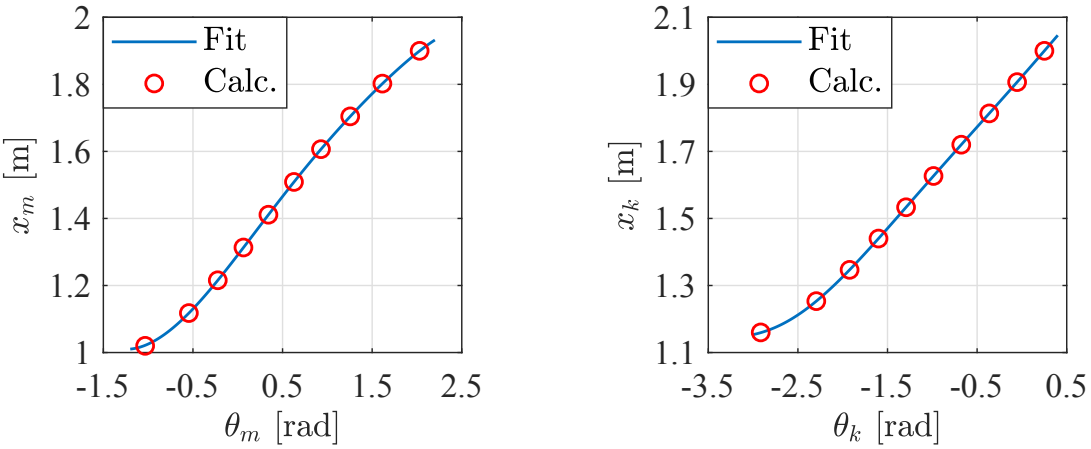

(a) Curve fit for main cylinder.

(b) Curve fit for knuckle cylinder.

Figure 2.11: Curve fit for inverse actuator kinematics. Taken from Paper F.

Another relation which has been developed in paper C is the time derivative of the inverse actuator kinematics. This describes the relation between the joint angular velocity and the cylinder velocity. By taking the time derivative of the actuator space kinematics, expressions for the cylinder velocities $\dot{x}_m$ and $\dot{x}_k$ can be made. The equations for the knuckle joint are given below, but the procedure is the same for the main joint. Taking the time derivative of Equations (2.54)-(2.60) yields:

$$\dot{\theta}_h = 0 \tag{2.62}$$

$$\dot{\theta}_i = \frac{x_k}{l_h \cdot l_k \cdot \sqrt{1 - \left(\frac{l_h^2 + l_k^2 - x_k^2}{2 \cdot l_h \cdot l_k}\right)^2}} \cdot \dot{x}_k \tag{2.63}$$

$$\dot{\theta}_j = -\frac{x_k}{l_h \cdot l_k \cdot \sqrt{1 - \left(\frac{l_h^2 + l_k^2 - x_k^2}{2 \cdot l_h \cdot l_k}\right)^2}} \cdot \dot{x}_k \tag{2.64}$$

$$\begin{aligned} \dot{l}_l &= \left(l_j^2 + l_k^2 - 2 \cdot l_j \cdot l_k \cdot c_{\theta_j}\right)^{-\frac{1}{2}} \cdot l_j \cdot l_k \cdot s_{\theta_j} \cdot \dot{\theta}_j \\ &= -\frac{\left(l_j^2 + l_k^2 - 2 \cdot l_j \cdot l_k \cdot c_{\theta_j}\right)^{-\frac{1}{2}} \cdot l_j \cdot s_{\theta_j} \cdot x_k}{l_h \cdot \sqrt{1 - \left(\frac{l_h^2 + l_k^2 - x_k^2}{2 \cdot l_h \cdot l_k}\right)^2}} \cdot \dot{x}_k \end{aligned} \tag{2.65}$$

$$\begin{aligned} \dot{\theta}_n &= -\frac{l_l^2 - l_n^2 + l_m^2}{2 \cdot l_l^2 \cdot l_n \cdot \sqrt{1 - \left(\frac{l_l^2 + l_n^2 - l_m^2}{2 \cdot l_l \cdot l_n}\right)^2}} \cdot \dot{l}_l \\ &= \frac{(l_l^2 - l_n^2 + l_m^2) \cdot \left(l_j^2 + l_k^2 - 2 \cdot l_j \cdot l_k \cdot c_{\theta_j}\right)^{-\frac{1}{2}} \cdot l_j \cdot s_{\theta_j} \cdot x_k}{2 \cdot l_l^2 \cdot l_n \cdot l_h \cdot \sqrt{1 - \left(\frac{l_l^2 + l_n^2 - l_m^2}{2 \cdot l_l \cdot l_n}\right)^2} \cdot \sqrt{1 - \left(\frac{l_h^2 + l_k^2 - x_k^2}{2 \cdot l_h \cdot l_k}\right)^2}} \cdot \dot{x}_k \end{aligned} \tag{2.66}$$

$$\begin{aligned} \dot{\theta}_l &= \frac{-1}{\sqrt{1 - \left(\frac{l_i^2 + l_l^2 - x_k^2}{2 \cdot l_i \cdot l_l}\right)^2}} \cdot \frac{\dot{l}_l \cdot (l_l^2 + x_k^2 - l_i^2) - 2 \cdot l_l \cdot x_k \cdot \dot{x}_k}{2 \cdot l_i \cdot l_l^2} \\ &= \frac{x_k}{l_i \cdot l_l \cdot \sqrt{1 - \left(\frac{l_i^2 + l_l^2 - x_k^2}{2 \cdot l_i \cdot l_l}\right)^2}} \cdot \dot{x}_k - \frac{l_l^2 + x_k^2 - l_i^2}{2 \cdot l_i \cdot l_l^2 \cdot \sqrt{1 - \left(\frac{l_i^2 + l_l^2 - x_k^2}{2 \cdot l_i \cdot l_l}\right)^2}} \cdot \dot{l}_l \\ &= \frac{x_k}{l_i \cdot l_l \cdot \sqrt{1 - \left(\frac{l_i^2 + l_l^2 - x_k^2}{2 \cdot l_i \cdot l_l}\right)^2}} \cdot \dot{x}_k + \frac{(l_l^2 + x_k^2 - l_i^2) \cdot \left(l_j^2 + l_k^2 - 2 \cdot l_j \cdot l_k \cdot c_{\theta_j}\right)^{-\frac{1}{2}} \cdot l_j \cdot s_{\theta_j} \cdot x_k}{2 \cdot l_i \cdot l_l^2 \cdot l_h \cdot \sqrt{1 - \left(\frac{l_i^2 + l_l^2 - x_k^2}{2 \cdot l_i \cdot l_l}\right)^2} \cdot \sqrt{1 - \left(\frac{l_h^2 + l_k^2 - x_k^2}{2 \cdot l_h \cdot l_k}\right)^2}} \cdot \dot{x}_k \end{aligned} \tag{2.67}$$

$$\begin{aligned} \dot{\theta}_k &= \dot{\theta}_n + \dot{\theta}_l \\ &= \left(\frac{(l_l^2 - l_n^2 + l_m^2) \cdot \left(l_j^2 + l_k^2 - 2 \cdot l_j \cdot l_k \cdot c_{\theta_j}\right)^{-\frac{1}{2}} \cdot l_j \cdot s_{\theta_j} \cdot x_k}{2 \cdot l_l^2 \cdot l_n \cdot l_h \cdot \sqrt{1 - \left(\frac{l_l^2 + l_n^2 - l_m^2}{2 \cdot l_l \cdot l_n}\right)^2} \cdot \sqrt{1 - \left(\frac{l_h^2 + l_k^2 - x_k^2}{2 \cdot l_h \cdot l_k}\right)^2}} + \frac{x_k}{l_i \cdot l_l \cdot \sqrt{1 - \left(\frac{l_i^2 + l_l^2 - x_k^2}{2 \cdot l_i \cdot l_l}\right)^2}} \right. \\ &\quad \left. + \frac{(l_l^2 + x_k^2 - l_i^2) \cdot \left(l_j^2 + l_k^2 - 2 \cdot l_j \cdot l_k \cdot c_{\theta_j}\right)^{-\frac{1}{2}} \cdot l_j \cdot s_{\theta_j} \cdot x_k}{2 \cdot l_i \cdot l_l^2 \cdot l_h \cdot \sqrt{1 - \left(\frac{l_i^2 + l_l^2 - x_k^2}{2 \cdot l_i \cdot l_l}\right)^2} \cdot \sqrt{1 - \left(\frac{l_h^2 + l_k^2 - x_k^2}{2 \cdot l_h \cdot l_k}\right)^2}} \right) \cdot \dot{x}_k \end{aligned} \tag{2.68}$$

Solving Equation (2.68) with respect to $\dot{x}_k$ yields:

$$\theta^{\dagger}_{x_k} = \left(\frac{(l_l^2 - l_n^2 + l_m^2) \cdot \left(l_j^2 + l_k^2 - 2 \cdot l_j \cdot l_k \cdot c_{\theta_j}\right)^{-\frac{1}{2}} \cdot l_j \cdot s_{\theta_j} \cdot x_k}{2 \cdot l_l^2 \cdot l_n \cdot l_h \cdot \sqrt{1 - \left(\frac{l_l^2 + l_n^2 - l_m^2}{2 \cdot l_l \cdot l_n}\right)^2} \cdot \sqrt{1 - \left(\frac{l_h^2 + l_k^2 - x_k^2}{2 \cdot l_h \cdot l_k}\right)^2}} + \frac{x_k}{l_i \cdot l_l \cdot \sqrt{1 - \left(\frac{l_i^2 + l_l^2 - x_k^2}{2 \cdot l_i \cdot l_l}\right)^2}} \right.$$
$$\left. + \frac{(l_l^2 + x_k^2 - l_i^2) \cdot \left(l_j^2 + l_k^2 - 2 \cdot l_j \cdot l_k \cdot c_{\theta_j}\right)^{-\frac{1}{2}} \cdot l_j \cdot s_{\theta_j} \cdot x_k}{2 \cdot l_i \cdot l_l^2 \cdot l_h \cdot \sqrt{1 - \left(\frac{l_i^2 + l_l^2 - x_k^2}{2 \cdot l_i \cdot l_l}\right)^2} \cdot \sqrt{1 - \left(\frac{l_h^2 + l_k^2 - x_k^2}{2 \cdot l_h \cdot l_k}\right)^2}} \right)^{-1} \tag{2.69}$$

$$\dot{x}_k = \theta^{\dagger}_{x_k} \cdot \dot{\theta}_k \tag{2.70}$$

2.3.5 Jacobian Matrix and Inverse Jacobian

The Jacobian matrix for the HMF 2020K4 and its inverse are used to describe the relation between the crane tip velocity and the joint velocities. The Jacobian matrix has been derived in paper E, in which the slew cylinder, main cylinder, and knuckle cylinder are used for motion control. In this case the crane has three degrees of freedom without any kinematic redundancy. The Denavit-Hartenberg parameters for this configuration are listed in Table 2.6.

Table 2.6: Denavit-Hartenberg parameters for the HMF 2020K4 when the slew cylinder, main cylinder, and knuckle cylinder are used for motion control.

$\mathbf{R}_z$	$\mathbf{T}_z$	$\mathbf{T}_x$	$\mathbf{R}_x$
θ_s	l_{1z}	$-l_{1x}$	$90°$
θ_m	0	0	$-90°$
0	l_{2z}	l_{2x}	$90°$
θ_k	0	0	$-90°$
0	$-l_{3z}$	l_{3x}	0

The transformation matrix $\mathbf{A}_{DH}$ from the base of the crane to the tip of the crane can be established as a sequence of transformations based on the Denavit-Hartenberg parameters, shown in Equation (2.71).

$$\mathbf{A}_{DH} = \mathbf{R}_z(\theta_s)\cdot\mathbf{T}_z(l_{1z})\cdot\mathbf{T}_x(-l_{1x})\cdot\mathbf{R}_x(90°)\cdot\mathbf{R}_z(\theta_m)\cdot\mathbf{R}_x(-90°)\cdot\mathbf{T}_z(l_{2z}) \cdot\mathbf{T}_x(l_{2x})\cdot\mathbf{R}_x(90°)\cdot\mathbf{R}_z(\theta_k)\cdot\mathbf{R}_x(-90°)\cdot\mathbf{T}_z(-l_{3z})\cdot\mathbf{T}_x(l_{3x}) \tag{2.71}$$

The final matrix $\mathbf{A}_{DH}$ is shown in Equation (2.72). The joint kinematics from the crane base to the crane tip are now contained in x_{Tip}, y_{Tip}, and z_{Tip}.

$$\mathbf{A}_{DH} = \begin{bmatrix} c_{\theta_s}\cdot c_{\theta_m+\theta_k} & -s_{\theta_s} & -c_{\theta_s}\cdot s_{\theta_m+\theta_k} & x_{Tip} \\ s_{\theta_s}\cdot c_{\theta_m+\theta_k} & c_{\theta_s} & -s_{\theta_s}\cdot s_{\theta_m+\theta_k} & y_{Tip} \\ s_{\theta_m+\theta_k} & 0 & c_{\theta_m+\theta_k} & z_{Tip} \\ 0 & 0 & 0 & 1 \end{bmatrix} \tag{2.72}$$

$$x_{Tip} = c_{\theta_s}\cdot(-l_{1x} + l_{2x}\cdot c_{\theta_m} - l_{2z}\cdot s_{\theta_m} + l_{3x}\cdot c_{\theta_m+\theta_k} + l_{3z}\cdot s_{\theta_m+\theta_k}) \tag{2.73}$$

$$y_{Tip} = s_{\theta_s}\cdot(-l_{1x} + l_{2x}\cdot c_{\theta_m} - l_{2z}\cdot s_{\theta_m} + l_{3x}\cdot c_{\theta_m+\theta_k} + l_{3z}\cdot s_{\theta_m+\theta_k}) \tag{2.74}$$

$$z_{Tip} = l_{1z} + l_{2x}\cdot s_{\theta_m} + l_{2z}\cdot c_{\theta_m} + l_{3x}\cdot s_{\theta_m+\theta_k} - l_{3z}\cdot c_{\theta_m+\theta_k} \tag{2.75}$$

To find the correlation between the crane tip velocities and the joint velocities, the Jacobian matrix must be defined. The correlation between crane tip velocities and joint velocities is shown in Equations (2.76) and (2.77).

$$\begin{bmatrix} \dot{x}_{Tip} \\ \dot{y}_{Tip} \\ \dot{z}_{Tip} \end{bmatrix} = \mathbf{J}\cdot\begin{bmatrix} \dot{\theta}_s \\ \dot{\theta}_m \\ \dot{\theta}_k \end{bmatrix} \tag{2.76}$$

$$\begin{bmatrix} \dot{\theta}_s \\ \dot{\theta}_m \\ \dot{\theta}_k \end{bmatrix} = \mathbf{J}^{-1}\cdot\begin{bmatrix} \dot{x}_{Tip} \\ \dot{y}_{Tip} \\ \dot{z}_{Tip} \end{bmatrix} \tag{2.77}$$

First, the Jacobian matrix is defined as the partial derivative of the crane tip position with respect to the joint angles, shown in Equation (2.78).

$$\mathbf{J} = \begin{bmatrix} \frac{\partial}{\partial\theta_s}(x_{Tip}) & \frac{\partial}{\partial\theta_m}(x_{Tip}) & \frac{\partial}{\partial\theta_k}(x_{Tip}) \\ \frac{\partial}{\partial\theta_s}(y_{Tip}) & \frac{\partial}{\partial\theta_m}(y_{Tip}) & \frac{\partial}{\partial\theta_k}(y_{Tip}) \\ \frac{\partial}{\partial\theta_s}(z_{Tip}) & \frac{\partial}{\partial\theta_m}(z_{Tip}) & \frac{\partial}{\partial\theta_k}(z_{Tip}) \end{bmatrix} \tag{2.78}$$

$$\frac{\partial}{\partial\theta_s}(x_{Tip}) = -s_{\theta_s}\cdot(-l_{1x} + l_{2x}\cdot c_{\theta_m} - l_{2z}\cdot s_{\theta_m} + l_{3x}\cdot c_{\theta_m+\theta_k} + l_{3z}\cdot s_{\theta_m+\theta_k}) \tag{2.79}$$

$$\frac{\partial}{\partial\theta_m}(x_{Tip}) = c_{\theta_s}\cdot(-l_{2x}\cdot s_{\theta_m} - l_{2z}\cdot c_{\theta_m} - l_{3x}\cdot s_{\theta_m+\theta_k} + l_{3z}\cdot c_{\theta_m+\theta_k}) \tag{2.80}$$

$$\frac{\partial}{\partial\theta_k}(x_{Tip}) = c_{\theta_s}\cdot(-l_{3x}\cdot s_{\theta_m+\theta_k} + l_{3z}\cdot c_{\theta_m+\theta_k}) \tag{2.81}$$

$$\frac{\partial}{\partial\theta_s}(y_{Tip}) = c_{\theta_s}\cdot(-l_{1x} + l_{2x}\cdot c_{\theta_m} - l_{2z}\cdot s_{\theta_m} + l_{3x}\cdot c_{\theta_m+\theta_k} + l_{3z}\cdot s_{\theta_m+\theta_k}) \tag{2.82}$$

$$\frac{\partial}{\partial\theta_m}(y_{Tip}) = s_{\theta_s}\cdot(-l_{2x}\cdot s_{\theta_m} - l_{2z}\cdot c_{\theta_m} - l_{3x}\cdot s_{\theta_m+\theta_k} + l_{3z}\cdot c_{\theta_m+\theta_k}) \tag{2.83}$$

$$\frac{\partial}{\partial\theta_k}(y_{Tip}) = s_{\theta_s}\cdot(-l_{3x}\cdot s_{\theta_m+\theta_k} + l_{3z}\cdot c_{\theta_m+\theta_k}) \tag{2.84}$$

$$\frac{\partial}{\partial\theta_s}(z_{Tip}) = 0 \tag{2.85}$$

$$\frac{\partial}{\partial\theta_m}(z_{Tip}) = l_{2x}\cdot c_{\theta_m} - l_{2z}\cdot s_{\theta_m} + l_{3x}\cdot c_{\theta_m+\theta_k} + l_{3z}\cdot s_{\theta_m+\theta_k} \tag{2.86}$$

$$\frac{\partial}{\partial\theta_k}(z_{Tip}) = -l_{3x}\cdot c_{\theta_m+\theta_k} - l_{3z}\cdot s_{\theta_m+\theta_k} \tag{2.87}$$

The inverse Jacobian matrix is used to generate the joint velocities, shown in Equations (2.88)-(2.100).

$$\mathbf{J}^\dagger \triangleq \mathbf{J}^{-1} = \begin{bmatrix} J_{11}^\dagger & J_{12}^\dagger & J_{13}^\dagger \\ J_{21}^\dagger & J_{22}^\dagger & J_{23}^\dagger \\ J_{31}^\dagger & J_{32}^\dagger & J_{33}^\dagger \end{bmatrix} \tag{2.88}$$

$$\dot{\theta}_s = J_{11}^\dagger\cdot\dot{x}_{Tip} + J_{12}^\dagger\cdot\dot{y}_{Tip} + J_{13}^\dagger\cdot\dot{z}_{Tip} \tag{2.89}$$

$$\dot{\theta}_m = J_{21}^\dagger\cdot\dot{x}_{Tip} + J_{22}^\dagger\cdot\dot{y}_{Tip} + J_{23}^\dagger\cdot\dot{z}_{Tip} \tag{2.90}$$

$$\dot{\theta}_k = J_{31}^\dagger\cdot\dot{x}_{Tip} + J_{32}^\dagger\cdot\dot{y}_{Tip} + J_{33}^\dagger\cdot\dot{z}_{Tip} \tag{2.91}$$

$$J_{11}^\dagger = \frac{-s_{\theta_s}}{-l_{1x} + l_{2x}\cdot c_{\theta_m} - l_{2z}\cdot s_{\theta_m} + l_{3x}\cdot c_{\theta_m+\theta_k} + l_{3z}\cdot s_{\theta_m+\theta_k}} \tag{2.92}$$

$$J_{12}^\dagger = \frac{c_{\theta_s}}{-l_{1x} + l_{2x}\cdot c_{\theta_m} - l_{2z}\cdot s_{\theta_m} + l_{3x}\cdot c_{\theta_m+\theta_k} + l_{3z}\cdot s_{\theta_m+\theta_k}} \tag{2.93}$$

$$J_{13}^\dagger = 0 \tag{2.94}$$

$$J_{21}^\dagger = \frac{-c_{\theta_s}\cdot(l_{3x}\cdot c_{\theta_m+\theta_k} + l_{3z}\cdot s_{\theta_m+\theta_k})}{-l_{2x}\cdot l_{3x}\cdot s_{\theta_k} + l_{2x}\cdot l_{3z}\cdot c_{\theta_k} + l_{2z}\cdot l_{3x}\cdot c_{\theta_k} + l_{2z}\cdot l_{3z}\cdot s_{\theta_k}} \tag{2.95}$$

$$J_{22}^\dagger = \frac{-s_{\theta_s}\cdot(l_{3x}\cdot c_{\theta_m+\theta_k} + l_{3z}\cdot s_{\theta_m+\theta_k})}{-l_{2x}\cdot l_{3x}\cdot s_{\theta_k} + l_{2x}\cdot l_{3z}\cdot c_{\theta_k} + l_{2z}\cdot l_{3x}\cdot c_{\theta_k} + l_{2z}\cdot l_{3z}\cdot s_{\theta_k}} \tag{2.96}$$

$$J_{23}^\dagger = \frac{-l_{3x}\cdot s_{\theta_m+\theta_k} + l_{3z}\cdot c_{\theta_m+\theta_k}}{-l_{2x}\cdot l_{3x}\cdot s_{\theta_k} + l_{2x}\cdot l_{3z}\cdot c_{\theta_k} + l_{2z}\cdot l_{3x}\cdot c_{\theta_k} + l_{2z}\cdot l_{3z}\cdot s_{\theta_k}} \tag{2.97}$$

$$J_{31}^\dagger = \frac{c_{\theta_s}\cdot(l_{2x}\cdot c_{\theta_m} - l_{2z}\cdot s_{\theta_m} + l_{3x}\cdot c_{\theta_m+\theta_m} + l_{3z}\cdot s_{\theta_m+\theta_k})}{-l_{2x}\cdot l_{3x}\cdot s_{\theta_k} + l_{2x}\cdot l_{3z}\cdot c_{\theta_k} + l_{2z}\cdot l_{3x}\cdot c_{\theta_k} + l_{2z}\cdot l_{3z}\cdot s_{\theta_k}} \tag{2.98}$$

$$J_{32}^\dagger = \frac{s_{\theta_s}\cdot(l_{2x}\cdot c_{\theta_m} - l_{2z}\cdot s_{\theta_m} + l_{3x}\cdot c_{\theta_m+\theta_m} + l_{3z}\cdot s_{\theta_m+\theta_k})}{-l_{2x}\cdot l_{3x}\cdot s_{\theta_k} + l_{2x}\cdot l_{3z}\cdot c_{\theta_k} + l_{2z}\cdot l_{3x}\cdot c_{\theta_k} + l_{2z}\cdot l_{3z}\cdot s_{\theta_k}} \tag{2.99}$$

$$J_{33}^\dagger = \frac{l_{2x}\cdot s_{\theta_m} + l_{2z}\cdot c_{\theta_m} + l_{3x}\cdot s_{\theta_m+\theta_k} - l_{3z}\cdot c_{\theta_m+\theta_k}}{-l_{2x}\cdot l_{3x}\cdot s_{\theta_k} + l_{2x}\cdot l_{3z}\cdot c_{\theta_k} + l_{2z}\cdot l_{3x}\cdot c_{\theta_k} + l_{2z}\cdot l_{3z}\cdot s_{\theta_k}} \tag{2.100}$$

With the Jacobian matrix and the inverse Jacobian matrix defined, transformations between the Cartesian space and joint space can be performed.

2.4 Hanging Load Dynamics

The hanging load dynamics has been derived in paper C and paper E for the two- and three-dimensional case respectively. Figure 2.12 shows the hanging load definitions in three dimensions along with the main boom angle θ_m, knuckle boom angle θ_k, and swing angles α (in-plane angle) and β (out-of-plane angle). For the two-dimensional case, the angle $\beta = 0$ since the slewing motion is not used.

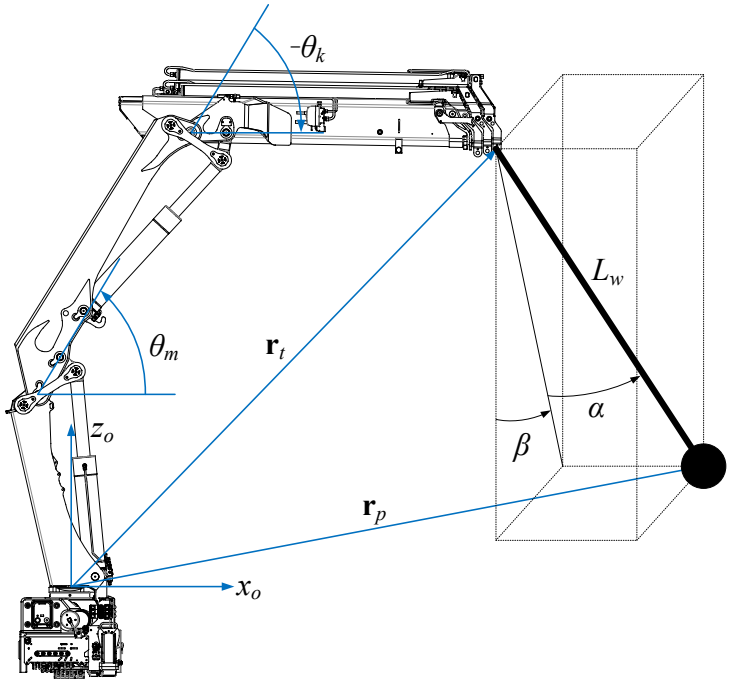

Figure 2.12: Definitions of crane tip and hanging load geometries. Taken from Paper D.

To derive the equations of motion for the hanging load, the Euler-Lagrange equations are used. To save space in the following equations, the notation $\cos(\alpha) = c_\alpha$ and $\sin(\alpha) = s_\alpha$ is used. With the boom tip position defined as $\mathbf{r}_t = [x_t, y_t, z_t]^T$, the payload position $\mathbf{r}_p$ is calculated as follows.

$$\mathbf{r}_p = \mathbf{r}_t + L_w \cdot \begin{bmatrix} s_\alpha \\ c_\alpha \cdot s_\beta \\ -c_\alpha \cdot c_\beta \end{bmatrix} \tag{2.101}$$

The payload velocity is calculated by taking the time derivative of the payload position.

$$\dot{\mathbf{r}}_p = \dot{\mathbf{r}}_t + L_w \cdot \begin{bmatrix} \dot{\alpha} \cdot c_\alpha \\ \dot{\beta} \cdot c_\alpha \cdot c_\beta - \dot{\alpha} \cdot s_\alpha \cdot s_\beta \\ \dot{\alpha} \cdot s_\alpha \cdot c_\beta + \dot{\beta} \cdot c_\alpha \cdot s_\beta \end{bmatrix} + \dot{L}_w \cdot \begin{bmatrix} s_\alpha \\ c_\alpha \cdot s_\beta \\ -c_\alpha \cdot c_\beta \end{bmatrix} \tag{2.102}$$

The Lagrangian $\mathcal{L}$ of the system is defined as the kinetic energy $\mathcal{K}$ minus the potential energy $\mathcal{P}$, and is shown in Equation (2.103).

$$\mathcal{L} = \mathcal{K} - \mathcal{P} \tag{2.103}$$

The kinetic energy of the payload is:

$$\mathcal{K} = \frac{1}{2} \cdot m_p \cdot \dot{\mathbf{r}}_p^T \cdot \dot{\mathbf{r}}_p \tag{2.104}$$

The potential energy of the payload is:

$$\mathcal{P} = m_p \cdot g \cdot (z_{Tip} - L_w \cdot c_\alpha \cdot c_\beta) \tag{2.105}$$

Selecting the coordinate $\mathbf{q} = [\alpha, \beta]^T$, the Euler-Lagrange equation is defined in Equation 2.106.

$$\frac{d}{dt}\frac{\partial \mathcal{L}}{\partial \dot{\mathbf{q}}} - \frac{\partial \mathcal{L}}{\partial \mathbf{q}} = 0 \tag{2.106}$$

For the following equations the multiplication sign $(\cdot)$ is omitted to save space. Expanding the Lagrangian $\mathcal{L} = \mathcal{K} - \mathcal{P}$ yields:

$$\begin{aligned}\mathcal{L} = \frac{1}{2} m_p \Big(& \dot{x}_t^2 + \dot{y}_t^2 + \dot{z}_t^2 + \dot{\alpha}^2 L_w^2 + c_\alpha^2 \dot{\beta}^2 L_w^2 + \dot{L}_w^2 + 2c_\alpha \dot{x}_t \dot{\alpha} L_w + 2s_\alpha \dot{x}_t \dot{L}_w - 2s_\alpha s_\beta \dot{y}_t \dot{\alpha} L_w \\ & + 2c_\alpha c_\beta \dot{y}_t \dot{\beta} L_w + 2c_\alpha s_\beta \dot{y}_t \dot{L}_w + 2s_\alpha c_\beta \dot{z}_t \dot{\alpha} L_w + 2c_\alpha s_\beta \dot{z}_t \dot{\beta} L_w - 2c_\alpha c_\beta \dot{z}_t \dot{L}_w \Big) \\ & - m_p g \left(z_t - c_\alpha c_\beta L_w \right)\end{aligned} \tag{2.107}$$

Solving the Euler-Lagrange equation using the angle α yields:

$$\begin{aligned}\frac{\partial \mathcal{L}}{\partial \alpha} = & \, m_p \Big(-s_\alpha c_\alpha \dot{\beta}^2 L_w^2 - s_\alpha \dot{x}_t \dot{\alpha} L_w + c_\alpha \dot{x}_t \dot{L}_w - c_\alpha s_\beta \dot{y}_t \dot{\alpha} L_w - s_\alpha c_\beta \dot{y}_t \dot{\beta} L_w \\ & - s_\alpha s_\beta \dot{y}_t \dot{L}_w + c_\alpha c_\beta \dot{z}_t \dot{\alpha} L_w - s_\alpha s_\beta \dot{z}_t \dot{\beta} L_w + s_\alpha c_\beta \dot{z}_t \dot{L}_w - g s_\alpha c_\beta L_w \Big)\end{aligned} \tag{2.108}$$

$$\frac{\partial \mathcal{L}}{\partial \dot{\alpha}} = m_p \left(\dot{\alpha} L_w^2 + c_\alpha \dot{x}_t L_w - s_\alpha s_\beta \dot{y}_t L_w + s_\alpha c_\beta \dot{z}_t L_w \right) \tag{2.109}$$

$$\begin{aligned}\frac{d}{dt}\frac{\partial \mathcal{L}}{\partial \dot{\alpha}} = & \, m_p \Big(\ddot{\alpha} L_w^2 + 2\dot{\alpha} L_w \dot{L}_w - s_\alpha \dot{x}_t \dot{\alpha} L_w + c_\alpha \ddot{x}_t L_w + c_\alpha \dot{x}_t \dot{L}_w \\ & - c_\alpha s_\beta \dot{y}_t \dot{\alpha} L_w - s_\alpha c_\beta \dot{y}_t \dot{\beta} L_w - s_\alpha s_\beta \ddot{y}_t L_w - s_\alpha s_\beta \dot{y}_t \dot{L}_w \\ & + c_\alpha c_\beta \dot{z}_t \dot{\alpha} L_w - s_\alpha s_\beta \dot{z}_t \dot{\beta} L_w + s_\alpha c_\beta \ddot{z}_t L_w + s_\alpha c_\beta \dot{z}_t \dot{L}_w \Big)\end{aligned} \tag{2.110}$$

$$\begin{aligned}\frac{d}{dt}\frac{\partial \mathcal{L}}{\partial \dot{\alpha}} - \frac{\partial \mathcal{L}}{\partial \alpha} = & \, m_p \Big(c_\alpha \ddot{x}_t L_w - s_\alpha s_\beta \ddot{y}_t L_w + s_\alpha c_\beta \ddot{z}_t L_w + \ddot{\alpha} L_w^2 \\ & + 2\dot{\alpha} L_w \dot{L}_w + s_\alpha c_\alpha \dot{\beta}^2 L_w^2 + g s_\alpha c_\beta L_w \Big) = 0\end{aligned} \tag{2.111}$$

Solving Equation 2.111 for $\ddot{\alpha}$ yields the first equation of motion:

$$\ddot{\alpha} = \frac{1}{L_w} \left(-c_\alpha \ddot{x}_t + s_\alpha s_\beta \ddot{y}_t - s_\alpha c_\beta \ddot{z}_t - 2\dot{\alpha} \dot{L}_w - s_\alpha c_\alpha \dot{\beta}^2 L_w - g s_\alpha c_\beta \right) \tag{2.112}$$

Solving the Euler-Lagrange equation using the angle β yields:

$$\frac{\partial \mathcal{L}}{\partial \beta} = m_p \Big(-s_\alpha c_\beta \dot{y}_t \dot{\alpha} L_w - c_\alpha s_\beta \dot{y}_t \dot{\beta} L_w + c_\alpha c_\beta \dot{y}_t \dot{L}_w - s_\alpha s_\beta \dot{z}_t \dot{\alpha} L_w + c_\alpha c_\beta \dot{z}_t \dot{\beta} L_w + c_\alpha s_\beta \dot{z}_t \dot{L}_w - g c_\alpha s_\beta L_w \Big) \tag{2.113}$$

$$\frac{\partial \mathcal{L}}{\partial \dot{\beta}} = m_p \Big(c_\alpha^2 \dot{\beta} L_w^2 + c_\alpha c_\beta \dot{y}_t L_w + c_\alpha s_\beta \dot{z}_t L_w \Big) \tag{2.114}$$

$$\frac{d}{dt}\frac{\partial \mathcal{L}}{\partial \dot{\beta}} = m_p \Big(-2 s_\alpha c_\alpha \dot{\alpha} \dot{\beta} L_w^2 + c_\alpha^2 \ddot{\beta} L_w^2 + 2 c_\alpha^2 \dot{\beta} L_w \dot{L}_w - s_\alpha c_\beta \dot{y}_t \dot{\alpha} L_w - c_\alpha s_\beta \dot{y}_t \dot{\beta} L_w + c_\alpha c_\beta \ddot{y}_t L_w + c_\alpha c_\beta \dot{y}_t \dot{L}_w - s_\alpha s_\beta \dot{z}_t \dot{\alpha} L_w + c_\alpha c_\beta \dot{z}_t \dot{\beta} L_w + c_\alpha s_\beta \ddot{z}_t L_w + c_\alpha s_\beta \dot{z}_t \dot{L}_w \Big) \tag{2.115}$$

$$\frac{d}{dt}\frac{\partial \mathcal{L}}{\partial \dot{\beta}} - \frac{\partial \mathcal{L}}{\partial \beta} = m_p \Big(c_\alpha c_\beta \ddot{y}_t L_w + c_\alpha s_\beta \ddot{z}_t L_w - 2 s_\alpha c_\alpha \dot{\alpha} \dot{\beta} L_w^2 + 2 c_\alpha^2 \dot{\beta} L_w \dot{L}_w + c_\alpha^2 \ddot{\beta} L_w^2 + g c_\alpha s_\beta L_w \Big) = 0 \tag{2.116}$$

Solving Equation 2.116 for $\ddot{\beta}$ yields the second equation of motion:

$$\ddot{\beta} = \frac{1}{c_\alpha L_w} \Big(-c_\beta \ddot{y}_t - s_\beta \ddot{z}_t + 2 s_\alpha \dot{\alpha} \dot{\beta} L_w - 2 c_\alpha \dot{\beta} \dot{L}_w - g s_\beta \Big) \tag{2.117}$$

2.5 Optimization and Genetic Algorithms

Mathematical optimization refers to the process of finding parameters that minimize (or maximize) an objective function. The function may include various constraints which must be satisfied. A general formulation of a mixed-integer nonlinear optimization problem is shown in Equation (2.118) where the goal is to minimize the function $f(x)$, where x is the design variable. The problem is subjected to nonlinear constraints, bounds, and integer constraints. It should be noted that any linear constraint can be expressed inside the nonlinear constraint functions $c(x)$ and $c_{eq}(x)$.

$$\min_x f(x) \quad \text{subject to} \begin{cases} c_i(x) \leq 0, & i = 1...n_c \\ c_{eq,j}(x) = 0, & j = 1...n_{ceq} \\ l_b \leq x \leq u_b \\ x(c_{int}) \in \mathbb{Z} \end{cases} \tag{2.118}$$

where

$c(x)$	=	nonlinear inequality constraints
$c_{eq}(x)$	=	nonlinear equality constraints
n_c	=	number of nonlinear inequality constraints
n_{ceq}	=	number of nonlinear equality constraints
l_b	=	lower bound of x
u_b	=	upper bound of x
c_{int}	=	elements of x with integer constraints

During this project, a genetic algorithm was made and used for optimization in Paper A. Genetic algorithms are inspired by biological evolution and belong to a class of population-based optimization algorithms. It is a global optimization algorithm and is able to solve nonlinear, constrained, and mixed-integer problems. For a given objective function, a set of candidate solutions play the role of individuals in a population and are evaluated each iteration. Mechanisms such as selection, crossover, mutation, and elitism are then used to update the candidate solutions. These terms are explained in the following paragraphs. Since individuals are only ranked based on their objective value, genetic algorithms can be used to optimize non-convex and discontinuous objective functions without any information about the underlying function or its gradient.

The selection process typically consists of ranking the individuals from best to worst, and then selecting two individuals as parents to generate an offspring. The offspring is then used in the updated population. Different methods for selection can be used, one example is where the probability of choosing an individual is proportional to its fitness. Tournament selection is another method which can also be used. A different approach is to randomly select parents only from the best ranking individuals, for example the top 20 %. All methods may prove to be successful, but there is no consensus on which method is best.

Crossover refers to the process of generating new individuals from two parents, and is sometimes considered the equivalent of sexual reproduction. Crossover can be used both with binary numbers and real numbers, the former being similar to recombination of DNA. For real numbered problems, crossover is typically done using some weighing function, either mean, random weight, or blend crossover, see Equation 2.119 below. For mean crossover the weight is fixed to $U = 0.5$. Random weight uses a uniform random number $U \in [0, 1]$, updated for each offspring. This stochastic approach is typically preferred, and will also eliminate the generation of identical individuals if the same two parents are selected multiple times. Blend crossover is another method used to go outside the range of the parents, and uses the parameter $b \in [0, 1]$ with $U \in [-b, 1 + b]$. This will typically help with exploration of the objective function.

$$x_{offspring} = U \cdot x_{parent,1} + (1 - U) \cdot x_{parent,2} \tag{2.119}$$

Mutation is used to modify a single individual to be used in the updated population. This is often considered the equivalent of asexual reproduction. The values of the individual are slightly altered, for example by adding or subtracting a random number, either uniform or normal distributed. For multi-dimensional problems a set of random numbers are used, one for each dimension. In either case, a mutation range can be defined, for example a small portion of the available objective function search space. This is shown in Equations (2.120) and (2.121) using the upper and lower bounds u_b and l_b, mutation factor $k_m \in [0, 1]$, and the uniform random number $U \in [0, 1]$. The parameter r_m denotes the calculated mutation range for the given search space.

$$r_m = (u_b - l_b) \cdot k_m \tag{2.120}$$

$$x_{offspring} = x_{parent} + r_m \cdot U - \frac{r_m}{2} \tag{2.121}$$

Elitism consists of copying the best individuals, for example the top 2 %, directly into the next generation. This does not have an analogy to nature, but ensures that the best solutions are not discarded and also increases the probability of them creating children. A consequence of this is that the best objective value never increases between iterations.

These mechanisms will generally lead to a near-optimal solution without being stuck in a local minima. However, since the genetic algorithm uses stochastic processes the convergence can not be fully guaranteed.

As for satisfying the constraints of the problem, various methods can be used. Adding a penalty term to solutions which violate the constraints is an effective and efficient approach. Considering the constraint $c_i(x) \leq 0$, an approach is to make a modified objective function $F(x)$ which includes a penalty term proportional to the constraint violation, where μ is the penalty factor. This is shown in Equation (2.122).

$$F(x) = f(x) + \mu_c \cdot \sum_{i=1}^{n_c} \max(0, c_i(x)) \tag{2.122}$$

Similarly, the penalty for the nonlinear equality constraint $c_{eq,j}(x) = 0$ can be expressed as:

$$F(x) = f(x) + \mu_{ceq} \cdot \sum_{j=1}^{n_{ceq}} |c_{eq,j}(x)| \tag{2.123}$$

For bounded constraints limiting the variable x before each function evaluation is often the simplest approach. This way the objective function will never be evaluated with solutions that violate the bounded constraints. This is shown below:

$$x = \min(\max(l_b, x), u_b) \tag{2.124}$$

Implementing the bounded constraints as a penalty function can be done, and is shown in Equations (2.125)-(2.126) where x has n dimensions.

$$F(x) = f(x) + \mu_{lb} \cdot \sum_{i=1}^{n} \max(l_{b,i} - x_i, 0) \tag{2.125}$$

$$F(x) = f(x) + \mu_{ub} \cdot \sum_{i=1}^{n} \max(x_i - u_{b,i}, 0) \tag{2.126}$$

For integer constraints, it may be necessary to ensure that the solution does not violate the constraints before evaluating the objective function. This is especially important for objective functions with discrete operation modes. As such, rounding the value x for each element c_{int} to the nearest integer before function evaluation is a simple and effective approach, shown in Equation (2.127).

$$\forall i \in c_{int}, \quad x_i = \text{round}(x_i) \tag{2.127}$$

Alternatively, a penalty term can be made which is proportional to the distance from the closest integer. This is shown in Equation (2.128).

$$\forall i \in c_{int}, \quad F(x) = f(x) + \mu_{int} \cdot |\,\text{round}(x_i) - x_i| \tag{2.128}$$

Each of the penalty factors μ_c, μ_{ceq}, μ_{lb}, μ_{ub}, and μ_{int} can either be set to a sufficiently large value, or increased for each iteration. Since the genetic algorithm does not rely on any information about the underlying objective function, using penalty for constraint violations is a simple and fast method. It should be noted that there is no guarantee that the genetic algorithm finds a solution that does not violate any constraints, however solutions with small violations will have a higher probability of becoming parents than solutions with large violations.

To summarize, a typical procedure for the genetic algorithm will be as follows:

1. Generate a population of random candidate solutions
2. Limit the x value between l_b and u_b
3. Round elements of x with integer constraints
4. For each candidate solution:
   (a) Evaluate the objective function
   (b) Calculate the penalty for each constraint
   (c) Add the penalties to the objective value
5. Selection:
   (a) Sort the population from best to worst
   (b) Select the top 20 % as potential parents
6. Crossover:
   (a) Select two random parents
   (b) Perform blend crossover to create a child
   (c) Repeat to generate 80 % of the new population
7. Mutation:
   (a) Select a random parent
   (b) Mutate parent to create a child
   (c) Repeat to generate 18 % of the new population
8. Elitism:
   (a) Copy the top 2 % of parents into the new population
9. If stop criteria is not met, go to 2.
10. Stop optimization

Typically, this procedure will quickly disregard bad solutions due to its small selection percentage. This parameter along with population size, crossover percentage, mutation percentage, and elitism percentage may be tuned by the user.

2.6 Machine Learning and Neural Networks

Machine learning is a subset of artificial intelligence which aims to build models based on sampled data. It revolves around computers learning from the provided data to be able to carry out a task. Neural networks are a subset of machine learning and is loosely based on the biological brain. In paper F a neural network was trained to estimate the deflection of the crane tip while lifting a payload. Measurements from the laboratory were used as training data for the network, and the network predicts the deflection in x- and z-direction based on the cylinder positions.

A classical multilayer perceptron with a single hidden layer was used, and will be described in this section. Each node contains weights and biases and uses a linear combination of its inputs followed by a nonlinear activation function, chosen to be $y = \tanh(x)$ since it is monotonic with an output range of [-1, 1]. In addition, input scaling is implemented in the input layer to normalize the data to the range [-1, 1] in order to stay in the center region of the tanh activation function. Output scaling is used on the output layer to scale the outputs from [-1, 1] to a desired range. An overview of the neural network used in paper F is shown in Figure 2.13, illustrating the input scaling, output scaling, and ten hidden neurons. An illustration of a single node with its connections is shown in Figure 2.14.

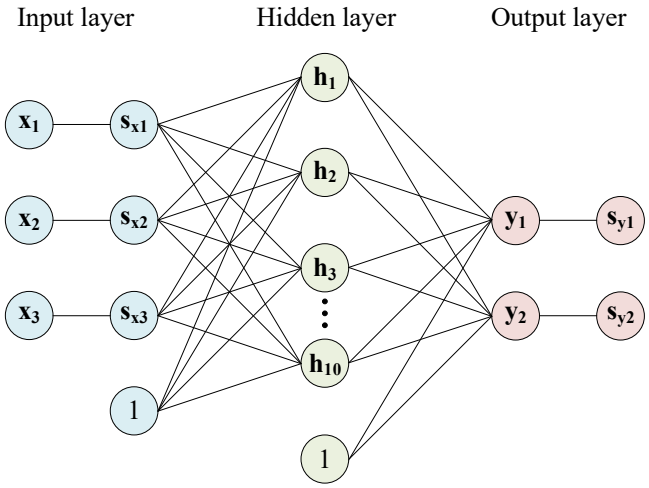

Figure 2.13: Overview of a neural network with scaled inputs and outputs. Taken from Paper F.

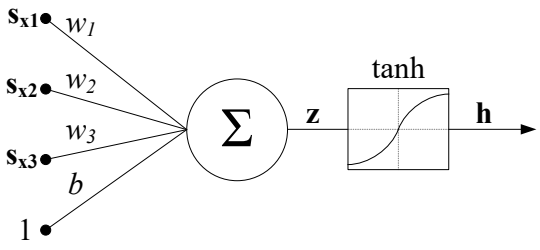

Figure 2.14: Illustration of a single node.

2.6.1 Forward Propagation

Forward propagation refers to calculating the outputs of the network with a set of inputs. The first step is input scaling of the raw input vector $\mathbf{x}$, shown in Equations (2.129)-(2.133). The input is scaled to lie between -1 and 1 based on the maximum and

minimum value of the input training data $\mathbf{x}_{training}$.

$$\mathbf{s_x} = (\mathbf{x} - \mathbf{x}_{min}) \cdot \frac{\mathbf{s}_{\mathbf{x},max} - \mathbf{s}_{\mathbf{x},min}}{\mathbf{x}_{max} - \mathbf{x}_{min}} + \mathbf{s}_{\mathbf{x},min} \tag{2.129}$$

$$\mathbf{x}_{min} = \min(\mathbf{x}_{training}) \tag{2.130}$$

$$\mathbf{x}_{max} = \max(\mathbf{x}_{training}) \tag{2.131}$$

$$\mathbf{s}_{\mathbf{x},min} = -1 \tag{2.132}$$

$$\mathbf{s}_{\mathbf{x},max} = 1 \tag{2.133}$$

Forward propagation for the hidden layer and output layer using tanh as the activation function is shown in Equations (2.134)-(2.137) using matrix notation. Note that all the parameters of the network are contained in $\mathbf{W}$ and $\mathbf{b}$.

$$\mathbf{z_h} = \mathbf{W_h} \cdot \mathbf{s_x} + \mathbf{b_h} \tag{2.134}$$

$$\mathbf{h} = \tanh(\mathbf{z_h}) \tag{2.135}$$

$$\mathbf{z_y} = \mathbf{W_y} \cdot \mathbf{h} + \mathbf{b_y} \tag{2.136}$$

$$\mathbf{y} = \tanh(\mathbf{z_y}) \tag{2.137}$$

where

$\mathbf{W_h}$	=	weight matrix of the hidden layer
$\mathbf{b_h}$	=	bias vector of the hidden layer
$\mathbf{W_y}$	=	weight matrix of the output layer
$\mathbf{b_y}$	=	bias vector of the output layer

Output scaling is similar to the input scaling, and in this case the network output $\mathbf{y}$ lies between -1 and 1 due to the tanh function. The scaling is based on the training data $\mathbf{y}_{training}$ to generate the scaled output $\mathbf{s_y}$ and is shown in Equations (2.138)-(2.142).

$$\mathbf{s_y} = (\mathbf{y} - \mathbf{y}_{min}) \cdot \frac{\mathbf{s}_{\mathbf{y},max} - \mathbf{s}_{\mathbf{y},min}}{\mathbf{y}_{max} - \mathbf{y}_{min}} + \mathbf{s}_{\mathbf{y},min} \tag{2.138}$$

$$\mathbf{y}_{min} = -1 \tag{2.139}$$

$$\mathbf{y}_{max} = 1 \tag{2.140}$$

$$\mathbf{s}_{\mathbf{y},min} = \min(\mathbf{y}_{training}) \tag{2.141}$$

$$\mathbf{s}_{\mathbf{y},max} = \max(\mathbf{y}_{training}) \tag{2.142}$$

2.6.2 Backpropagation

Backpropagation is the process of computing the gradient of the cost function with respect to the weights in the network. This is typically done using the chain rule and gradient descent. The training data consists of a matrix, where each column is a single measurement. The cost function is calculated by taking the squared Frobenius norm of the scaled output minus the output training data. The cost function is defined as:

$$C = \frac{1}{2} \cdot \left\| \mathbf{s_y} - \mathbf{y}_{training} \right\|_F^2 \tag{2.143}$$

In order to train the network, the partial derivatives of the cost function must be calculated. Note that the derivative of the activation function is $\frac{d}{dx}\tanh(x) = 1-\tanh^2(x)$. The calculations for the output layer is given in Equations (2.144)-(2.147).

$$\frac{\partial C}{\partial \mathbf{y}} = \mathbf{s_y} - \mathbf{y}_{training} \tag{2.144}$$

$$\frac{\partial \mathbf{y}}{\partial \mathbf{z_y}} = 1 - \tanh^2(\mathbf{z_y}) \tag{2.145}$$

$$\frac{\partial C}{\partial \mathbf{z_y}} = \frac{\partial C}{\partial \mathbf{y}} \cdot \frac{\partial \mathbf{y}}{\partial \mathbf{z_y}} \tag{2.146}$$

$$\frac{\partial \mathbf{z_y}}{\partial \mathbf{W_y}} = \mathbf{h}^T \tag{2.147}$$

The partial derivative of the cost function with respect to the weights and bias for the output layer can now be calculated. Dividing by the number of training examples N is done to create an average across the whole training set.

$$\frac{\partial C}{\partial \mathbf{W_y}} = \frac{1}{N} \cdot \frac{\partial C}{\partial \mathbf{z_y}} \cdot \frac{\partial \mathbf{z_y}}{\partial \mathbf{W_y}} \tag{2.148}$$

$$\frac{\partial C}{\partial \mathbf{b_y}} = \frac{1}{N} \cdot \sum_{j=1}^{N} \left(\frac{\partial C}{\partial \mathbf{z}_{\mathbf{y},ij}} \right) \tag{2.149}$$

The calculations for the hidden layer using the chain rule are given below:

$$\frac{\partial \mathbf{z_y}}{\partial \mathbf{h}} = \mathbf{W}_\mathbf{y}^T \tag{2.150}$$

$$\frac{\partial \mathbf{h}}{\partial \mathbf{z_h}} = 1 - \tanh^2(\mathbf{z_h}) \tag{2.151}$$

$$\frac{\partial C}{\partial \mathbf{z_h}} = \frac{\partial \mathbf{z_y}}{\partial \mathbf{h}} \cdot \frac{\partial C}{\partial \mathbf{z_y}} \cdot \frac{\partial \mathbf{h}}{\partial \mathbf{z_h}} \tag{2.152}$$

$$\frac{\partial \mathbf{z_h}}{\partial \mathbf{W_h}} = \mathbf{s}_\mathbf{x}^T \tag{2.153}$$

$$\frac{\partial C}{\partial \mathbf{W_h}} = \frac{1}{N} \cdot \frac{\partial C}{\partial \mathbf{z_h}} \cdot \frac{\partial \mathbf{z_h}}{\partial \mathbf{W_h}} \tag{2.154}$$

$$\frac{\partial C}{\partial \mathbf{b_h}} = \frac{1}{N} \cdot \sum_{j=1}^{N} \left(\frac{\partial C}{\partial \mathbf{z}_{\mathbf{h},ij}} \right) \tag{2.155}$$

The partial derivatives can now be used to update the weights and biases. This is a special form of gradient descent since the partial derivatives are calculated analytically, without the need for numerical approximation. To avoid overfitting of the network, L2 regularization has been used, which is a simple and effective approach. L2 regularization requires only one additional parameter λ, and achieves better generalization by limiting the weights in the neural network. The parameter η denotes the learning rate. The cost function now includes what is effectively the square of the weights, while the partial derivative of the cost function includes the weight itself. This means that L2 regularization can be implemented without any additional computation. The adjusted cost function and

the updates to the weights are shown in Equations (2.156)-(2.160).

$$C^* = C + \frac{\lambda}{2 \cdot N} \cdot \left(\|\mathbf{W_h}\|_F^2 + \|\mathbf{b_h}\|_F^2 + \|\mathbf{W_y}\|_F^2 + \|\mathbf{b_y}\|_F^2 \right) \tag{2.156}$$

$$\mathbf{W_h} \leftarrow \mathbf{W_h} - \eta \cdot \left(\frac{\partial C}{\partial \mathbf{W_h}} + \lambda \cdot \mathbf{W_h} \right) \tag{2.157}$$

$$\mathbf{b_h} \leftarrow \mathbf{b_h} - \eta \cdot \left(\frac{\partial C}{\partial \mathbf{b_h}} + \lambda \cdot \mathbf{b_h} \right) \tag{2.158}$$

$$\mathbf{W_y} \leftarrow \mathbf{W_y} - \eta \cdot \left(\frac{\partial C}{\partial \mathbf{W_y}} + \lambda \cdot \mathbf{W_y} \right) \tag{2.159}$$

$$\mathbf{b_y} \leftarrow \mathbf{b_y} - \eta \cdot \left(\frac{\partial C}{\partial \mathbf{b_y}} + \lambda \cdot \mathbf{b_y} \right) \tag{2.160}$$

Chapter 3

Research Method and Results

This chapter presents the developed control algorithms, simulation results, and experimental results from the published papers during this project. Firstly, the development of a path controller is presented, which acts as a stepping stone for the development of the following control systems. Secondly, investigation of adaptive feedforward control of pressure compensated DCVs is presented. Subsequently, the topic of anti-swing control is presented, where the development of anti-swing control systems in two and three dimensions is showcased. Further, the design of EHAs for motion control of hydraulically actuated cranes is investigated. Lastly, the development of a deflection compensator for the HMF 2020K4 loader crane is presented.

3.1 Path Control in Actuator Space

Paper A presents the development of a path controller operating in actuator space. The concept of the actuator space is introduced, which means that the cylinder length coordinates are used as state variables, instead of the joint angles or the Cartesian coordinates of the crane tip. For the HMF 2020K4 crane in the laboratory the actuator space coordinates are the rotational angle of the slew column θ_s, the length of the main cylinder x_m, and the length of the knuckle cylinder x_k. By using the actuator space for path control the motion of each actuator is inherently minimized, which will typically reduce energy consumption. One of the nonlinearities for hydraulic cylinders is the jump in friction forces around zero velocity due to stiction between the piston and the outer barrel. This effect is greatly reduced since the actuator velocity does not change sign between two points. An illustration of the joint space and actuator space for a typical crane is shown in Figure 3.1.

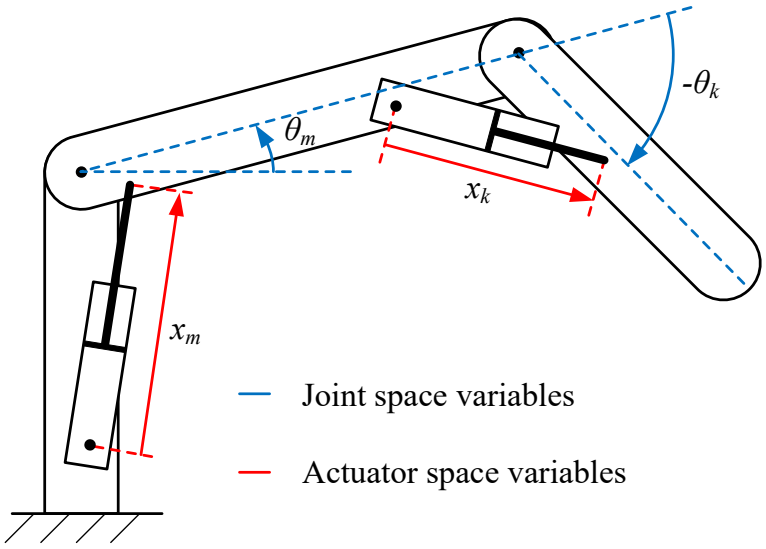

Figure 3.1: Joint space coordinates and actuator space coordinates for a two degree of freedom crane.

Since the cylinders are connected to pressure compensated DCVs, the relationship between the control signal and the actuator velocity becomes linear. In addition, the velocity constraints of the actuators become constant, given by the maximum valve flow and cylinder area. This is in contrast to joint space or Cartesian space where these constraints will be highly nonlinear. The developed path controller also includes acceleration constraints to reduce oscillations and fatigue, corresponding to the slope of the trapezoidal velocity profile. Based on Equation (3.1) from [77] the maximum acceleration is defined in Equation (3.3). Using these equations, the constraints of the actuators are now defined in terms of the state variables, their derivatives, and parameters from the hydraulic components.

$$T_r \geq \frac{6}{\omega_n} \tag{3.1}$$

$$T_r = \frac{v_{max}}{a_{max}} \tag{3.2}$$

$$a_{max} \leq \frac{\omega_n \cdot v_{max}}{6} \tag{3.3}$$

where

T_r	=	ramp time of velocity profile
ω_n	=	natural frequency of the system
v_{max}	=	maximum actuator velocity
a_{max}	=	maximum actuator acceleration

Given a list of points in actuator space, x_{list}, the path controller generates trapezoidal velocity profiles for each actuator based on the velocity and acceleration constraints, shown in Equations (3.4)-(3.13). The first step is to calculate the ramp time T_r and total time T for the three actuators. Δx denotes the distance between two points, and $i = 1..3$

denotes each actuator.

$$\Delta x_i = |x_{i,list} - x_i| \tag{3.4}$$

$$T_{r_i} = \frac{v_{i,max}}{a_{i,max}} \tag{3.5}$$

$$T_i = \frac{\Delta x_i + T_{r_i} \cdot v_{i,max}}{v_{i,max}} \tag{3.6}$$

In some scenarios the ramp time will be larger than half the total time, and the velocity profile will no longer be continuous. This happens when $\Delta x < T_r \cdot v_{max}$. A correction is made to turn the velocity profile into a symmetrical triangular profile, with the corrected ramp time $\hat{T}_r$ and total time $\hat{T}$:

$$\hat{T}_i = \begin{cases} 2 \cdot \sqrt{\frac{\Delta x_i}{a_{i,max}}} & \text{if } T_{r_i} > \frac{T_i}{2} \\ T_i & \text{otherwise} \end{cases} \tag{3.7}$$

$$\hat{T}_{r_i} = \begin{cases} \frac{\hat{T}_i}{2} & \text{if } T_{r_i} > \frac{T_i}{2} \\ T_{r_i} & \text{otherwise} \end{cases} \tag{3.8}$$

To ensure synchronous motion for all actuators, the common total time $\tilde{T}$ is used:

$$\tilde{T} = \max(\hat{T}_i) \tag{3.9}$$

The calculations of the corrected maximum velocity $\hat{v}$ and trapezoidal velocity profile $\tilde{v}$ are given as:

$$\hat{v}_i = \frac{\Delta x_i}{\tilde{T} - \hat{T}_{r_i}} \tag{3.10}$$

$$\tilde{v}_i = \begin{cases} \frac{t \cdot \hat{v}_i}{\hat{T}_{r_i}} & \text{if } t < \hat{T}_{r_i} \\ \hat{v}_i & \text{if } \hat{T}_{r_i} \leq t < \tilde{T} - \hat{T}_{r_i} \\ \hat{v}_i - \frac{(t - \tilde{T} + \hat{T}_{r_i}) \cdot \hat{v}_i}{\hat{T}_{r_i}} & \text{if } \tilde{T} - \hat{T}_{r_i} \leq t < \tilde{T} \end{cases} \tag{3.11}$$

The trapezoidal velocity reference v_{ref} and position reference x_{ref} are then computed using the velocity profile $\tilde{v}$ and time integration:

$$v_{i,ref} = \tilde{v}_i \cdot \text{sign}(x_{i,list} - x_i) \tag{3.12}$$

$$x_{i,ref} = \int v_{i,ref} dt + x_{i,start} \tag{3.13}$$

The parameters for the trapezoidal velocity profile is shown in Figure 3.2.

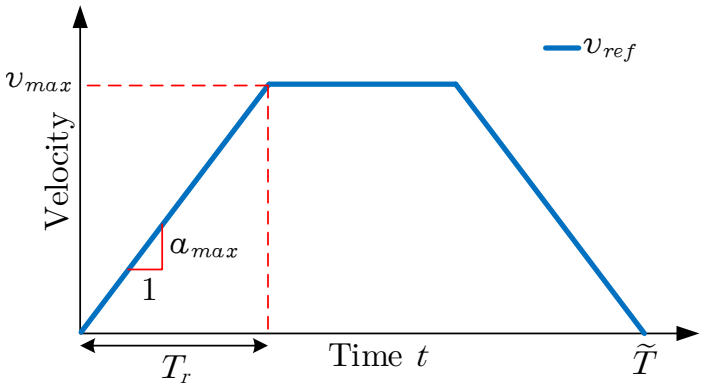

Figure 3.2: Parameters for trapezoidal velocity profile. Taken from Paper A.

The generated references are used in the control system utilizing velocity feedforward and position feedback control. The control law is shown in Equation (3.14) where k_p denotes the gain of the P-controller and k_{FF} the feedforward gain.

$$u = v_{ref} \cdot k_{FF} + (x_{ref} - x) \cdot k_p \tag{3.14}$$

The system has been simulated in MATLAB/Simulink using a model of the crane, the developed path controller, and the selected control law. The list of points is made to cover a wide range of motion for the crane. To define the acceleration constraints the natural frequency for each actuator has been estimated using a model of the crane and is shown in Table 3.1 together with the maximum velocity.

Table 3.1: Maximum velocity and estimated natural frequency for each actuator.

Actuator	$v_{max,in}$	$v_{max,out}$	ω_n
Slew	0.1 rad/s	0.1 rad/s	1 rad/s
Main	0.046 m/s	0.032 m/s	4 rad/s
Knuckle	0.047 m/s	0.036 m/s	5 rad/s

Some effort has been made to tune the controller parameters and optimize the crane motion using simulation. A genetic algorithm similar to the one in Section 2.5 has been used to tune the parameters. For the genetic algorithm an objective function has been made using the position error e and the time derivative of the control signal $\dot{u}$, shown in Equation (3.15). The normalization vectors $\mathbf{C}_1$ and $\mathbf{C}_2$ ensure a unitless objective function. The design goal is to reduce the position error, as well as oscillations in the control signal. Reducing the oscillations in the control signal will help mitigate some phenomena in real-world applications, namely jerky motion, fatigue, and excitation of unmodeled dynamics. The parameters from the optimization which minimizes the objective function is shown in Table 3.2.

$$f = \sum_{i=1}^{3} (\mathbf{C}_{1,i} \cdot \mathrm{RMS}(e_i) + \mathbf{C}_{2,i} \cdot \mathrm{RMS}(\dot{u}_i)) \tag{3.15}$$

where

$\mathbf{C}_1$ = normalization vector 1, $[1\ \text{rad}^{-1}, 1\ \text{m}^{-1}, 1\ \text{m}^{-1}]^T$

$\mathbf{C}_2$ = normalization vector 2, $[1\ \text{s}, 1\ \text{s}, 1\ \text{s}]^T$

Table 3.2: Controller parameters from optimization.

Actuator	k_p
Slew	4.68 rad^{-1}
Main	4.72 m^{-1}
Knuckle	19.71 m^{-1}

The position reference during simulation is shown in Figure 3.3. The trapezoidal velocity reference translates into a smooth position reference.

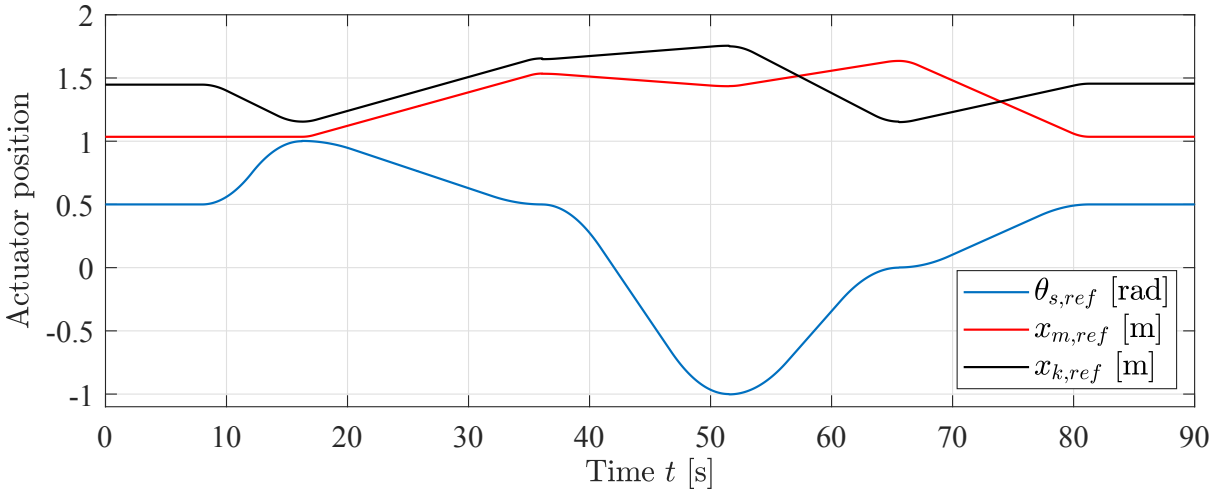

Figure 3.3: Actuator position reference during path control simulation.

The position error for each actuator which is less than 0.01 m for both cylinders and 0.04 rad for the slewing angle, shown in Figure 3.4. The position error is without major oscillations, which was desired from the optimization.

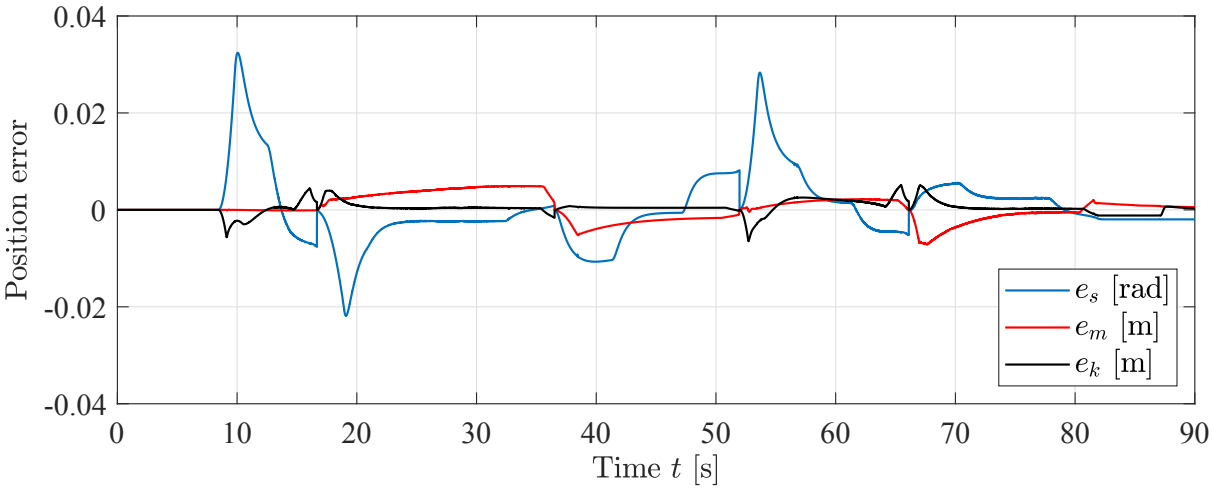

Figure 3.4: Actuator position error during path control simulation.

The path controller was also implemented on the HMF crane in the laboratory to verify the performance experimentally. A new list of points was made to fit the limited space in the laboratory. The position error in the laboratory is shown in Figure 3.5. It can be seen that the position error is similar in magnitude to the simulations, albeit with some oscillations for the slewing motion. Some small oscillations is expected since the crane has some flexibility, but the similar position error indicates that the tuning has been successful.

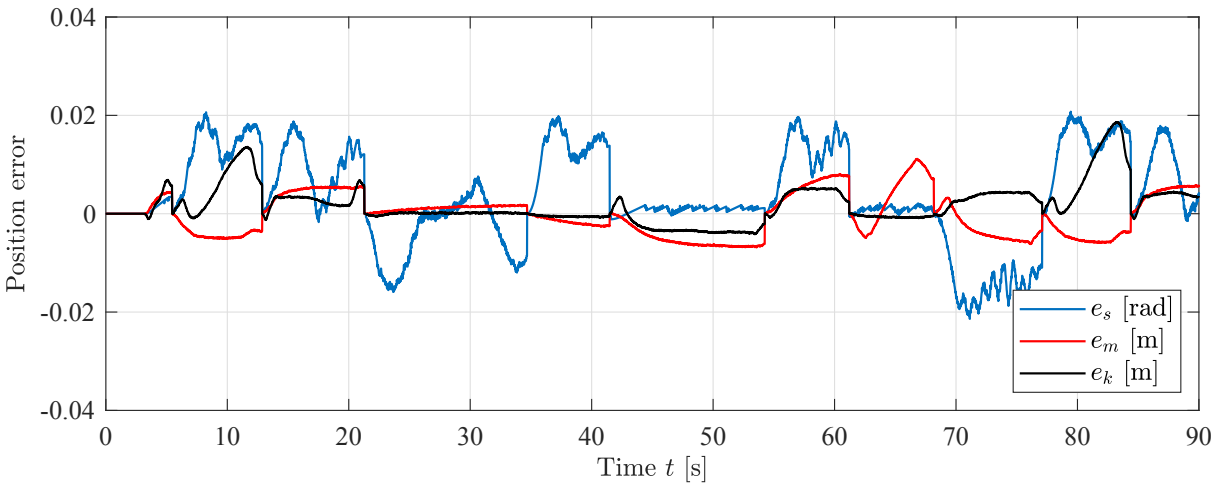

Figure 3.5: Actuator position error during path control in laboratory.

3.2 Adaptive Feedforward Control

With the effectiveness of feedforward control of pressure compensated DCVs, an adaptive feedforward controller was developed and investigated in paper B. The MIT-rule [78] has been used to derive an adaptive controller, shown in Figure 3.6. The update law and controller output are given in Equations (3.16) and (3.17).

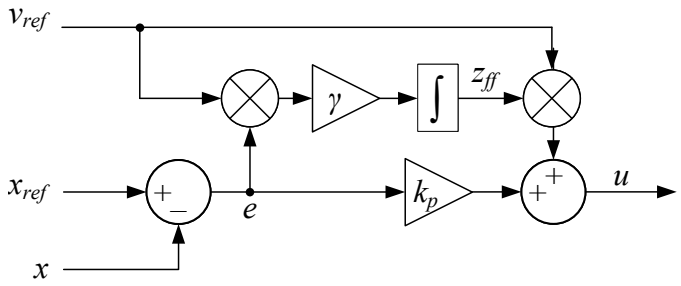

Figure 3.6: MIT-rule adaptive feedforward controller.

$$\dot{z}_{ff} = \gamma \cdot v_{ref} \cdot e \tag{3.16}$$

$$u = k_p \cdot e + z_{ff} \cdot v_{ref} \tag{3.17}$$

The sign-sign method has also been investigated which is a modification of the MIT-rule. In this case the update law is given as:

$$\dot{z}_{ff} = \gamma \cdot \text{sign}(v_{ref}) \cdot \text{sign}(e) \tag{3.18}$$

One of the novelties of this paper is the development of a differential adaptive feedforward controller. This comes from the fact that the actuator is a differential cylinder with different out-stroke and in-stroke velocities for an equal control input. Consequently, the controller should be able to handle model uncertainties in both directions of motion. Therefore two separate states z_{ff}^{+} and z_{ff}^{-} have been introduced for out-stroke and in-stroke motion respectively. Some control logic is introduced to ensure that the update law and controller output are only active when moving in the relevant direction. Figure 3.7 shows the differential adaptive controller based on the MIT-rule.

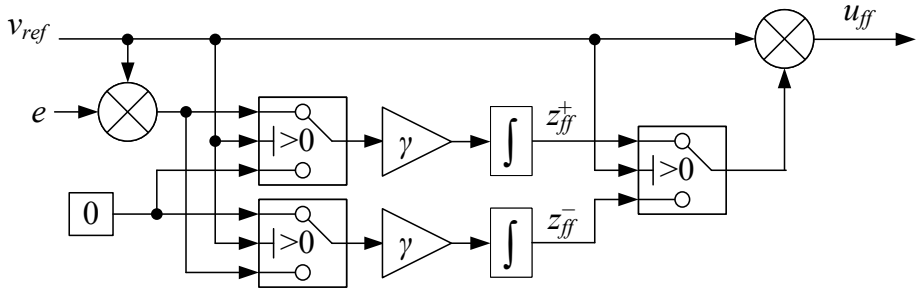

Figure 3.7: Differential MIT-rule adaptive feedforward controller

The governing equations for the differential MIT-rule adaptive feedforward are shown in Equations (3.19)-(3.22).

$$\dot{z}_{ff}^{+} = \begin{cases} \gamma \cdot v_{ref} \cdot e & \text{if } v_{ref} > 0 \\ 0 & \text{otherwise} \end{cases} \tag{3.19}$$

$$\dot{z}_{ff}^{-} = \begin{cases} 0 & \text{if } v_{ref} > 0 \\ \gamma \cdot v_{ref} \cdot e & \text{otherwise} \end{cases} \tag{3.20}$$

$$u_{ff} = \begin{cases} z_{ff}^{+} \cdot v_{ref} & \text{if } v_{ref} > 0 \\ z_{ff}^{-} \cdot v_{ref} & \text{otherwise} \end{cases} \tag{3.21}$$

$$u = k_p \cdot e + u_{ff} \tag{3.22}$$

where

z_{ff}^{+} = out-stroke feedforward gain
z_{ff}^{-} = in-stroke feedforward gain
u_{ff} = feedforward controller output

A simulation was conducted in MATLAB/Simulink using a model of the crane, the path controller from section 3.1, and the developed differential adaptive controllers. Due to the use of sign(x), the adaptation gain γ is different for the two controllers. The gain has been experimentally set to $\gamma = 200$ s·m^{-3} for the MIT-rule feedforward, and $\gamma = 0.1$ m^{-1} for the sign-sign feedforward. The references for position and velocity for the knuckle cylinder are shown in Figure 3.8.

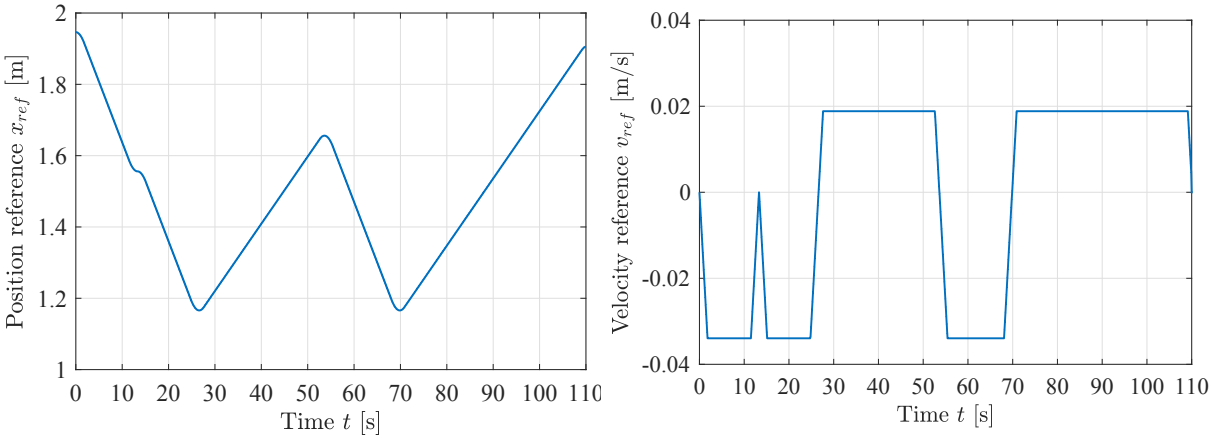

(a) Position reference

(b) Velocity reference

Figure 3.8: Point-to-point path references for the knuckle cylinder in adaptive feedforward simulation. Taken from Paper B.

The resulting knuckle cylinder position error for the MIT-rule feedforward controller during simulation is shown in Figure 3.9. It can be seen that the position error decreases to a bounded error of ±6 mm, showcasing the success of the adaptive controller. In addition, a plot of the feedforward states z_{ff} is given in Figure 3.10. It can be seen that they converge to a value approximately equal to the theoretical constant feedforward gain.

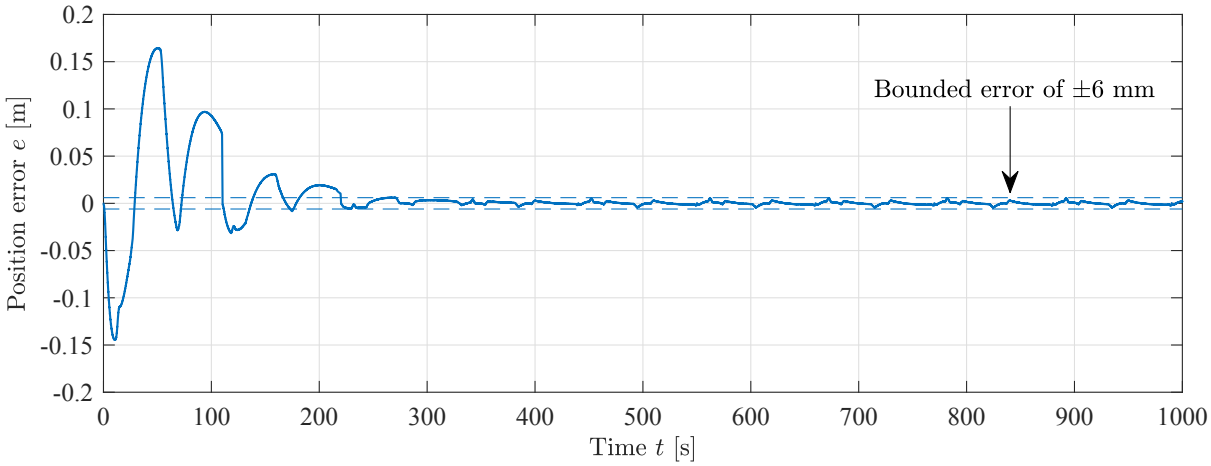

Figure 3.9: Knuckle cylinder position error during MIT-rule feedforward simulation, $\gamma = 200$ s·m^{-3}. Taken from Paper B.

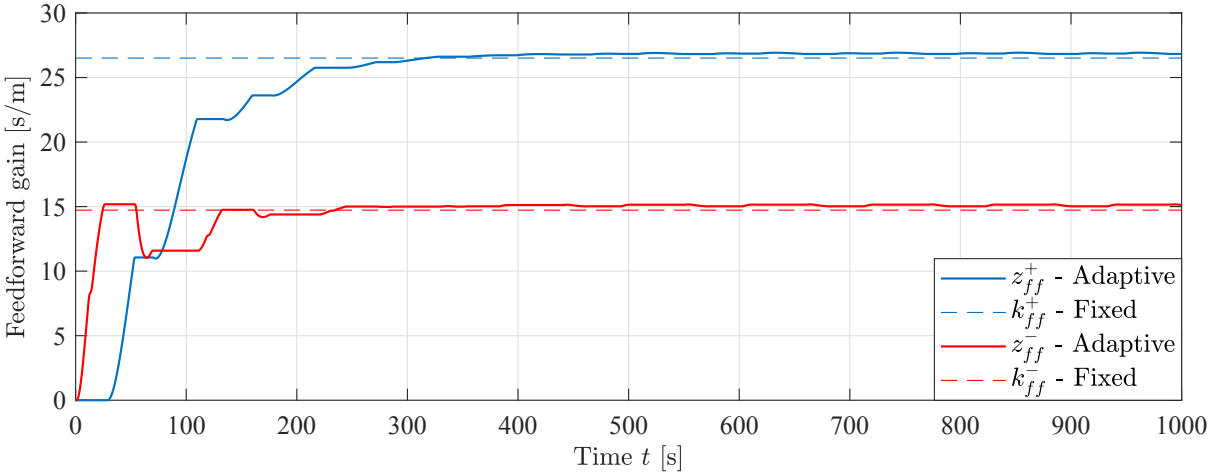

Figure 3.10: Feedforward states during MIT-rule feedforward simulation, $\gamma = 200$ s·m^{-3}. Taken from Paper B.

The cylinder position error for the sign-sign feedforward controller is shown in Figure 3.11. The same bounded error of ±6 mm is shown with the dashed lines, however convergence is slower.

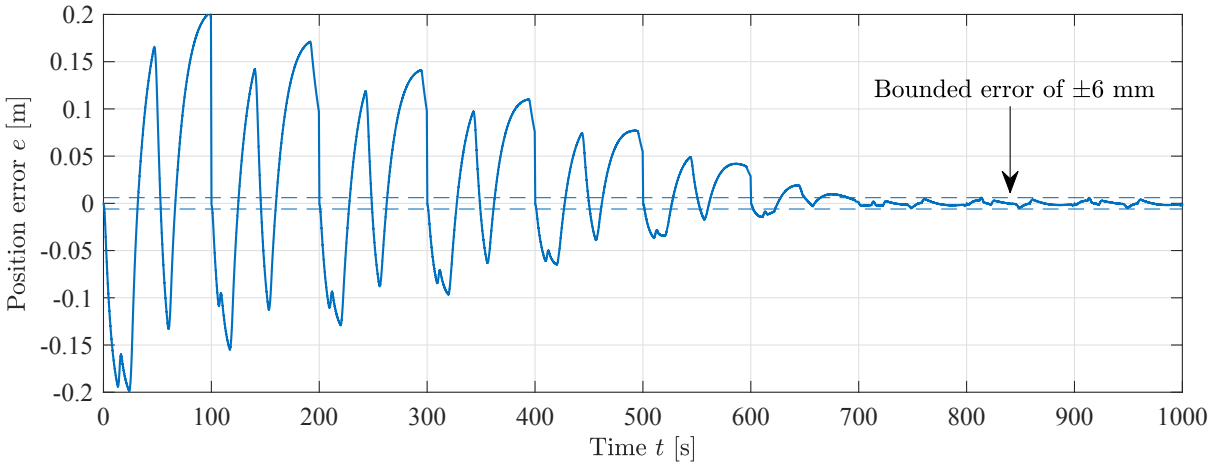

Figure 3.11: Cylinder position error during sign-sign feedforward simulation, $\gamma = 0.1$ m^{-1}. Taken from Paper B.

The RMS position error after convergence of the states z_{ff} is shown in Table 3.3, along with the results from using a fixed gain controller. Although the fixed gain feedforward is based on ideal model parameters, the MIT-rule adaptive feedforward controller exhibits a 23% decrease in RMS position error. This showcases the improved performance and feasibility of the novel adaptive controller.

Table 3.3: RMS position error after convergence in simulation.

	MIT-Rule	Sign-Sign	Fixed Gain
RMS error	1.6 mm	2.1 mm	2.1 mm

Experiments are performed to verify the performance of the adaptive controller. A similar reference as in the simulations are used on the knuckle cylinder, and the position error for the MIT-rule and sign-sign controller is shown in Figures 3.12 and 3.13, respectively. In this case both controllers converge to a bounded error of ±14 mm, however the MIT-rule converges faster.

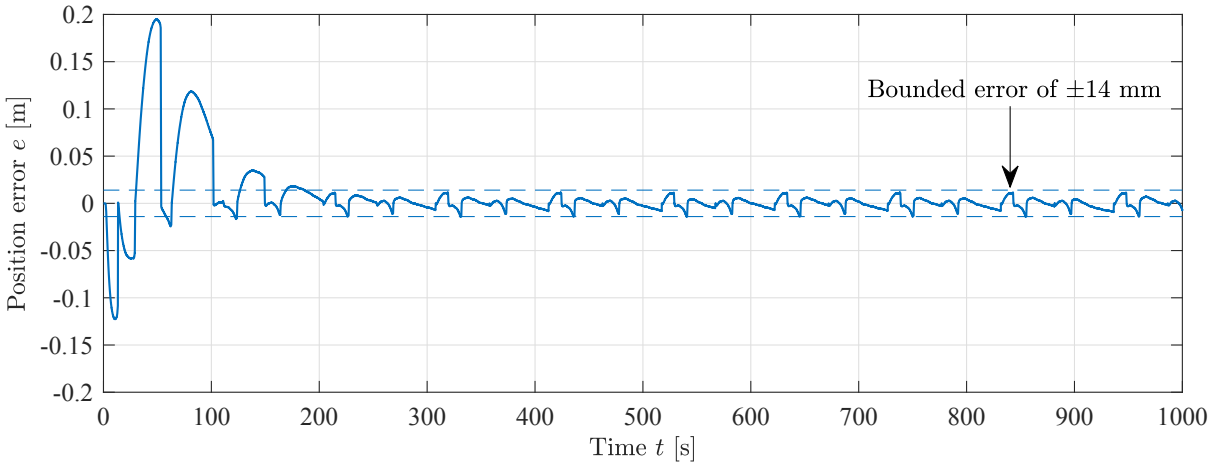

Figure 3.12: Position error during MIT-rule feedforward experiment, $\gamma = 200\ \mathrm{s \cdot m^{-3}}$. Taken from Paper B.

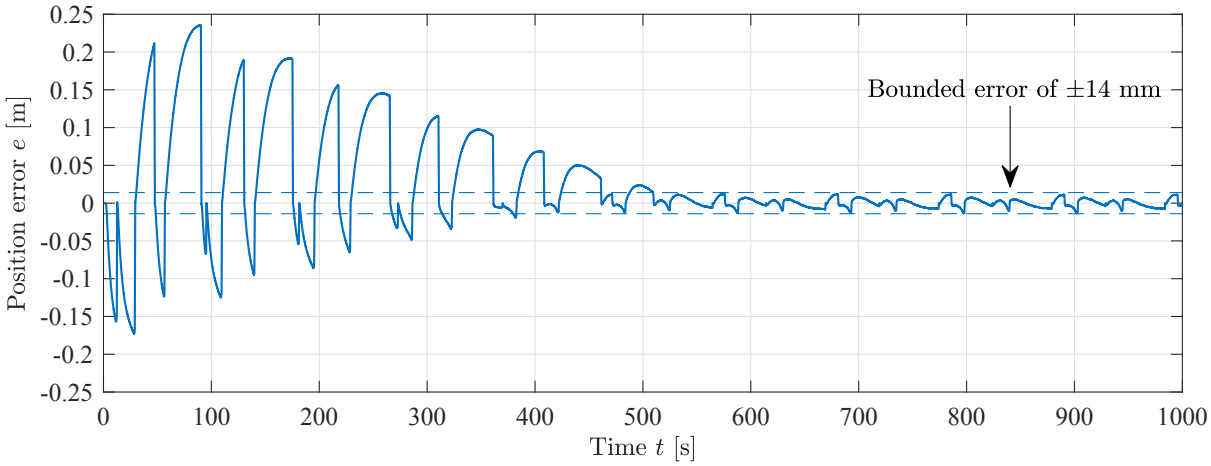

Figure 3.13: Position error during sign-sign feedforward experiment, $\gamma = 0.1\ \mathrm{m^{-1}}$. Taken from Paper B.

The states z_{ff} for the MIT-rule feedforward during the experiment are shown in Figure 3.14. The theoretical values for a fixed feedforward gain is shown with dashed lines, and it can be seen that the states converge to values different from the theoretical ones. The state z_{ff}^{+} is higher, while the state z_{ff}^{-} is lower. Further, the ratio of the feedforward gains is not equal to the cylinder area ratio ϕ, i. e. $\frac{z_{ff}^{-}}{z_{ff}^{+}} \neq \frac{A_r}{A_p}$. This may be attributed to the slight uncertainty of the area characteristic and flow curve for the spool in the DCV. This shows the importance of using two separate feedforward states which are not mathematically linked by the cylinder area ratio ϕ, as they are able to minimize the position error in both directions of motion regardless of their ratio. This would not be possible if a single state was used, as with the traditional MIT-rule. This showcases that the controller is able to adapt to the model uncertainties. Regarding the time it takes for the system to converge it should be noted that the gain z_{ff} starts at zero. For a commercial product this would only be the case during factory testing, after which the system would be fully trained and ready for deployment. During normal operation the system would only need

to adapt to smaller changes in system parameters.

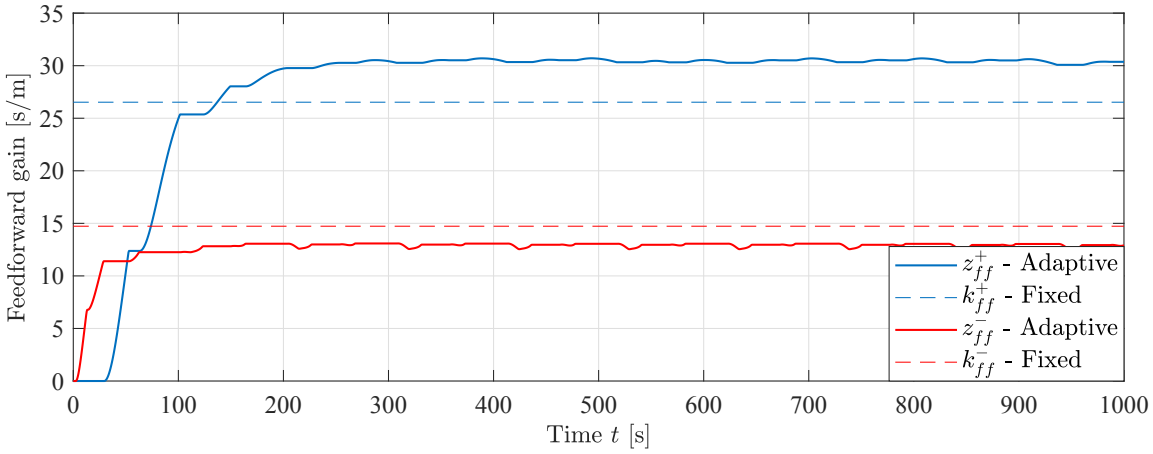

Figure 3.14: Feedforward states during MIT-rule feedforward experiment, $\gamma = 200$ s·m^{-3}. Taken from Paper B.

RMS position error from the experiment for the different feedforward controllers is shown in Table 3.4. It can be seen that the RMS position errors are slightly larger than in the simulations, but this is primarily due to the unmodeled flexibility of the crane. However, the use of independent out-stroke and in-stroke states z_{ff}^{+} and z_{ff}^{-} provides greatly increased performance on the physical crane in the presence of model uncertainties.

Table 3.4: RMS position error after convergence in experiment.

	MIT-Rule	Sign-Sign	Fixed Gain
RMS error	5.2 mm	5.3 mm	24.9 mm

3.3 Anti-swing Control

Most cranes are used to lift payloads hanging from a wire or similar. When lifting suspended loads the crane will induce undesirable load swing due to the crane motion. This can lead to reduced operational efficiency as well as being a safety hazard. Anti-swing control is a topic which aims to eliminate the load swing. Controlling a suspended load is difficult, as the system is underactuated, meaning the degrees of freedom are greater than the number of controlled actuators.

Anti-swing control is a vital part of this project and has been developed and investigated in two papers, namely paper C and paper E. The former investigates planar anti-swing control in two dimensions, while the latter extends this into the three-dimensional case. The control strategy is the same in both papers and consists of using the measured payload angle to generate a set of actuator velocities that counteract the swinging payload. An illustration of the control strategy is shown in Figure 3.15.

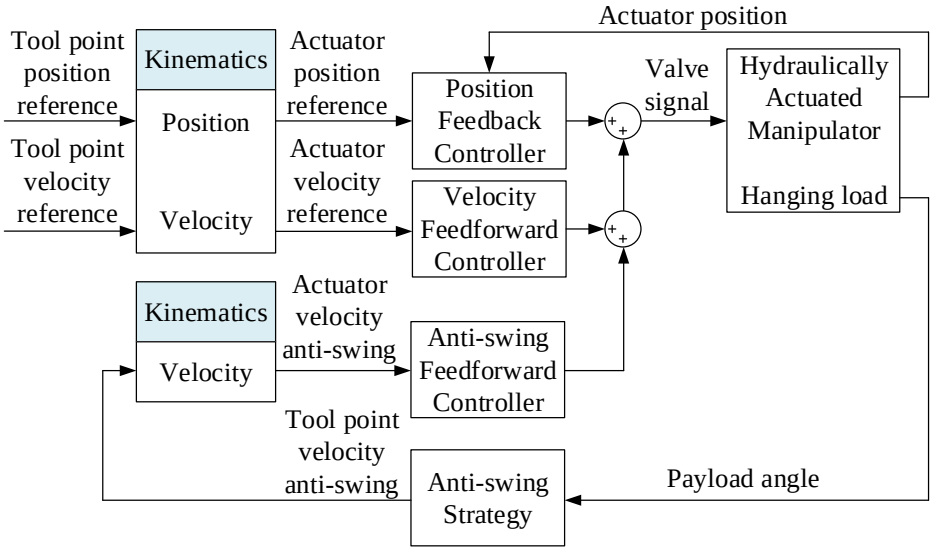

Figure 3.15: Anti-swing control strategy. Taken from Paper C.

The 3D anti-swing controller uses the swing angles α and β and anti-swing gain k_a to generate a set of toolpoint velocities. Actuator kinematics (Act. Kin), inverse Jacobian (Inv. Jac), and inverse actuator kinematics (Inv. Act.) from section 2.3 are then used to generate the actuator velocities. An illustration of the 3D anti-swing control system is shown in Figure 3.16.

The anti-swing toolpoint velocities are transformed into the actuator space, shown in Equations (3.23)-(3.26). The anti-swing cylinder velocities $\dot{x}_{m,a}$ and $\dot{x}_{k,a}$ are then multiplied by k_{ff} to generate the valve opening. The control outputs for the control system are shown in Equations (3.27)-(3.29).

$$\begin{bmatrix} \dot{x}_{t,a} \\ \dot{y}_{t,a} \\ \dot{z}_{t,a} \end{bmatrix} = k_a \cdot \begin{bmatrix} \alpha \\ \beta \\ 0 \end{bmatrix} \tag{3.23}$$

$$\begin{bmatrix} \dot{\theta}_{s,a} \\ \dot{\theta}_{m,a} \\ \dot{\theta}_{k,a} \end{bmatrix} = J^{\dagger} \cdot \begin{bmatrix} \dot{x}_{t,a} \\ \dot{y}_{t,a} \\ \dot{z}_{t,a} \end{bmatrix} \tag{3.24}$$

$$\dot{x}_{m,a} = \theta^{\dagger}_{x_m} \cdot \dot{\theta}_{m,a} \tag{3.25}$$

$$\dot{x}_{k,a} = \theta^{\dagger}_{x_k} \cdot \dot{\theta}_{k,a} \tag{3.26}$$

$$u_s = (\theta_{s,ref} - \theta_s) \cdot k_{p,s} + (\dot{\theta}_{s,ref} + \dot{\theta}_{s,a}) \cdot k_{ff,s} \tag{3.27}$$

$$u_m = (x_{m,ref} - x_m) \cdot k_{p,m} + (\dot{x}_{m,ref} + \dot{x}_{m,a}) \cdot k_{ff,m} \tag{3.28}$$

$$u_k = (x_{k,ref} - x_k) \cdot k_{p,k} + (\dot{x}_{k,ref} + \dot{x}_{k,a}) \cdot k_{ff,k} \tag{3.29}$$

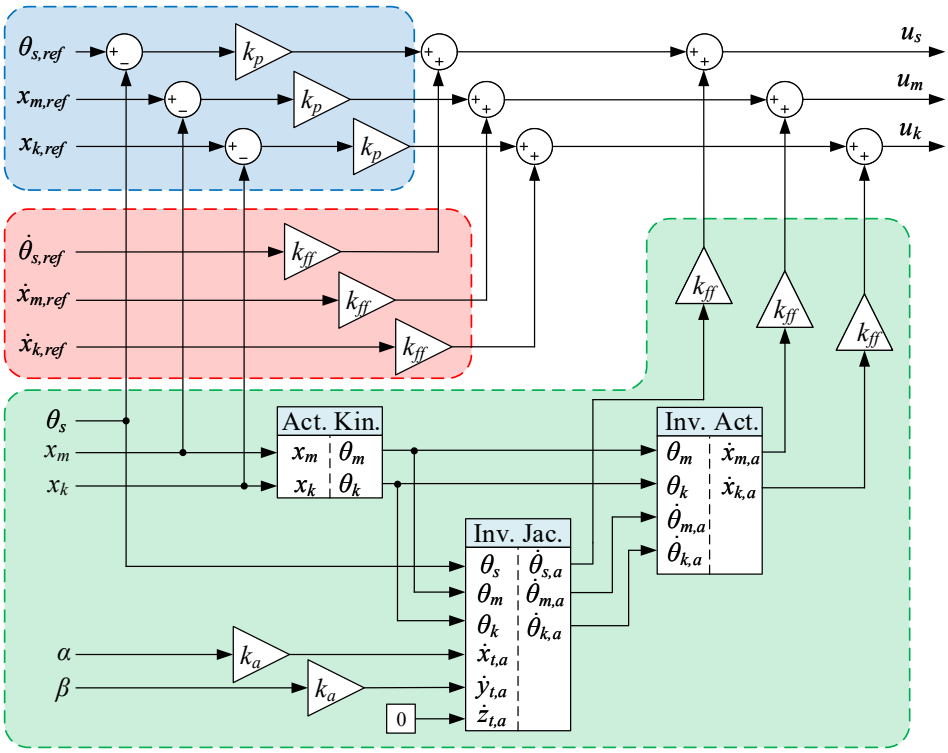

Figure 3.16: Illustration of the 3D anti-swing control system, with feedback controller (blue), feedforward controller (red), and anti-swing controller (green). Taken from Paper E.

In order to determine the anti-swing gain k_a a closed loop analysis was conducted using the hanging load dynamics and control law. The hanging load dynamics and control law are recalled as:

$$\ddot{\alpha} = \frac{1}{L_w} \cdot \left(-c_\alpha \cdot \ddot{x}_t + s_\alpha \cdot s_\beta \cdot \ddot{y}_t - s_\alpha \cdot c_\beta \cdot \ddot{z}_t - 2\dot{\alpha} \cdot \dot{L}_w - s_\alpha \cdot c_\alpha \cdot \dot{\beta}^2 \cdot L_w - g \cdot s_\alpha \cdot c_\beta \right) \tag{3.30}$$

$$\ddot{\beta} = \frac{1}{c_\alpha \cdot L_w} \cdot \left(-c_\beta \cdot \ddot{y}_t - s_\beta \cdot \ddot{z}_t + 2 \cdot s_\alpha \cdot \dot{\alpha} \cdot \dot{\beta} \cdot L_w - 2 \cdot c_\alpha \cdot \dot{\beta} \cdot \dot{L}_w - g \cdot s_\beta \right) \tag{3.31}$$

$$\dot{x}_t = \alpha \cdot k_a \tag{3.32}$$

$$\dot{y}_t = \beta \cdot k_a \tag{3.33}$$

$$\dot{z}_t = 0 \tag{3.34}$$

Taking the time derivative of the control law and inserting into the hanging load dynamics yields the nonlinear closed loop dynamics of the system:

$$\ddot{x}_t = \dot{\alpha} \cdot k_a \tag{3.35}$$

$$\ddot{y}_t = \dot{\beta} \cdot k_a \tag{3.36}$$

$$\ddot{z}_t = 0 \tag{3.37}$$

$$\ddot{\alpha} = \frac{1}{L_w} \cdot \left(-c_\alpha \cdot \dot{\alpha} \cdot k_a + s_\alpha \cdot s_\beta \cdot \dot{\beta} \cdot k_a - 2\dot{\alpha} \cdot \dot{L}_w - s_\alpha \cdot c_\alpha \cdot \dot{\beta}^2 \cdot L_w - g \cdot s_\alpha \cdot c_\beta \right) \tag{3.38}$$

$$\ddot{\beta} = \frac{1}{c_\alpha \cdot L_w} \cdot \left(-c_\beta \cdot \dot{\beta} \cdot k_a + 2 \cdot s_\alpha \cdot \dot{\alpha} \cdot \dot{\beta} \cdot L_w - 2 \cdot c_\alpha \cdot \dot{\beta} \cdot \dot{L}_w - g \cdot s_\beta \right) \tag{3.39}$$

By linearizing the system around $\alpha \approx \beta \approx 0$ and $\dot{L}_w \approx 0$ the damping provided by the anti-swing gain k_a can be calculated. Linearization followed by a Laplace transform gives the following decoupled system dynamics:

$$\ddot{\alpha} = -\frac{\dot{\alpha} \cdot k_a}{L_w} - \frac{g \cdot \alpha}{L_w} \tag{3.40}$$

$$\ddot{\beta} = -\frac{\dot{\beta} \cdot k_a}{L_w} - \frac{g \cdot \beta}{L_w} \tag{3.41}$$

$$s^2 \cdot \alpha = -\frac{s \cdot \alpha \cdot k_a}{L_w} - \frac{g \cdot \alpha}{L_w} \tag{3.42}$$

$$s^2 \cdot \beta = -\frac{s \cdot \beta \cdot k_a}{L_w} - \frac{g \cdot \beta}{L_w} \tag{3.43}$$

The transfer function is the same for both angles, given as:

$$s^2 + \frac{s \cdot k_a}{L_w} + \frac{g}{L_w} = 0 \tag{3.44}$$

$$s^2 + 2 \cdot s \cdot \zeta \cdot \omega + \omega^2 = 0 \tag{3.45}$$

The bandwidth and damping ratio can be calculated as:

$$\omega = \sqrt{\frac{g}{L_w}} \tag{3.46}$$

$$\zeta = \frac{k_a}{2 \cdot \sqrt{L_w \cdot g}} \tag{3.47}$$

The anti-swing gain can now be expressed based on the desired damping ratio, and allows for gain scheduling based on the wire length:

$$k_a = 2 \cdot \zeta \cdot \sqrt{L_w \cdot g} \tag{3.48}$$

The anti-swing control system is tested using a model of the crane in MATLAB/Simulink. The crane is using the path controller described in section 3.1. The actuator position references are shown in Figure 3.17, and an illustration of the planar Cartesian motion is shown in Figure 3.18. The resulting undamped swing angles are shown in Figure 3.19. The wire length is $L_w = 2$ m and the payload has a mass of $m = 62.5$ kg.

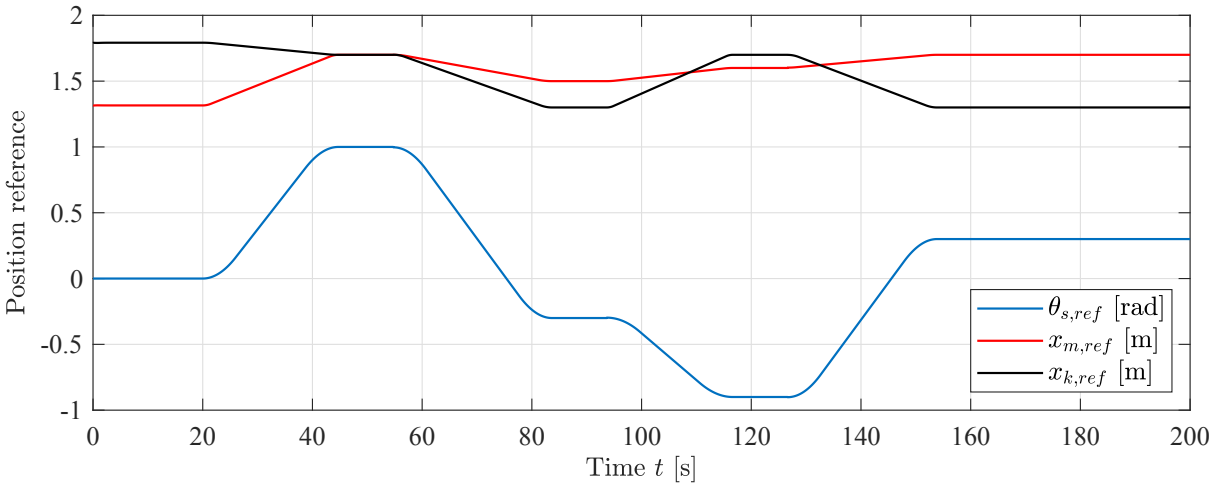

Figure 3.17: Actuator position reference for anti-swing simulation.

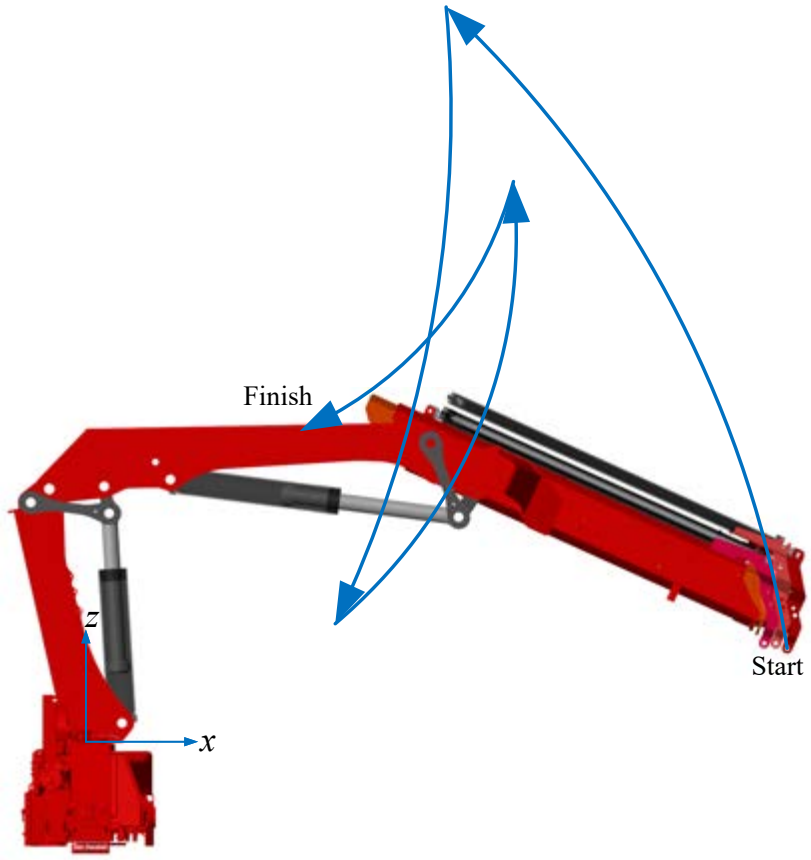

Figure 3.18: Illustration of the planar Cartesian motion for the crane for anti-swing simulation.

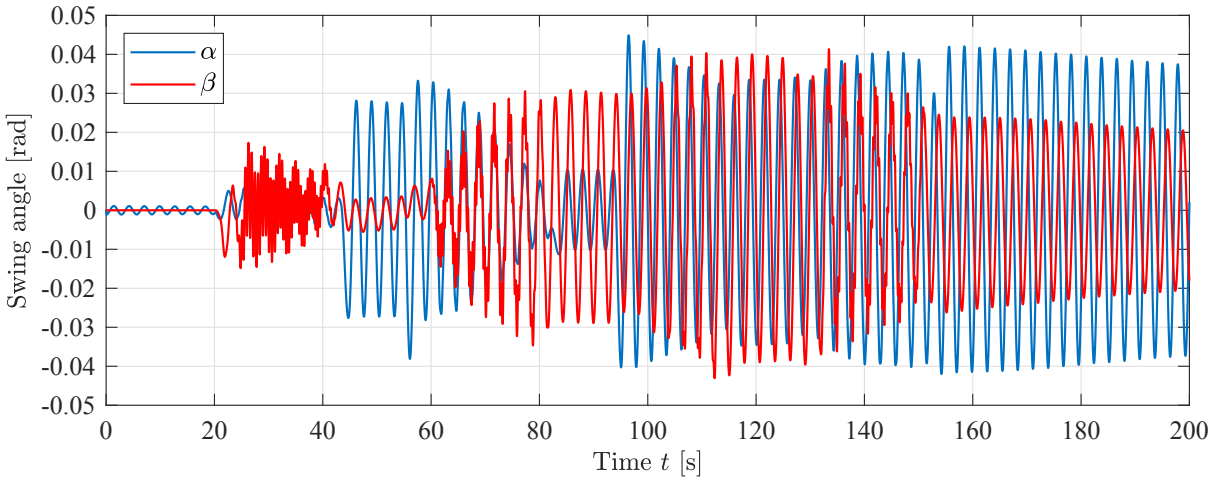

Figure 3.19: Swing angles without anti-swing control during simulation.

Selecting the anti-swing gain $k_a = 5$ m/s, the swing angles are shown in Figure 3.20. It can be seen that the in-plane angle α is successfully suppressed, but the out-of-plane angle β experiences high frequency oscillations. The source of these oscillations is identified as the flexibility of the slewing mechanism, which affects the hanging load motion.

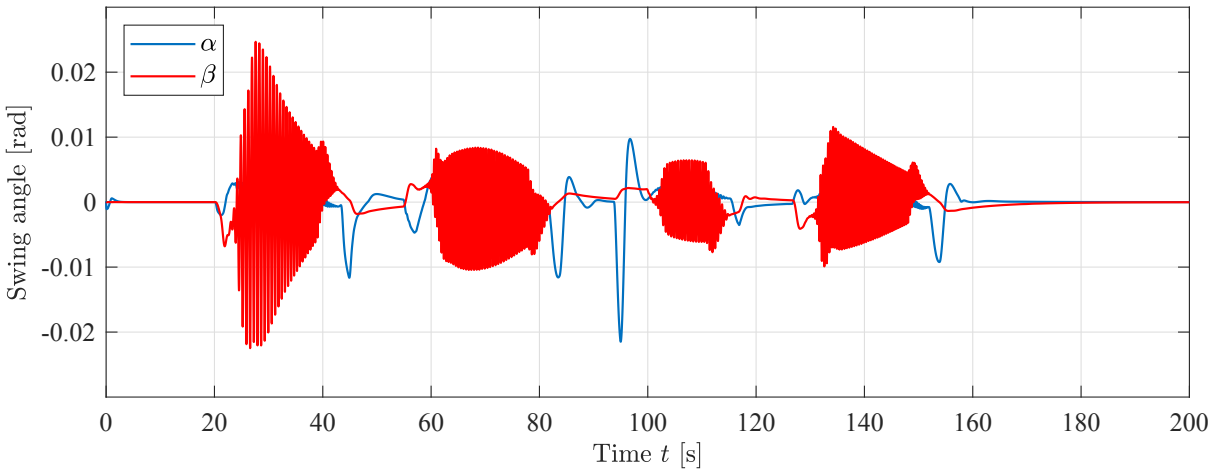

Figure 3.20: Swing angles with anti-swing control during simulation.

Pressure feedback is implemented for the slew cylinder to compensate for the oscillations. The implementation is shown in Equation (3.49), where the filter gain $k_{pf} = 0.02\ \text{bar}^{-1}$ and filter frequency $\omega_{pf} = 15$ rad/s form a high pass filter, along with the load pressure p_L. Comparing figure Figure 3.20 and Figure 3.21 it can be seen that the high frequency oscillations for the angle β are successfully suppressed using the described pressure feedback.

$$\hat{u}_s = u_s - \frac{k_{pf} \cdot s}{s + \omega_{pf}} \cdot p_L \tag{3.49}$$

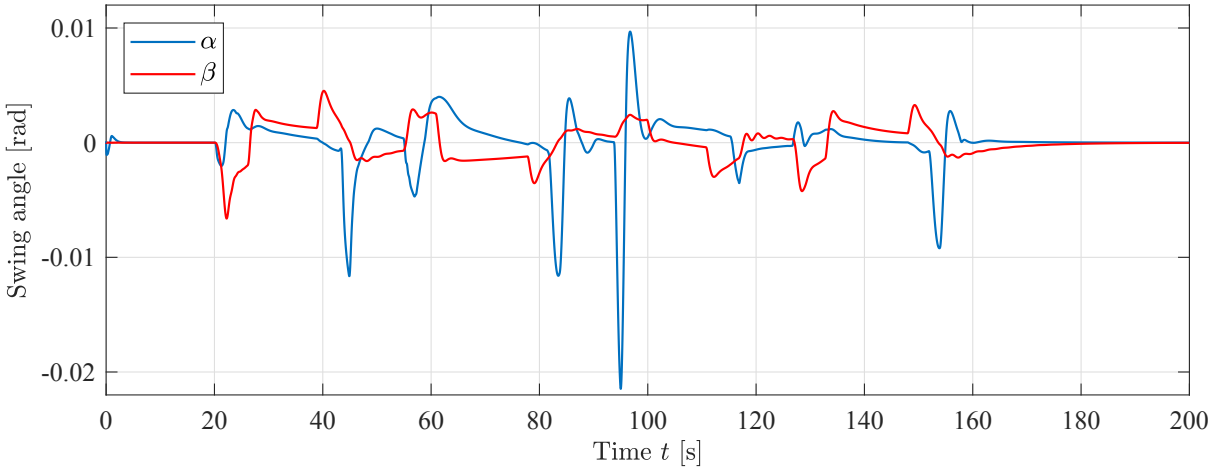

Figure 3.21: Swing angles with anti-swing and pressure feedback during simulation.

A quantitative analysis comparing the RMS value of the position errors for the three actuators and the two swing angles is shown in Table 3.5. The results are from the simulations without anti-swing control, with anti-swing control (AS), and with both anti-swing control and pressure feedback (AS+PF). It can be seen that the anti-swing controller has a negative impact on the position errors, but this is expected and acceptable since the primary focus of the control system is to suppress the swing angles. For the hanging

payload, both the anti-swing control and the pressure feedback give a large reduction in the swing angles, with a decrease in the RMS value of approximately 90 %. The introduction of the pressure feedback yields a significant improvement for the angle β.

Table 3.5: Quantitative anti-swing simulation results.

Variable	No control	AS	AS+PF
RMS(α) [mrad]	21.21	2.55	2.52
RMS(β) [mrad]	16.97	4.25	1.47
RMS(e_s) [mrad]	3.17	9.03	9.73
RMS(e_m) [mm]	0.35	3.21	3.27
RMS(e_k) [mm]	1.54	2.79	2.78

Experiments are also conducted to verify the performance of the anti-swing control system. The payload angle is measured using an inertial measurement unit attached to the hook of the crane. The path is altered due to limited space, and the pressure feedback is tuned to match the physical crane, with $k_{pf} = 0.04$ bar^{-1} and $\omega_{pf} = 1$ rad/s. It should be noted that the system experienced heavy oscillations without pressure feedback enabled, therefore only two different experiments were conducted. The swing angles α and β without anti-swing control are shown in Figure 3.22, and the swing angles with anti-swing control are shown in Figure 3.23. Comparing these two Figures it can be seen that the angle α is greatly reduced, while β still has some oscillations. This can be attributed to the fact that β is the most affected by the slewing motion and the instability issues mentioned.

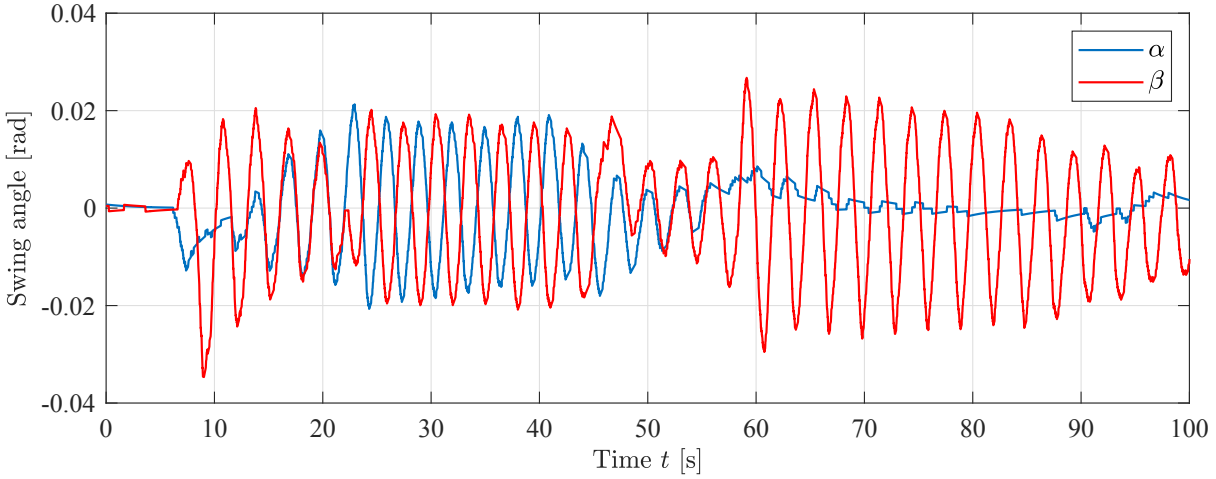

Figure 3.22: Swing angles without anti-swing control during experiment.

The RMS values of the swing angles and position errors with and without anti-swing control are shown in Table 3.6. The angle α is reduced by 75 %, with a slight impact on position error on the main and knuckle cylinder. The anti-swing controller has a large impact on the slew position error, quantifying the challenges faced with the slewing motion, but still a 51 % reduction for the out-of-plane angle β was obtained.

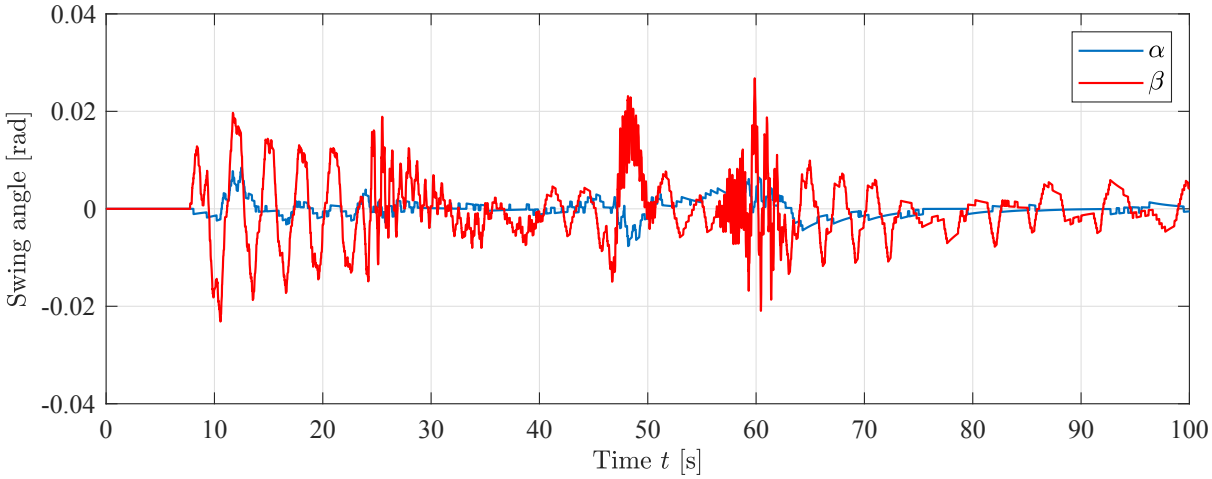

Figure 3.23: Swing angles with anti-swing control during experiment.

Table 3.6: Quantitative results from anti-swing experiment.

Variable	No control	Anti-swing
RMS(α) [mrad]	7.19	1.75
RMS(β) [mrad]	12.94	6.29
RMS(e_s) [mrad]	26.12	66.88
RMS(e_m) [mm]	2.91	3.26
RMS(e_k) [mm]	2.19	2.36

3.4 Electro-hydrostatic Actuators

The topic of EHAs has received increased research interest in the recent years due to the increased efficiency, compactness, and dynamic performance these actuators may provide. Focus has been directed towards drives utilizing a hydraulic cylinder, as this is a critical component with no viable electric counterpart in high power applications due to its high force capability, power density, and ruggedness. The EHA is typically using a high performance electric servomotor as the prime mover, and this hybrid drive approach aims to provide the best of both worlds in terms of efficiency, dynamic performance, and force capability. Paper D presents a novel concept of an EHA and provides the design and numerical analysis of the system applied to a hydraulic loader crane. In addition, a comparison with a load-sensing hydraulic system is made to evaluate the performance and efficiency of the EHA. The novel concept is shown in Figure 3.24, which utilizes pilot-operated check valves (POCVs) and an accumulator to compensate for the difference between the two areas of the cylinder. Electrically actuated poppet valves are used for load holding, and relief valves are used to protect against overpressure. A PMSM is driving a four quadrant pump which enables energy regeneration.

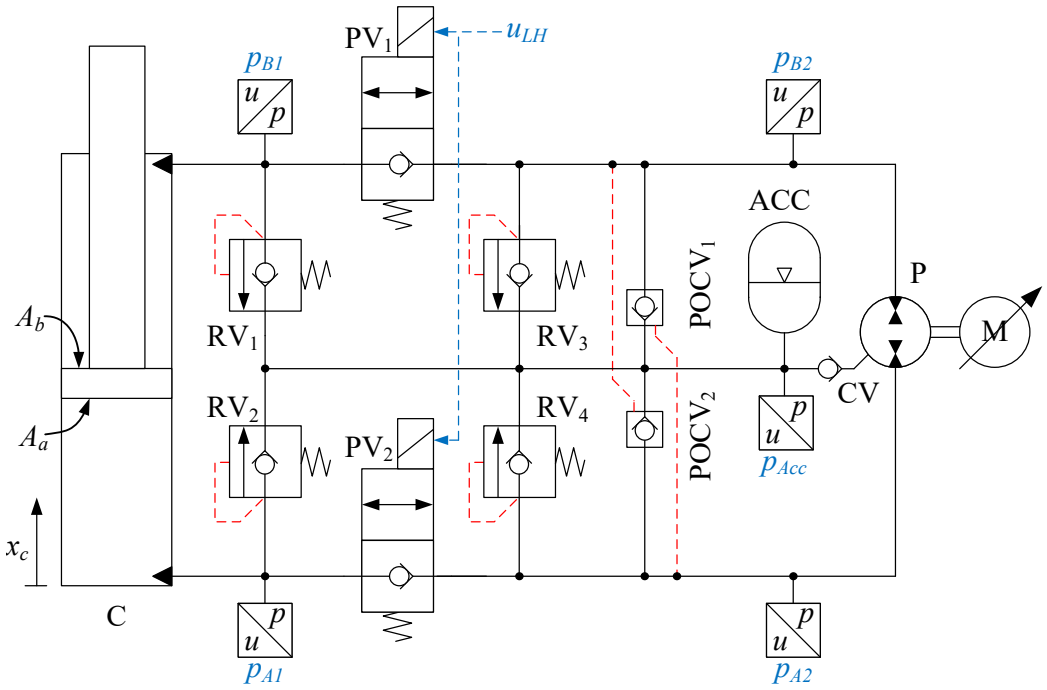

Figure 3.24: EHA with poppet valves (PV) for load holding, relief valves (RV) for over-pressure protection, and pilot-operated check valves (POCV) and accumulator (ACC) for flow compensation.

Four-quadrant operation is one of the main advantages of the EHA and Figure 3.25 shows how the system operates illustrating the load force, cylinder velocity, and hydraulic flows for each quadrant. Red lines and blue lines denote high pressure and low pressure, respectively. The accumulator is always connected to the low pressure, and the flow in and out of the POCVs change depending on the quadrant.

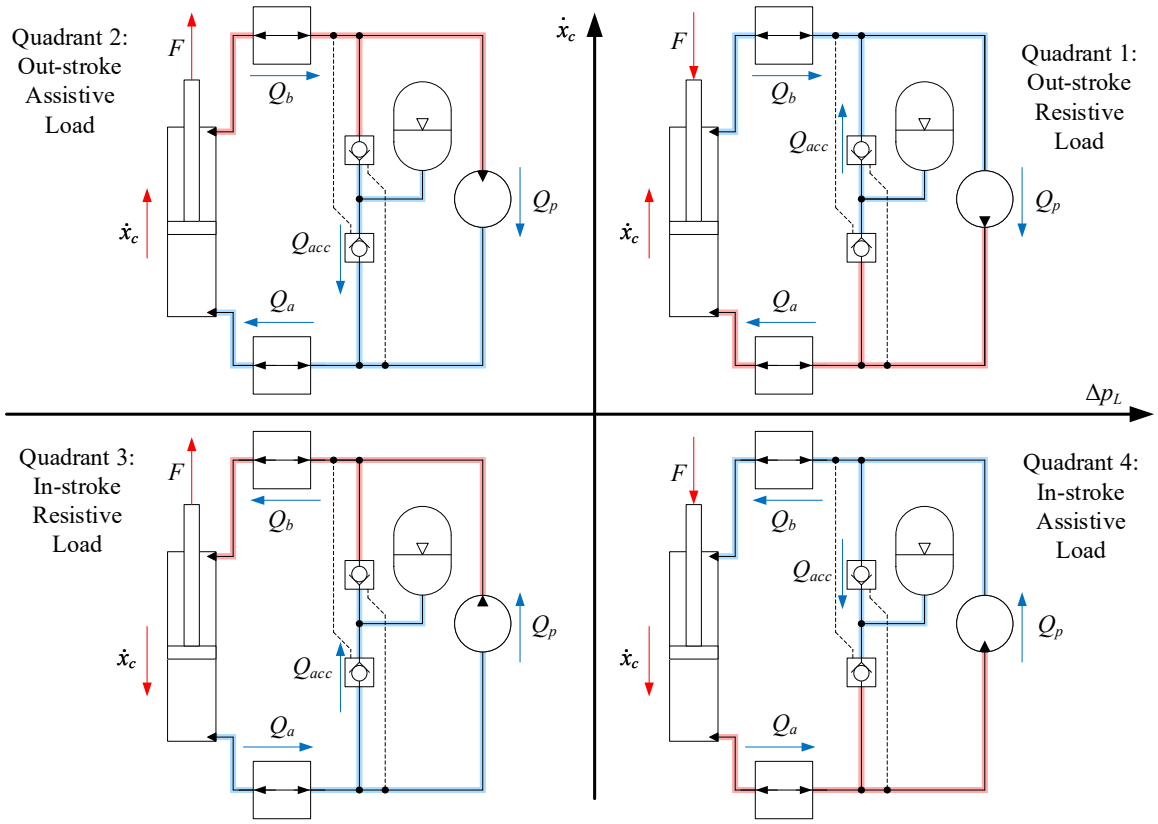

Figure 3.25: Four-quadrant operation of the simplified circuit with load holding valves energized. Taken from Paper D.

The EHA is designed to use the hydraulic cylinders on the HMF 2020K4 loader crane. A system pressure of 300 bar and a required flow of 40 L/min is used for the design, yielding a peak power of 20 kW. The valve sizes are primarily dependent on the system pressure and flow, but oversizing the valves to minimize pressure drop may improve efficiency. Selecting the pump and motor for the EHA is a different process than for a traditional hydraulic system. For valve controlled systems a constant speed 1500 rpm induction motor is often used, for which the pump displacement is dictated by the required flow, and the motor torque rating is based on the system pressure and selected pump displacement. On the other hand, servomotors are inherently variable speed devices, and design considerations for the motor and pump include system pressure, required flow, peak power, and maximum pump speed. For an EHA the pump's maximum speed, maximum pressure, and displacement is used in combination with the servomotor's speed-torque curve to calculate the system's operating region. A list of the selected components is shown in Table 3.7, and the flow-pressure curve for the selected motor and pump is shown in Figure 3.26. Note that the design point is closer to the maximum rating than the continuous rating, as the servomotor is not expected to run continuously when used for position control.

Table 3.7: Components of the EHA shown in Figure 3.24.

Component	**Manufacturer**	**Model number**	**Data**
Servomotor (M)	Beckhoff	AM8064R	11.5 kW
Hydraulic pump (P)	Bosch Rexroth	A10FZG018	18 cm^3/rev
Accumulator (ACC)	Bosch Rexroth	HAB20	18.1 l
Check valve (CV)	Sun Hydraulics	CXADXCN	28 l/min
Pilot-operated check valve (POCV)	Sun Hydraulics	CKCBXCN	57 l/min
Relief valve (RV)	Sun Hydraulics	RDDALCN	95 l/min
2/2 poppet valve (PV)	Parker Hannifin	DSH121CR	90 l/min

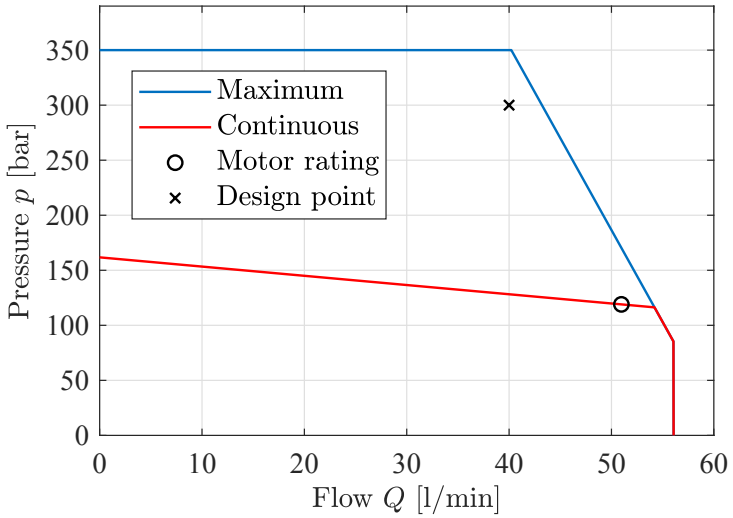

Figure 3.26: Flow-pressure curve for the EHA with the selected motor and pump. Taken from Paper D.

Based on the selected components modeling of the hydraulic valves and electric motor can be done as shown in chapter 2. The pump losses are modeled using laminar leakage on the hydraulic side and viscous friction on the mechanical side. The friction force in the cylinder is modeled with the viscous friction coefficient b_c and Coulomb friction force F_c as a function of the cylinder velocity $\dot{x}_c$. The parameter $\dot{x}_0$ is used to smooth the friction around zero velocity. The forces acting on the cylinder lifting a mass m are shown in Equations (3.50) and (3.51).

$$m \cdot \ddot{x}_c = \Delta p_L \cdot A_a - m \cdot g - F_{fric} \tag{3.50}$$

$$F_{fric} = b_c \cdot \dot{x}_c + F_c \cdot \tanh\left(\frac{\dot{x}_c}{\dot{x}_0}\right) \tag{3.51}$$

A control system is designed which sends a speed reference to the servodrive and an on/off signal to the load holding valves. The controller uses velocity feedforward, position feedback, and pressure feedback to control the cylinder position via the servodrive. Some switching logic opens and closes the load holding valves. An illustration of the control system is shown in Figure 3.27.

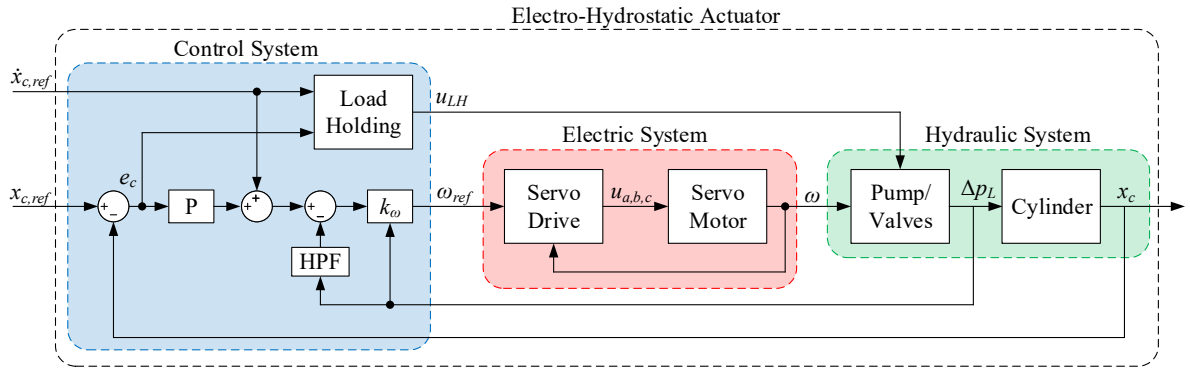

Figure 3.27: Overview of the EHA with control system, electric system, and hydraulic system. Taken from Paper D.

The constant k_ω is the ratio from cylinder velocity to motor speed, defined in Equation (3.53). It can be calculated from the cylinder areas A_a and A_b, load pressure difference Δp_L, and pump displacement D. In addition, pressure feedback is used with a high pass filter, shown in Equation (3.54).

$$\omega_{ref} = k_\omega \cdot (k_p \cdot e_c + \dot{x}_{ref} - u_{PF}) \tag{3.52}$$

$$k_\omega = \begin{cases} \dfrac{A_a}{D}, & \Delta p_L > 0 \\ \dfrac{A_b}{D}, & \text{otherwise} \end{cases} \tag{3.53}$$

$$u_{PF} = \frac{k_{pf} \cdot s}{s + \omega_{pf}} \cdot \Delta p_L \tag{3.54}$$

$$\Delta p_L = p_{A1} - \frac{A_b}{A_a} \cdot p_{B1} \tag{3.55}$$

The load holding signal u_{LH} which opens the load holding valves is defined in Equation (3.56) and uses the cylinder position error e_c and cylinder velocity reference $\dot{x}_{c,ref}$.

$$u_{LH} = \begin{cases} 1, & |e_c| > 0.1 \text{ mm or } |\dot{x}_{c,ref}| > 0 \text{ m/s} \\ 0, & \text{otherwise} \end{cases} \tag{3.56}$$

A model of the EHA was implemented in MATLAB/Simulink to verify the control system. In this simulation the EHA lifts a payload vertically in all four quadrants of operation. Simulation parameters are shown in Table 3.8.

Table 3.8: Simulation parameters for the EHA.

Name	**Parameter**	**Value**
Proportional gain	k_p	5 s^{-1}
Pressure feedback gain	k_{pf}	0.001 m/(bar·s)
Pressure feedback bandwidth	ω_{pf}	5.32 rad/s
Load mass	m	30000 kg
Viscous friction	b_c	150 kNs/m
Coulomb friction	F_c	4 kN
Smoothing parameter	$\dot{x}_0$	0.001 m/s

Cylinder position and position error during the simulation are shown in Figure 3.28. The system shows excellent position tracking in all four quadrants with a position error of approximately 1 mm. The cylinder is following a trapezoidal velocity profile from $x_c = 0.5$ m and is traveling 0.2 m.

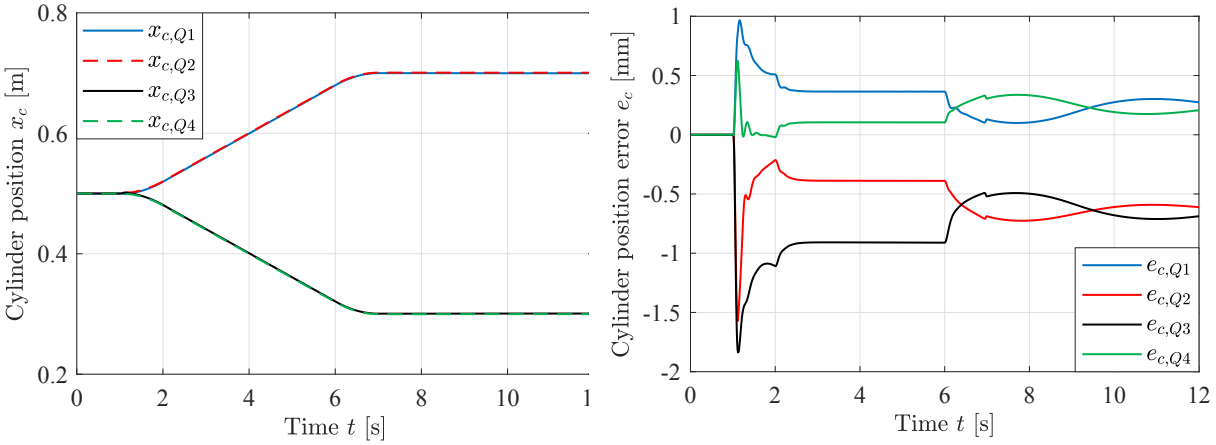

(a) Cylinder position x_c.

(b) Cylinder position error e_c.

Figure 3.28: Cylinder position and position error in four quadrants for the EHA during simulation. Taken from Paper D.

The system efficiency is of significant interest for the EHA, and it is calculated based on the power going from/to the DC-bus and cylinder. The system consumes approximately 15 kW when pumping, and delivers approximately 10 kW when motoring. The efficiency during motion is between 0.78 and 0.85, shown in Figure 3.29.

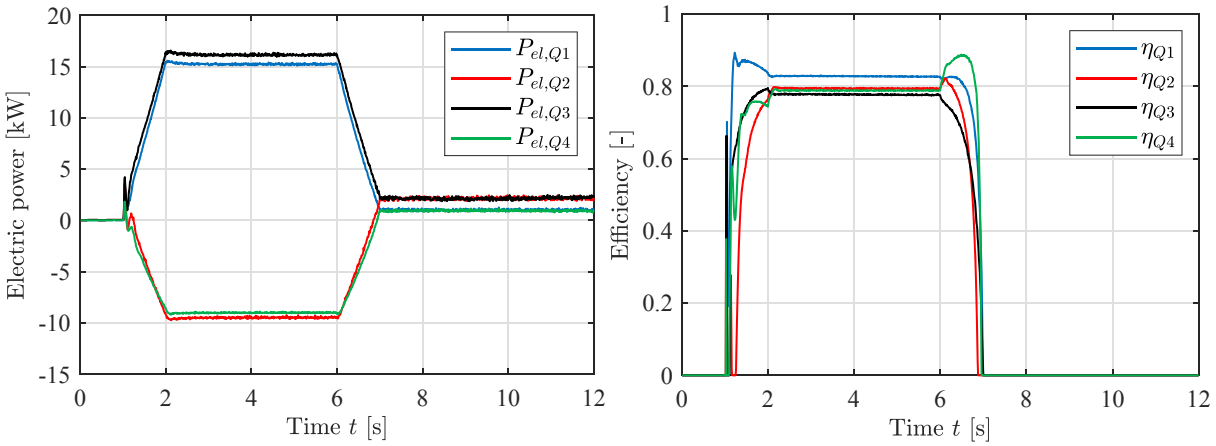

(a) Electric power P_{el} from/to the DC-bus.

(b) Efficiency η of the system.

Figure 3.29: Electric power and efficiency for all four quadrants. Operation in quadrants 1 and 3 consume power, while operation in quadrants 2 and 4 regenerate power. Taken from Paper D.

A comparison is made with a traditional hydraulic system which uses an induction motor as the prime mover, a load sensing pump, and pressure compensated DCVs, similar to what is described in chapter 2. Numerical simulations of a 2-DOF anti-swing controller described in paper C is used as a load case, utilizing two of the cylinders on the crane for planar motion. In this case two EHAs are used, one for each cylinder. The energy consumption and position error of both systems are used to evaluate their performance. A block diagram of the system topology for the load case is shown in Figure 3.30, where the green block contains the controllers from paper C, the blue block is the developed EHA, and the red block contains the crane model. The cylinder position reference during the load case is shown in Figure 3.31, and an illustration of the Cartesian motion is shown in Figure 3.32.

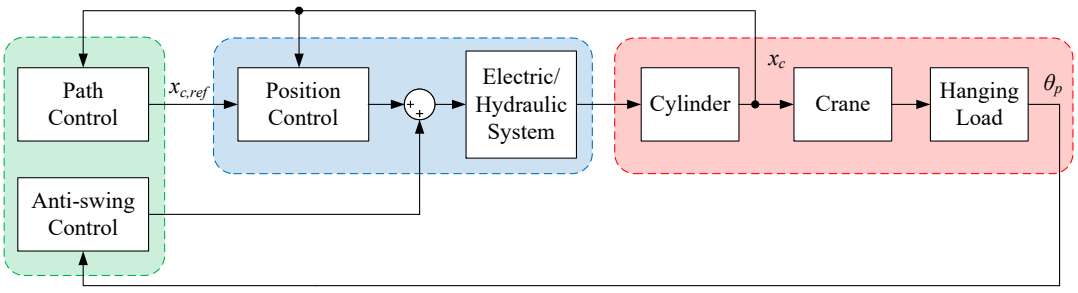

Figure 3.30: Block diagram of the load case with path control, anti-swing control, and crane model. Taken from Paper D.

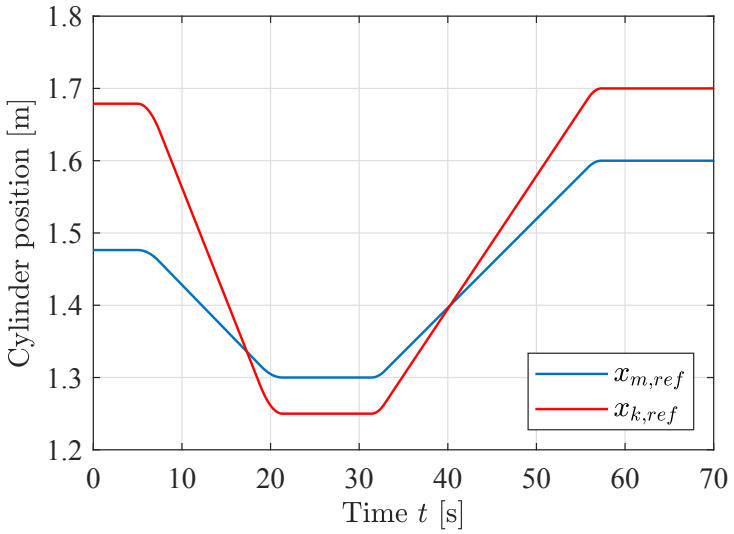

Figure 3.31: Cylinder position reference for two EHAs during anti-swing load case. Taken from Paper D.

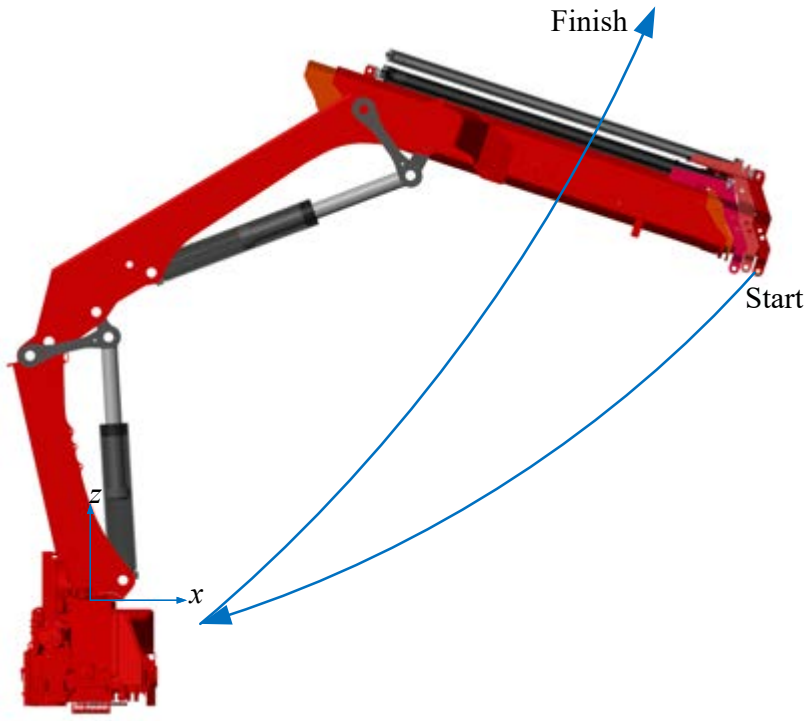

Figure 3.32: Illustration of the Cartesian motion for the crane during anti-swing load case.

The results for the valve-controlled system are shown in Figure 3.33. During motion 46 kJ were delivered to the cylinders while 505 kJ was consumed from the grid. This yields an overall efficiency of less than 10 %.

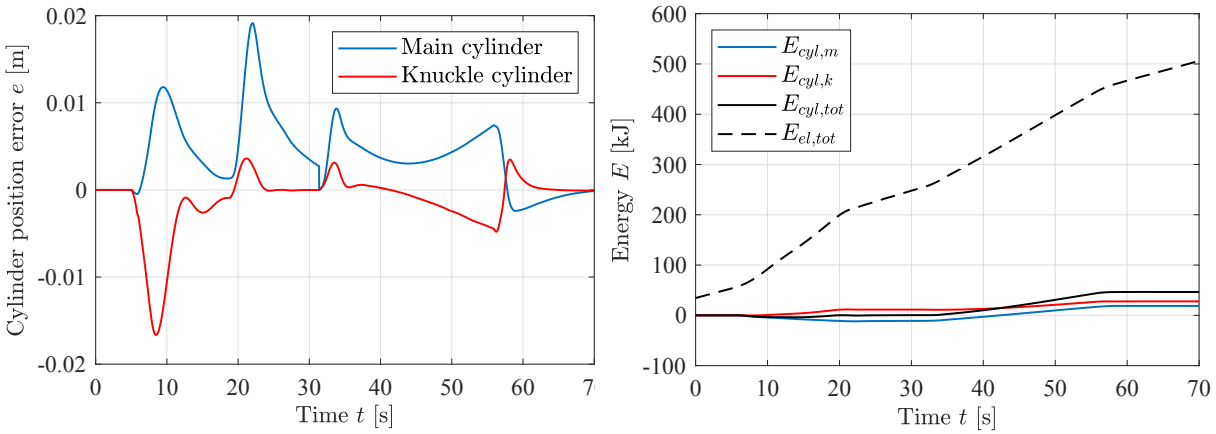

(a) Cylinder position error.

(b) Consumed energy.

Figure 3.33: Position error and consumed energy during motion with valve-controlled actuators. Taken from Paper D.

The results for the EHAs are shown in Figure 3.34. The position error is similar to the valve-controlled system, but the consumed energy is much lower. After completing the motion 47 kJ was delivered to the cylinders while 88 kJ was consumed from the grid. This yields an overall efficiency of 53 %.

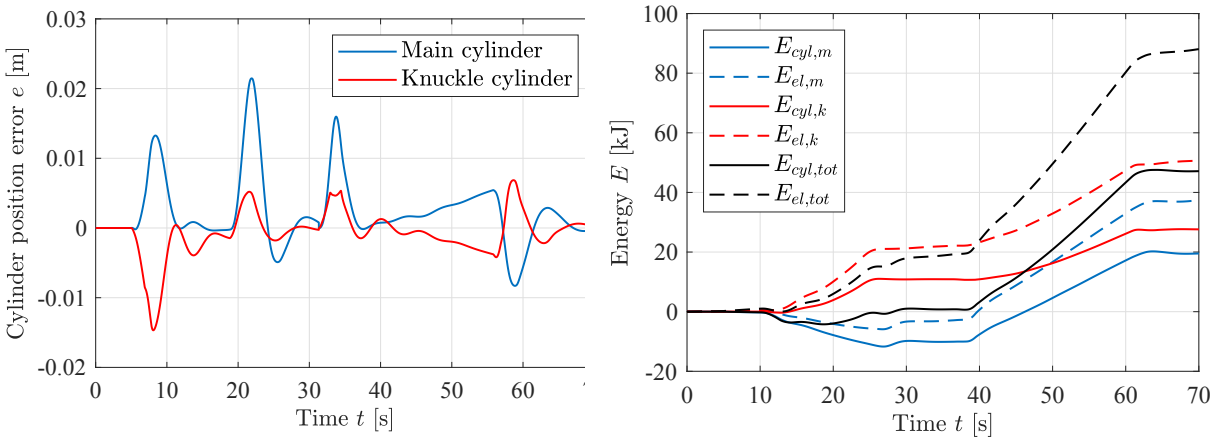

(a) Cylinder position error.

(b) Consumed energy.

Figure 3.34: Position error and consumed energy during motion with EHAs. Taken from Paper D.

During the load case with anti-swing the performance of the valve-controlled system and the EHA was almost identical. The main difference is the energy consumption which is greatly reduced by using the novel system, shown in Table 3.9. These results showcase the superior efficiency of the novel EHA.

Table 3.9: Performance of the valve-controlled system and the electro-hydrostatic system during anti-swing load case.

Parameter	Valve-controlled	Electro-hydrostatic
Main cylinder error	5.8 mm	5.8 mm
Knuckle cylinder error	5.4 mm	3.3 mm
Energy consumed	505 kJ	88 kJ

3.5 Deflection Compensation

Many hydraulic cranes exhibit significant structural flexibility due to their weight-optimized design. The resulting deflection from lifting payloads may not be critical for manual operation since the operator can see the exact position of the crane tip at all times. However, when using closed loop motion control the calculated crane tip position based on rigid-body kinematics may be inaccurate due to the flexibility. This position error can be a safety issue when operating autonomously and, if not properly compensated for, may lead to collisions with the environment.

In paper F a novel method for deflection compensation is presented, which counteracts both the static and dynamic deflection of the HMF 2020K4 loader crane while running path control with a payload. Experiments are conducted using a laser tracker in the laboratory to measure the crane tip position with and without a payload in various positions, effectively measuring the deflection. The experimental setup is shown in Figure 3.35 and Figure 3.36. The measured crane tip position in the xz-plane with and without load is shown in Figure 3.37. The crane position for one of the measurements is illustrated in black. Deflection is calculated as the difference between the position with and without load.

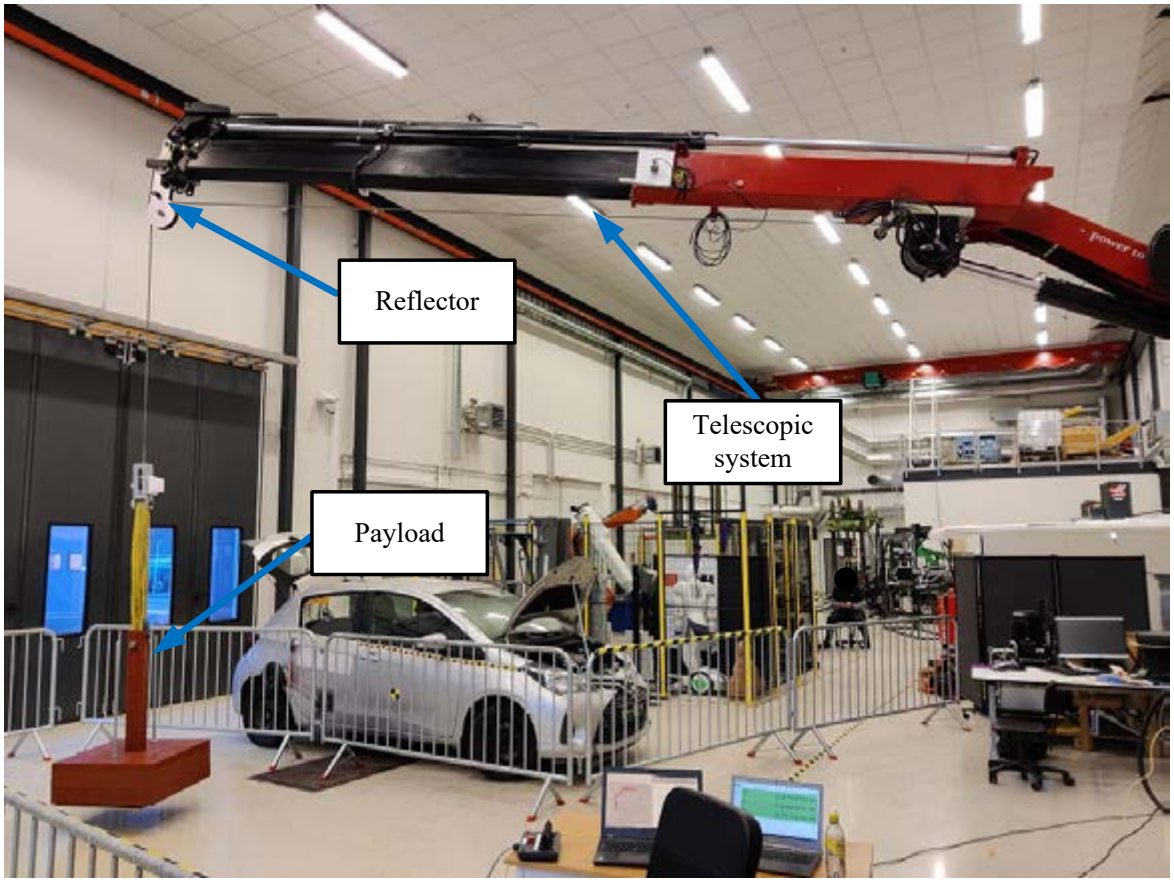

Figure 3.35: The HMF 2020K4 loader crane in the laboratory with a hanging payload. Taken from Paper F.

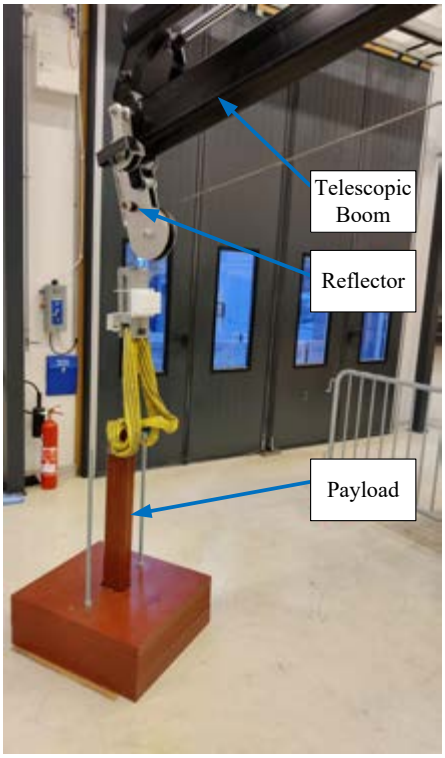

(a) Crane tip showing the telescopic boom, reflector, and payload.

(b) Leica Absolute Tracker AT960.

Figure 3.36: Experimental setup for deflection compensation in the laboratory. The laser tracker measures the crane tip position using the attached reflector. Taken from Paper F.

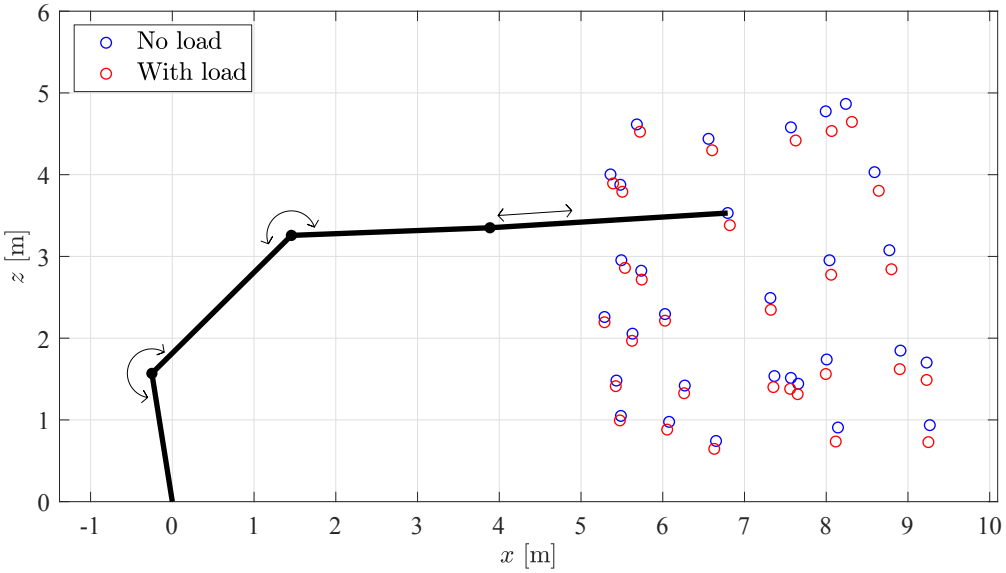

Figure 3.37: Laboratory measurements of the crane tip position in the xz-plane with and without load. Crane position illustrated in black with its three degrees of freedom. Taken from Paper F.

The novel method uses two separate controllers for static compensation and dynamic

compensation. An illustration of the control system with the two compensators is shown in Figure 3.38. The crane uses three of the actuators, namely the main cylinder, knuckle cylinder, and telescopic cylinder, yielding planar motion with kinematic redundancy.

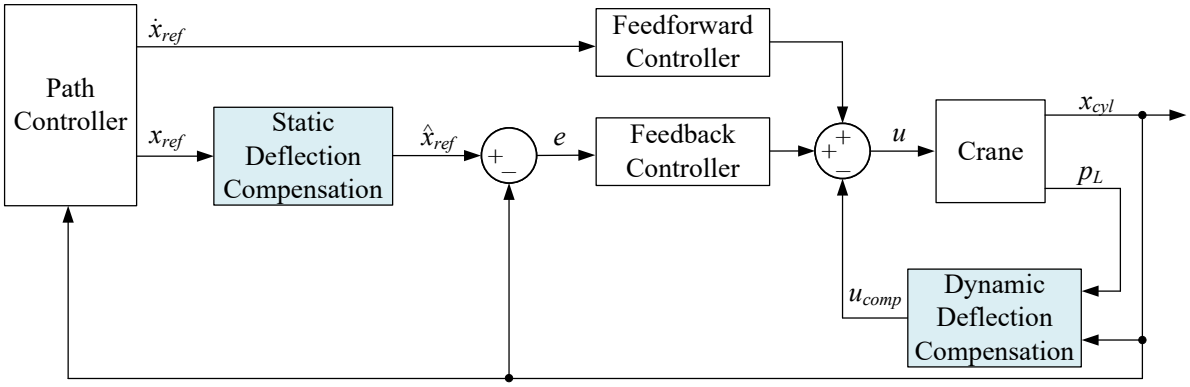

Figure 3.38: Control strategy with the novel deflection compensators highlighted in light blue.

The static deflection compensator is a model-based feedforward controller consisting of a neural network deflection estimator and kinematic functions. The measurements from the laboratory are used to train the neural network deflection estimator, similar to what is shown in section 2.6. An illustration of the static deflection compensator is shown in Figure 3.39. The deflection estimator (Def. Est.) outputs the Cartesian deflection of the crane tip, and therefore actuator kinematics (Act. Kin.) and forward kinematics (For. Kin.) are used to transform the cylinder position references into Cartesian space. Inverse kinematics (Inv. Kin.) and inverse actuator kinematics (Inv. Act.) are then used to transform the modified Cartesian position references back into actuator space. These kinematic expressions are described in detail in section 2.3.

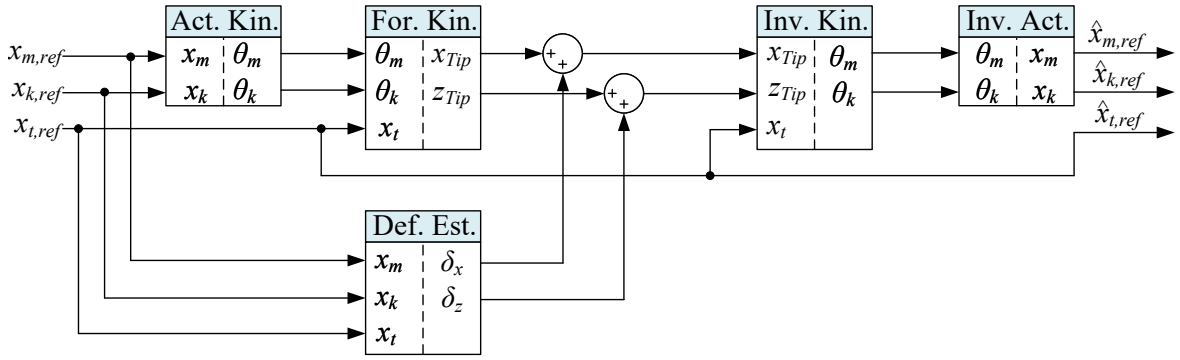

Figure 3.39: Block diagram of the static deflection compensator. Taken from Paper F.

The dynamic deflection compensator uses an eigenfrequency estimator, adaptive band-pass filter, and pressure feedback to generate a control signal to counteract the oscillations of the crane tip. An experiment is conducted where a load impulse is generated at different telescopic lengths, in which the eigenfrequency is extracted from the time series data. Curve fitting is then used to estimate the eigenfrequency of the crane as a function

of the telescopic length x_t. This is shown in Figure 3.40. The equation for the estimated eigenfrequency is given as:

$$\hat{\omega}_{Tip}(x_t) = 0.11\frac{\text{rad/s}}{\text{m}^2}\cdot x_t^2 - 1.716\frac{\text{rad/s}}{\text{m}}\cdot x_t + 11.63 \text{ rad/s} \tag{3.57}$$

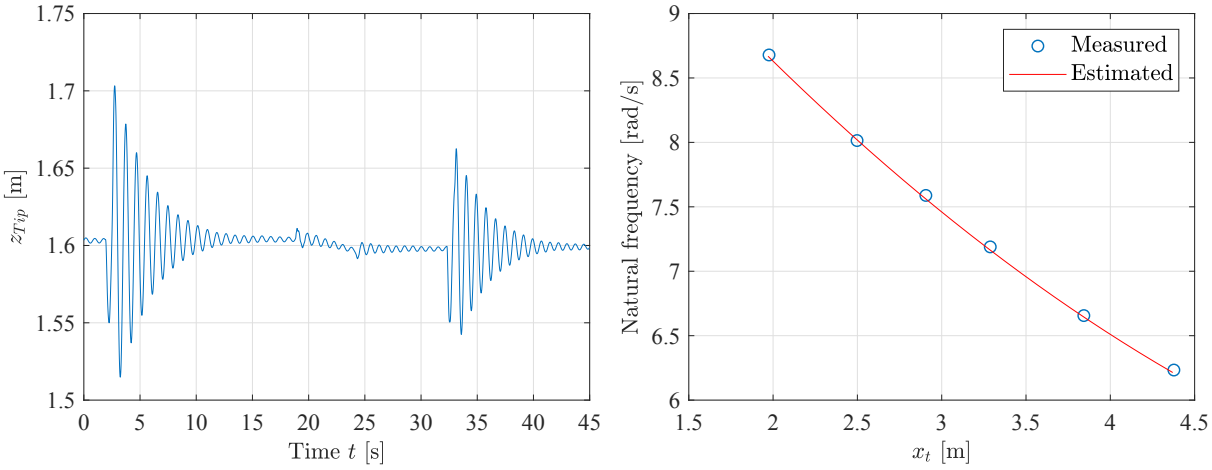

(a) Crane tip oscillations from experiment.

(b) Eigenfrequency as a function of telescopic length x_t.

Figure 3.40: Eigenfrequency estimation for the dynamic deflection compensator. Taken from Paper F.

The adaptive bandpass filter is a critically damped filter with the transfer function given in Equation (3.58). The dynamic compensator uses the filter, load pressure, and feedback gain k_{pL} to generate a control signal u_{comp}, given in Equation (3.59). The control signal is sent to the valve on the main cylinder.

$$G_{BP}(s) = \frac{2\cdot s\cdot\omega_f}{s^2 + 2\cdot s\cdot\omega_f + \omega_f^2} = 2\cdot\frac{\omega_f}{s+\omega_f}\cdot\frac{s}{s+\omega_f} \tag{3.58}$$

$$u_{comp} = k_{pL}\cdot p_L\cdot G_{BP}(s) \tag{3.59}$$

The adaptive bandpass filter has been implemented as a digital filter by utilizing a lowpass and highpass filter, shown in Equations (3.60)-(3.64). The center frequency of the filter is set to the estimated eigenfrequency of the crane. y_{HP}, y_{LP}, and y_{BP} denote the output of the highpass, lowpass, and bandpass filter respectively.

$$\omega_f = \hat{\omega}_{Tip}(x_t) \tag{3.60}$$

$$\alpha = \frac{1}{1+\omega_f\cdot T_s} \tag{3.61}$$

$$y_{HP,i} = \alpha\cdot y_{HP,i-1} + \alpha\cdot(p_{L,i} - p_{L,i-1}) \tag{3.62}$$

$$y_{LP,i} = \alpha\cdot y_{LP,i-1} + (1-\alpha)\cdot y_{HP,i} \tag{3.63}$$

$$y_{BP,i} = 2\cdot y_{LP,i} \tag{3.64}$$

where

i	=	sample number
p_L	=	load pressure
y	=	filter output(s)
T_s	=	sample time, 0.01 s
$\hat{\omega}_{Tip}$	=	estimated tip eigenfrequency

Simulations are conducted in MATLAB/Simulink to verify the feasibility and performance of the deflection compensator. A simplified model of the flexibility is created by using a rotational spring between the first telescopic boom and the knuckle boom. This simplification is done for the purpose of testing the compensator by creating some static and dynamic deflection in the simulation model. It should be noted that the neural network is re-trained with the measurements from the simplified flexible model. An illustration of the simplified model is shown in Figure 3.41.

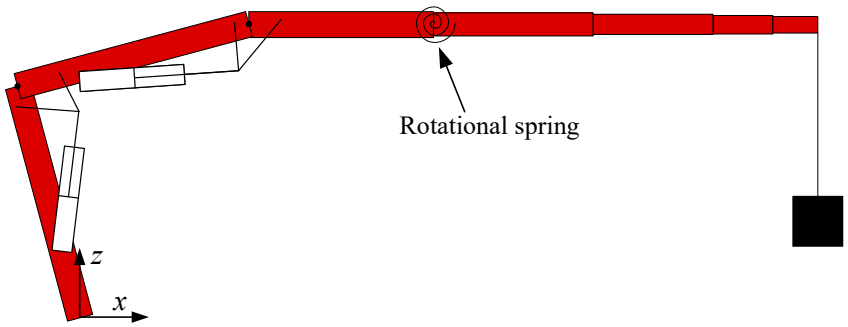

Figure 3.41: Illustration of the simplified flexible model used for deflection compensation. Taken from Paper F.

The crane is using the path controller from section 3.1 during the simulations. Three scenarios are tested, one without load, one with load, and one with load and deflection compensation enabled. A load impulse is done at $t = 20$ s to further analyze the dynamic compensator. The crane follows a path from $[x_m, x_k, x_t]^T = [1.38 \text{ m}, 1.8 \text{ m}, 4 \text{ m}]^T$ to $[1.43 \text{ m}, 1.85 \text{ m}, 2 \text{ m}]^T$, where the telescope is retracted and crane tip is lifted. Figure 3.42 shows the vertical position z_{Tip} during the simulations, since the deflection is largest in the z-direction. Figure 3.43 shows an illustration of the Cartesian motion. After 6 seconds the static deflection is effectively removed. The oscillations induced by the load impulse are successfully dampened by the dynamic deflection compensator.

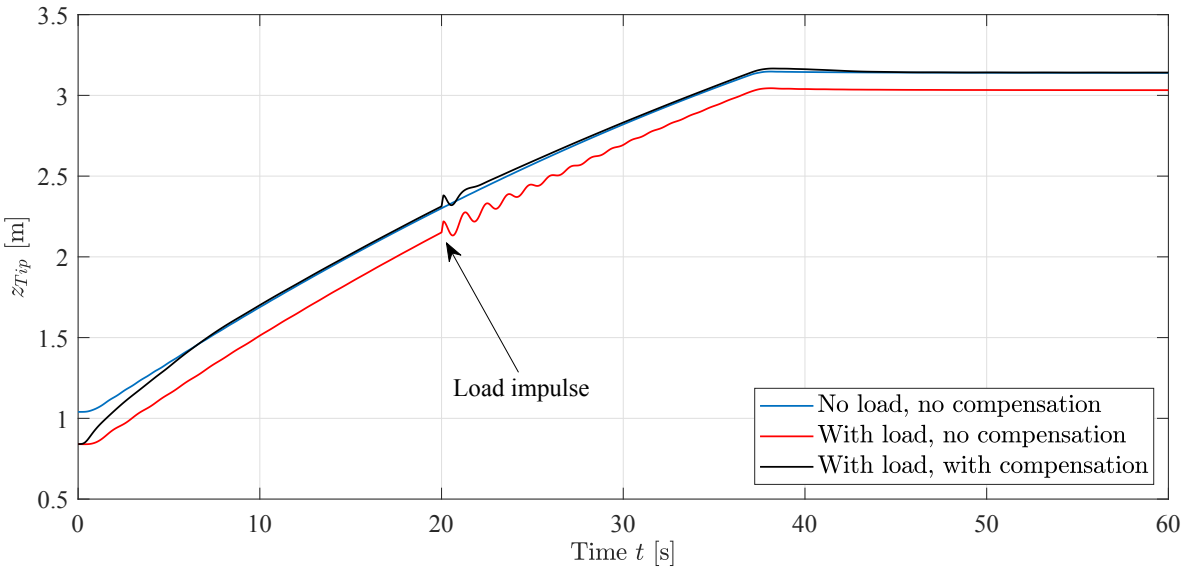

Figure 3.42: The vertical coordinate of the crane tip, z_{Tip}, is plotted as a function of time from three different simulations. Taken from Paper F.

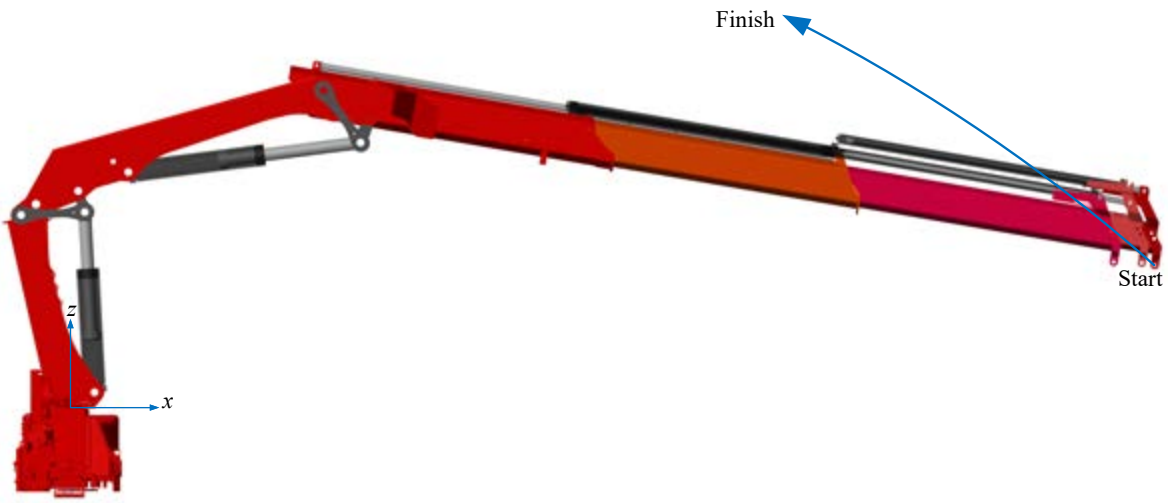

Figure 3.43: Illustration of the Cartesian motion for deflection compensation simulation.

Experiments are conducted in the laboratory on the HMF 2020K4 loader crane to verify the developed deflection compensator. The crane is using the path controller and following a similar path as in the simulations, i.e. retracting the telescope and lifting the crane tip. The path is run three times, one without load, one with load, and one with load and deflection compensation. A plot of z_{Tip} over time is shown in Figure 3.44. It can be seen that the novel compensator is able to compensate for the static deflection, in addition to removing the oscillations. At the end of the motion the static deflection of the vertical coordinate of the crane tip, z_{Tip}, was reduced from 56.8 mm to 5.7 mm, which is a 90 % decrease.

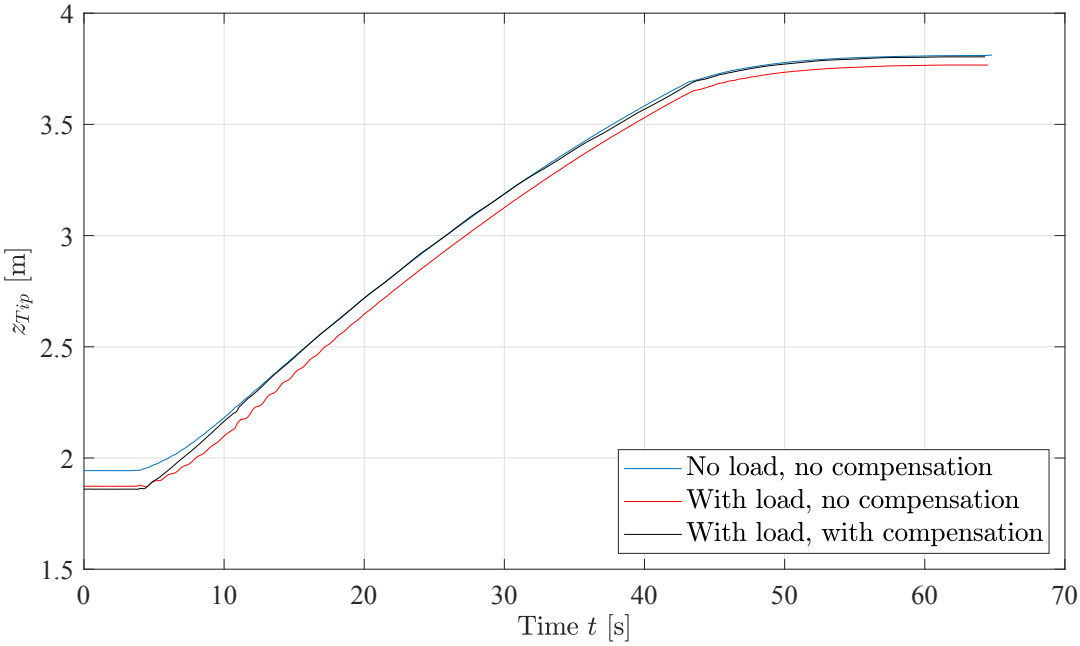

Figure 3.44: The vertical coordinate of the crane tip, z_{Tip}, plotted as a function of time from three different experiments. Taken from Paper F.

The effects from the deflection compensator are given in Figure 3.45, showing the change in cylinder position reference $\Delta x_{ref} = \hat{x}_{ref} - x_{ref}$ from the static compensator and the control signal u_{comp} from the dynamic compensator. It can be seen that the static deflection compensator is continuously modifying both cylinder position references, showing the contributions from the kinematic functions. The dynamic deflection compensator is actively suppressing oscillations during the whole motion.

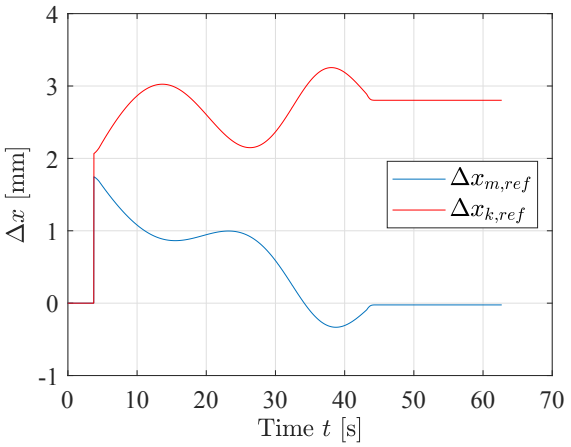

(a) Change in cylinder position reference from the static deflection compensator.

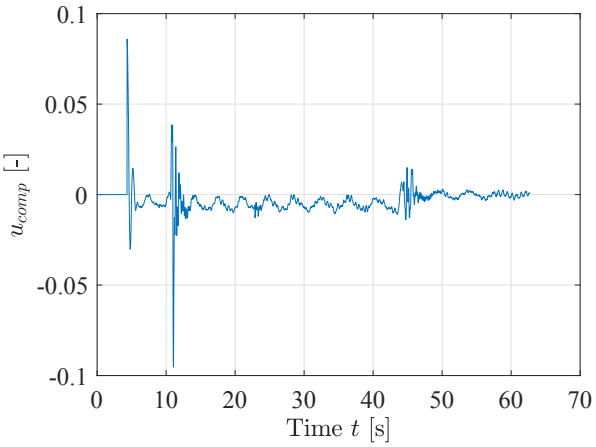

(b) Control signal from the dynamic deflection compensator.

Figure 3.45: Effects of the static and dynamic deflection compensator in laboratory.

Chapter 4

Concluding Remarks

4.1 Conclusions

The work presented in this thesis has been devoted to the development of motion control systems for hydraulically actuated cranes. Several types of controllers have been developed and applied to an HMF 2020K4 loader crane, both with and without a hanging payload. The control systems proposed in this thesis are able to meet the challenges faced with automation of lifting and handling operations using hydraulic cranes, such as load swing from hanging payloads and structural flexibility.

The path controller developed in paper A represents the first milestone for this project. The introduction of actuator space is particularly suited for hydraulic cranes using pressure compensated directional control valves. The relations between the controller and actuator become either linear or constant, greatly simplifying the control design. This is exploited in the path controller where velocity and acceleration constraints can be easily selected based on system parameters. The use of actuator space also inherently minimizes actuator motion and eliminates changing velocity signs when traveling between two points. This reduces the stick-slip phenomenon for the hydraulic cylinder, which may lead to jerky motion, and will typically reduce the energy consumption of the crane. In addition, the use of optimization algorithms to tune the control system parameters to minimize oscillations is another technique which further improves the performance of the system. Both simulation and experimental results show good setpoint tracking and minimal oscillations.

The adaptive feedforward controller developed in paper B takes further advantage of actuator space and the pressure compensated directional control valves. Feedforward control is a common and effective method for electro-hydraulic motion control systems, and the developed adaptive controller shows a large performance improvement when implemented of a hydraulically actuated crane with differential cylinders. One of the challenges faced with these cylinders is the jump in both velocity and force gain when changing direction of motion. This has been solved by developing a differential controller with two feedforward states for out-stroke and in-stroke motion, respectively. Both simulation and experimental results show a significant reduction in position error, and that the novel differential controller is adapting in both directions of motion independently.

The anti-swing control systems presented in papers C and E represent a major con-

tribution to this thesis, as they aim to tackle the challenges faced when using hanging payloads. Due to the complexity of this topic the development of the anti-swing controller is spread across two papers, for the two- and three-dimensional case, respectively. Both the hanging load dynamics and rigid-body kinematics are derived to enable the development of the anti-swing controllers. An analysis of the closed loop hanging load dynamics is used to calculate the feedback gain for the controller, while the kinematic functions are used to transform the controller output into actuator space. Simulations and experiments are conducted and show a significant reduction in the payload angle during motion. For the three-dimensional case pressure feedback is also implemented and successfully tackles stability issues associated with the slewing motion.

The electro-hydrostatic actuator developed in paper D investigates the feasibility of this hybrid drive topology which is becoming increasingly popular, applied to a hydraulic crane. In addition to showing how to model and select the electric and hydraulic components, the performance of the developed system is evaluated using simulations. The electro-hydrostatic actuator shows high energy efficiency in four quadrant operation and good tracking performance. A comparison is made with a traditional hydraulic system using a load case with path control and anti-swing. The results show virtually identical position tracking performance between the two systems, but the electro-hydrostatic actuator exhibits a significant reduction in energy consumption of 82 %.

The deflection compensator developed in paper F solves the challenge of using large and flexible hydraulic cranes with heavy payloads for closed loop motion control. The developed system uses a static deflection compensator in a feedforward topology, and a dynamic deflection compensator in a feedback topology. By using a wide set of techniques including neural networks, pressure feedback, kinematics, and curve fitting, the compensator is able to counteract both the static deflection due to gravity and dynamic deflection due to motion. Results from simulations and experiments show that the static compensator is able to minimize the crane tip deflection, and that the dynamic compensator successfully suppresses oscillations during motion.

Overall, the systems developed during this project have shown the possibility of increasing the level of automation for large hydraulic cranes with hanging payloads. The use of simulation tools has facilitated rapid development of the motion control systems presented. The experiments conducted in the laboratory using the developed control systems have been vital to showcasing the feasibility of the controllers in a real-world scenario. In conclusion, the research presented has answered the three research questions formulated for this project. Section 3.1 showed how a path control algorithm was developed to control the motion of the crane in actuator space. This control system has been used both with and without a hanging load. In section 3.3 a method for suppressing the pendulum motion of the hanging payload was presented. This controller was implemented for the two-dimensional and three-dimensional case. Finally, section 3.5 showed the development of a deflection compensator which counteracts the deflection due to the weight of the payload. This controller counteracts both static and dynamic deflections.

4.2 Future Work

During the development of the different control systems in this project, several interesting topics arose which could be further investigated. For the path controller developed in paper A, an experiment could be made to further study the differences between path control in actuator space and Cartesian space in terms of speed, robustness, and energy consumption. As the motion of each actuator is inherently minimized in actuator space, it is expected that the developed path controller is superior to a Cartesian path controller.

The developed adaptive feedforward controller includes a feedback term, in contrast to typical feedforward controllers. This suggests that the stability of the system is affected by the parameters in the feedback loop. A analysis could be conducted, both analytically and experimentally, to investigate the stability of the system with the adaptive controller.

For papers C and E, anti-swing control is implemented using a fixed wire length. An analytical expression of the required anti-swing gain for a given wire length has already been made, but further studies should include a variable wire length during motion. In addition, actively using the winch in the anti-swing controller could also be investigated, as this has been done for electric overhead cranes in literature.

For the deflection compensator only the in-plane deflection has been considered since the gravitational forces primarily act in-plane. The telescopic boom has an offset which may cause out-of-plane bending, and could be studied further. In future investigations the out-of-plane dynamic deflection should be considered, as the rotating motion of the crane will induce some out-of-plane vibrations.

Regarding potential improvements, for the anti-swing controller the payload angle has been measured using an inertial measurement unit attached to the hook of the crane. This sensor uses a wired connection to the base of the crane, which may be infeasible in the field, especially with variable wire lengths. Further investigation of a more suitable sensor could be conducted, while still being compatible with the developed anti-swing controller. In addition, measurements of the crane tip deflection was conducted with an expensive high precision Leica laser tracker. The possibility to use a less expensive sensor or another measurement technique could be investigated to make the developed control system more attractive for commercial products.

Bibliography

[1] Subsea knuckle boom crane. https://www.nov.com/-/media/nov/images/products/rig/marine-and-construction/offshore-cranes/subsea-knuckleboom-cranes-full.jpg. Accessed: 2022-08-05.

[2] Q. Zhang. Hydraulic linear actuator velocity control using a feedforward-plus-pid control. *International Journal of Flexible Automation and Integrated Manufacturing*, 7:277–292, 1999.

[3] Jesper K. Sørensen, Michael R. Hansen, and Morten K. Ebbensen. Boom Motion Control Using Pressure Control Valve. volume 8th FPNI Ph.D Symposium on Fluid Power of *Fluid Power Systems Technology*, 2014.

[4] Jesper Kirk Sørensen, Michael Rygaard Hansen, and Morten Kjeld Ebbesen. Load independent velocity control on boom motion using pressure control valve. In *The Fourteenth Scandinavian International Conference on Fluid Power*, 2015.

[5] Chi-Ying Lin and Po-Ying Chen. Precision tracking control of a biaxial piezo stage using repetitive control and double-feedforward compensation. *Mechatronics*, 21(1):239–249, 2011.

[6] Frank Boeren, Dennis Bruijnen, Niels van Dijk, and Tom Oomen. Joint input shaping and feedforward for point-to-point motion: Automated tuning for an industrial nanopositioning system. *Mechatronics*, 24(6):572–581, 2014. Control of High-Precision Motion Systems.

[7] Michiel A. Beijen, Marcel F. Heertjes, Hans Butler, and Maarten Steinbuch. Mixed feedback and feedforward control design for multi-axis vibration isolation systems. *Mechatronics*, 61:106–116, 2019.

[8] Atsushi Yamaguchi, Iman Yousefi, and Takeshi Ishihara. Reduction in the fluctuating load on wind turbines by using a combined nacelle acceleration feedback and lidar-based feedforward control. *Energies*, 13(17), 2020.

[9] Yongzhi Wang, Andrea Da Ronch, and Maryam Ghandchi Tehrani. Adaptive feedforward control for gust-induced aeroelastic vibrations. *Aerospace*, 5(3), 2018.

[10] Andrzej Pawlowski, Carlos Rodríguez, José Luis Guzmán, Manuel Berenguel, and Sebastián Dormido. Measurable disturbances compensation: Analysis and tuning of feedforward techniques for dead-time processes. *Processes*, 4(2), 2016.

[11] Finn Haugen. Control of a Buoyancy-Based Pilot Underwater Lifting Body. *Modeling, Identification and Control*, 31(2):67–77, 2010.

[12] Ahmet Furkan Guc, Zafer Yumrukcal, and Onur Ozcan. Nonlinear identification and optimal feedforward friction compensation for a motion platform. *Mechatronics*, 71:102408, 2020.

[13] Ke Li, Yeming Zhang, Shaoliang Wei, and Hongwei Yue. Evolutionary algorithm-based friction feedforward compensation for a pneumatic rotary actuator servo system. *Applied Sciences*, 8(9), 2018.

[14] Alexander Keck, Jan Zimmermann, and Oliver Sawodny. Friction parameter identification and compensation using the elastoplastic friction model. *Mechatronics*, 47:168–182, 2017.

[15] Y. S. Park, H. S. Cho, and K. C. Koh. Robot positioning based on point-to-point motion capability. In *IEEE/RRSJ International Conference on Intelligent Robots and Systems, Takamatsu (JP), 10/30/2000–11/05/2000.*

[16] Amit Ailon and Ilan Zohar. Point-to-point control and trajectory tracking in wheeled mobile robots: some further results and applications. *IFAC Proceedings Volumes*, 41(2):9546 – 9551, 2008. 17th IFAC World Congress.

[17] K. Alipour and S. A. A. Moosavian. Point-to-point stable motion planning of wheeled mobile robots with multiple arms for heavy object manipulation. In *2011 IEEE International Conference on Robotics and Automation*, pages 6162–6167, 2011.

[18] Petter Krus and Jan-Ove Palmberg. Vector control of a hydraulic crane. *International Off-Highway and Powerplant Congress and Exposition*, 1992.

[19] L. Beiner. Identification and control of a hydraulic forestry crane. *Mechatronics*, 7(6):537–547, 1997.

[20] Jouni Mattila and Tapio Virvalo. Energy-efficient motion control of a hydraulic manipulator. *Proceedings of the 2000 IEEE International Conference on Robotics and Automation San Francisco. CA*, 2000.

[21] Serdar Kucuk and Zafer Bingul. The inverse kinematics solutions of industrial robot manipulators. *Proceedings of the IEEE International Conference on Mechatronics*, 2004.

[22] Donald L. Pieper. The kinematics of manipulators under computer control. *PhD thesis, Stanford University, Department of Mechanical Engineering*, 1968.

[23] Richard P. Paul. *Robot manipulators: mathematics, programming, and control: the computer control of robot manipulators.* MIT Press, Cambridge, MA., 1981.

[24] M. K. Bak, M. K. Ebbesen, and M. R. Hansen. Optimal path generation for offshore pipe handling crane. *The 13th Scandinavian International Conference on Fluid Power*, 2013.

[25] Morten K. Bak, Michael R. Hansen, and Hamid R. Karimi. Robust tool point control for offshore knuckle boom crane. *Preprints of the 18th IFAC World Congress, Milano (Italy)*, 2011.

[26] Morten Kjeld Ebbesen and Michael Rygaard Hansen. Tool point control of material handling crane in marine operations. In *Proceedings of the 24th International Congress on Condition Monitoring and Diagnostics Engineering Management*. COMADEM International, 2011.

[27] Justin Cinkelj, Roman Kamnik, Peter Cepon, Matjaz Mihelj, and Marko Munih. Robotic control system for hydraulic telescopic handler. *19th International Workshop on Robotics in Alpe-Adria-Danube Region*, 2010.

[28] Morten Kjeld Ebbesen, Torben Ole Andersen, and Michael Rygaard Hansen. Optimal control of hydraulically actuated flexible multibody systems. In *Proceedings of 2nd International Conference on Computational Methods in Fluid Power (FPNI'06)*. Department of Mechanical Engineering, Aalborg University, 2006.

[29] Morten Kjeld Ebbesen, Michael Rygaard Hansen, and Torben Ole Andersen. Optimal velocity control of hydraulically actuated flexible loader crane. In R. Larsson and K. Runesson, editors, *Proceedings of the 20th Nordic Seminar on Computational Mechanics*, Proceedings of the Nordic Seminar on Computational Mechanics, (NSCM). Chalmers tekniska högskola, 2007.

[30] Morten Kjeld Ebbesen and Michael Rygaard Hansen. Correction scheme for tool point velocity control of a flexible hydraulically actuated manipulator. In *IASTED International Conference Modelling, Identification, and Control : Proceedings.*, pages 298–305, 2010.

[31] Morten Ebbesen, Torben Andersen, and Michael Hansen. *Trajectory Planning for Hydraulically Actuated Flexible Loader Crane.*

[32] Henrik C. Pedersen, Brian Nielsen, Torben O. Andersen, Michael R. Hansen, and Peder Pedersen. Resolved motion control of a hydraulic loader crane. *1st International Conference on Computational Methods in Fluid Power Technology*, 2003.

[33] Magnus B. Kjelland, Ilya Tyapin, Geir Hovland, and Michael R. Hansen. Tool-point control for a redundant heave compensated hydraulic manipulator. *Proceedings of the 2012 IFAC Workshop on Automatic Control in Offshore Oil and Gas Production, Norwegian University of Science and Technology, Trondheim, Norway*, 2012.

[34] M. B. Kjelland, M. R. Hansen, I. Tyapin, and G. Hovland. Tool-point control of a planar hydraulically actuated manipulator with compensation of non-actuated degree of freedom. In *2012 12th International Conference on Control, Automation and Systems*, pages 672–677, 2012.

[35] Uwe Mettin, Pedro X. La Hera, Daniel Ortiz Morales, Anton S. Shiriaev, Leonid B. Freidovich, and Simon Westerberg. Path-constrained trajectory planning and time-independent motion control: Application to a forestry crane. 2009.

[36] Mikkel M. Pedersen, Michael R. Hansen, and Morten Ballebye. Developing a tool point control scheme for a hydraulic crane using interactive real-time dynamic simulation. *Modeling, Identification and Control, Vol. 31, No. 4*, 2010.

[37] Ho-Hoon Lee, Sung-Kun Cho, and Jae-Sung Cho. A new anti-swing control of overhead cranes. *IFAC Proceedings Volumes*, 30(13):115 – 120, 1997. IFAC Workshop on Automation in the Steel Industry: Current Practice and Future Developments (ASI'97), Kyongju, Korea, 16-18 July 1997.

[38] Ho-Hoon Lee. Modeling and Control of a Three-Dimensional Overhead Crane. *Journal of Dynamic Systems, Measurement, and Control*, 120(4):471–476, 12 1998.

[39] Sung-Kun Cho and Ho-Hoon Lee. An anti-swing control of a 3-dimensional overhead crane. In *Proceedings of the 2000 American Control Conference. ACC (IEEE Cat. No.00CH36334)*, volume 2, pages 1037–1041 vol.2, 2000.

[40] Ho-Hoon Lee and Seung-Gap Choi. A model-based anti-swing control of overhead cranes with high hoisting speeds. In *Proceedings 2001 ICRA. IEEE International Conference on Robotics and Automation (Cat. No.01CH37164)*, volume 3, pages 2547–2552 vol.3, 2001.

[41] Hahn Park, Dongkyoung Chwa, and Keum-Shik Hong. A feedback linearization control of container cranes: Varying rope length. *International Journal of Control, Automation, and Systems*, 5, 08 2007.

[42] D. Schindele, I. Menn, and H. Aschemann. Nonlinear optimal control of an overhead travelling crane. In *2009 IEEE Control Applications, (CCA) Intelligent Control, (ISIC)*, pages 1045–1050, 2009.

[43] Ho-Hoon Lee. A new approach for the anti-swing control of overhead cranes with high-speed load hoisting. *International Journal of Control*, 76(15):1493–1499, 2003.

[44] Y. Fang, W. E. Dixon, D. M. Dawson, and E. Zergeroglu. Nonlinear coupling control laws for an underactuated overhead crane system. *IEEE/ASME Transactions on Mechatronics*, 8(3):418–423, 2003.

[45] Ho-Hoon Lee and Sung-Kun Cho. A new fuzzy-logic anti-swing control for industrial three-dimensional overhead cranes. In *Proceedings 2001 ICRA. IEEE International Conference on Robotics and Automation (Cat. No.01CH37164)*, volume 3, pages 2956–2961 vol.3, 2001.

[46] Sung-Kun Cho and Ho-Hoon Lee. A fuzzy-logic antiswing controller for three-dimensional overhead cranes. *ISA Transactions*, 41(2):235 – 243, 2002.

[47] M. Park, D. Chwa, and S. Hong. Antisway tracking control of overhead cranes with system uncertainty and actuator nonlinearity using an adaptive fuzzy sliding-mode control. *IEEE Transactions on Industrial Electronics*, 55(11):3972–3984, 2008.

[48] Q. H. Ngo and K. Hong. Sliding-mode antisway control of an offshore container crane. *IEEE/ASME Transactions on Mechatronics*, 17(2):201–209, 2012.

[49] *A Robust Anti-Swing Trajectory Control of Overhead Cranes With High-Speed Load Hoisting: Experimental Study*, volume Volume 8: Dynamic Systems and Control, Parts A and B of *ASME International Mechanical Engineering Congress and Exposition*, 11 2010.

[50] Ho-Hoon Lee. A new design approach for the anti-swing trajectory control of overhead cranes with high-speed hoisting. *International Journal of Control*, 77(10):931–940, 2004.

[51] Ho-Hoon Lee, Yi Liang, and Del Segura. A Sliding-Mode Antiswing Trajectory Control for Overhead Cranes With High-Speed Load Hoisting. *Journal of Dynamic Systems, Measurement, and Control*, 128(4):842–845, 04 2006.

[52] W.E. Singhose, Warren Seering, and M. Singer. Input shaping for vibration reduction with specified insensitivity to modeling errors. *Proc. Japan-USA Symp. Flexible Automation*, 1, 01 1996.

[53] Khalid L. Sorensen, William Singhose, and Stephen Dickerson. A controller enabling precise positioning and sway reduction in bridge and gantry cranes. *Control Engineering Practice*, 15(7):825 – 837, 2007. Special Issue on Award Winning Applications.

[54] Magnus B. Kjelland and Michael R. Hansen. Using input shaping and pressure feedback to suppress oscillations in slewing motion of lightweight flexible hydraulic crane. *International Journal of Fluid Power*, 16(3):141–148, 2015.

[55] G. Boschetti, D. Richiedei, and A. Trevisani. Delayed reference control for multi-degree-of-freedom elastic systems: Theory and experimentation. *Control Engineering Practice*, 19(9):1044 – 1055, 2011.

[56] G. Boschetti, R. Caracciolo, D. Richiedei, and A. Trevisani. A non-time based controller for load swing damping and path-tracking in robotic cranes. *Journal of Intelligent & Robotic Systems*, 76(2):201–217, 2014.

[57] M. B. Kjelland, M. R. Hansen, I. Tyapin, and G. Hovland. Tool-point control of a planar hydraulically actuated manipulator with compensation of non-actuated degree of freedom. In *2012 12th International Conference on Control, Automation and Systems*, pages 672–677, 2012.

[58] H.N. Rahimi and M. Nazemizadeh. Dynamic analysis and intelligent control techniques for flexible manipulators: a review. *Advanced Robotics*, 28(2):63–76, 2014.

[59] K. Lochan, B.K. Roy, and B. Subudhi. A review on two-link flexible manipulators. *Annual Reviews in Control*, 42:346–367, 2016.

[60] Dipendra Subedi, Ilya Tyapin, and Geir Hovland. Dynamic modeling of planar multi-link flexible manipulators. *Robotics*, 10(2):70, 2021.

[61] K. Lochan, B.K. Roy, and B. Subudhi. Recursive lagrangian dynamic modeling and simulation of multi-link spatial flexible manipulator arms. *Appl. Math. Mech.-Engl. Ed.*, 30:1283–1294, 2009.

[62] W. Beres, J.Z. Sasiadek, and G. Vukovich. Control and dynamic analysis of multilink flexible manipulator. In *[1993] Proceedings IEEE International Conference on Robotics and Automation*, pages 478–483 vol.3, 1993.

[63] Ivan Giorgio and Dionisio Del Vescovo. Non-linear lumped-parameter modeling of planar multi-link manipulators with highly flexible arms. *Robotics*, 7(4):60, 2018.

[64] Julian Wanner and Oliver Sawodny. A lumped parameter model of the boom of a mobile concrete pump. In *2019 18th European Control Conference (ECC)*, pages 2808–2813, 2019.

[65] Changyin Sun, Wei He, and Jie Hong. Neural network control of a flexible robotic manipulator using the lumped spring-mass model. *IEEE Transactions on Systems, Man, and Cybernetics: Systems*, 47(8):1863–1874, 2017.

[66] H.A. Talebi, R.V. Patel, and H. Asmer. Dynamic modeling of flexible-link manipulators using neural networks with application to the ssrms. In *Proceedings. 1998 IEEE/RSJ International Conference on Intelligent Robots and Systems. Innovations in Theory, Practice and Applications (Cat. No.98CH36190)*, volume 1, pages 673–678 vol.1, 1998.

[67] Fabio Comi, Aitor Orive Miguel, Francesco Cavenago, Gianni Ferretti, Gianantonio Magnani, and Andrea Rusconi. Modelling, validation and control of delian flexible manipulator. *IFAC-PapersOnLine*, 52(15):364–369, 2019. 8th IFAC Symposium on Mechatronic Systems MECHATRONICS 2019.

[68] R. Lozano, A. Valera, P. Albertos, and S. Arimoto. Pd control of robot manipulators considering joint flexibility, actuators dynamics and friction. In *Proceedings of the 1997 American Control Conference (Cat. No.97CH36041)*, volume 5, pages 2638–2641 vol.5, 1997.

[69] Daniel Newman and Joshua Vaughan. Concurrent design of linear control with input shaping for a two-link flexible manipulator arm. *IFAC-PapersOnLine*, 51(14):66–71, 2018. 14th IFAC Workshop on Time Delay Systems TDS 2018.

[70] Z Mohamed, M Khairudin, A R Husain, and B Subudhi. Linear matrix inequality-based robust proportional derivative control of a two-link flexible manipulator. *Journal of Vibration and Control*, 22(5):1244–1256, 2016.

[71] Qinyuan Xu, Weihua Wang, Hongwei Xia, Yanmin Wang, and Yong Feng. Second-order non-singular terminal sliding mode optimal control of uncertain flexible manipulator. In *2018 IEEE 8th Annual International Conference on CYBER Technology in Automation, Control, and Intelligent Systems (CYBER)*, pages 1376–1381, 2018.

[72] K. Lochan, B.K. Roy, and B. Subudhi. Smc controlled chaotic trajectory tracking of two-link flexible manipulator with pid sliding surface. *IFAC-PapersOnLine*, 49(1):219–224, 2016. 4th IFAC Conference on Advances in Control and Optimization of Dynamical Systems ACODS 2016.

[73] H.A. Talebi, R.V. Patel, and K. Khorasani. Inverse dynamics control of flexible-link manipulators using neural networks. In *Proceedings. 1998 IEEE International Conference on Robotics and Automation (Cat. No.98CH36146)*, volume 1, pages 806–811 vol.1, 1998.

[74] Yuan-Gang Tang, Fu-Chun Sun, Fuchun Sun, and Ting-Liang Hu. Tip position control of a flexible-link manipulator with neural networks. *International Journal of Control, Automation and Systems*, 4(3):308–317, 06 2006.

[75] Yuangang Tang, Fuchun Sun, and Zengqi Sun. Neural network control of flexible-link manipulators using sliding mode. *Neurocomputing*, 70(1):288–295, 2006. Neural Networks.

[76] Yu Zhang, Tangwen Yang, and Zengqi Sun. Neuro-sliding-mode control of flexible-link manipulators based on singularly perturbed model. *Tsinghua Science and Technology*, 14(4):444–451, 2009.

[77] Morten Kollerup Bak. *Model Based Design of Electro-Hydraulic Motion Control Systems for Offshore Pipe Handling Equipment*. PhD thesis, University of Agder, Faculty of Engineering and Science, 2014.

[78] I.M. Mareels, B.D. Anderson, R.R. Bitmead, M. Bodson, and S.S. Sastry. Revisiting the mit rule for adaptive control. *IFAC Proceedings Volumes*, 20(2):161 – 166, 1987. 2nd IFAC Workshop on Adaptive Systems in Control and Signal Processing 1986, Lund, Sweden, 30 June-2 July 1986.

Paper A

Development of Point-to-Point Path Control in Actuator Space for Hydraulic Knuckle Boom Crane

This paper has been published as:

Jensen, K.J.; Kjeld Ebbesen, M.; Rygaard Hansen, M. Development of Point-to-Point Path Control in Actuator Space for Hydraulic Knuckle Boom Crane.
Actuators **2020**, *9(2)*, 27. doi:10.3390/act9020027

actuators

MDPI

Article

Development of Point-to-Point Path Control in Actuator Space for Hydraulic Knuckle Boom Crane

Konrad Johan Jensen *, Morten Kjeld Ebbesen and Michael Rygaard Hansen

Department of Engineering Sciences, University of Agder, 4879 Grimstad, Norway; morten.k.ebbesen@uia.no (M.K.E); michael.r.hansen@uia.no (M.R.H)

* Correspondence: konrad.j.jensen@uia.no

Received: 25 February 2020; Accepted: 7 April 2020; Published: 9 April 2020

Abstract: This paper presents a novel method for point-to-point path control for a hydraulic knuckle boom crane. The developed path control algorithm differs from previous solutions by operating in the actuator space instead of the joint space or Cartesian space of the crane. By operating in actuator space, almost all the parameters and constraints of the system become either linear or constant, which greatly reduces the complexity of both the control algorithm and path generator. For a given starting point and endpoint, the motion for each actuator is minimized compared to other methods. This ensures that any change in direction of motion is avoided, thereby greatly minimizing fatigue, jerky motion, and energy consumption. However, where other methods may move the tool-point in a straight line from start to end, the method in actuator space will not. In addition, when working in actuator space in combination with pressure-compensated control valves, there is no need for linearization of the system or feedback linearization due to the linear relationship between the control signal and the actuator velocities. The proposed solution has been tested on a physical system and shows good setpoint tracking and minimal oscillations.

Keywords: path control; actuator space; knuckle boom crane; hydraulics

1. Introduction

Presently, most hydraulic lifting and handling machines are manually operated. With an increasing demand for automation and higher efficiency, path control can be an important tool to achieve this. In this paper, a hydraulically actuated knuckle boom crane has been considered for path control. A typical offshore knuckle boom crane is shown in Figure 1.

The knuckle boom crane is used in a variety of industries, both onshore and offshore. This makes it a good platform for testing and development of new automation technologies. Also, it contains some of the major challenges associated with automation and path control of hydraulically actuated manipulators.

First, the relation between the controlled actuators, namely the hydraulic cylinders, and the state variables will depend on the joint angles in a nonlinear way. Secondly, the hydraulic control valves have some nonlinearity in the form of deadband, in addition to having limited bandwidth. Furthermore, the hydraulic cylinders are subjected to stiction, which may result in jerky motion when operating around zero velocity. This, in combination with the substantial structural flexibility of a weight optimized crane, may result in reduced performance and unnecessary fatigue of the crane.

Different approaches for motion control of hydraulic cranes have previously been investigated, including vector control, feed forward control, pressure control, and force control, see [1–6]. Modeling of hydraulic cranes has been investigated in [7–10]. Point-to-point control of robots has been studied in [11–13].

Figure 1. Typical offshore knuckle boom crane, courtesy of National Oilwell Varco©.

For non-redundant manipulators, tool-point control is typically done using inverse kinematics, [14–16]. By supplying a desired tool-point position, the joint angles for the manipulator can be calculated. This has been done on a hydraulic telescopic handler in [17], for a hydraulic crane in [18], and for flexible loader cranes in [19–23].

Tool-point control for a redundant loader crane was done in [24], and for a hydraulic manipulator in [25,26], where the redundancy was solved using the pseudo-inverse Jacobian method.

Trajectory planning was developed and implemented on a redundant forestry crane in [27]. The crane was controlled in 6-DOF joint space, while the task was described in 3D Cartesian space. This imposes highly nonlinear velocity constraints for the joints.

In [28], a tool-point control scheme was developed for a loader crane using interactive real-time simulation. This included velocity control in the joint space, configuration control, flow sharing, and an operator-in-the-loop.

In this paper, the idea of using the actuator space in manipulator control is introduced. It revolves around using the actuators length coordinates as the state variables. This will typically be the stroke of a hydraulic cylinder, and the rotational angle of a hydraulic motor. In Figure 2, the joint space joint angles θ_1 and θ_2, and the actuator space cylinder strokes x_1 and x_2 for a typical knuckle boom crane are shown.

For a typical hydraulic crane, the control signals are the openings of the pressure-compensated hydraulic valves. A constant valve opening will give a constant flow, and constant cylinder velocity $\dot{x}$. However, the angular velocity of the joint $\dot{\theta}$ will not be constant. By using the cylinder stroke x as the state variable, we ensure a linear relation between the control signals and the state variables.

By using the actuator space with point-to-point path control, the motion of each actuator is inherently minimized. This will reduce fatigue and energy consumption. In addition, by ensuring that all the actuators finish their motion profile at the same time, the peak hydraulic flow of the system is minimized, which equates to indirect flow sharing. Furthermore, by avoiding change in the sign of the actuator velocity it is possible to avoid one of the main non-linearities associated with hydraulic cylinder drives, namely the jump in friction forces around zero velocity caused by stiction between piston and cylinder.

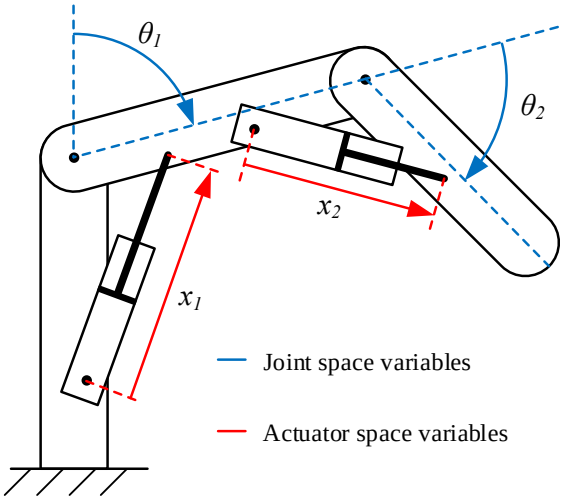

Figure 2. Joint space coordinates and actuator space coordinates shown for a two degree of freedom crane.

One thing to note is that when using point-to-point in actuator space, the tool-point will not follow a straight line in Cartesian space, due to the nonlinear relation between the two spaces. The tool-point will rather tend to move in an arc between two points in Cartesian space.

In this paper, model-based design has been used in combination with laboratory experiments. A simulation of the system has been made using a hydraulic-mechanical model and the developed control algorithms. The simulation results have been verified with laboratory experiments.

2. Considered System

In this paper, an HMF 2020K4 loader crane has been used for experiments. This crane has a total of 5 actuators: slew cylinder, main cylinder, knuckle cylinder, telescopic cylinder, and a winch. In this case, the winch and telescopic cylinder have been omitted, leaving the system with three degrees of freedom and no redundancy which, basically, corresponds to a knuckle boom crane. An illustration of the crane is shown in Figure 3.

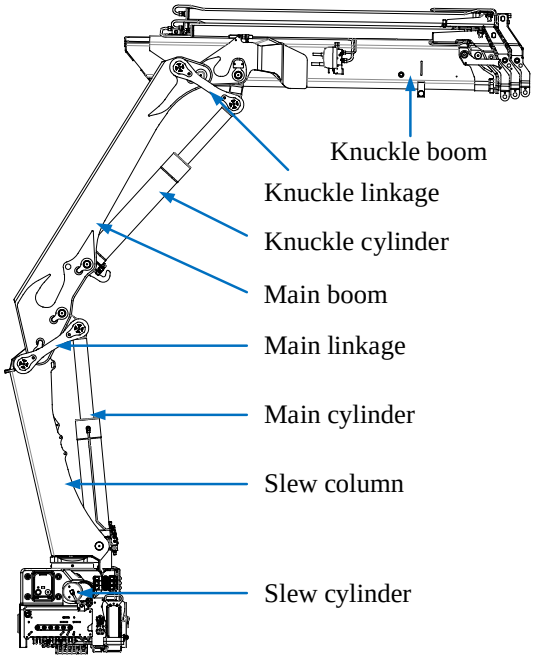

Figure 3. Illustration of the HMF 2020K4 loader crane.

The slew cylinder is rotating the crane with a rack and pinion. The main cylinder and the knuckle cylinder are connected to their respective booms through a linkage system.

Each actuator is controlled via a pressure-compensated proportional directional valve which ensure load independent flow control of the actuators. Counterbalance valves are also used for load holding, assisting in lowering of the booms, and pressure relief of pressure surges. An illustration of the hydraulic system for the knuckle cylinder is shown in Figure 4.

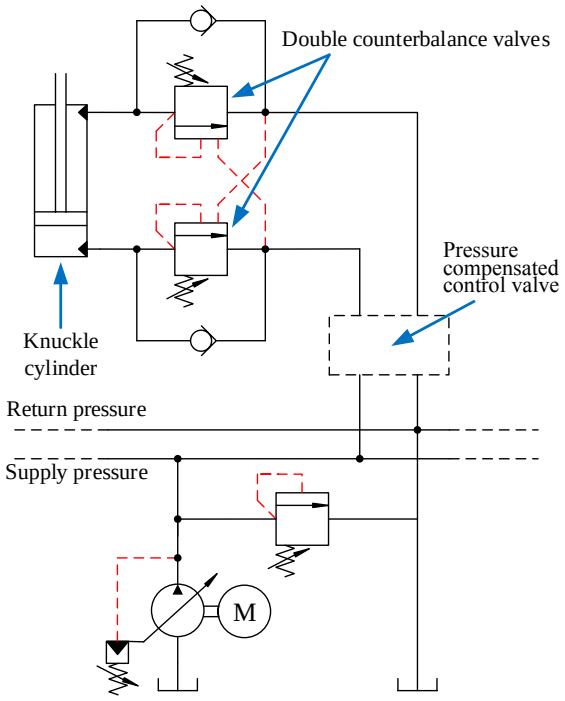

Figure 4. Hydraulic circuit for the knuckle cylinder.

The slew cylinder and knuckle cylinder have double counterbalance valves, while the main cylinder only has one.

The HMF 2020K4 is connected to a National Instruments CompactRIO, which has I/O modules for connecting the sensors and for sending control signals to the valves. There are position sensors on the main cylinder and knuckle cylinder, and an angle sensor between the base and the slew column. The CompactRIO contains the path generator algorithm and the control algorithm.

2.1. Difference from Robotic Systems

As motion control of robots is an extensively studied subject, inspiration can be taken from it when developing motion control of hydraulic manipulators and more specifically, cranes. However, there are clear differences which affect the development of controllers and algorithms. First, the actuators for robots are typically motors connected to each joint of the robot's arms. For the HMF 2020K4 crane, the actuators are cylinders connected to the booms via linkages. For robots, the equation of motion is generally written as shown in Equation (1).

$$M(q) \cdot \ddot{q} + C(q, \dot{q}) \cdot \dot{q} + G(q) = \tau \quad (1)$$

where,

$M(q)$ = Inertia matrix;
$C(q, \dot{q})$ = Coriolis and centripetal force matrix;
$G(q)$ = Gravitational force vector;
τ = Applied torque in each joint;
$q, \dot{q}, \ddot{q}$ = Joint angle, angular velocity and angular acceleration;

Since cranes typically move with accelerations several orders of magnitude smaller than gravity and with relatively low velocities, the effect of the terms $M(q) \cdot \ddot{q}$ and $C(q, \dot{q}) \cdot \dot{q}$ are, typically, less important than the gravitational loads $G(q)$. As for actuation, for a robot the motor torque τ is applied in each joint. For a crane with cylinders, the applied torque of each joint is the product of the effective torque arm $r(q)$, which is a nonlinear function of q, and the cylinder force F_c, which depends on the cylinder pressures and flows. The governing equations associated with the hydraulics are shown in Equations (2)–(6).

$$\tau = r(q) \cdot F_c \tag{2}$$

$$F_c = p_a \cdot A_a - p_b \cdot A_b \tag{3}$$

$$\dot{p}_a = \frac{\beta \cdot (Q_a - \dot{V}_a)}{V_a} \tag{4}$$

$$\dot{p}_b = \frac{\beta \cdot (Q_b - \dot{V}_b)}{V_b} \tag{5}$$

$$\frac{Q_a}{A_a} = -\frac{Q_b}{A_b} = \dot{x}_c \tag{6}$$

where,

$r(q)$ = Effective torque arm;
F_c = Cylinder force;
p_a = Pressure in chamber a;
p_b = Pressure in chamber b;
A_a = Cylinder area a-side;
A_b = Cylinder area b-side;
Q_a = Flow into chamber a;
Q_b = Flow into chamber b;
V_a = Volume of chamber a;
V_b = Volume of chamber b;
β = Oil bulk modulus;
$\dot{x}_c$ = Cylinder velocity.

With a pressure-compensated directional valve, the control signal controls the flows Q_a and Q_b. Since the pressure compensator senses the load pressure to ensure the desired flow, the joint torques are automatically adjusted to give the desired motion. The nonlinear dynamics does not disappear, but it is compensated for in the hydraulic circuit, instead of in the controller.

3. System Modeling

For the purpose of verifying the developed control strategies, a time domain simulation model of the crane has been developed in the commercial simulation tool SimulationX. This model contains the mechanical system with booms and linkages, and the hydraulic system with pressure-compensated proportional directional valves and counterbalance valves. The structural flexibility of the mechanical system has not been considered.

The model of the crane is a dynamic hydraulic-mechanical model. The mechanical model is a 3D multibody system, while the hydraulic model is a 1D system. The cylinders have been replaced with force elements which connect the mechanical and hydraulic model, similar to Equations (2)–(6). A 3D view of the crane from SimulationX is shown in Figure 5.

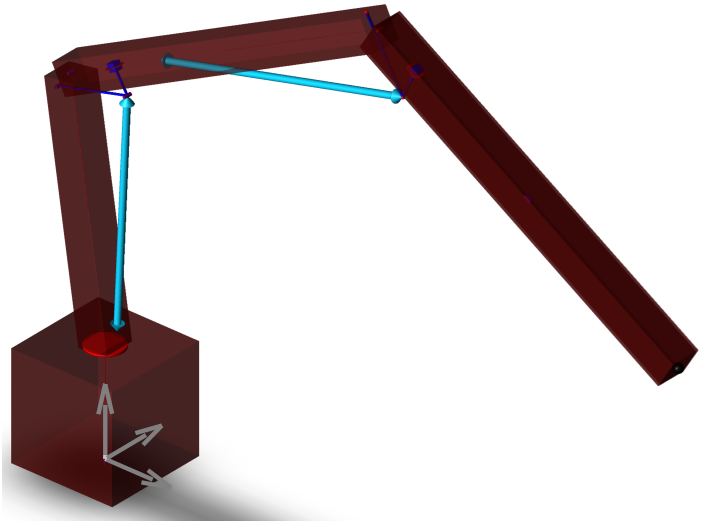

Figure 5. 3D view of the crane in SimulationX.

The mass of the booms has been estimated based on available CAD drawings. As an example, the main boom has a mass of $m = 700$ kg, a length of $L = 2.4$ m, and a mass moment of inertia around the axis of the main hinge of $I = 1350$ kg·m^2.

An illustration of the pressure-compensated proportional directional valve is shown in Figure 6.

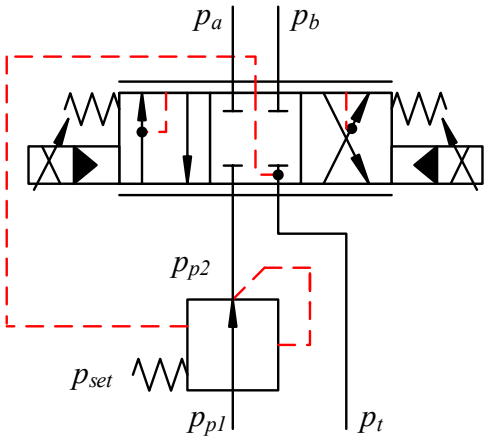

Figure 6. Hydraulic pressure-compensated directional valve.

To mimic the behavior of the pressure compensator, a pressure source has been used for p_{p2}. Equation (7) describes how the pressure is calculated.

$$p_{p2} = \begin{cases} p_a + p_{set} & \text{if } u \leq 0 \\ p_b + p_{set} & \text{otherwise} \end{cases} \tag{7}$$

where,

p_{p2} = compensated pressure;
p_a = pressure at port a;
p_b = pressure at port b;
p_t = tank pressure;
p_{set} = spring pressure setting, set to 10 bar;
u = position of the spool, $-1 \leq u \leq 1$.

The sensing of the load pressures p_a and p_b ensure that the pressure drop over the valve always equals p_{set}, and the flow is load independent. This is shown in Equation (8).

$$\begin{aligned} Q &= C_d \cdot A_d \cdot u \cdot \sqrt{\frac{2}{\rho} \cdot (p_a - p_{p2})} \\ &= C_d \cdot A_d \cdot u \cdot \sqrt{\frac{2}{\rho} \cdot p_{set}} \\ &= Q_{max} \cdot u \end{aligned} \tag{8}$$

where,

C_d = discharge coefficient;
A_d = maximum discharge area;
ρ = mass density;
Q_{max} = maximum valve flow.

To ensure that the valve will always be able to give the desired flow, a safety factor of $u_{threshold} = 0.8$ has been used for the path generator. This will help the setpoint to stay below Q_{max}, even when the system is falling behind the reference and the controller needs to catch up, shown in Equation (9).

$$Q_{ref,max} = Q_{max} \cdot u_{threshold} \tag{9}$$

where,

$Q_{ref,max}$ = maximum valve flow reference;
$u_{threshold}$ = safety factor, 0.8.

An illustration of the counterbalance valves is shown in Figure 7.

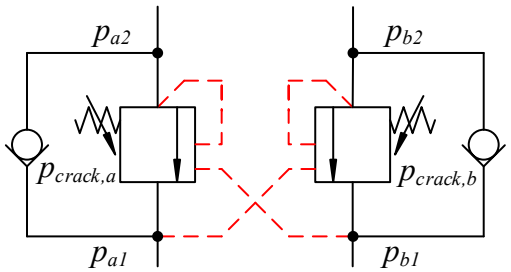

Figure 7. Double counterbalance valve.

The unitless openings of the counterbalance valves are calculated in Equations (10)–(13).

$$\tilde{u}_a = \frac{p_{a2} + \rho \cdot p_{b1} - p_{crack,a}}{\Delta p} \tag{10}$$

$$u_a = \min(\max(0, \tilde{u}_a), 1) \tag{11}$$

$$\tilde{u}_b = \frac{p_{b2} + \rho \cdot p_{a1} - p_{crack,b}}{\Delta p} \tag{12}$$

$$u_b = \min(\max(0, \tilde{u}_b), 1) \tag{13}$$

where,

$\tilde{u}_a$ = unconstrained opening of valve a;
$\tilde{u}_b$ = unconstrained opening of valve b;
u_a = opening of valve a;
u_b = opening of valve b;
p_{a1} = pressure at valve a input sid;
p_{a2} = pressure at valve a actuator side;
p_{b1} = pressure at valve b input side;
p_{b2} = pressure at valve b actuator side;
$p_{crack,a}$ = crack pressure of valve a;
$p_{crack,b}$ = crack pressure of valve b;
ρ = pilot area ratio;
Δp = pressure difference between fully closed and fully open, 10 bar .

When u_a and u_b are 0, the valves are closed. When they are 1, the valves are fully open. During operation, the valves tend to be somewhere between 0 and 1, meaning that they are throttling the flow. The valves are modeled as first order transfer functions in the simulation model to induce some time delay and dynamics, since the valves have a finite bandwidth.

The model from SimulationX has been exported as C-code to MATLAB/Simulink for testing and prototyping of the path generator algorithm and control algorithm.

4. Control Architecture

The control architecture consists of two parts: the control system which measures the cylinder positions and sends control signals to the valves, and the path generator algorithm which generates the setpoints for position and velocity for each actuator.

4.1. Path Generator

The point-to-point path generator operates in actuator space, which uses the cylinder length coordinates as state variables. The main and knuckle cylinder length coordinates are used directly, but since the slew cylinder is connected to the slew column via a rack and pinion, the slew angle is used instead of the slew cylinder length coordinate. Please note that the slew angle is proportional to the slew cylinder length coordinate. This means that the state variables are:

$$x = \begin{bmatrix} \theta_s & x_m & x_k \end{bmatrix}^T \tag{14}$$

where,

θ_s= angle of slew column;
x_m = length of main cylinder;
x_k = length of knuckle cylinder.

By operating in actuator space, the relationship between the input and the velocity of each actuator becomes linear, since the pressure-compensated directional control valves ensure a load independent hydraulic flow for a given valve input. The valves have some deadband, but this is counteracted with a deadband compensator in the controller.

In addition, when operating in actuator space, the velocity constraints become constant, defined by the maximum flow of the control valves and the cylinder area. This is not the case in joint space or Cartesian space, in which the velocity constraints will be nonlinear. This greatly simplifies both the path generation and control of the system.

In addition to the position and velocity constraints, artificial acceleration constraints have been imposed on the system to reduce fatigue and oscillations. The acceleration constraints correspond to the slopes of the trapezoidal velocity profiles. For the acceleration constraint, the following rule of thumb from [29] has been used, which minimizes overshoot for trapezoidal velocity profiles.

$$T_r \geq \frac{6}{\omega_n} \tag{15}$$

where,

T_r = ramp time for velocity profile;
ω_n = natural frequency of the system.

A substitution can be made with the following assumptions.

$$T_r = \frac{v_{max}}{a_{max}} \tag{16}$$

$$a_{max} \leq \frac{\omega_n \cdot v_{max}}{6} \tag{17}$$

where,

a_{max} = maximum allowable acceleration;
v_{max} = maximum velocity of actuator.

By using this substitution, all the constraints of the actuators are defined in terms of the state variables and their derivatives, and parameters from hydraulic components. Please note that the estimate of the natural frequency should be low to account for any estimation errors. This will ensure that the system will always be able to follow the trapezoidal velocity profile with minimal overshoot.

The input to the path generator is a list of the desired actuator positions, and the current actuator positions. A block diagram of the point-to-point path controller is shown in Figure 8.

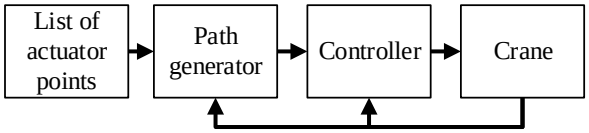

Figure 8. Point-to-point path controller structure.

From the list of points in actuator space, the path generator calculates trapezoidal velocity profiles for each actuator, based on their maximum velocity and maximum allowable acceleration. The safety factor $u_{threshold}$ is used for the velocity, as introduced in Section 3.

Equations (18)–(28) are used to calculate the trapezoidal velocity profiles for the three actuators. This also includes a correctional step if the ramp time is larger than half the total time. In addition, it is ensured that the actuators reach the desired point at the same time. Since the actuators reach the desired point at the same time, the maximum required flow is reduced, because in most cases only one of them will run at full speed. This would not be the case if they all ran full speed at the start, and then two of the actuators waited for the third to finish the motion, in which case the maximum flow would be large at the beginning of the motion.

The ramp time T_r and total time T are calculated as follows for the 3 actuators:

$$i = 1..3 \tag{18}$$

$$\Delta x_i = \left| x_{i,list} - x_i \right| \tag{19}$$

$$T_{r_i} = \frac{v_{i,max}}{a_{i,max}} \tag{20}$$

$$T_i = \frac{\Delta x_i + T_{r_i} \cdot v_{i,max}}{v_{i,max}} \tag{21}$$

A corrected ramp time $\hat{T}_r$ and total time $\hat{T}$ are now introduced for each actuator. They will alter the velocity profile if the ramp time is larger than half of the total time. This happens when $\Delta x < T_r \cdot v_{max}$. In this case, the velocity profile is altered into a triangle, with $\hat{T}_r = \frac{\hat{T}}{2}$:

$$\hat{T}_i = \begin{cases} 2 \cdot \sqrt{\frac{\Delta x_i}{a_{i,max}}} & \text{if } T_{r_i} > \frac{T_i}{2} \\ T_i & \text{otherwise} \end{cases} \tag{22}$$

$$\hat{T}_{r_i} = \begin{cases} \frac{\hat{T}_i}{2} & \text{if } T_{r_i} > \frac{T_i}{2} \\ T_{r_i} & \text{otherwise} \end{cases} \tag{23}$$

The common total time $\tilde{T}$ is used to ensure that all actuators finish their motion at the same time:

$$\tilde{T} = \max(\hat{T}_i) \tag{24}$$

The corrected maximum velocity $\hat{v}$ and trapezoidal velocity profile $\tilde{v}$ are then described as follows:

$$\hat{v}_i = \frac{\Delta x_i}{\tilde{T} - \hat{T}_{r_i}} \tag{25}$$

$$\tilde{v}_i = \begin{cases} \frac{t \cdot \hat{v}_i}{\hat{T}_{r_i}} & \text{if } t < \hat{T}_{r_i} \\ \hat{v}_i & \text{if } \hat{T}_{r_i} \leq t < \tilde{T} - \hat{T}_{r_i} \\ \hat{v}_i - \frac{(t - \tilde{T} + \hat{T}_{r_i}) \cdot \hat{v}_i}{\hat{T}_{r_i}} & \text{if } \tilde{T} - \hat{T}_{r_i} \leq t < \tilde{T} \end{cases} \tag{26}$$

The trapezoidal velocity reference v_{ref} and position reference x_{ref} are then computed:

$$v_{i,ref} = \tilde{v}_i \cdot \text{sign}(x_{i,list} - x_i) \tag{27}$$

$$x_{i,ref} = \int v_{i,ref} dt + x_{i,start} \tag{28}$$

The parameters for the trapezoidal velocity profile are shown in Figure 9.

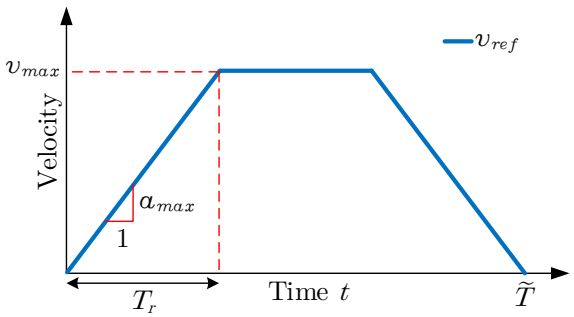

Figure 9. Parameters for velocity profile.

An example of a trapezoidal velocity profile for three actuators is shown in Figure 10.

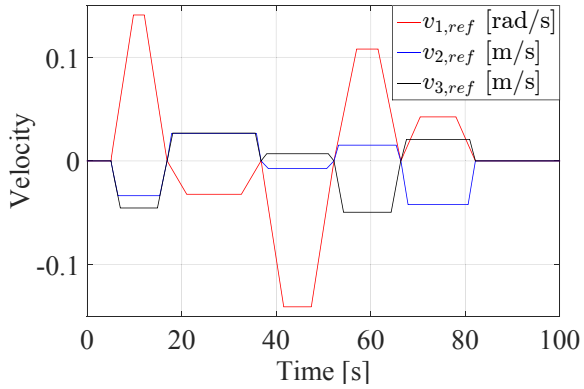

Figure 10. Example of trapezoidal velocity reference for three actuators.

As seen in Figure 10, the maximum velocity for each segment changes, corresponding to the value of the corrected maximum velocity $\hat{v}$.

4.2. Control Structure

The selected control structure is a P-controller for position, and a feed forward gain for velocity. The feed forward gain is simply the ratio from valve opening to actuator velocity, which is determined from the components in the system. An illustration of the selected control system is shown in Figure 11.

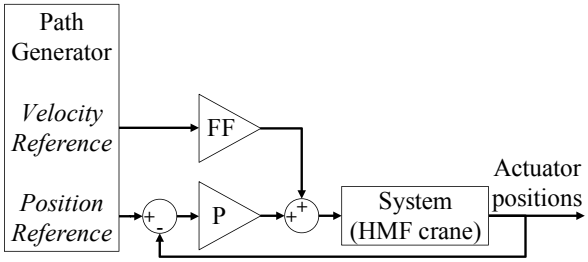

Figure 11. Control system block diagram.

Since both the references and the output of the system are in the actuator space, a simple linear controller can be used. Please note that the system from valve input to actuator position is linear after deadband compensation has been added. The equation for the control input u is given in Equation (29).

$$u = v_{ref} \cdot v_{FF} + (x_{ref} - x) \cdot k_p \tag{29}$$

5. System Simulation

Using the crane model described in Section 3, and path generator and control structure from Section 4, a complete system simulation has been performed in MATLAB/Simulink. A list of points for the path generator has been made to ensure a wide range of operation, both with respect to the actuator velocities and positions.

5.1. Simulation Setup

For the simulation, the natural frequency for each actuator has been estimated from the system model. A low estimate of the natural frequency has been used in the path controller to define the acceleration constraints, shown in Table 1.

Table 1. Estimated natural frequencies for the three actuators.

$\omega_{n,1}$	1 rad/s
$\omega_{n,2}$	4 rad/s
$\omega_{n,3}$	5 rad/s

The maximum velocities used are given in Table 2.

Table 2. Maximum velocities for the three actuators.

Actuator	$v_{max,in}$	$v_{max,out}$
Slew	0.1 rad/s	0.1 rad/s
Main	0.046 m/s	0.032 m/s
Knuckle	0.047 m/s	0.036 m/s

Since a complete model of the system, path generator, and controller is available in a virtual environment, some effort has been made to tune the controller to optimize the crane motion. The virtual environment is well suited for design and numerical test of controllers and tunable parameters. Emphasis has been made to ensure minimal tracking error, as well as reducing the oscillations in the control signal. Minimizing the tracking error ensures an overall good system performance, both in simulation and real-world applications. Minimizing the oscillations in the control signal will help reducing certain unwanted phenomena in real-world applications, namely fatigue, jerky motion, and excitation of unmodeled dynamics. The tunable parameters in the controller, $k_{p,1}$, $k_{p,2}$, and $k_{p,3}$, have all been tested manually, as well as using optimization.

An objective function has been made to both minimize the tracking error and the oscillations in the control signal, using a weighted summation. The objective function to be minimized uses the data from each iteration of the simulation, and is shown in Equation (30).

$$f = \sum_{i=1}^{3} (C_{1,i} \cdot RMS(e_i) + C_{2,i} \cdot RMS(\dot{u}_i)) \tag{30}$$

where,

C_1 = normalization vector 1, $[1\ \text{rad}^{-1}\ 1\ \text{m}^{-1}\ 1\ \text{m}^{-1}]^T$;
C_2 = normalization vector 2, $[1\ \text{s}\ 1\ \text{s}\ 1\ \text{s}]^T$;
e = actuator position error;
$\dot{u}$ = time derivative of control signal.

The normalization vectors C_1 and C_2 ensure that the objective function is unitless.

Since the control signal u is proportional to the actuator velocity, the time derivative of the control signal $\dot{u}$ will be proportional to the actuator acceleration. By minimizing $\dot{u}$, unwanted accelerations will also be minimized.

By using the RMS value, both positive and negative tracking errors will be reduced. In addition, the variable time step of the simulation will not affect the objective function.

It should be noted that even though the weighted summation of e and $\dot{u}$ might seem arbitrary, it still ensures that both design criteria will contribute to the total objective function. This ensures that potential solutions that have a low tracking error, but large oscillations, will not be selected, and vice versa.

A simplified Genetic Algorithm has been used to minimize the objective function. Inspiration was taken from [30]. The Genetic Algorithm was selected based on its robustness and ability to minimize non-smooth functions. The algorithm employs a population of potential solutions. Crossover, mutation, and elitism are then used to create a new population every iteration. A flowchart of the Genetic Algorithm is shown in Figure 12.

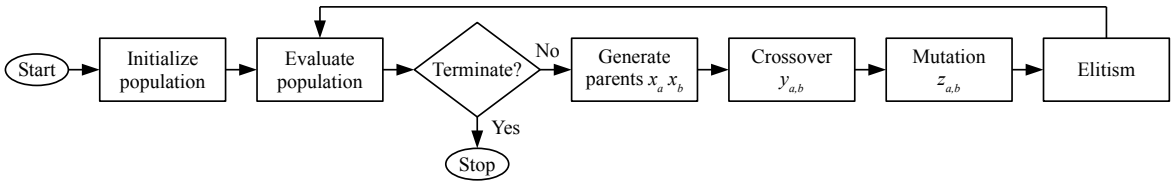

Figure 12. Flowchart of the Genetic Algorithm.

To generate the parents, the individuals are sorted from best to worst and assigned in pairs. The generated list of pairs of parents follows this ranking sequence, see Table 3. x_1 denotes the best individual and so on.

Table 3. Genetic Algorithm parent pair generation sequence.

x_a	x_b
x_1	x_2
x_1	x_3
x_2	x_3
x_1	x_4
x_2	x_4
x_3	x_4
x_1	x_5
x_2	x_5
x_3	x_5
x_4	x_5
⋮	⋮

The crossover function uses a random weighing from the parents to create the genes for the offspring, shown in Equation (31).

$$y_{a,b} = x_a \cdot R_{a,b} + x_b \cdot (1 - R_{a,b}) \tag{31}$$

where,

$y_{a,b}$ = offspring of parent a and b;
x_a = parent a;
x_b = parent b;
$R_{a,b}$ = random number [0,1] for crossover between a and b.

After the crossover, mutation is performed on 20% of the individuals which are randomly selected, based on Equations (32)–(33).

$$r_m = (u_b - l_b) \cdot k_m \tag{32}$$

$$z_{a,b} = y_{a,b} + r_m \cdot R_{a,b} + \frac{r_m}{2} \tag{33}$$

where,

u_b = upper bound for parameters;
l_b = lower bound for parameters;
k_m = mutation factor [0,1];
r_m = mutation range;
$z_{a,b}$ = mutated offspring;
$y_{a,b}$ = offspring of parent a and b;
$R_{a,b}$ = random number [0,1] for offspring $y_{a,b}$.

The last step is elitism, which copies the best 2% of individuals from the previous generation into the new generation without modification. This ensures that the smallest objective value does not increase from generation to generation, in addition to ensuring that the best solutions will generate even more offspring.

5.2. Simulation Results

The simulation results shown here have been made using the selected parameters from Section 5.1. The controller parameters from the Genetic Algorithm which minimized the objective function are shown in Table 4.

Table 4. Controller parameters from minimization.

$k_{p,1}$	4.68	rad^{-1}
$k_{p,2}$	4.72	m^{-1}
$k_{p,3}$	19.71	m^{-1}

Figure 13 shows the position reference made by the path generator. The trapezoidal velocity reference gives a smooth position reference.

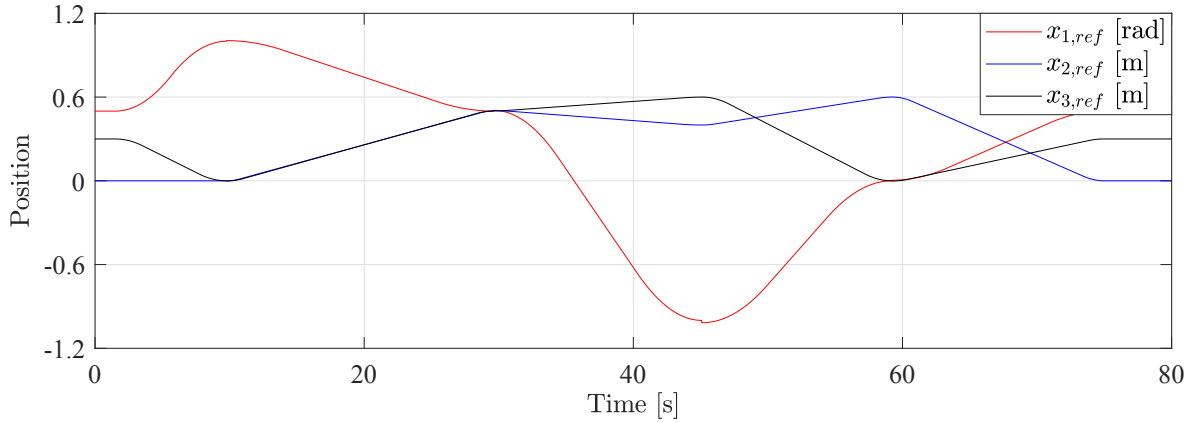

Figure 13. Position reference from simulation.

Figure 14 shows the valve input during operation. The maximum valve input is approximately 0.8 during the simulation, which corresponds to the safety factor $u_{threshold}$. This figure also shows that the valve inputs are not oscillating, which helps to reduce fatigue in a real-world scenario.

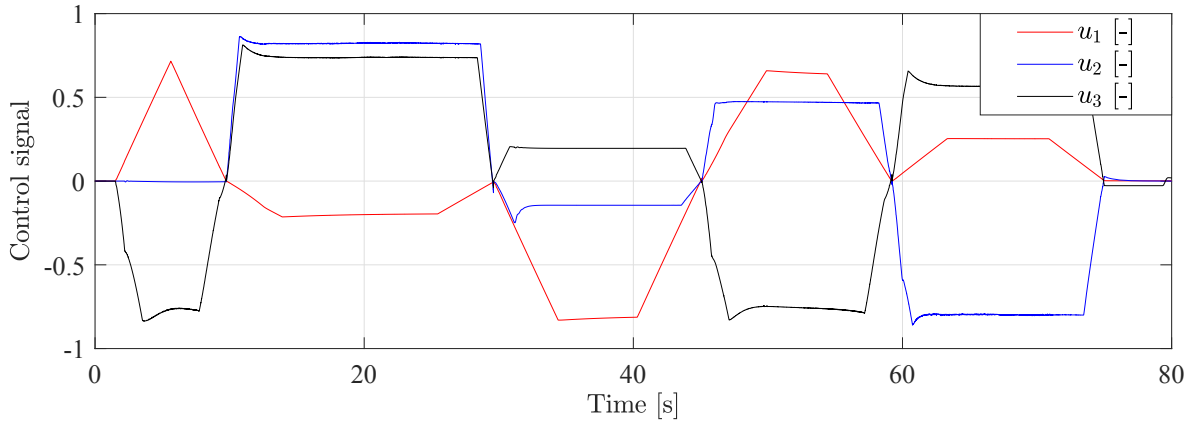

Figure 14. Valve input from simulation.

Figure 15 shows the position error for each actuator, which is less than 0.01 m for the cylinders, and less than 0.04 rad for the slew column.

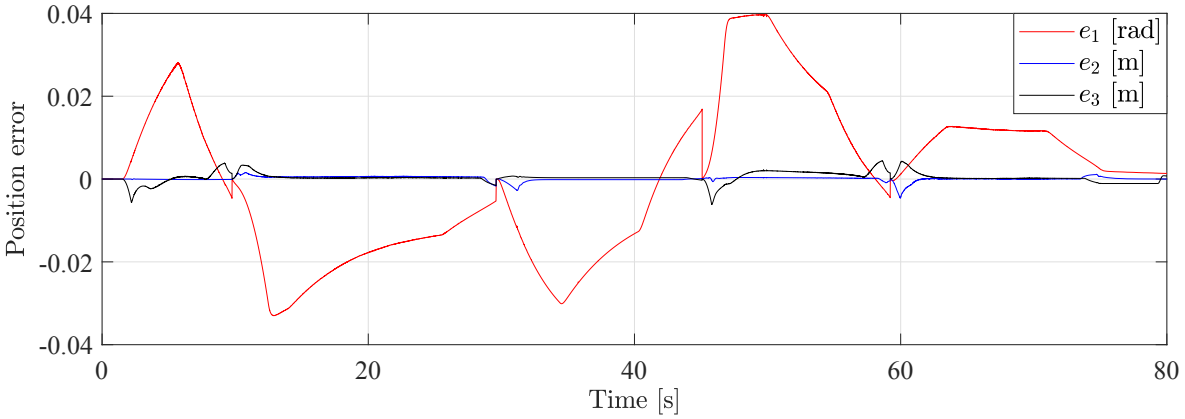

Figure 15. Position error from simulation.

These results show that the path generator and controller have good tracking performance without large oscillations in the system.

6. Practical Implementation

Laboratory experiments have been made with the HMF 2020K4 loader crane to verify and compare the results from the simulations, and to ensure that the proposed controller is feasible in a real-world scenario.

The control system and path generator have been implemented on a CompactRIO connected to the crane, and have been programmed in LabVIEW. The CompactRIO supports the LabVIEW MathScript Module, which allows MATLAB code to be used. This means that the algorithms developed in MATLAB/Simulink in Section 4 have been used directly.

Deadband compensation has been implemented for the laboratory experiments. The deadband for each actuator are shown in Table 5.

Table 5. Deadband for each actuator.

Actuator	Out, u^+	In, u^-
Slew	0.23	-0.26
Main	0.24	-0.22
Knuckle	0.21	-0.31

The formula for the deadband compensation is shown in Equation (34).

$$\hat{u} = \begin{cases} u^+ + (1 - u^+) \cdot u & \text{if } u > \tilde{u} \\ u^- + (1 + u^-) \cdot u & \text{if } u < -\tilde{u} \\ 0 & \text{otherwise} \end{cases} \tag{34}$$

where,

$\hat{u}$ = compensated control signal;
u = control signal;
u^+ = deadband out;
u^- = deadband in;
$\tilde{u}$ = desired deadband, 0.01.

By adding a small deadband $\tilde{u}$, it is ensured that the valves will be able to stay closed when no movement is needed.

A path has been made from a list of desired actuator positions to test the system performance.

Figure 16 shows the control signal for each actuator in the laboratory test. The maximum control signal is approximately 0.8, which corresponds to the safety factor $u_{threshold}$.

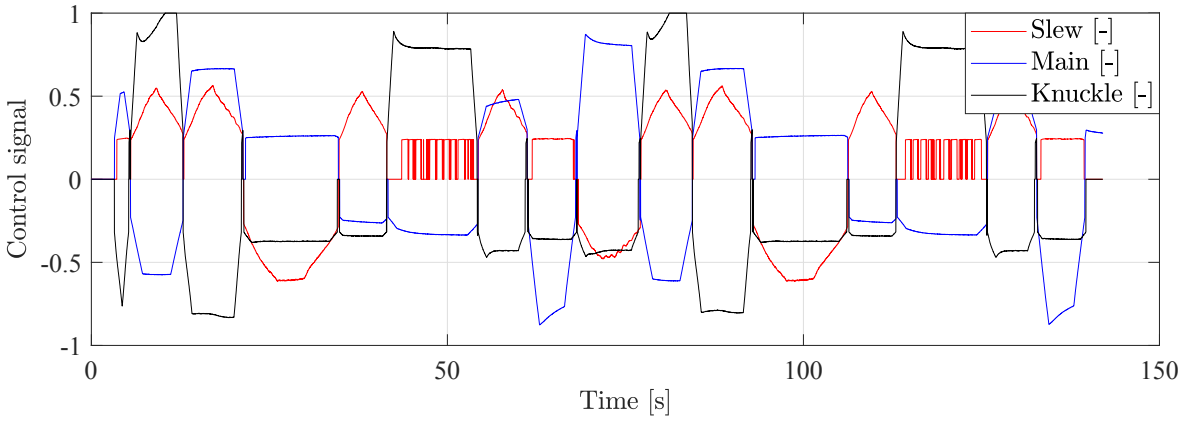

Figure 16. Control signal from laboratory test.

It can also be seen that the control signals are not oscillating during regular motion, which was a criterion from Section 5. At around 50 s and 120 s the control signal for the slew valve is sitting at the edge of the deadband while moving slowly, which makes it appear to be oscillating heavily. At 10 s and 80 s the control signal for the knuckle valve saturates slightly as it tries to keep up with the reference.

Figure 17 shows the velocity for each actuator in the laboratory test.

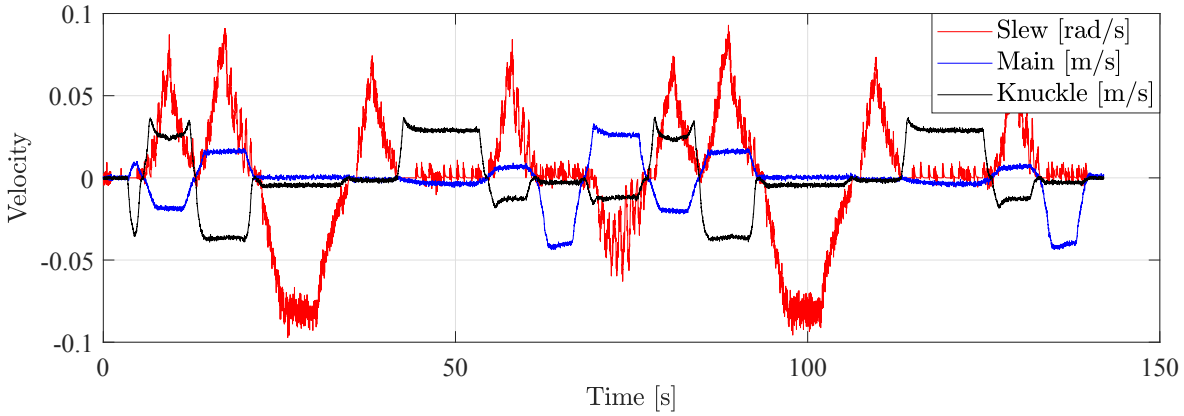

Figure 17. Velocity from laboratory test.

The velocity of each actuator is proportional to the control signal, as expected with pressure-compensated valves. This also verifies that the actuators are moving at a constant velocity. The noise comes from the fact that the velocity signal is the derivative of the position sensor measurements.

Figure 18 shows the position error for each actuator in the laboratory test.

It can be seen that the errors are similar to the position errors from the simulation results in Section 5.2. This shows that the tuning has been successful.

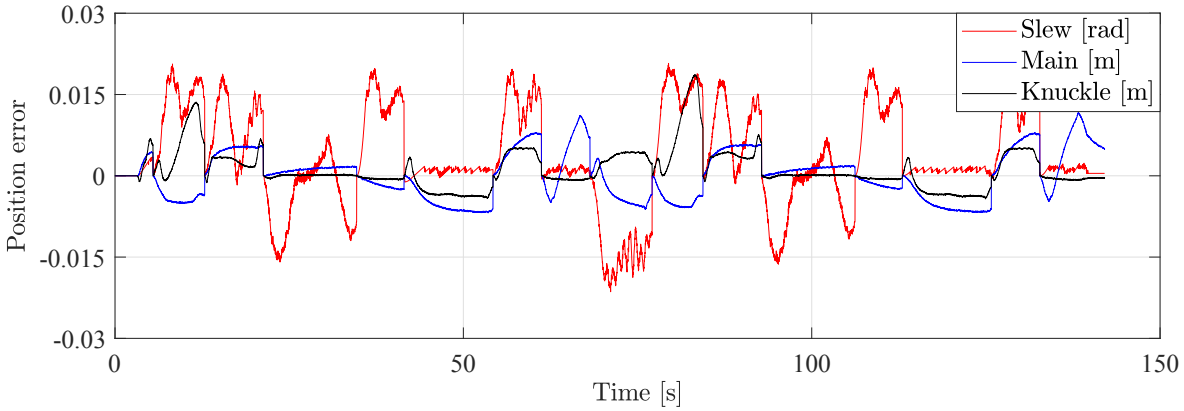

Figure 18. Position error from laboratory test.

7. Conclusions

In this paper, an HMF 2020K4 loader crane has been used as a testing platform for path control. By using a time domain simulation model of the crane, a path generator algorithm and control algorithm have successfully been developed and implemented. The novel path generator operates in actuator space, which indirectly linearizes the system and its constraints based on crane component specifications. This makes it possible to use a simple P-controller with feed forward without the need for plant linearization or feedback linearization.

An effort has also been made to optimize the controller, using a Genetic Algorithm for minimization, to ensure minimal tracking error as well as reducing oscillations in the system.

Simulation results show that the path generator and control system yield good performance. Tests performed in the laboratory also confirm the result, which show good setpoint tracking and minimal oscillations.

The proposed solution allows for simpler controller design compared to other methods, which eases implementation and tuning. In addition, the elimination of stiction during motion is a unique and advantageous feature of the proposed solution.

Future work can include extending the path control to cranes and hydraulic manipulators with kinematic redundancy. Implementation of path control with hanging loads can also be investigated where payload dynamics affect the manipulator. A performance evaluation of the proposed solution compared to other methods can also be made.

Author Contributions: Conceptualization, K.J.J., M.K.E. and M.R.H.; methodology, K.J.J.; software, K.J.J.; validation, K.J.J.; formal analysis, K.J.J.; investigation, K.J.J.; data curation, K.J.J.; writing–original draft preparation, K.J.J.; writing–review and editing, K.J.J., M.K.E. and M.R.H.; visualization, K.J.J.; supervision, M.K.E. and M.R.H. All authors have read and agreed to the published version of the manuscript.

Funding: This research was funded by the Norwegian Ministry of Education and Research grant number 155597. The APC was funded by the University of Agder.

Conflicts of Interest: The authors declare no conflict of interest.

References

1. Krus, P.; Palmberg, J.O. Vector Control of a Hydraulic Crane. *Int.-Off-Highw. Powerpl. Congr. Expo.* **1992**. [CrossRef]
2. Beiner, L. Identification and Control of a Hydraulic Forestry Crane. *Mechatronics* **1997**, *7*, 537–547. [CrossRef]
3. Mattila, J.; Virvalo, T. Energy-efficient Motion Control of a Hydraulic Manipulator. In Proceedings of the 2000 IEEE International Conference on Robotics and Automation, San Francisco, CA, USA, 24–28 April 2000. [CrossRef]
4. Zhang, Q. Hydraulic Linear Actuator Velocity Control Using a Feedforward-plus-PID Control. *Int. J. Flex. Autom. Integr. Manuf.* **1999**, *7*, 277–292.

5. Sørensen, J.K.; Hansen, M.R.; Ebbensen, M.K. Boom Motion Control Using Pressure Control Valve. In Proceedings of the 8th Fluid Power Net International Ph.D Symposium on Fluid Power, Lappeenranta, Finland, 11–13 June 2014. [CrossRef]
6. Sørensen, J.K.; Hansen, M.R.; Ebbesen, M.K. Load Independent Velocity Control on Boom Motion Using Pressure Control Valve. In Proceedings of the Fourteenth Scandinavian International Conference on Fluid Power, Tampere, Finland, 21–23 May 2015.
7. Hera, P.L.; Morales, D.O. Model-Based Development of Control Systems for Forestry Cranes. *J. Control. Sci. Eng.* **2015**. [CrossRef]
8. Dai, L.; Wu, Y.; Wang, J.; Li, Y.; Liu, Y. Modeling and Control of Flexible Hydraulic Robotic Arm. *Adv. Eng. Forum* **2012**, *2–3*, 334–339. [CrossRef]
9. Nielsen, B.; Pedersen, H.C.; Andersen, T.O.; Hansen, M.R. Modelling and simulation of mobile hydraulic crane with telescopic arm. *Aust. J. Mech. Eng.* **2005**, *2*, 105–116. [CrossRef]
10. Pedersen, H.C.; Andersen, T.O.; Nielsen, B.K. Comparison of Methods for Modeling a Hydraulic Loader Crane With Flexible Translational Links. *J. Dyn. Syst. Meas. Control.* **2015**, *137*. [CrossRef]
11. Park, Y.S.; Cho, H.S.; Koh, K.C. *Robot Positioning Based on Point-to-Point Motion Capability*; University of North Texas Libraries: Denton, TX, USA, 2000.
12. Ailon, A.; Zohar, I. Point-to-point control and trajectory tracking in wheeled mobile robots: Some further results and applications. In Proceedings of the 17th IFAC World Congress, Seoul, Korea, 6–11 July 2008; Volume 41, pp. 9546–9551. [CrossRef]
13. Alipour, K.; Moosavian, S.A.A. Point-to-point stable motion planning of wheeled mobile robots with multiple arms for heavy object manipulation. In Proceedings of the 2011 IEEE International Conference on Robotics and Automation, Shanghai, China, 9–13 May 2011; pp. 6162–6167.
14. Kucuk, S.; Bingul, Z. The Inverse Kinematics Solutions of Industrial Robot Manipulators. In Proceedings of the IEEE International Conference on Mechatronics, Istanbul, Turkey, 5–5 June 2004; pp. 274–279. [CrossRef]
15. Pieper, D.L. The Kinematics of Manipulators under Computer Control. Ph.D. Thesis, Department of Mechanical Engineering, the Stanford University, Stanford, CA, USA, 24 October 1968.
16. Paul, R.P. *Robot Manipulators: Mathematics, Programming, and Control: The Computer Control of Robot Manipulators*; MIT Press: Cambridge, MA, USA, 1981. Available online: https://books.google.no/books?id=UzZ3LAYqvRkC&printsec=frontcover&redir_esc=y#v=onepage&q&f=false (accessed on 9 April 2020)
17. Cinkelj, J.; Kamnik, R.; Cepon, P.; Mihelj, M.; Munih, M. Robotic control system for hydraulic telescopic handler. In Proceedings of the 19th International Workshop on Robotics in Alpe-Adria-Danube Region, Budapest, Hungary, 24–26 June 2010. [CrossRef]
18. Bak, M.K.; Hansen, M.R.; Karimi, H.R. Robust Tool Point Control for Offshore knuckle boom crane. In Proceedings of the 18th IFAC World Congress, Milano, Italy, 28 August–2 September 2011.
19. Ebbesen, M.; Andersen, T.; Hansen, M. Optimal Control of Hydraulically Actuated Flexible Multibody Systems. In Proceedings of the 2nd International Conference on Computational Methods in Fluid Power, FPNI'06, Aalborg, Denmark, 2–3 August 2006.
20. Ebbesen, M.; Hansen, M.; Andersen, T. Optimal Velocity Control of Hydraulically Actuated Flexible Loader Crane.In Proceedings of the 20th Nordic Seminar on Computational Mechanics, Gothenburg, Sweden, 23–24 November, 2007.
21. Ebbesen, M.K.; Hansen, M.R. Correction Scheme for Tool Point Velocity Control of a Flexible Hydraulically Actuated Manipulator. In Proceedings of the International Conference Modelling, Identification, and Control, Innsbruck, Austria, 15–17 February 2010; pp. 298–305.
22. Ebbesen, M.; Andersen, T.; Hansen, M. Trajectory Planning for Hydraulically Actuated Flexible Loader Crane. In Proceedings of the 12th AIAA/ISSMO Multidisciplinary Analysis and Optimization Conference, Victoria, BC, Canada, 10–12 September 2008. [CrossRef]
23. Ebbesen, M.; Hansen, M. Tool Point Control of Material Handling Crane in Marine Operations. In Proceedings of the 24th International Congress on Condition Monitoring and Diagnostics Engineering Management, COMADEM International, Stavanger, Norway, 30 May–1 June 2011.
24. Pedersen, H.C.; Nielsen, B.; Andersen, T.O.; Hansen, M.R.; Pedersen, P. Resolved Motion Control of a Hydraulic Loader Crane. In Proceedings of the 1st International Conference on Computational Methods in Fluid Power Technology, Melbourne, Australia, 26–28 November 2003.

25. Kjelland, M.B.; Tyapin, I.; Hovland, G.; Hansen, M.R. Tool-point control for a redundant heave compensated hydraulic manipulator. In Proceedings of the 2012 IFAC Workshop on Automatic Control in Offshore Oil and Gas Production, Norwegian University of Science and Technology, Trondheim, Norway, 31 May–1 June 2012; pp. 299–304.
26. Kjelland, M.B.; Hansen, M.R.; Tyapin, I.; Hovland, G. Tool-point control of a planar hydraulically actuated manipulator with compensation of non-actuated degree of freedom. In Proceedings of the 12th International Conference on Control, Automation and Systems, JeJu Island, Korea, 17–21 October 2012; pp. 672–677.
27. Mettin, U.; Hera, P.X.L.; Morales, D.O.; Shiriaev, A.S.; Freidovich, L.B.; Westerberg, S. Path-constrained Trajectory Planning and Time-independent Motion Control: Application to a Forestry Crane. In Proceedings of the 14th International Conference on Advanced Robotics, Munich, Germany, 22–26 June 2009.
28. Pedersen, M.M.; Hansen, M.R.; Ballebye, M. Developing a Tool Point Control Scheme for a hydraulic crane using interactive real-time dynamic simulation. *Model. Identif. Control.* **2010**, *31*, 133–143. [CrossRef]
29. Bak, M.K. Model Based Design of Electro-Hydraulic Motion Control Systems for Offshore Pipe Handling Equipment. Ph.D. Thesis, University of Agder, Grimstad, Norway, 2014. Available online: https://uia.brage.unit.no/uia-xmlui/handle/11250/194938 (accessed on 9 April 2020)
30. How the Genetic Algorithm Works. Available online: https://se.mathworks.com/help/gads/how-the-genetic-algorithm-works.html (accessed on 20 March 2020)

© 2020 by the authors. Licensee MDPI, Basel, Switzerland. This article is an open access article distributed under the terms and conditions of the Creative Commons Attribution (CC BY) license (http://creativecommons.org/licenses/by/4.0/).

Paper B

Adaptive Feedforward Control of a Pressure Compensated Differential Cylinder

This paper has been published as:

Jensen, K.J.; Ebbesen, M.K.; Hansen, M.R. Adaptive Feedforward Control of a Pressure Compensated Differential Cylinder. *Appl. Sci.* **2020**, *10(21)*, 7847. doi:10.3390/app10217847

applied sciences

MDPI

Article

Adaptive Feedforward Control of a Pressure Compensated Differential Cylinder

Konrad Johan Jensen *, Morten Kjeld Ebbesen and Michael Rygaard Hansen

Department of Engineering Sciences, University of Agder, 4879 Grimstad, Norway; morten.k.ebbesen@uia.no (M.K.E.); michael.r.hansen@uia.no (M.R.H.)

* Correspondence: konrad.j.jensen@uia.no

Received: 29 September 2020; Accepted: 31 October 2020; Published: 5 November 2020

Abstract: This paper presents the design, simulation and experimental verification of adaptive feedforward motion control for a hydraulic differential cylinder. The proposed solution is implemented on a hydraulic loader crane. Based on common adaptation methods, a typical electro-hydraulic motion control system has been extended with a novel adaptive feedforward controller that has two separate feedforward states, i.e, one for each direction of motion. Simulations show convergence of the feedforward states, as well as 23% reduction in root mean square (RMS) cylinder position error compared to a fixed gain feedforward controller. The experiments show an even more pronounced advantage of the proposed controller, with an 80% reduction in RMS cylinder position error, and that the separate feedforward states are able to adapt to model uncertainties in both directions of motion.

Keywords: adaptive control; hydraulics; differential cylinder; feedforward; motion control

1. Introduction

For hydraulically actuated systems such as cranes, the hydraulic cylinder is the most common actuator since it can provide a linear motion with, generally speaking, a large force to volume ratio, a high efficiency and at a modest price. For systems which require a cylinder force in both directions, a double acting cylinder is needed, and the differential cylinder is an obvious choice due to its low cost and simple design. The main disadvantage is the difference in effective hydraulic area which leads to a jump in both velocity and force gain when changing sign of direction, i.e., around zero velocity.

For many hydraulic systems, the pressure compensated directional control valve is a practical choice due to the fact that it provides load independent flow control of the actuators. The pressure compensator senses the load pressure, and adjusts the pressure drop over the directional control valve to give a load independent flow. Since the velocity of the actuator is proportional to the hydraulic flow through the valve, this translates to load independent velocity control. For manually operated systems, the velocity control makes it easy for an operator to control systems that are subjected to large variations in external load.

For closed loop control systems, the load independent velocity control can be utilized in a control system using feedforward [1]. In this case, both a position reference and a velocity reference are generated in the control system. An example of a typical closed loop electro-hydraulic motion control system with feedforward is shown in Figure 1. The feedback controller uses the position reference and the measured cylinder position, whereas the feedforward controller uses the velocity reference. The pressure compensator is connected to a supply line which is shared with other actuators. The red dashed lines show the hydraulic pilot lines for the counterbalance valve and the pressure compensator.

It should be noted that feedforward control cannot be used alone. A feedback controller is also needed to help track the position reference, to eliminate steady state position error, and to counteract any drift. Normally the feedforward gain is based on system components, and is defined as the

ratio of valve opening to actuator velocity. With this in mind, it follows that modeling errors and model uncertainties, in addition to external disturbances and system dynamics, may yield sub-optimal performance with a fixed feedforward gain.

This paper focuses on modeling and motion control of a hydraulic loader crane with pressure compensated differential cylinders. An adaptive feedforward controller is investigated to improve performance of the motion control system. Two different approaches to feedforward control have been implemented, the first is based on the MIT-rule [2], and the second is based on the sign-sign algorithm [3].

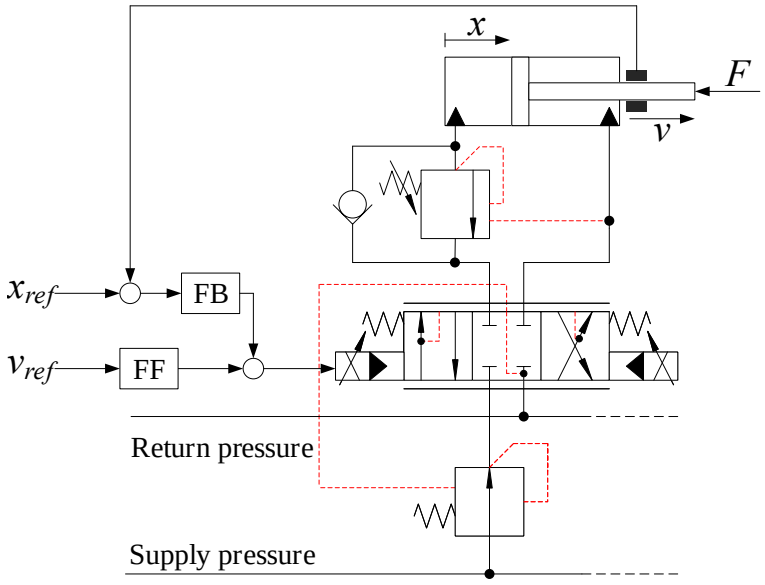

Figure 1. Electro-hydraulic motion control system with feedforward.

2. Background and Method

Adaptive systems have long been used for system identification and parameter estimation. One of the first methods is described in [4]. Another common method is the least mean squares algorithm, which was developed in [5]. An example of this is shown in Equations (1)–(3). Given the linear system:

$$Y = \theta^T \cdot X \tag{1}$$

$$E = Y - \hat{\theta}^T \cdot X \tag{2}$$

$$\dot{\hat{\theta}} = \gamma \cdot X \cdot E^T \tag{3}$$

where

Y = system output;
θ = system parameters;
X = system input;
E = estimation error;
$\hat{\theta}$ = estimated parameters;
γ = adaptation gain, constant.

The estimated parameters will converge towards the system parameters. The idea of using the sign function in the adaptive law comes from the sign-sign least mean squares algorithm, and was first introduced by [3]. Equation (3) then becomes:

$$\dot{\hat{\theta}} = \gamma \cdot \text{sign}(X) \cdot \text{sign}(E^T) \tag{4}$$

By taking the sign of the estimation error and system input, the adaptation becomes insensitive to the magnitudes of E and X, and as such only the adaptation gain γ sets the adaptation speed.

The MIT rule is also used for adaptive control, and is described in [2]. A typical application is model reference adaptive control, shown in Figure 2. Based on the model output y_m, an additional control output $\hat{u}$ is multiplied with the command signal u_c to shape the plant output y. The equations for the model reference adaptive control is shown in Equations (5) and (6).

$$\dot{\hat{u}} = -\gamma \cdot y_m \cdot (y - y_m) \tag{5}$$

$$u = u_c \cdot \hat{u} \tag{6}$$

where

u = control output;
$\hat{u}$ = adaptive control output;
u_c = command signal;
y_m = model output;
y = plant output.

Early work in adaptive control can be found in [6–10]. Other work on adaptive control include [11] which investigates adaptive feedback and feedforward control of robot manipulators, Reference [12] which models and implements adaptive control of a flexible arm, and [13] which uses model reference adaptive control on linear time-varying plants. Adaptive fuzzy sliding mode control is investigated and implemented on an inverted pendulum in [14].

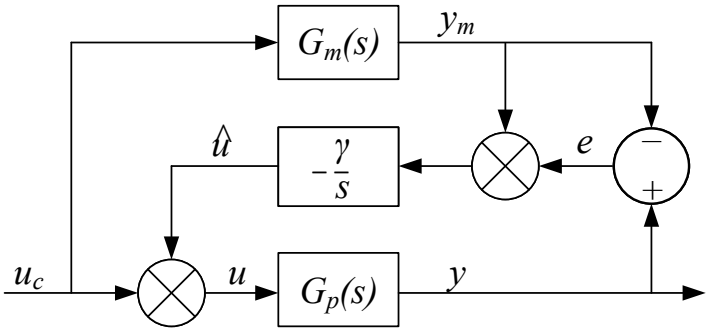

Figure 2. Model reference adaptive control based on MIT-rule.

Newer applications of adaptive control systems include adaptive friction compensation with an adaptive velocity estimator to compensate for the estimated non-linear friction force [15]. In [16], a fuzzy model reference adaptive control of an active magnetic bearing for a milling process is investigated to reduce the milling dynamics. Adaptive integral robust control of an electro-hydraulic servo system is investigated in [17], using parameter estimation and integral control to compensate for disturbances and plant uncertainties. Adaptive control of quadrotors is investigated in [18], which uses an cerebellar model arithmetic computer to adapt to model uncertainties and disturbances. In [19], adaptive control based on least-mean-fourth is implemented for a three-phase grid connected solar system, which is able to provide load balancing and power factor correction.

As for motion control of hydraulic systems, different approaches have previously been investigated, including vector control [20], pressure control [21,22], force control [23,24], and feedforward control [25].

To the knowledge of the authors, adaptive feedforward motion control of hydraulic cylinders has not previously been investigated, and this paper will focus on this novel concept.

In this paper, two adaptive controllers have been tested on a hydraulic differential cylinder and compared to a fixed gain feedforward controller. Based on a typical fixed gain feedforward controller, an adaptive controller can be made by extending it with the MIT rule. An illustration of a control system with feedforward with fixed gain is shown in Figure 3.

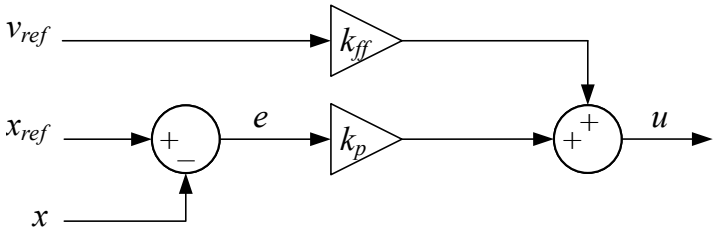

Figure 3. Feedforward with fixed gain.

Defining the position error e as the position reference x_{ref} minus the measured position x, the control output for this control system is given in Equation (7)

$$u = k_p \cdot e + k_{ff} \cdot v_{ref} \tag{7}$$

where

u = controller output;
k_p = proportional gain;
e = position error;
k_{ff} = feedforward gain;
v_{ref} = velocity reference.

Extending the traditional feedforward controller into an adaptive feedforward controller is done by replacing the fixed feedforward gain with the MIT-rule. An illustration of the adaptive feedforward scheme is shown in Figure 4.

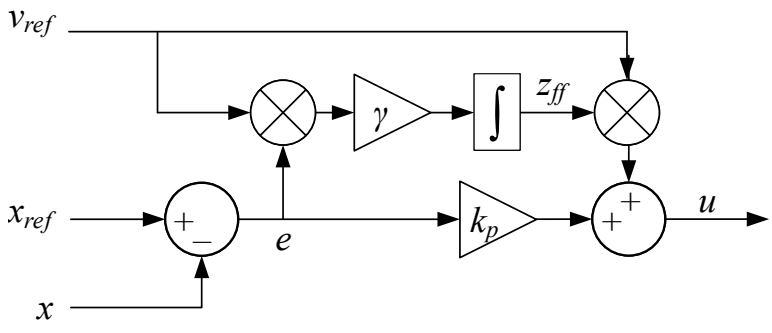

Figure 4. MIT-rule adaptive feedforward.

The MIT-rule adaptive feedforward controller uses the position error, the velocity reference, and the constant γ to update the feedforward gain. The update law and the control output for this adaptive control system is then given in Equations (8) and (9).

$$\dot{z}_{ff} = \gamma \cdot v_{ref} \cdot e \tag{8}$$

$$u = k_p \cdot e + z_{ff} \cdot v_{ref} \tag{9}$$

where

γ = adaptation gain;
z_{ff} = feedforward gain.

Extending this controller to use sign-sign is then straightforward. An illustration of the sign-sign adaptive feedforward scheme is shown in Figure 5.

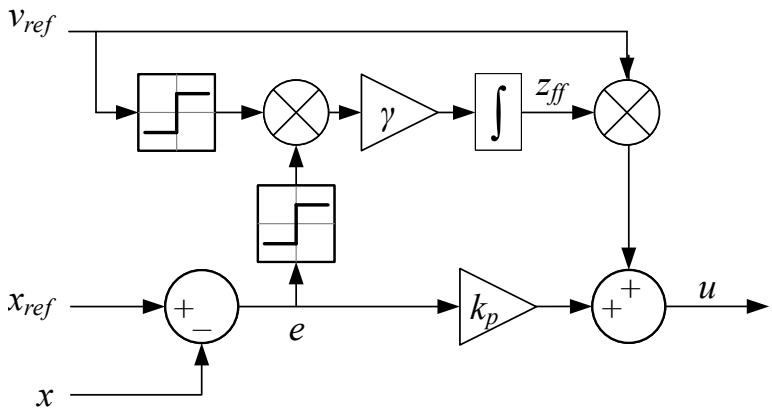

Figure 5. Sign-sign adaptive feedforward.

The update law and the control output for this adaptive control system is shown in Equations (10) and (11).

$$\dot{z}_{ff} = \gamma \cdot \text{sign}(v_{ref}) \cdot \text{sign}(e) \tag{10}$$

$$u = k_p \cdot e + z_{ff} \cdot v_{ref} \tag{11}$$

It should be noted that the sign function can produce unnecessary chattering when the input is oscillating around zero, due to the inherent discontinuity. Therefore the sign function has been replaced with the tanh function, shown in Equation (12).

$$\text{sign}(e) \approx \tanh(k \cdot e) \tag{12}$$

This gives a smooth output when the input is oscillating around zero. Increasing the parameter k gives a sharper rise and a closer approximation to $\text{sign}(e)$. Another advantage of using tanh is that the adaptation stops when the position error is zero. The parameter k has been set to $k = 100\ \text{m}^{-1}$ and $k = 100\ \text{s} \cdot \text{m}^{-1}$ for the position error and velocity reference, respectively.

3. Considered System

In this paper an 2020K4 loader crane made by HMF Group A/S, Højbjerg, Denmark has been used for experiments. An illustration of the crane is shown in Figure 6. This crane has two hydraulic differential cylinders: the main cylinder, and the knuckle cylinder. For this paper, the knuckle cylinder has been used for simulation and experiments, since it can experience both resistive and assistive loads in both directions of motion, equivalent to four quadrant operation. The relevant data for the knuckle cylinder is shown in Table 1, and the data for the knuckle boom is given in Figure 7 and Table 2.

Each actuator is controlled via a pressure compensated proportional directional control valve which ensures load independent flow control of the actuators. Counterbalance valves made by Oil Control S.p.A, Modena, Italy are also used for load holding, assisting in lowering of the booms, and pressure relief of pressure surges. An illustration of the hydraulic system for the knuckle cylinder is shown in Figure 8.

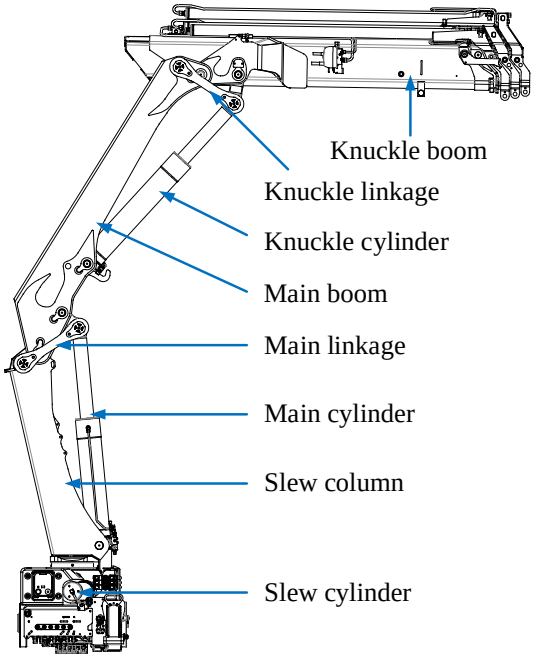

Figure 6. Illustration of the HMF 2020K4 loader crane.

Table 1. Knuckle cylinder data.

Name	Parameter	Value
Piston diameter	D_p	0.15 m
Piston area	A	0.0177 m^2
Rod diameter	D_r	0.1 m
Annulus area	A_a	0.0098 m^2
Piston area ratio	$\phi = \frac{A_a}{A}$	0.5556
Valve maximum flow	Q_{max}	40 L/min

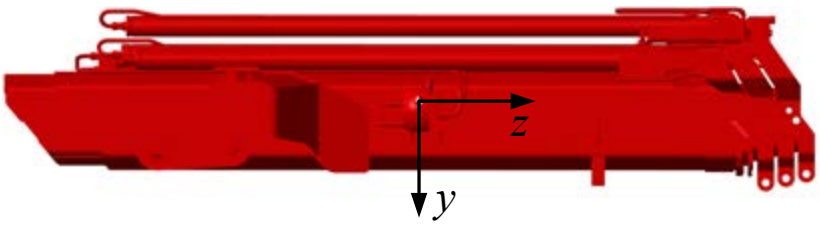

Figure 7. Knuckle boom center of mass.

Table 2. Knuckle boom data.

Name	Parameter	Value
Mass	m_k	851.972 kg
Inertia matrix	I_k	$\begin{bmatrix} 579.552 & 8.74629 & 11.5456 \\ 8.74629 & 573.285 & 0.174433 \\ 11.5456 & 0.174433 & 32.2491 \end{bmatrix}$ kg·m^2

The control system is implemented on a CompactRIO 9075 controller made by National Instruments, Austin, TX, USA. The CompactRIO contains the reference generator and feedforward motion controllers. The block diagram of the connections is shown in Figure 9.

The CompactRIO communicates with a PC, sends control signals to the valves, and reads the sensors on the crane.

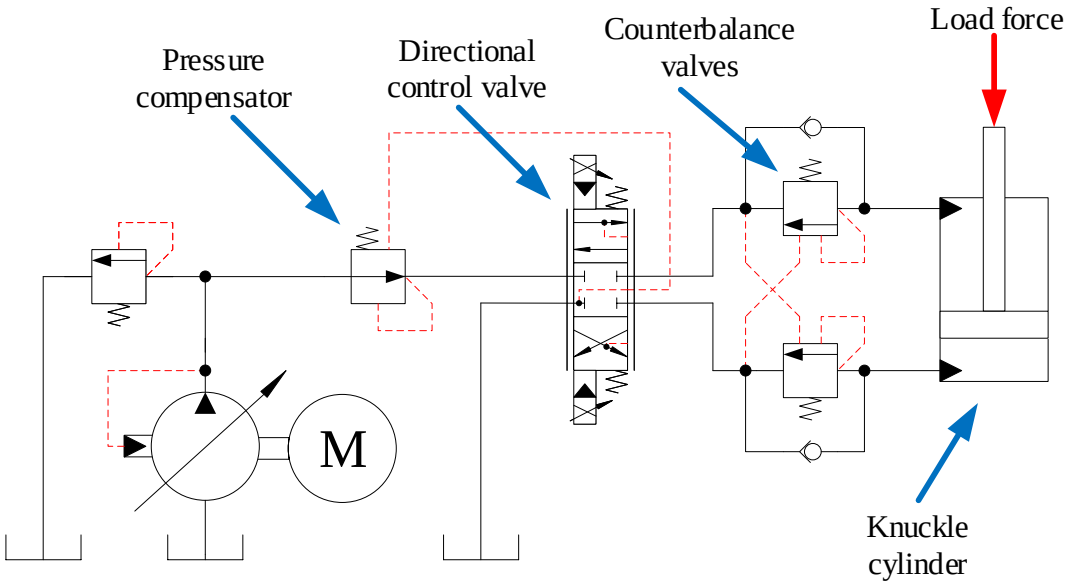

Figure 8. Hydraulic system for the knuckle cylinder.

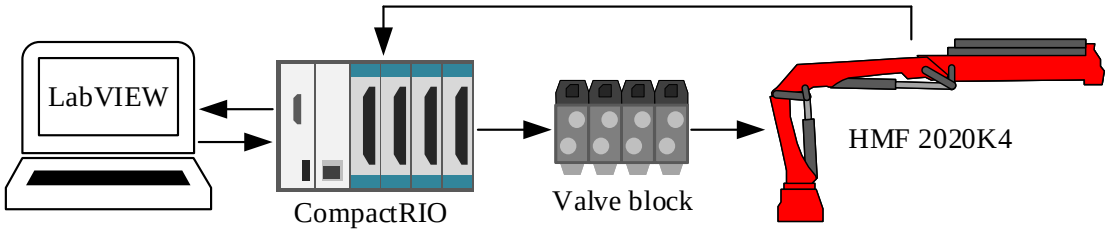

Figure 9. Connection between the crane and CompactRIO controller.

4. Modelling

A dynamic model of the crane has been made in Simscape™ by MathWorks®, Natick, MA, USA. 3D computer-aided design (CAD) models have been imported into the model using the Multibody library. The hydraulic circuit has been made using the hydraulic library of Simscape™. A picture of the CAD model is shown in Figure 10.

In the configuration shown in Figure 10, the knuckle cylinder experiences both resistive and assistive loads in both directions of motion when retracting fully, and extending back out again. The knuckle cylinder is controlled by a pressure compensated directional control valve, shown in Figure 11.

The pressure compensator ensures that there is a constant pressure drop over the directional control valve, which gives a load independent flow. The governing equations of the pressure compensator are given in Equations (13)–(15).

$$u_{pc} = \frac{p_{set} + p_{load} - p_p}{\Delta p} \tag{13}$$

$$p_{load} = \begin{cases} p_a & \text{if } u_{spool} \geq 0 \\ p_b & \text{otherwise} \end{cases} \tag{14}$$

$$Q_{pc} = k_{pc} \cdot u_{pc} \cdot \sqrt{p_i - p_p} \tag{15}$$

where

u_{pc} = opening of compensator, $0 \leq u_{pc} \leq 1$
p_p = compensated pressure at port p;
Δp = pressure difference between fully closed and fully open;
p_a = pressure at port a;
p_b = pressure at port b;
p_t = tank pressure;
p_{set} = spring pressure setting;
p_{load} = load pressure;
u_{spool} = position of the main spool, $-1 \leq u_{spool} \leq 1$;
Q_{pc} = flow in pressure compensator;
k_{pc} = flow gain of compensator;
p_i = compensator inlet pressure.

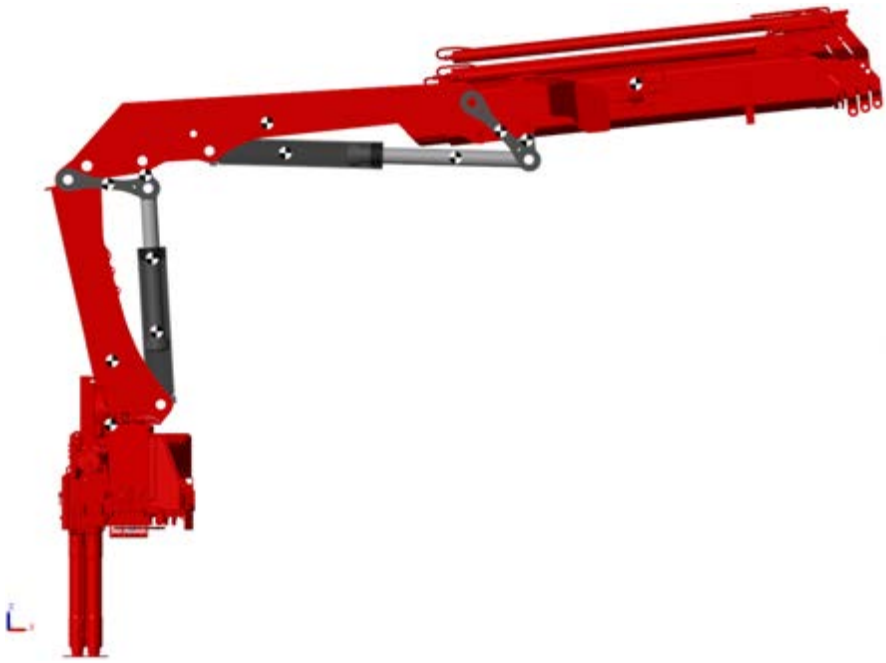

Figure 10. 3D view of the simulation model of the HMF 2020K4 in Simscape.

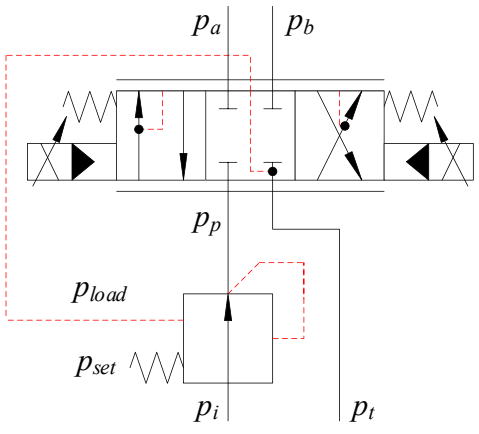

Figure 11. Hydraulic pressure compensated directional control valve for the knuckle cylinder.

The steady state of p_p is then given by Equation (16).

$$p_p = p_{load} + p_{set} \tag{16}$$

The sensing of the load pressures p_a and p_b ensures that the pressure drop over the directional control valve always equals p_{set}, and that the flow is load independent. This is shown in the orifice equation in Equation (17).

$$\begin{aligned} Q &= C_d \cdot A_d \cdot u_{spool} \cdot \sqrt{\frac{2}{\rho} \cdot (p_p - p_{load})} \\ &= C_d \cdot A_d \cdot u_{spool} \cdot \sqrt{\frac{2}{\rho} \cdot p_{set}} \\ &= Q_{max} \cdot u_{spool} \end{aligned} \tag{17}$$

where

Q = flow in the valve;
C_d = discharge coefficient;
A_d = maximum discharge area;
ρ = mass density;
Q_{max} = maximum valve flow;

Double counterbalance valves are used on the knuckle cylinder. An illustration of the counterbalance valves is shown in Figure 12.

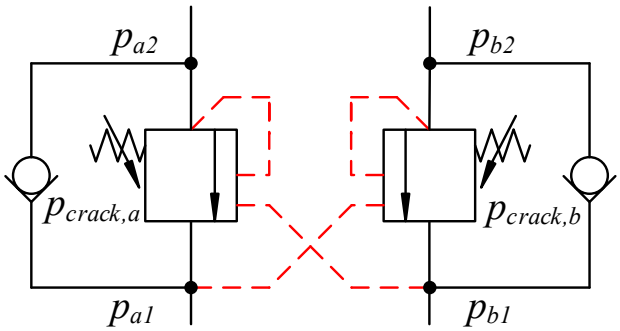

Figure 12. Double counterbalance valve.

The unitless openings of the counterbalance valves are calculated in Equations (18) and (19).

$$u_a = \frac{p_{a2} + \psi \cdot p_{b1} - p_{crack,a}}{\Delta p} \tag{18}$$

$$u_b = \frac{p_{b2} + \psi \cdot p_{a1} - p_{crack,b}}{\Delta p} \tag{19}$$

where

u_a = opening of valve a, $0 \leq u_a \leq 1$;
u_b = opening of valve b, $0 \leq u_b \leq 1$;
p_{a1} = pressure at valve a input side;
p_{a2} = pressure at valve a actuator side;
p_{b1} = pressure at valve b input side;
p_{b2} = pressure at valve b actuator side;

$p_{crack,a}$ = crack pressure of valve a;
$p_{crack,b}$ = crack pressure of valve b;
ψ = pilot area ratio;
Δp = pressure difference between fully closed and fully open.

When u_a and u_b are 0, the valves are closed. When they are 1, the valves are fully open. During assistive loads the valves tend to be somewhere between 0 and 1, meaning that they are throttling the flow. The dynamics of the valves are included as a time constant, since the valves have a finite bandwidth.

5. Adaptive Control Design

Since the actuator is a hydraulic differential cylinder, two separate states z_{ff}^{+} and z_{ff}^{-} are used for out-stroke and in-stroke motion to handle model uncertainties both directions of motion. Consequently, both the feedforward control output and the update law for the two gains are only active during out-stroke or in-stroke motion respectively. To handle this, some switching logic is introduced based on the sign of the velocity reference. The block diagram for the differential MIT-rule adaptive feedforward is shown in Figure 13.

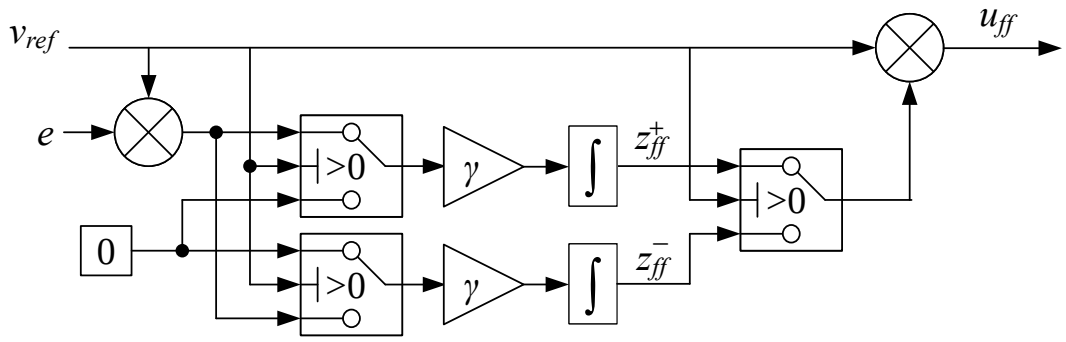

Figure 13. Differential MIT-rule adaptive feedforward.

The governing equations for the differential MIT-rule adaptive feedforward are shown in Equations (20)–(23).

$$\dot{z}_{ff}^{+} = \begin{cases} \gamma \cdot v_{ref} \cdot e, & v_{ref} > 0 \\ 0, & \text{otherwise} \end{cases} \tag{20}$$

$$\dot{z}_{ff}^{-} = \begin{cases} 0, & v_{ref} > 0 \\ \gamma \cdot v_{ref} \cdot e, & \text{otherwise} \end{cases} \tag{21}$$

$$u_{ff} = \begin{cases} z_{ff}^{+} \cdot v_{ref}, & v_{ref} > 0 \\ z_{ff}^{-} \cdot v_{ref}, & \text{otherwise} \end{cases} \tag{22}$$

$$u = k_p \cdot e + u_{ff} \tag{23}$$

where

z_{ff}^{+} = out-stroke feedforward gain;
z_{ff}^{-} = in-stroke feedforward gain;
u_{ff} = feedforward controller output.

Extending the controller to sign-sign is straightforward. The block diagram for the differential sign-sign adaptive feedforward is shown in Figure 14.

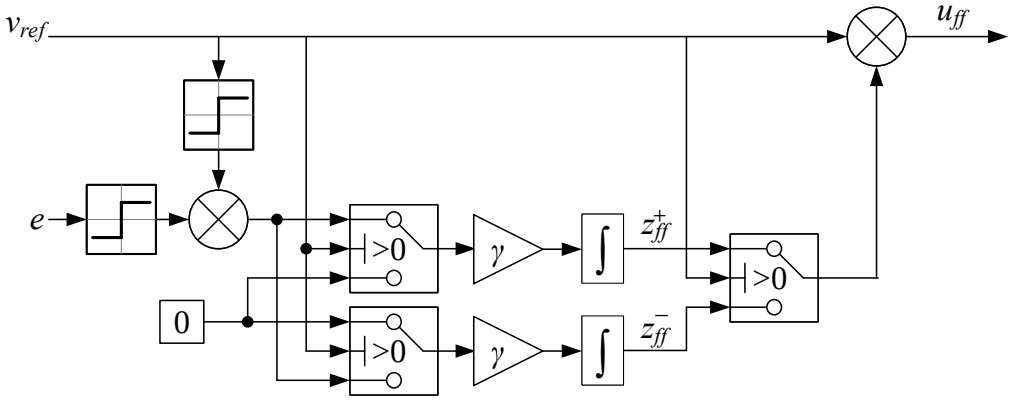

Figure 14. Differential sign-sign adaptive feedforward.

The governing equations for the differential sign-sign adaptive feedforward are shown in Equations (24)–(27).

$$\dot{z}_{ff}^{+} = \begin{cases} \gamma \cdot \text{sign}(v_{ref}) \cdot \text{sign}(e), & v_{ref} > 0 \\ 0, & \text{otherwise} \end{cases} \tag{24}$$

$$\dot{z}_{ff}^{-} = \begin{cases} 0, & v_{ref} > 0 \\ \gamma \cdot \text{sign}(v_{ref}) \cdot \text{sign}(e), & \text{otherwise} \end{cases} \tag{25}$$

$$u_{ff} = \begin{cases} z_{ff}^{+} \cdot v_{ref}, & v_{ref} > 0 \\ z_{ff}^{-} \cdot v_{ref}, & \text{otherwise} \end{cases} \tag{26}$$

$$u = k_p \cdot e + u_{ff} \tag{27}$$

6. Simulation Results

For the simulation, a point-to-point trapezoidal velocity path generator has been used as a reference. The point-to-point path generator has previously been developed in [26]. The path generator operates in actuator space, which eliminates the effects of the non-linearities between the hydraulic cylinder strokes and the joint angles in joint space. A path has been made such that the cylinder experiences both resistive and assistive loads in both directions of motion. The references for position and velocity are shown in Figure 15. The adaptation gain γ is different for the two controllers, due to the use of $\text{sign}(x)$, and has been experimentally set to $\gamma = 200\ \text{s} \cdot \text{m}^{-3}$ for the MIT-rule feedforward, and $\gamma = 0.1\ \text{m}^{-1}$ for the sign-sign feedforward. The unit is adapted accordingly to obtain the correct output.

The position error for the MIT-rule feedforward simulation is shown in Figure 16. The position error decreases towards a bounded error of ± 6 mm, which is shown with the dashed lines. The RMS error after convergence is 1.6 mm, showing high performance.

The states z_{ff} for the MIT-rule feedforward simulation are shown in Figure 17. The dashed lines show the theoretical values for a fixed feedforward gain. The states converge to values slightly larger than the theoretical ones. This small discrepancy can be attributed to the constant velocity reference and ramped position reference. When moving with a ramp position reference, there will always be a small constant position error without an integrator in the position controller. Having a slightly larger feedforward gain helps reducing this constant position error by giving the cylinder a small velocity boost. Since the position error is measured, the adaptive controller is able to adapt the feedforward gains to minimize the position error.

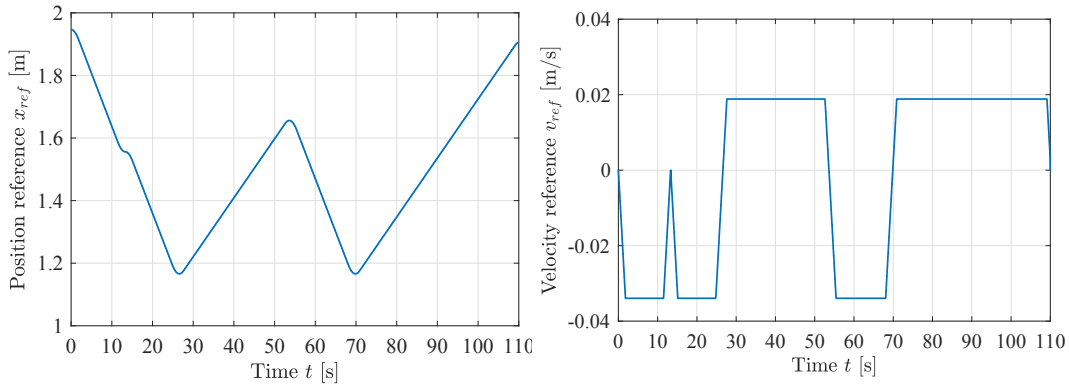

(**a**) (**b**)

Figure 15. Point-to-point path references for simulation. (**a**) Position reference; (**b**) Velocity reference.

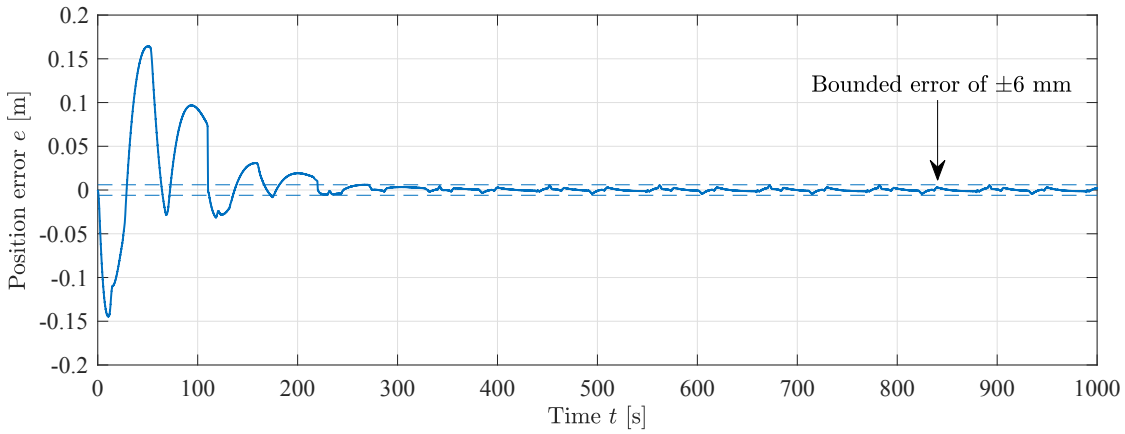

Figure 16. Cylinder position error during MIT-rule feedforward simulation, $\gamma = 200\ \mathrm{s} \cdot \mathrm{m}^{-3}$.

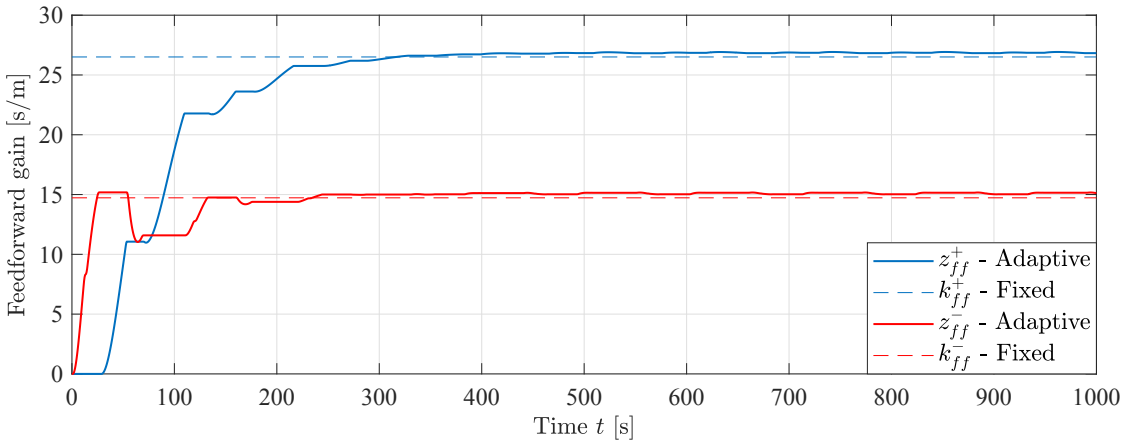

Figure 17. Feedforward states during MIT-rule feedforward simulation, $\gamma = 200\ \mathrm{s} \cdot \mathrm{m}^{-3}$.

Figure 18 shows the control signals u_{ff} and u_{fb} from the feedforward and feedback controller, respectively. Given that the total control signal $u = u_{fb} + u_{ff}$, it can be seen that the contribution from the feedforward controller clearly dominates, providing more than 95% at steady state.

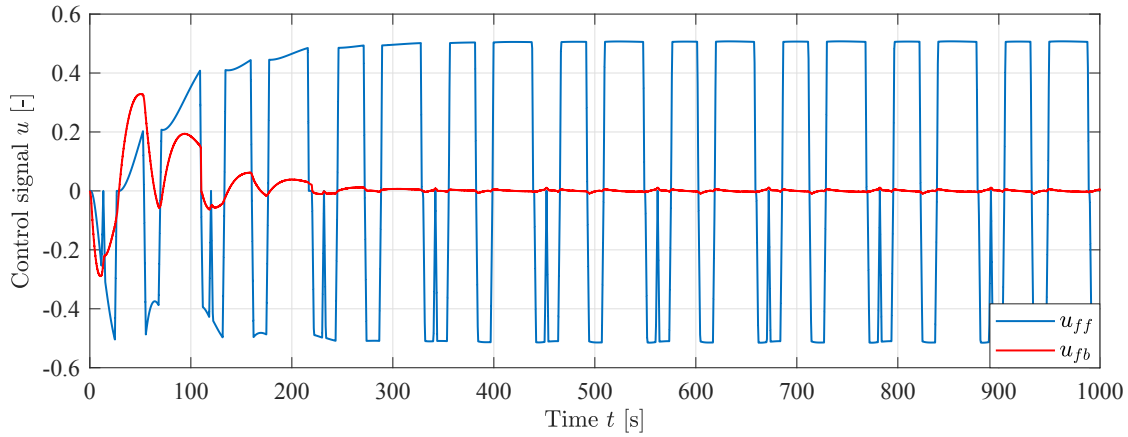

Figure 18. Control signals from feedforward and feedback during simulation, $\gamma = 200\ \mathrm{s} \cdot \mathrm{m}^{-3}$.

The position error for the sign-sign feedforward simulation is shown in Figure 19. The same bounded error of ±6 mm is shown with the dashed lines. The RMS error after convergence is 2.1 mm.

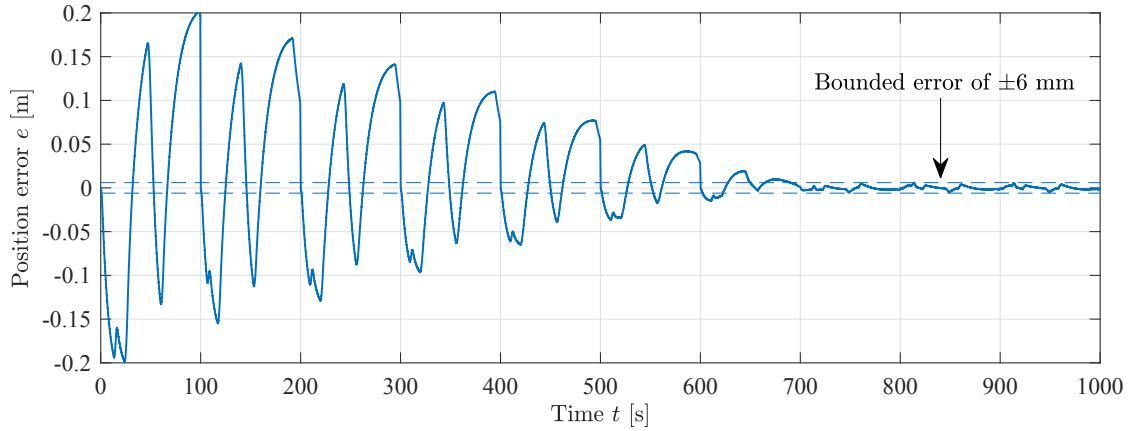

Figure 19. Cylinder position error during sign-sign feedforward simulation, $\gamma = 0.1\ \mathrm{m}^{-1}$.

The states z_{ff} for the sign-sign feedforward simulation are shown in Figure 20. The dashed lines show the theoretical values for a fixed feedforward gain. The same results can be seen here as with the MIT-rule, the states converge to values slightly larger than the theoretical ones, although convergence is slower with 700 s compared to 400 s.

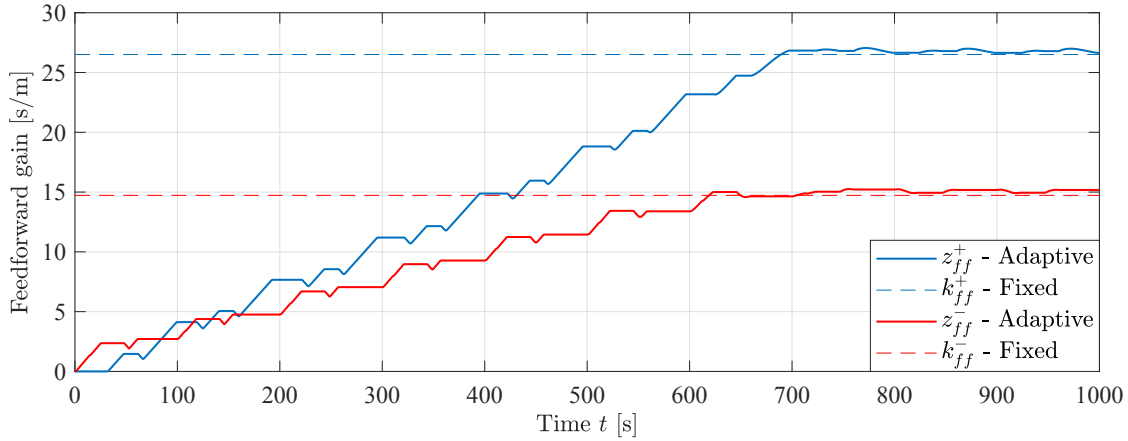

Figure 20. Feedforward states during sign-sign feedforward simulation, $\gamma = 0.1\ \mathrm{m}^{-1}$.

To show the difference in performance between the fixed gain controller and the adaptive controllers, a simulation with fixed gain feedforward has been made and compared with the MIT-rule feedforward at a simulation time where the states z_{ff} have converged, at $t = 800$ s. This is shown in Figure 21. It can be seen that the position error for the MIT-rule feedforward is lower compared to the fixed gain feedforward, showing that the MIT-rule feedforward controller outperforms the fixed gain controller even with an ideal model with correlation between cylinder velocity and feedforward gain.

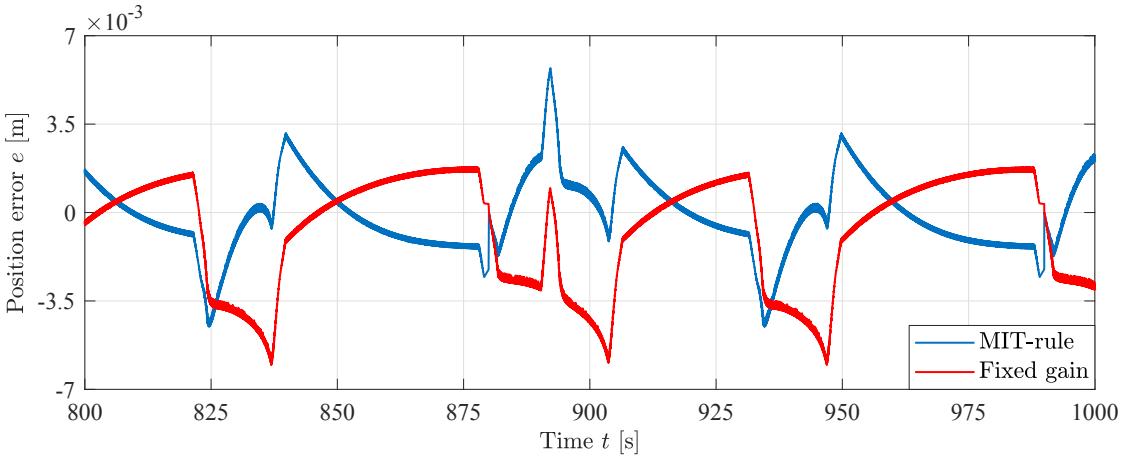

Figure 21. Position error comparison between MIT-rule and fixed gain feedforward in simulation.

The RMS position error for each controller after convergence of the states z_{ff} is shown in Table 3. Even though the fixed gain feedforward is based on an ideal model, the MIT-rule adaptive feedforward controller yields better position tracking with a 23% decrease in RMS position error. This shows the improved performance of the adaptive controller.

Table 3. Comparison of RMS position error after convergence in simulation.

	MIT-Rule	Sign-Sign	Fixed Gain
RMS error	1.6 mm	2.1 mm	2.1 mm

7. Experimental Results

The three controllers have been implemented on the CompactRIO controller in the laboratory. The control laws are implemented in discrete-time based on backward euler integration. A picture of the HMF 2020K4 loader crane in the laboratory is shown in Figure 22. The figure shows the crane in the starting position. During motion the knuckle boom is folded down.

There is some deadband in the valves on the HMF 2020K4 loader crane, and therefore deadband compensation has been implemented for the laboratory experiments. The identified deadbands for the knuckle boom valve are shown in Table 4.

Table 4. Identified deadbands for the knuckle boom valve.

Name	Parameter	Value
Out-stroke deadband	u^+	0.21
In-stroke deadband	u^-	−0.31

The equation for the deadband compensation is shown in Equation (28). By adding a small deadband $\tilde{u}$, it is ensured that the valve will be able to stay closed when no movement is needed.

$$\hat{u} = \begin{cases} u^+ + (1 - u^+) \cdot u, & u > \tilde{u} \\ u^- + (1 + u^-) \cdot u, & u < -\tilde{u} \\ 0, & \text{otherwise} \end{cases} \tag{28}$$

where

$\hat{u}$ = compensated control signal;
u = control signal;
u^+ = Out-stroke deadband;
u^- = In-stroke deadband;
$\tilde{u}$ = desired deadband, 0.001.

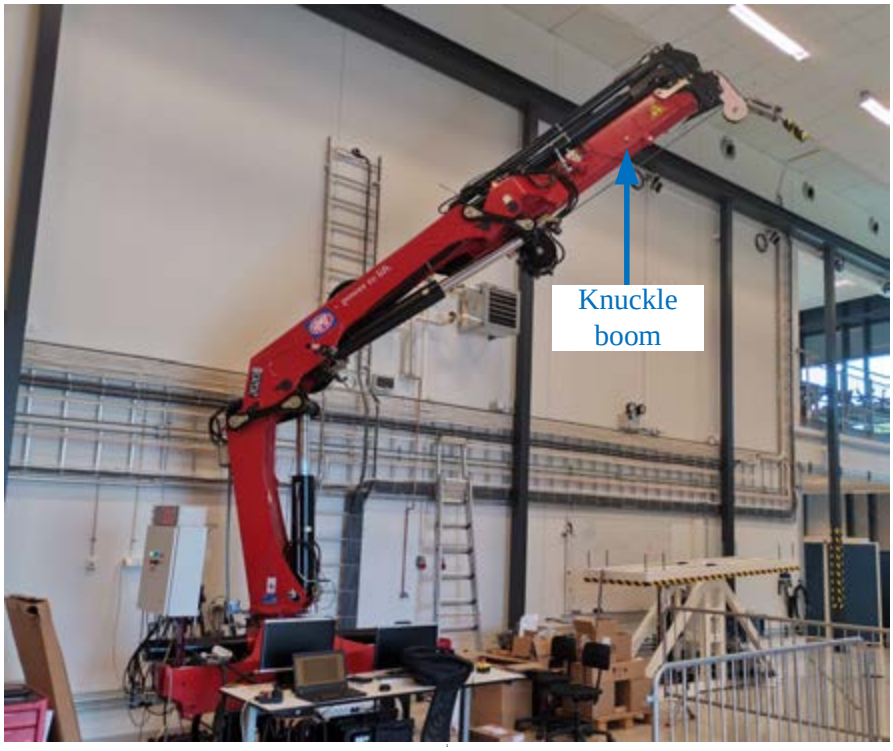

Figure 22. HMF 2020K4 loader crane in the laboratory.

The cylinder is running with a point-to-point path in actuator space equal to the simulations. The position error for the MIT-rule feedforward is shown in Figure 23. It is shown that the position error decreases towards a bounded error of ±14 mm. The RMS error after convergence is 5.2 mm. The convergence of the position error is similar to the simulations, showing that the proposed adaptive controller is feasible in a real world scenario, albeit with slightly larger position error.

The states z_{ff} for the MIT-rule feedforward experiment are shown in Figure 24. The dashed lines show the theoretical values for a fixed feedforward gain. The states converge to values that differ from the theoretical ones. The state z_{ff}^+ is higher than the theoretical, while the state z_{ff}^- is lower. This means that there exist some model uncertainties that the controller is able to adapt to. In addition, the ratio of the feedforward gains differs from the cylinder area ratio ϕ, i. e. $\frac{z_{ff}^-}{z_{ff}^+} \neq \frac{A_a}{A}$, showing the importance of using two separate feedforward states. Since the two states are not mathematically linked by the cylinder area ratio ϕ, they are able to converge to values that minimizes position error

in both directions of motion regardless of their ratio. This would not be possible if the traditional MIT-rule with a single state was used.

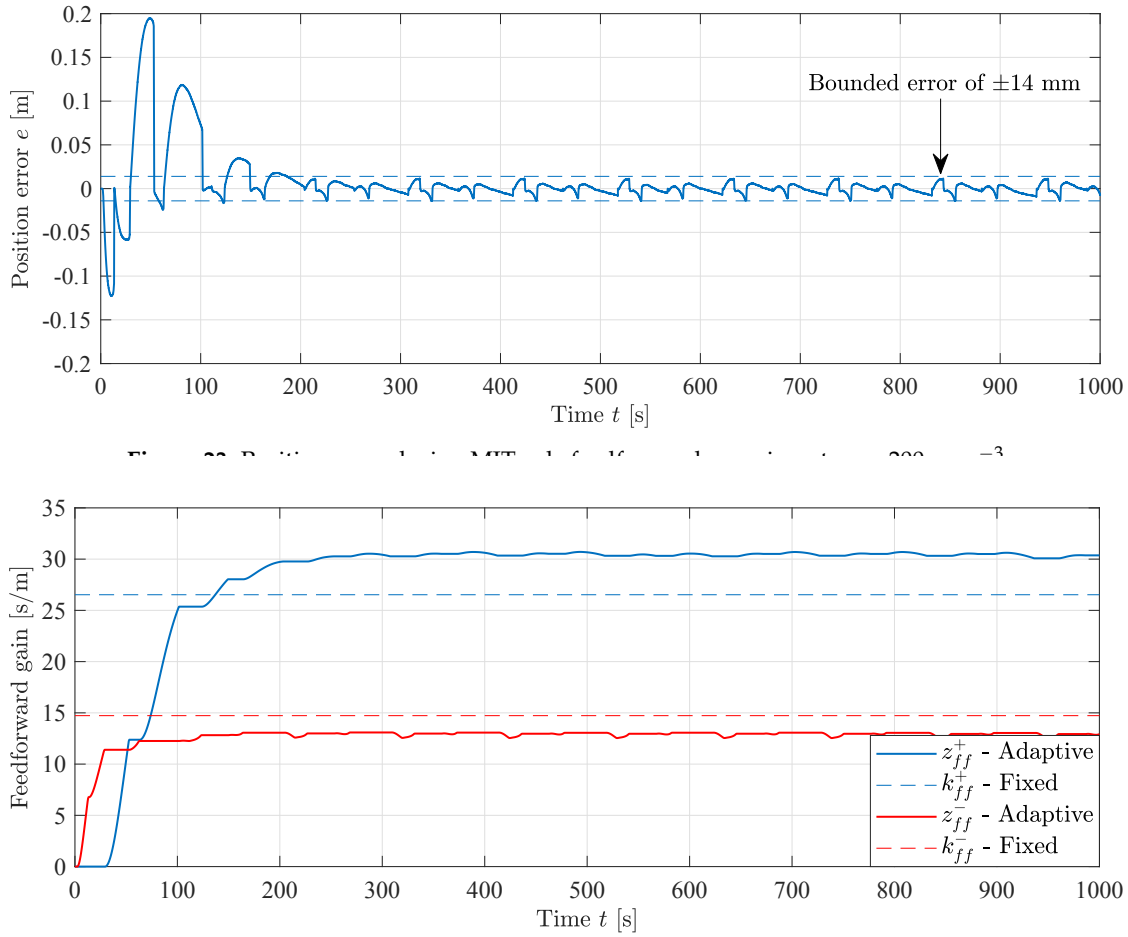

Figure 24. Feedforward states during MIT-rule feedforward experiment, $\gamma = 200\ \mathrm{s} \cdot \mathrm{m}^{-3}$.

The position error for the sign-sign feedforward is shown in Figure 25. The same bounded error of ±14 mm is shown. The RMS error after convergence is 5.3 mm.

The states z_{ff} for the sign-sign feedforward experiment are shown in Figure 26. Similar results can be seen here as with the MIT-rule, the states converge to values that differ from the theoretical ones. The dashed lines show the theoretical values for a fixed feedforward gain. The convergence is slower than the MIT-rule feedforward, and even though convergence speed is not critical, it may be a minor disadvantage compared to the MIT-rule feedforward.

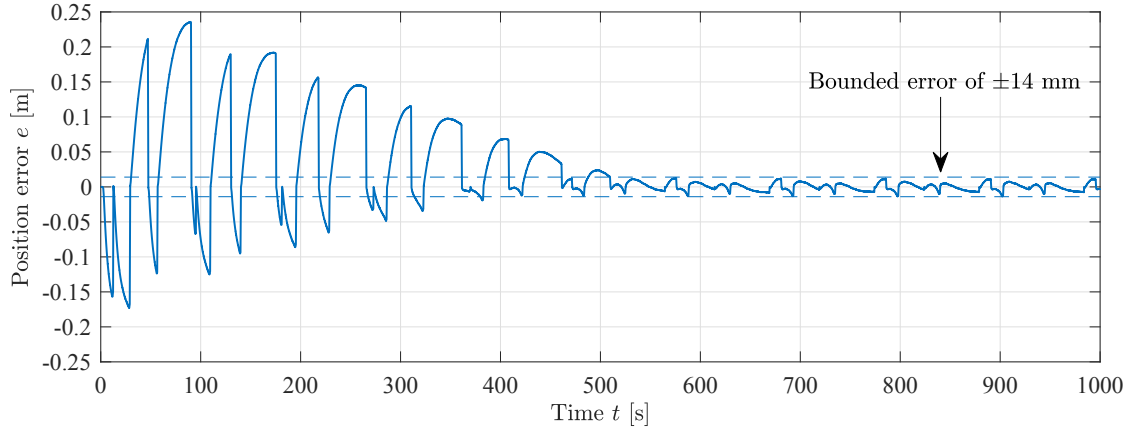

Figure 25. Position error during sign-sign feedforward experiment, $\gamma = 0.1\ \mathrm{m}^{-1}$.

The same comparison as in the simulations is made in the laboratory. An experiment with fixed gain feedforward has been made and compared with the MIT-rule feedforward at a time where the states z_{ff} have converged, at $t = 800$ s. Figure 27 shows the difference in performance between the fixed gain controller and the adaptive controller, where the position error for the MIT-rule feedforward is significantly lower compared to the fixed gain feedforward.

The RMS position error for each controller after convergence of the states z_{ff} is shown in Table 5. The two adaptive feedforward controllers yield excellent performance with an 80% decrease in RMS position error.

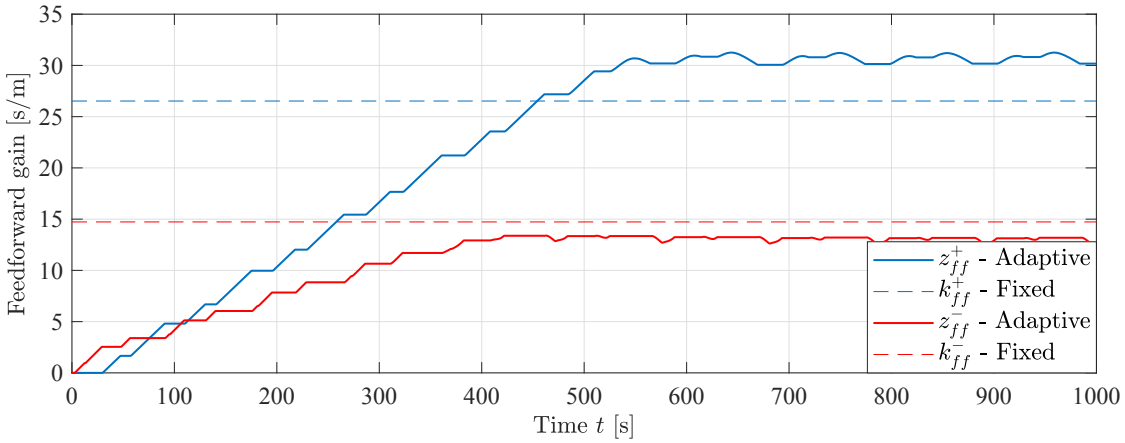

Figure 26. Feedforward states during sign-sign feedforward experiment, $\gamma = 0.1$ m^{-1}.

In general, the RMS position errors are slightly larger than in the simulations, but this is expected and can be attributed to the unmodeled flexibility of the crane, and other unmodeled dynamics. However, the advantage of the adaptive feedforward controller is clear. The independent adaptation of the out-stroke and in-stroke states z_{ff}^{+} and z_{ff}^{-} provides significantly increased performance on a physical system with model uncertainties.

Table 5. Comparison of RMS position error after convergence in experiment.

	MIT-Rule	Sign-Sign	Fixed Gain
RMS error	5.2 mm	5.3 mm	24.9 mm

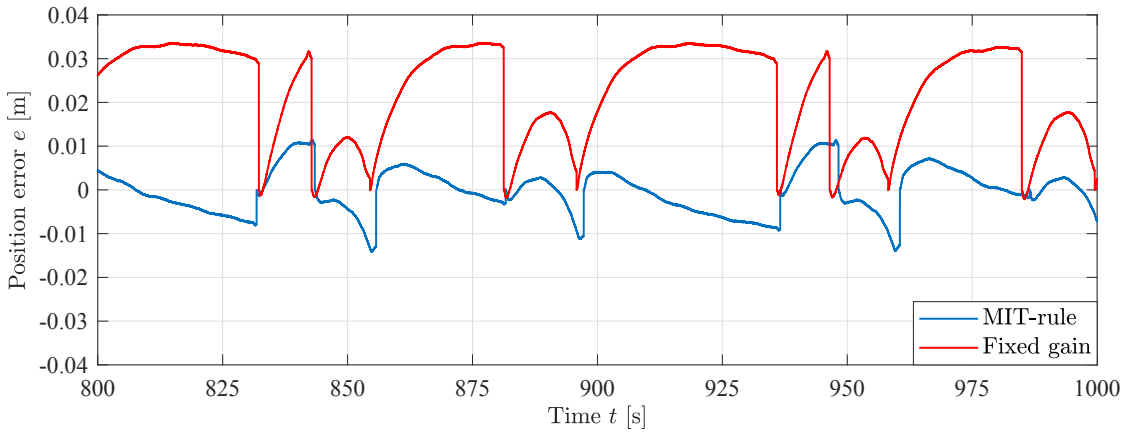

Figure 27. Position error with fixed and adaptive gains.

8. Conclusions

In this paper two adaptive feedforward motion controllers are designed, simulated, evaluated, implemented and experimentally verified on a loader crane with hydraulic differential cylinders. The controllers are based on common and proven adaptation methods to extend a typical electro-hydraulic motion control system into a novel adaptive feedforward motion controller. One of the challenges associated with a differential cylinder, namely the jump in both velocity and force gain when changing sign of direction, is solved by creating two separate feedforward states for out-stroke and in-stroke motion of the hydraulic differential cylinder, respectively. This separation makes the controller able to adapt to model uncertainties where the ratio between the in-stroke and out-stroke feedforward gains is not equal to the cylinder area ratio ϕ. Adaptation of the feedforward states only occurs when the hydraulic cylinder is moving in the direction of motion associated with the feedforward state.

Simulation results show high performance with good position tracking and that the states z_{ff} converge to values slightly higher than the theoretical ones. The cylinder position error is lowest for the MIT-rule controller with an RMS error of 1.6 mm, and shows faster convergence than the sign-sign controller. Compared to a fixed gain feedforward controller, where the gain is equal to the ratio of valve opening to cylinder velocity, the RMS error is reduced by 23%, showing the improved performance of the novel adaptive feedforward controllers.

Experiments in the laboratory show even better results than in the simulations. The adaptive feedforward controllers converge and show good position tracking, while the MIT-rule feedforward converges faster than the sign-sign feedforward. Compared to a fixed gain feedforward, the RMS position error is reduced by 80% to 5.2 mm for the MIT-rule. The results show the feasabillty of the novel adaptive feedforward controllers on a physical system. In addition, the differential structure of the controllers shows its advantage, as the ratio of the feedforward states converges to values different than the cylinder area ratio ϕ, showing the excellent performance of the adaptive feedforward controller and its capability of handling model uncertainties in both directions of motion.

Future work may include stability analysis of the adaptive controllers, since the feedforward gains are dependent on feedback of the cylinder position error e. The effects of the adaptation gain γ may also be investigated to see if there exists an upper boundary where the system becomes unstable.

Author Contributions: Conceptualization, K.J.J., M.K.E. and M.R.H.; methodology, K.J.J.; software, K.J.J.; validation, K.J.J.; formal analysis, K.J.J.; investigation, K.J.J.; data curation, K.J.J.; writing–original draft preparation, K.J.J.; writing–review and editing, K.J.J., M.K.E. and M.R.H.; visualization, K.J.J.; supervision, M.K.E. and M.R.H. All authors have read and agreed to the published version of the manuscript.

Funding: This research was funded by the Norwegian Ministry of Education and Research grant number 155597. The APC was funded by the University of Agder.

Conflicts of Interest: The authors declare no conflict of interest.

References

1. Bak, M.K.; Hansen, M.R. Analysis of Offshore Knuckle Boom Crane—Part Two: Motion Control. *Model. Identif. Control.* **2013**, *34*, 175–181. [CrossRef]
2. Mareels, I.M.; Anderson, B.D.; Bitmead, R.R.; Bodson, M.; Sastry, S.S. Revisiting the Mit Rule for Adaptive Control. *IFAC Proc. Vol.* **1987**, *20*, 161–166. [CrossRef]
3. Lucky, R.W. Techniques for adaptive equalization of digital communication systems. *Bell Syst. Tech. J.* **1966**, *45*, 255–286. [CrossRef]
4. Widrow, B. Adaptive sampled-data systems. *IFAC Proc. Vol.* **1960**, *1*, 433–439. [CrossRef]
5. Widrow, B.; Hoff, M.E. Adaptive Switching Circuits. *1960 IRE Wescon Conv. Rec.* **1960**, 96–104.
6. Unbehauen, H. Theory and Application of Adaptive Control. *IFAC Proc. Vol.* **1985**, *18*, 1–17. [CrossRef]
7. Truxal, J.G. Adaptive control. *IFAC Proc. Vol.* **1963**, *1*, 386–392. [CrossRef]
8. Strietzel, R.; Töpfer, H. Feedforward Adaption to Control Processes in Chemical Engineering. *IFAC Proc. Vol.* **1985**, *18*, 115–120. [CrossRef]

9. M'Saad, M.; Duque, M.; Landau, I. Robust LQ Adaptive Controller for Industrial Processes. *IFAC Proc. Vol.* **1985**, *18*, 91–97. [CrossRef]
10. Unbehauen, H.D. Adaptive Systems for Process Control. *IFAC Proc. Vol.* **1986**, *19*, 15–23. [CrossRef]
11. Oh, B.; Jamshidi, M.; Seraji, H. Two Adaptive Control Structures of Robot Manipulators. *IFAC Proc. Vol.* **1989**, *22*, 371–377. [CrossRef]
12. Van den Bossche, E.; Dugard, L.; Landau, I. Adaptive Control of a Flexible Arm. *IFAC Proc. Vol.* **1987**, *20*, 271–276. [CrossRef]
13. Tsakalis, K.; Ioannou, P. Adaptive control of linear time-varying plants. *Automatica* **1987**, *23*, 459–468. [CrossRef]
14. Huŝek, P. Adaptive fuzzy sliding mode control for uncertain nonlinear systems. *IFAC Proc. Vol.* **2014**, *47*, 540–545. [CrossRef]
15. Sato, K.; Tsuruta, K. Adaptive Friction Compensation for Linear Slider with adaptive differentiator. *IFAC Proc. Vol.* **2010**, *43*, 467–472. [CrossRef]
16. Lee, R.M.; Chen, T.C. Adaptive Control of Active Magnetic Bearing against Milling Dynamics. *Appl. Sci* **2016**, *6*, 52. [CrossRef]
17. Yang, G.; Yao, J.; Le, G.; Ma, D. Adaptive integral robust control of hydraulic systems with asymptotic tracking. *Mechatronics* **2016**, *40*, 78–86. [CrossRef]
18. Nicol, C.; Macnab, C.; Ramirez-Serrano, A. Robust adaptive control of a quadrotor helicopter. *Mechatronics* **2011**, *21*, 927–938. [CrossRef]
19. Agarwal, R.K.; Hussain, I.; Singh, B. LMF-Based Control Algorithm for Single Stage Three-Phase Grid Integrated Solar PV System. *IEEE Trans. Sustain. Energy* **2016**, *7*, 1379–1387. [CrossRef]
20. Krus, P.; Palmberg, J.O. Vector Control of a Hydraulic Crane. *Int. Off Highw. Powerpl. Congr. Expo.* **1992**. [CrossRef]
21. Sørensen, J.K.; Hansen, M.R.; Ebbensen, M.K. Boom Motion Control Using Pressure Control Valve. In Proceedings of the 8th FPNI Ph.D Symposium on Fluid Power, Lappeenranta, Finland, 11–13 June 2014. [CrossRef]
22. Sørensen, J.K.; Hansen, M.R.; Ebbesen, M.K. Load Independent Velocity Control on Boom Motion Using Pressure Control Valve. In Proceedings of the Fourteenth Scandinavian International Conference on Fluid Power, Tampere, Finland, 20–22 May 2015.
23. Beiner, L. Identification and Control of a Hydraulic Forestry Crane. *Mechatronics* **1997**, *7*, 537–547. [CrossRef]
24. Mattila, J.; Virvalo, T. Energy-efficient Motion Control of a Hydraulic Manipulator. In Proceedings of the 2000 IEEE International Conference on Robotics and Automation, San Francisco. CA, USA, 24–28 April 2000. [CrossRef]
25. Zhang, Q. Hydraulic Linear Actuator Velocity Control Using a Feedforward-plus-PID Control. *Int. J. Flex. Autom. Integr. Manuf.* **1999**, *7*, 277–292.
26. Jensen, K.J.; Kjeld Ebbesen, M.; Rygaard Hansen, M. Development of Point-to-Point Path Control in Actuator Space for Hydraulic Knuckle Boom Crane. *Actuators* **2020**, *9*, 27. [CrossRef]

Publisher's Note: MDPI stays neutral with regard to jurisdictional claims in published maps and institutional affiliations.

© 2020 by the authors. Licensee MDPI, Basel, Switzerland. This article is an open access article distributed under the terms and conditions of the Creative Commons Attribution (CC BY) license (http://creativecommons.org/licenses/by/4.0/).

Paper C

Anti-swing control of a hydraulic loader crane with a hanging load

This paper has been published as:

Jensen, K.J.; Kjeld Ebbesen, M.; Rygaard Hansen, M. Anti-swing control of a hydraulic loader crane with a hanging load. *Mechatronics* **2021**, 77, 102599. doi:10.1016/j.mechatronics.2021.102599

Mechatronics 77 (2021) 102599

Contents lists available at ScienceDirect

Mechatronics

journal homepage: www.elsevier.com/locate/mechatronics

Anti-swing control of a hydraulic loader crane with a hanging load ☆

Konrad Johan Jensen *, Morten Kjeld Ebbesen, Michael Rygaard Hansen

Department of Engineering Sciences, University of Agder, 4879 Grimstad, Norway

ARTICLE INFO

Keywords:
Loader crane
Anti-swing
Hydraulics
Kinematics
Feedforward

ABSTRACT

In this paper, anti-swing control for a hydraulic loader crane is presented. The difference between hydraulic and electric cranes are discussed to show the challenges associated with hydraulic actuation. The hanging load dynamics and relevant kinematics of the crane are derived to create the 2-DOF anti-swing controller. The anti-swing controller is added to the electro-hydraulic motion controller via feedforward. A dynamic simulation model of the crane is made, and the control system is evaluated in simulations with a path controller in actuator space. Simulation results show significant reduction in the load swing angle during motion. Experiments are carried out to verify the performance of the anti-swing controller, showing good suppression of the payload angle in practice.

1. Introduction

Anti-swing control is an extensively studied topic, with applications to cranes and hoists in factories, shipyards, and warehouses etc. However, any non-stationary lifting equipment will induce undesirable load swing in the hanging load when moving. This load swing can increase cycle times, reduce efficiency, and in the worst case lead to safety hazards and accidents. Various techniques have been tested to suppress load swing. This is a difficult task, as systems with hanging loads are underactuated, meaning the degrees of freedom are greater than the number of controlled actuators.

Typically the anti-swing controllers are implemented on electric overhead cranes, where one or several servomotors control the translational motion of the crane. The control system typically consists of two feedback controllers, one controlling the position of the crane and the other controlling the load swing. Early work on anti-swing control of overhead cranes includes [1–4], where linearized models are utilized. More advanced control systems including fuzzy logic, sliding mode, and robust control can be found in [5–16], where a nonlinear model of the crane is often used.

A method that can be used both for anti-swing and vibration reduction in flexible systems is input shaping. Based on system dynamics, for example bandwidth and damping ratio, an input signal is designed to be self-canceling [17–19].

Another similar method is called delayed reference control. In this case the reference generator is time shifted based on the measured payload angle [20,21].

Anti-swing control for hydraulic cranes is not an extensively studied area, but references include [22] which investigates tool-point control and anti-swing for a planar hydraulic crane.

For this paper, a hydraulic loader crane is considered, shown in Fig. 2. In this case the load is hanging from the crane tip, instead of the trolley of an overhead crane. Many hydraulic cranes use pressure compensated valves, which give a load independent velocity control for each actuator. For closed loop control systems, the load independent velocity control can be utilized in a control system using feedforward [23,24]. In this case, both a position reference and a velocity reference are generated in the control system. An example of a typical closed loop electro-hydraulic motion control system with feedforward (FF) and feedback (FB) is shown in Fig. 1.

The focus of this paper is on how to design anti-swing control for hydraulically actuated cranes. This paper presents a novel anti-swing controller which utilizes load independent velocity control in combination with kinematic transformations. Based on this, the novel method provides reference motion for the individual hydraulic degrees of freedom by combining contributions from a path controller and an anti-swing controller.

2. Considered system

In this paper an HMF 2020K4 loader crane is used as a case study for modeling, simulation, and experiments. Fig. 2 shows the main components of the HMF 2020K4 loader crane. Both the main cylinder and knuckle cylinder are used to compensate for the hanging

☆ This paper was recommended for publication by Associate Editor Peter Hehenberger.

* Corresponding author.
E-mail addresses: konrad.j.jensen@uia.no (K.J. Jensen), morten.k.ebbesen@uia.no (M.K. Ebbesen), michael.r.hansen@uia.no (M.R. Hansen).

https://doi.org/10.1016/j.mechatronics.2021.102599
Received 25 January 2021; Received in revised form 3 May 2021; Accepted 6 June 2021
Available online 20 June 2021
0957-4158/© 2021 The Author(s). Published by Elsevier Ltd. This is an open access article under the CC BY license (http://creativecommons.org/licenses/by/4.0/).

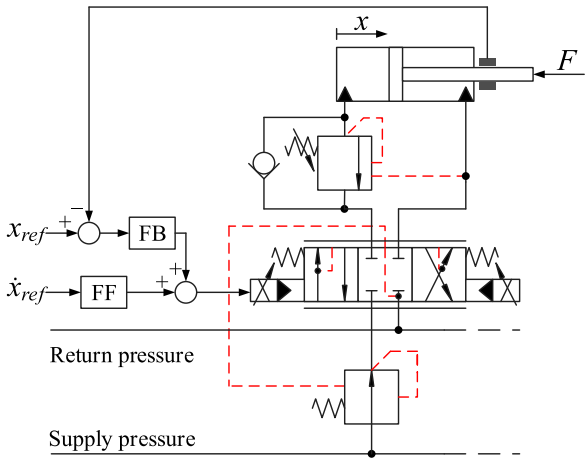

Fig. 1. Electro-hydraulic motion control system with feedforward.

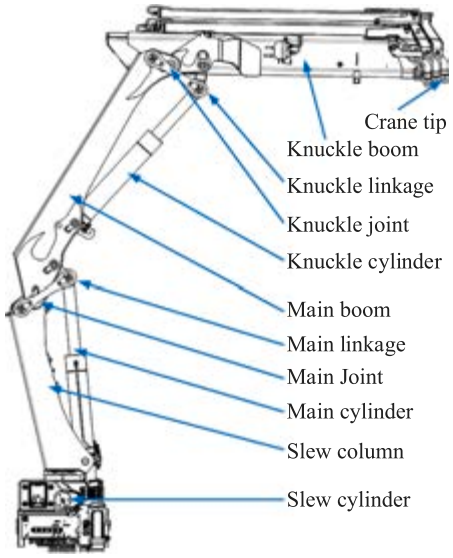

Fig. 2. Main components of the considered crane.

load dynamics. The relevant data for the main cylinder and knuckle cylinder are shown in Table 1. Each actuator is controlled via a pressure compensated proportional directional valve which ensures load independent flow control of the actuators. Counterbalance valves are also used for load holding, assisting in lowering of the booms, and pressure relief of pressure surges. An illustration of the hydraulic system for the knuckle cylinder is shown in Fig. 3. Fig. 4 shows the hanging load definitions along with the main boom angle θ_m, knuckle boom angle θ_k, and payload angle θ_p.

2.1. Difference from electric overhead cranes

Since research in anti-swing control of electric overhead cranes is an extensively studied subject, the differences between electric and hydraulic cranes are discussed in this section.

The difference in actuation is clear, an electric motor exerts a torque on the load based the motor current, while the hydraulic cylinder exerts a force on the load based on the hydraulic pressure. For some hydraulic systems, including the HMF 2020K4 loader crane, the pressure compensator senses the load pressure and automatically adjusts the pressure drop over the control valve to give load independent flow control. As a result, the hydraulic system is able to control the velocity of the load

Table 1
Data for the main cylinder and knuckle cylinder.

Description	Name	Value
Main piston diameter	$D_{p,m}$	0.16 m
Main piston area	A_m	0.0201 m^2
Main rod diameter	$D_{r,m}$	0.1 m
Main annulus area	$A_{a,m}$	0.0123 m^2
Main piston area ratio	$\phi_m = \frac{A_{a,m}}{A_m}$	0.6094
Main valve maximum flow	$Q_{max,m}$	40 l/min
Knuckle piston diameter	$D_{p,k}$	0.15 m
Knuckle piston area	A_k	0.0177 m^2
Knuckle rod diameter	$D_{r,k}$	0.1 m
Knuckle annulus area	$A_{a,k}$	0.0098 m^2
Knuckle piston area ratio	$\phi_k = \frac{A_{a,k}}{A_k}$	0.5556
Knuckle valve maximum flow	$Q_{max,k}$	40 l/min

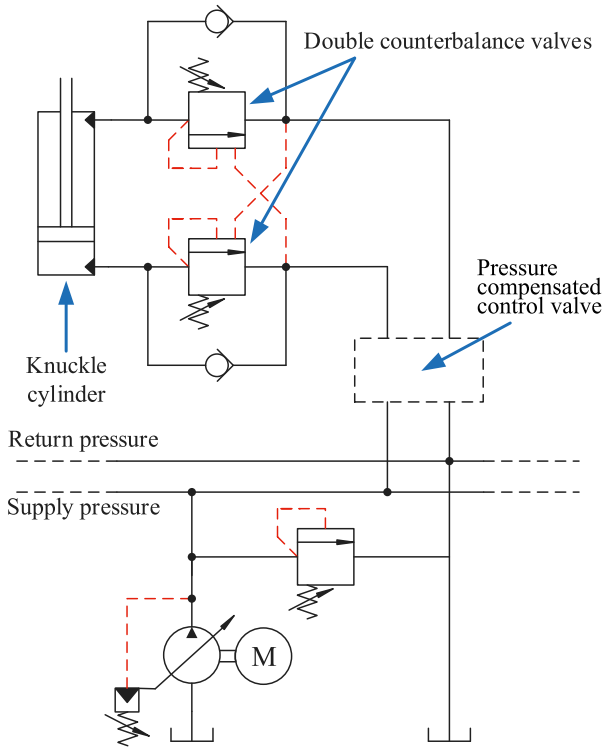

Fig. 3. Hydraulic circuit for the knuckle cylinder..

directly, whereas the electric system controls the force applied to the load.

Fig. 5 illustrates a typical overhead crane where the hanging load is connected to a trolley. The trolley is only able to move in the x-direction, and the electric motor exerts a force F_{motor} on the trolley through the wheels. The applied force affects both the trolley motion and payload motion, and is used to control the position along the x-axis as well as the payload angle θ_p.

2.2. Control strategy

The control strategy suggested in this paper is shown in Fig. 6. This control strategy is useful for any hydraulically actuated manipulator with a tool point and a number of joint angles controlled by means of hydraulic cylinders. This constitute a wide variety of load handling machinery. The main task is position control of the tool point and, classically, this may be combined with a velocity feedforward term. Feedback control is most easily implemented with reference to the actuator motion [25]. Therefore, inverse kinematics is employed to transfer from tool point coordinates via joint coordinates to actuator

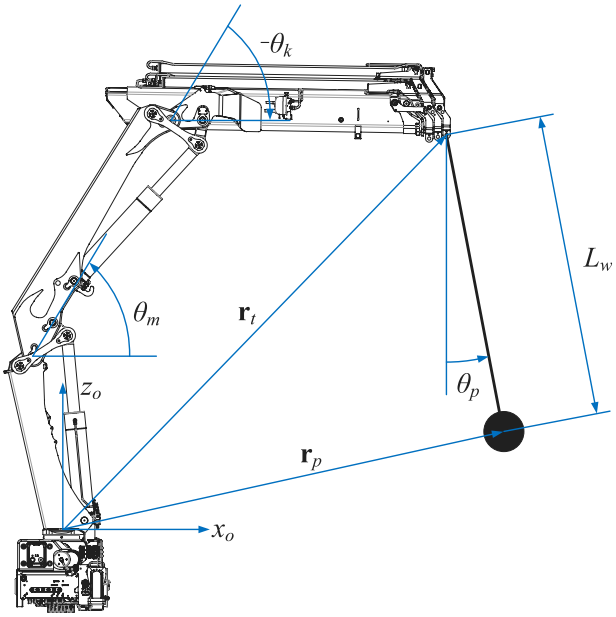

Fig. 4. Definitions of crane tip and hanging load geometries.

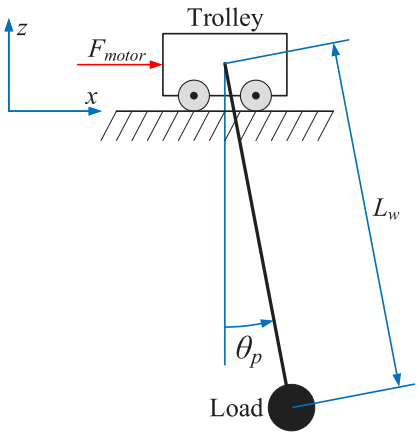

Fig. 5. Typical overhead crane with hanging load.

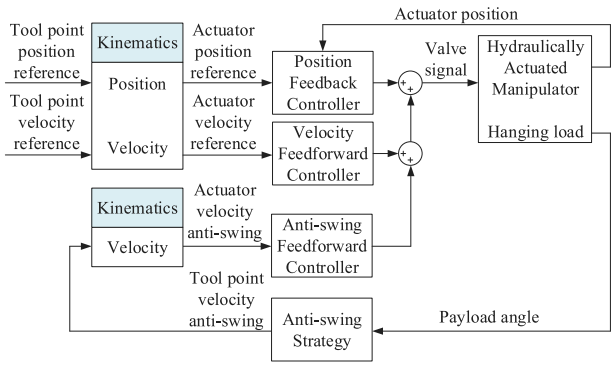

Fig. 6. Anti-swing control strategy.

coordinates. The anti-swing effort is introduced in parallel with the feedforward term, but is computed with the purpose of counteracting the continuously measured payload angle by adjusting the tool point velocity. Therefore, the anti-swing effort also requires a kinematic transformation into actuator space.

Fig. 7. 2D view of the crane model in MATLAB Simscape™.

The proposed control strategy can be implemented in several ways. In general, any tool point reference motion will be either 2-dimensional or 3-dimensional. For the 2-dimensional case, a minimum of two actuators is required, however, more may be employed yielding some degree of redundancy that can be handled by means of optimization within the null-space, see [26].

In this paper, only 2-dimensional motion is considered leaving four different possible combinations:

1. Main boom actuator and knuckle boom actuator
2. Main boom actuator and telescope actuator
3. Knuckle boom actuator and telescope actuator
4. Main boom actuator, knuckle boom actuator and telescope actuator.

To illustrate the presented control strategy, the necessary kinematic transformations together with the anti swing strategy have been developed and implemented for case 1.

3. System modeling

A dynamic model of the crane has been made in MATLAB Simscape™. 3D CAD models have been imported into the model using the Multibody library, and the hydraulic system has been modeled using the hydraulic library. A side view of the crane in the simulation model is shown in Fig. 7.

3.1. Hanging load dynamics

To derive the equations of motion for the hanging load using the payload angle θ_p, the Euler–Lagrange equations are used. For the following equations, the notation $s_{\theta_p} = \sin(\theta_p)$, $c_{\theta_p} = \cos(\theta_p)$ is used. With the boom tip position defined as $\mathbf{r}_t = [x_t \; z_t]^T$, the payload position can be calculated as follows.

$$\mathbf{r}_p = \mathbf{r}_t + L_w \cdot \begin{bmatrix} s_{\theta_p} \\ -c_{\theta_p} \end{bmatrix} \tag{1}$$

Assuming constant wire length, the payload velocity can be calculated by taking the time derivative of the payload position, shown in Eq. (2).

$$\dot{\mathbf{r}}_p = \dot{\mathbf{r}}_t + L_w \cdot \dot{\theta}_p \cdot \begin{bmatrix} c_{\theta_p} \\ s_{\theta_p} \end{bmatrix} \tag{2}$$

The Lagrangian $\mathcal{L}$ of the system is defined as the kinetic energy minus the potential energy, and is shown in Eq. (3).

$$\mathcal{L} = \mathcal{K} - \mathcal{P} \tag{3}$$

The kinetic energy of the payload is:

$$\mathcal{K} = \frac{1}{2} \cdot m_p \cdot \dot{\mathbf{r}}_p^T \cdot \dot{\mathbf{r}}_p \tag{4}$$

The potential energy of the payload is:

$$\mathcal{P} = m_p \cdot g \cdot \left(z_t - L_w \cdot c_{\theta_p} \right) \tag{5}$$

The total Lagrangian of the payload is then calculated in Eq. (6).

$$\begin{aligned} \mathcal{L} = {} & \frac{1}{2} \cdot m_p \cdot \left(\dot{x}_t^2 + L_w^2 \cdot \dot{\theta}_p^2 + 2 \cdot \dot{x}_t \cdot L_w \cdot \dot{\theta}_p \cdot c_{\theta_p} \right. \\ & \left. + \dot{z}_t^2 + 2 \cdot \dot{z}_t \cdot L_w \cdot \dot{\theta}_p \cdot s_{\theta_p} \right) \\ & - m_p \cdot g \cdot \left(z_t - L_w \cdot c_{\theta_p} \right) \end{aligned} \tag{6}$$

The equation of motion of the payload described by the coordinate θ_p is given by the Euler–Lagrange equation below.

$$\frac{d}{dt} \frac{\partial \mathcal{L}}{\partial \dot{\theta}_p} - \frac{\partial \mathcal{L}}{\partial \theta_p} = 0 \tag{7}$$

Some intermediate equations are then used to solve the Euler–Lagrange equation. They are shown in Eqs. (8)–(11).

$$\begin{aligned} \frac{\partial \mathcal{L}}{\partial \theta_p} = {} & m_p \cdot \left(-\dot{x}_t \cdot L_w \cdot \dot{\theta}_p \cdot s_{\theta_p} \right. \\ & \left. + \dot{z}_t \cdot L_w \cdot \dot{\theta}_p \cdot c_{\theta_p} - g \cdot L_w \cdot s_{\theta_p} \right) \end{aligned} \tag{8}$$

$$\frac{\partial \mathcal{L}}{\partial \dot{\theta}_p} = m_p \cdot \left(L_w^2 \cdot \dot{\theta}_p + \dot{x}_t \cdot L_w \cdot c_{\theta_p} + \dot{z}_t \cdot L_w \cdot s_{\theta_p} \right) \tag{9}$$

$$\begin{aligned} \frac{d}{dt} \frac{\partial \mathcal{L}}{\partial \dot{\theta}_p} = {} & m_p \cdot \left(L_w^2 \cdot \ddot{\theta}_p + \ddot{x}_t \cdot L_w \cdot c_{\theta_p} - \dot{x}_t \cdot L_w \cdot \dot{\theta}_p \cdot s_{\theta_p} \right. \\ & \left. + \ddot{z}_t \cdot L_w \cdot s_{\theta_p} + \dot{z}_t \cdot L_w \cdot \dot{\theta}_p \cdot c_{\theta_p} \right) \end{aligned} \tag{10}$$

$$\begin{aligned} \frac{d}{dt} \frac{\partial \mathcal{L}}{\partial \dot{\theta}_p} - \frac{\partial \mathcal{L}}{\partial \theta_p} = {} & m_p \cdot \left(L_w^2 \cdot \ddot{\theta}_p + \ddot{x}_t \cdot L_w \cdot c_{\theta_p} \right. \\ & \left. + \ddot{z}_t \cdot L_w \cdot s_{\theta_p} + g \cdot L_w \cdot s_{\theta_p} \right) \end{aligned} \tag{11}$$

The Euler–Lagrange equation can then be solved with respect to $\ddot{\theta}_p$ to give the describing differential equation of the payload, shown in Eq. (12). It is clear that the payload angle is dependent on the motion in both x- and z-direction, facilitating 2-DOF anti-swing control. The impact of the wire length L_w is also prominent, allowing for gain scheduling in the controller.

$$\ddot{\theta}_p = \frac{1}{L_w} \cdot \left(-\ddot{x}_t \cdot c_{\theta_p} - \ddot{z}_t \cdot s_{\theta_p} - g \cdot s_{\theta_p} \right) \tag{12}$$

3.2. Joint space kinematics

The joint space kinematics describes the relation between the joint angles and Cartesian coordinates of the crane tip. Fig. 8 shows the geometry which is used with the Denavit–Hartenberg parameters, where both booms are horizontal. The distances between consecutive joints are shown in Table 2. The Denavit–Hartenberg parameters are shown in Table 3, where **R** and **T** are rotational and translational matrices, respectively. The angles θ_m and θ_k denote the rotation about the main joint and knuckle joint, respectively.

The transformation matrix $\mathbf{A}_{DH}$ from the base of the crane to the tip of the crane can be established as a sequence of transformations based on the Denavit–Hartenberg parameters, shown in Eq. (13).

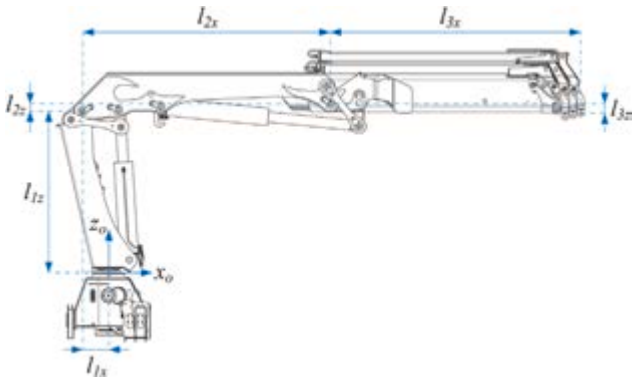

Fig. 8. Crane geometry used with Denavit–Hartenberg parameters.

Table 2
Coordinates shown in Fig. 8.

Name	Length [m]
l_{1x}	0.250
l_{1z}	1.569
l_{2x}	2.400
l_{2z}	0.070
l_{3x}	2.429
l_{3z}	0.093

Table 3
Denavit–Hartenberg parameters.

R_z	T_z	T_x	R_x
0	l_{1z}	$-l_{1x}$	90°
θ_m	0	0	−90°
0	l_{2z}	l_{2x}	90°
θ_k	0	0	−90°
0	$-l_{3z}$	l_{3x}	0

$$\begin{aligned} \mathbf{A}_{DH} = {} & \mathbf{T}_z(l_{1z}) \cdot \mathbf{T}_x(-l_{1x}) \cdot \mathbf{R}_x(90°) \cdot \mathbf{R}_z(\theta_m) \\ & \cdot \mathbf{R}_x(-90°) \cdot \mathbf{T}_z(l_{2z}) \cdot \mathbf{T}_x(l_{2x}) \cdot \mathbf{R}_x(90°) \\ & \cdot \mathbf{R}_z(\theta_k) \cdot \mathbf{R}_x(-90°) \cdot \mathbf{T}_z(-l_{3z}) \cdot \mathbf{T}_x(l_{3x}) \end{aligned} \tag{13}$$

The final matrix $\mathbf{A}_{DH}$ is shown in Eq. (14).

$$\mathbf{A}_{DH} = \begin{bmatrix} c_{\theta_m+\theta_k} & 0 & -s_{\theta_m+\theta_k} & x_t \\ 0 & 1 & 0 & 0 \\ s_{\theta_m+\theta_k} & 0 & c_{\theta_m+\theta_k} & z_t \\ 0 & 0 & 0 & 1 \end{bmatrix} \tag{14}$$

$$\begin{aligned} x_t = {} & -l_{1x} + l_{2x} \cdot c_{\theta_m} - l_{2z} \cdot s_{\theta_m} \\ & + l_{3x} \cdot c_{\theta_m+\theta_k} + l_{3z} \cdot s_{\theta_m+\theta_k} \end{aligned} \tag{15}$$

$$\begin{aligned} z_t = {} & l_{1z} + l_{2x} \cdot s_{\theta_m} + l_{2z} \cdot c_{\theta_m} \\ & + l_{3x} \cdot s_{\theta_m+\theta_k} - l_{3z} \cdot c_{\theta_m+\theta_k} \end{aligned} \tag{16}$$

The joint kinematics from the crane base to the crane tip are now contained in x_t and z_t.

To find the correlation between the desired crane tip velocities and the joint velocities, the inverse Jacobian matrix must be defined. The correlation between crane tip velocities and joint velocities is shown in Eqs. (17) and (18).

$$\begin{bmatrix} \dot{x}_t \\ \dot{z}_t \end{bmatrix} = \mathbf{J} \cdot \begin{bmatrix} \dot{\theta}_m \\ \dot{\theta}_k \end{bmatrix} \tag{17}$$

$$\begin{bmatrix} \dot{\theta}_m \\ \dot{\theta}_k \end{bmatrix} = \mathbf{J}^{-1} \cdot \begin{bmatrix} \dot{x}_t \\ \dot{z}_t \end{bmatrix} \tag{18}$$

First, the Jacobian matrix is defined as the partial derivative of the crane tip position with respect to the joint angles, shown in Eq. (19).

$$\mathbf{J} = \begin{bmatrix} \frac{\partial}{\partial \theta_m}(x_t) & \frac{\partial}{\partial \theta_k}(x_t) \\ \frac{\partial}{\partial \theta_m}(z_t) & \frac{\partial}{\partial \theta_k}(z_t) \end{bmatrix} \tag{19}$$

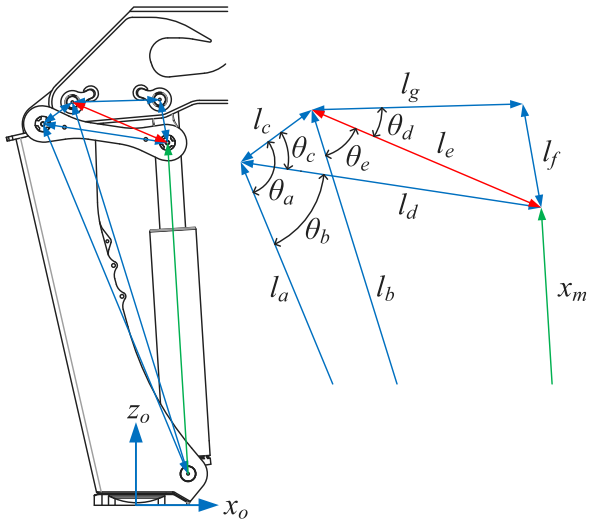

Fig. 9. Geometry of the linkage system for the main joint.

Table 4
Lengths of the main linkage.

Name	Length [m]
l_a	1.473
l_b	1.514
l_c	0.143
l_d	0.490
l_f	0.170
l_g	0.340

Inverting the Jacobian matrix yields the solution for the joint velocities, shown in Eqs. (20)–(22). The full calculations are shown in Appendix A.

$$\mathbf{J}^{\dagger} \triangleq \mathbf{J}^{-1} = \begin{bmatrix} J_{11}^{\dagger} & J_{12}^{\dagger} \\ J_{21}^{\dagger} & J_{22}^{\dagger} \end{bmatrix} \tag{20}$$

$$\dot{\theta}_m = J_{11}^{\dagger} \cdot \dot{x}_t + J_{12}^{\dagger} \cdot \dot{z}_t \tag{21}$$

$$\dot{\theta}_k = J_{21}^{\dagger} \cdot \dot{x}_t + J_{22}^{\dagger} \cdot \dot{z}_t \tag{22}$$

3.3. Actuator space kinematics

The actuator space kinematics describes the relation between the cylinder lengths and joint angles, where the joint angles are functions of the cylinder lengths, $\theta_m(x_m)$ and $\theta_k(x_k)$. Fig. 9 shows the geometry of the linkage system for the main joint. The coordinate x_m is the length of the hydraulic cylinder, and the length l_e is an intermediate length to help derive the actuator space kinematics. The lengths of the main linkage system are shown in Table 4.

The calculations of the actuator space kinematics are based on the law of cosines, since the linkage contains five triangles when the intermediate length l_e is introduced. An offset angle $\tilde{\theta}_m = 1.3$ rad is subtracted from the joint angle θ_m to ensure that the main boom is horizontal when $\theta_m = 0$. The calculations are shown in Eqs. (23)–(28), and the main joint angle θ_m is defined in Eq. (29). The calculations for the knuckle joint are given in Appendix B.

$$\theta_a = \arccos\left(\frac{l_a^2 + l_c^2 - l_b^2}{2 \cdot l_a \cdot l_c}\right) \tag{23}$$

$$\theta_b = \arccos\left(\frac{l_a^2 + l_d^2 - x_m^2}{2 \cdot l_a \cdot l_d}\right) \tag{24}$$

$$\theta_c = \theta_a - \theta_b \tag{25}$$

$$l_e = \sqrt{l_c^2 + l_d^2 - 2 \cdot l_c \cdot l_d \cdot c_{\theta_c}} \tag{26}$$

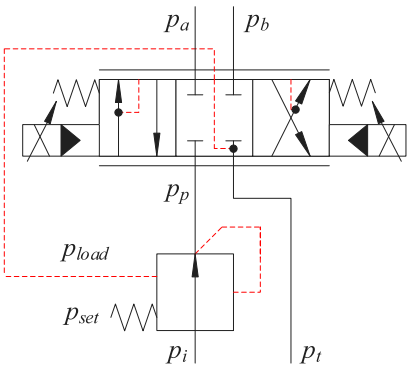

Fig. 10. Pressure compensated directional valve.

$$\theta_d = \arccos\left(\frac{l_e^2 + l_g^2 - l_f^2}{2 \cdot l_e \cdot l_g}\right) \tag{27}$$

$$\theta_e = \arccos\left(\frac{l_b^2 + l_e^2 - x_m^2}{2 \cdot l_b \cdot l_e}\right) \tag{28}$$

$$\theta_m = \theta_d + \theta_e - \tilde{\theta}_m \tag{29}$$

Based on Eq. (29), an analytical expression for $\dot{x}_m$ can be derived. This is done by taking the time derivative of $\theta_m(x_m)$, and then inverting to obtain an expression for $\dot{x}_m$. This is shown in Eq. (30). The full derivation of the cylinder velocity is given in Appendix C.

$$\dot{x}_m = \left(\frac{\partial \theta_m(x_m)}{\partial x_m}\right)^{-1} \cdot \dot{\theta}_m = \theta_{x_m}^{\dagger} \cdot \dot{\theta}_m \tag{30}$$

3.4. Hydraulic modeling

Both the main cylinder and the knuckle cylinder are controlled by pressure compensated directional valves. An illustration is shown in Fig. 10. The pressure compensator senses the load pressure to keep the pressure drop over the directional valve constant, thus ensuring a load independent flow. The governing equations of the pressure compensator are given in Eqs. (31)–(33).

$$u_{pc} = \frac{p_{set} + p_{load} - p_p}{\Delta p_c} \tag{31}$$

$$p_{load} = \begin{cases} p_a & \text{if } u_{spool} > 0 \\ p_b & \text{if } u_{spool} < 0 \\ p_t & \text{otherwise} \end{cases} \tag{32}$$

$$Q_{pc} = k_{pc} \cdot u_{pc} \cdot \sqrt{p_i - p_p} \tag{33}$$

where;

u_{pc}	= opening of compensator, $0 \leq u_{pc} \leq 1$
p_p	= compensated pressure at port p
Δp_c	= pressure difference when fully opened
p_a	= pressure at port a
p_b	= pressure at port b
p_t	= tank pressure
p_{set}	= spring pressure setting
p_{load}	= load pressure
u_{spool}	= position of the main spool, $-1 \leq u_{spool} \leq 1$
Q_{pc}	= flow in pressure compensator
k_{pc}	= flow gain of compensator
p_i	= compensator inlet pressure

The steady state of p_p is then given by Eq. (34).

$$p_p = p_{load} + p_{set} \tag{34}$$

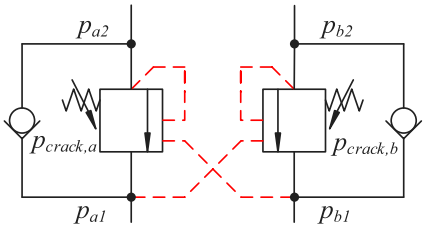

Fig. 11. Double counterbalance valves.

The sensing of the load pressures p_a and p_b ensures that the pressure drop over the directional control valve always equals p_{set}, and that the flow is load independent. This is shown in Eq. (35).

$$\begin{aligned} Q &= k_v \cdot u_{spool} \cdot \sqrt{p_p - p_{load}} \\ &= k_v \cdot u_{spool} \cdot \sqrt{p_{set}} \\ &= Q_{max} \cdot u_{spool} \end{aligned} \tag{35}$$

where;

k_v = flow gain of the directional valve
Q_{max} = maximum valve flow

To assist with load holding, lowering of the load, and protection against pressure surges, counterbalance valves are used between the directional valve and the hydraulic cylinder. Fig. 11 shows an illustration of double counterbalance valves, as used on the knuckle cylinder. The main cylinder uses a single counterbalance valve.

The governing equations of the counterbalance valves are shown in Eqs. (36) and (37).

$$u_a = \frac{p_{a2} + \psi \cdot p_{b1} - p_{crack,a}}{\Delta p_{CBV}} \tag{36}$$

$$u_b = \frac{p_{b2} + \psi \cdot p_{a1} - p_{crack,b}}{\Delta p_{CBV}} \tag{37}$$

where;

u_a = opening of valve a, $0 \leq u_a \leq 1$
u_b = opening of valve b, $0 \leq u_b \leq 1$
p_{a1} = pressure at valve a input side
p_{a2} = pressure at valve a actuator side
p_{b1} = pressure at valve b input side
p_{b2} = pressure at valve b actuator side
$p_{crack,a}$ = crack pressure of valve a
$p_{crack,b}$ = crack pressure of valve b
ψ = pilot area ratio
Δp_{CBV} = pressure difference when fully opened

The models of the pressure compensated directional valve and counterbalance valves are implemented using the hydraulics library in Simscape for the simulation purposes.

4. Control system design

From Eq. (12), it is clear that motion in both the x- and z-direction affects the payload angle dynamics. As such, the controller can utilize $\cos(\theta_p)$ and $\sin(\theta_p)$ for the motion in x- and z-direction to suppress the payload angle. The measured payload angle θ_p is used as feedback to generate crane tip velocities, as this eliminates the payload angle in steady state. As the function from control signal to crane tip motion is highly nonlinear, the kinematic functions derived earlier must be used. The full control system is shown in Fig. 12, outlining the feedback controller (blue), feedforward controller (red), and anti-swing controller (green). The anti-swing controller uses actuator kinematics (Act. Kin.), inverse Jacobian (Inv. Jac.), and inverse actuator kinematics (Inv. Act.).

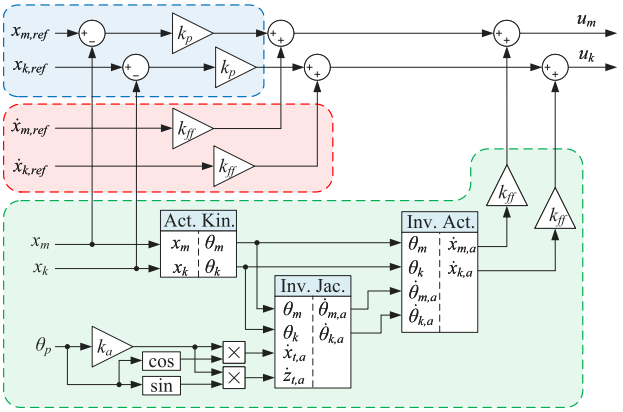

Fig. 12. Schematic of the proposed control system, with feedback controller (blue), feedforward controller (red), and anti-swing controller (green). (For interpretation of the references to color in this figure legend, the reader is referred to the web version of this article.)

Both the feedforward controller and anti-swing controller use the gain k_{ff} to calculate the valve opening from actuator velocity.

The control of the hydraulic cylinders uses feedback of the position error, and feedforward based on the velocity reference. Since the hydraulic system yields load independent velocity control, feedforward is an effective control method, as stated in [23] and [25]. The anti-swing gain k_a and the payload angle θ_p are used to generate two anti-swing crane tip velocities, $\dot{x}_{t,a}$ and $\dot{z}_{t,a}$ in order to suppress the payload angle. These velocities are transformed into joint space and then into actuator space, to yield the anti-swing cylinder velocities $\dot{x}_{m,a}$ and $\dot{x}_{k,a}$ for 2-DOF control. This is shown in Eqs. (38)–(42).

$$\dot{x}_{t,a} = \theta_p \cdot k_a \cdot \cos(\theta_p) \tag{38}$$

$$\dot{z}_{t,a} = \theta_p \cdot k_a \cdot \sin(\theta_p) \tag{39}$$

$$\begin{bmatrix} \dot{\theta}_{m,a} \\ \dot{\theta}_{k,a} \end{bmatrix} = \mathbf{J}^{\dagger} \cdot \begin{bmatrix} \dot{x}_{t,a} \\ \dot{z}_{t,a} \end{bmatrix} \tag{40}$$

$$\dot{x}_{m,a} = \theta^{\dagger}_{x_k} \cdot \dot{\theta}_{m,a} \tag{41}$$

$$\dot{x}_{k,a} = \theta^{\dagger}_{x_k} \cdot \dot{\theta}_{k,a} \tag{42}$$

The anti-swing cylinder velocities $\dot{x}_{m,a}$ and $\dot{x}_{k,a}$ are then multiplied by k_{ff} to generate the valve opening. The control outputs for the control system are shown in Eqs. (43) and (44).

$$u_m = (x_{m,ref} - x_m) \cdot k_{p,m} + \dot{x}_{m,ref} \cdot k_{ff,m} + \dot{x}_{m,a} \cdot k_{ff,m} \tag{43}$$

$$u_k = (x_{k,ref} - x_k) \cdot k_{p,k} + \dot{x}_{k,ref} \cdot k_{ff,k} + \dot{x}_{k,a} \cdot k_{ff,k} \tag{44}$$

4.1. Theoretical closed loop analysis

An analysis of the closed loop hanging load dynamics can be conducted based on the open loop hanging load dynamics and the selected control law. The control law controls the velocity of the crane tip. Recalling from earlier sections, the open loop dynamics and control law are given as:

$$\ddot{\theta}_p = \frac{1}{L_w} \cdot \left(-\ddot{x}_t \cdot c_{\theta_p} - \ddot{z}_t \cdot s_{\theta_p} - g \cdot s_{\theta_p} \right) \tag{45}$$

$$\dot{x}_t = \theta_p \cdot k_a \cdot c_{\theta_p} \tag{46}$$

$$\dot{z}_t = \theta_p \cdot k_a \cdot s_{\theta_p} \tag{47}$$

The expressions for $\ddot{x}_t$ and $\ddot{z}_t$ can be made by taking the time derivative of the crane tip velocities.

$$\ddot{x}_t = \dot{\theta}_p \cdot k_a \cdot (c_{\theta_p} - \theta_p \cdot s_{\theta_p}) \tag{48}$$

$$\ddot{z}_t = \dot{\theta}_p \cdot k_a \cdot (s_{\theta_p} + \theta_p \cdot c_{\theta_p}) \tag{49}$$

The closed loop hanging load dynamics can now be described as:

$$\ddot{\theta}_p = \frac{1}{L_w}\cdot\Big(-\dot{\theta}_p\cdot k_a\cdot(c_{\theta_p} - \theta_p\cdot s_{\theta_p})\cdot c_{\theta_p} \\ -\dot{\theta}_p\cdot k_a\cdot(s_{\theta_p} + \theta_p\cdot c_{\theta_p})\cdot s_{\theta_p} - g\cdot s_{\theta_p}\Big) \tag{50}$$

Linearization is conducted to analyze the damping that the control law provides. Linearizing around $\theta_p \approx 0$ yields:

$$\dot{x}_t = \theta_p\cdot k_a \tag{51}$$

$$\dot{z}_t = 0 \tag{52}$$

$$\ddot{x}_t = \dot{\theta}_p\cdot k_a \tag{53}$$

$$\ddot{z}_t = 0 \tag{54}$$

$$\ddot{\theta}_p = -\frac{\dot{\theta}_p\cdot k_a}{L_w} - \frac{g\cdot\theta_p}{L_w} \tag{55}$$

A Laplace transform of the linearized closed loop hanging load dynamics is conducted to find the damping ratio of the system. The closed loop hanging load dynamics is a second order system, given by:

$$s^2\cdot\theta_p = -\frac{s\cdot\theta_p\cdot k_a}{L_w} - \frac{g\cdot\theta_p}{L_w} \tag{56}$$

$$s^2 + \frac{s\cdot k_a}{L_w} + \frac{g}{L_w} = 0 \tag{57}$$

$$s^2 + 2\cdot s\cdot\zeta\cdot\omega + \omega^2 = 0 \tag{58}$$

The bandwidth and damping ratio of the linearized system are calculated as:

$$\omega = \sqrt{\frac{g}{L_w}} \tag{59}$$

$$\zeta = \frac{k_a}{2\cdot\sqrt{L_w\cdot g}} \tag{60}$$

It can be seen that the damping ratio ζ increases as the anti-swing gain k_a increases, and that the system is stable with $k_a > 0$. An analytical expression for the anti-swing gain can now be calculated based on desired damping ratio and wire length by rearranging Eq. (60).

$$k_a = 2\cdot\zeta\cdot\sqrt{L_w\cdot g} \tag{61}$$

The analytical expressions in Eqs. (50) and (61) are used in a numerical analysis of the closed loop nonlinear dynamics. A set of transient simulations with $L_w = 2$ m and initial conditions of $\theta_{p,0} = 0.1$ rad and $\dot{\theta}_{p,0} = 0$ rad/s are shown in Fig. 13 to showcase the damping that the anti-swing controller provides. To numerically analyze the performance of the anti-swing controller, the RMS value of θ_p as a function of ζ from the transient simulations is shown in Fig. 14. The minimum is at $\zeta \approx 0.5$, equating to $k_a \approx 4.5$ m/s.

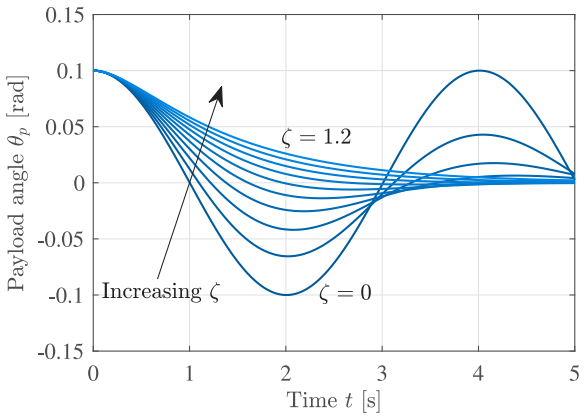

Fig. 13. Transient simulation of closed loop nonlinear hanging load dynamics with damping ratio $0 < \zeta < 1.2$.

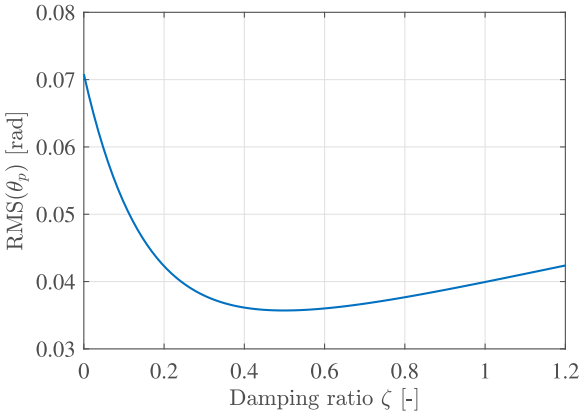

Fig. 14. RMS(θ_p) as a function of damping ratio for the closed loop nonlinear hanging load dynamics.

Table 5
Simulation parameters.

Description	Name	Value
Main feedback	$k_{p,m}$	5 m^{-1}
Main out-stroke feedforward	$k^+_{ff,m}$	30.16 s m^{-1}
Main in-stroke feedforward	$k^-_{ff,m}$	18.37 s m^{-1}
Knuckle feedback	$k_{p,k}$	20 m^{-1}
Knuckle out-stroke feedforward	$k^+_{ff,k}$	26.51 s m^{-1}
Knuckle in-stroke feedforward	$k^-_{ff,k}$	14.72 s m^{-1}
Wire length	L_w	2 m

5. System simulation

The system simulation is conducted in MATLAB Simscape™ with imported CAD models and the models derived in Section 3. For the position control, a path controller based on a trapezoidal velocity reference is used, as described in [25]. The path controller operates in actuator space, and uses segments of constant cylinder velocity. The relevant parameters for the simulation are shown in Table 5. Fig. 15 shows the cylinder position references for the simulation.

A comparison is made in Fig. 16, which shows the payload angle θ_p with $k_a = 0$ m/s and $k_a = 5$ m/s. The anti-swing controller eliminates the constant oscillations in the payload angle θ_p when the cylinder is running with constant velocity, and reduces the payload angle when the crane tip is accelerating. The anti-swing controller is effective for both in-stroke and out-stroke cylinder motion.

Fig. 17 shows the position error during simulation with and without anti-swing control. The position error is larger with the anti-swing controller, but reducing the payload angle θ_p is a higher priority than reducing the position error. Although the position error is higher when using anti-swing control, it goes towards zero after the payload angle is suppressed.

Fig. 18 shows the control signals for the feedback controller $u_{k,fb}$, feedforward controller $u_{k,ff}$, and anti-swing controller $u_{k,a}$ on the knuckle cylinder during simulation with $k_a = 5$ m/s. The main control signal u_k is without large oscillations, which is advantageous for the flexible loader crane. The contributions of the anti-swing controller can be seen as small spikes when the cylinders are accelerating, i.e. when the control signal is not constant.

To evaluate the effect of the wire length L_w, the crane is simulated with different wire lengths and anti-swing gains. From Eq. (12) it is shown that the payload angle dynamics is dependent on the inverse of the wire length L_w. To compensate for this a gain scheduling of k_a can be made to be a function of the wire length. A gain scheduling of the anti-swing gain equivalent to Eq. (61) with $\zeta = 0.5644$ is used for this simulation. This equates to $k_a = 5$ m/s at $L_w = 2$ m. This

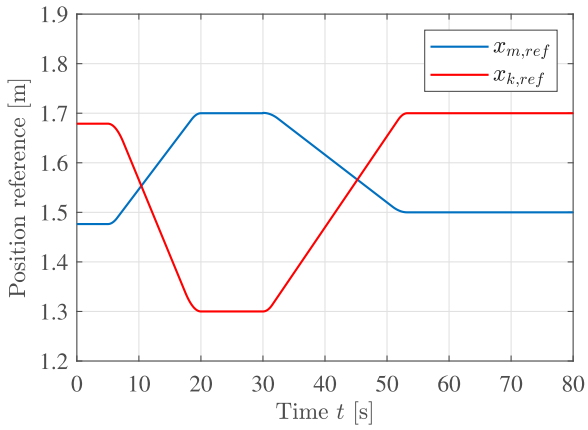

Fig. 15. Position reference for cylinders during simulation.

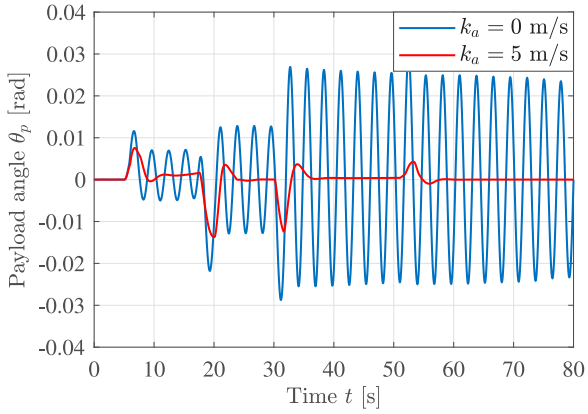

Fig. 16. Payload angle θ_p with (red line) and without (blue line) anti-swing control. (For interpretation of the references to color in this figure legend, the reader is referred to the web version of this article.)

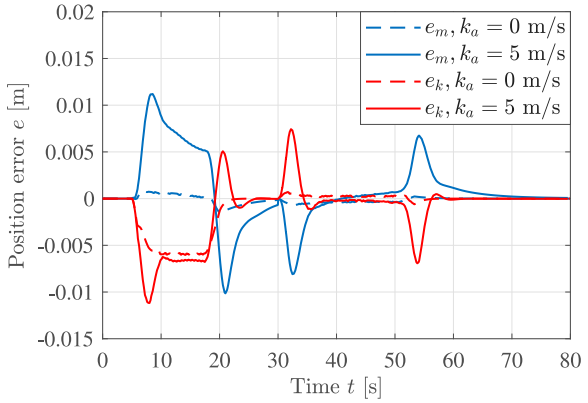

Fig. 17. Cylinder position error with (solid line) and without (dashed line) anti-swing control.

means that the wire length L_w needs to be measured in a practical application. The payload angle during motion for different wire lengths is shown in Fig. 19. The control system yields good suppression of the payload angle and eliminates the constant oscillations for the different wire lengths.

To evaluate the interaction between the position controller and anti-swing controller and identify any instability, a simulation is carried out with higher values of the anti-swing gain k_a. The payload angle is shown in Fig. 20 and the main cylinder position error is shown in

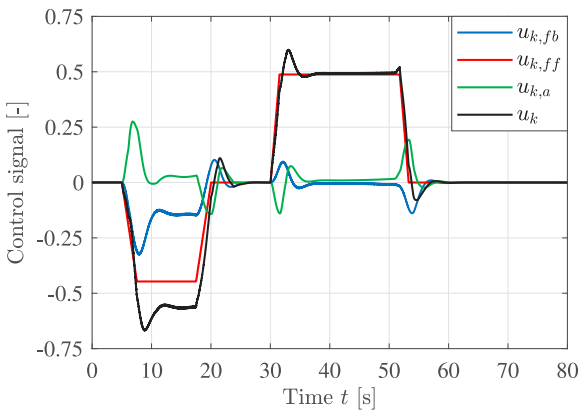

Fig. 18. Control signals for the knuckle cylinder with anti-swing control.

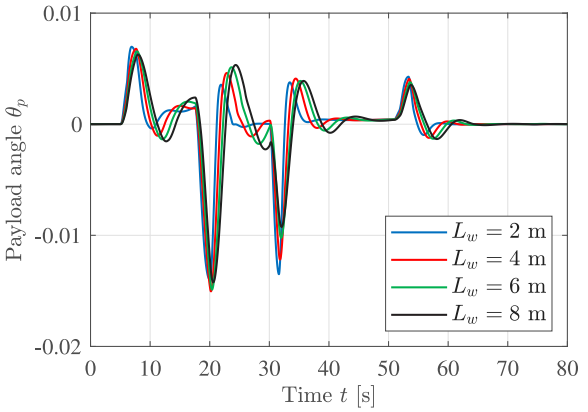

Fig. 19. Payload angle for different wire lengths L_w.

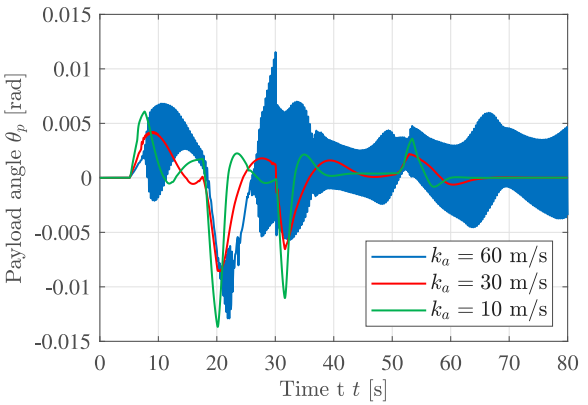

Fig. 20. Payload angle θ_p for different anti-swing gains k_a.

Fig. 21. Increasing the gain improves performance until oscillations appear in the nonlinear system. In Fig. 20 this is illustrated with three different gains where the oscillatory behavior is pronounced a k_a = 60 m/s.

6. Experimental results

The anti-swing controller is implemented on a CompactRIO on the HMF 2020K4 loader crane. A picture of the test setup is shown in Fig. 22. The sensor used in the experiments is the BNO055 Absolute Orientation Sensor from Bosch Sensortec. It outputs three Euler angles and they are all used to calculate the payload angle θ_p.

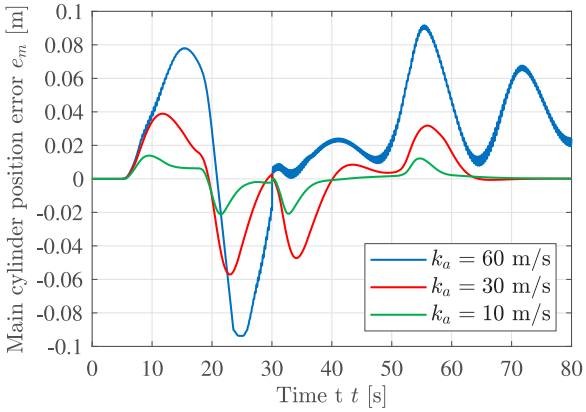

Fig. 21. Main cylinder position error e_m for different anti-swing gains k_a.

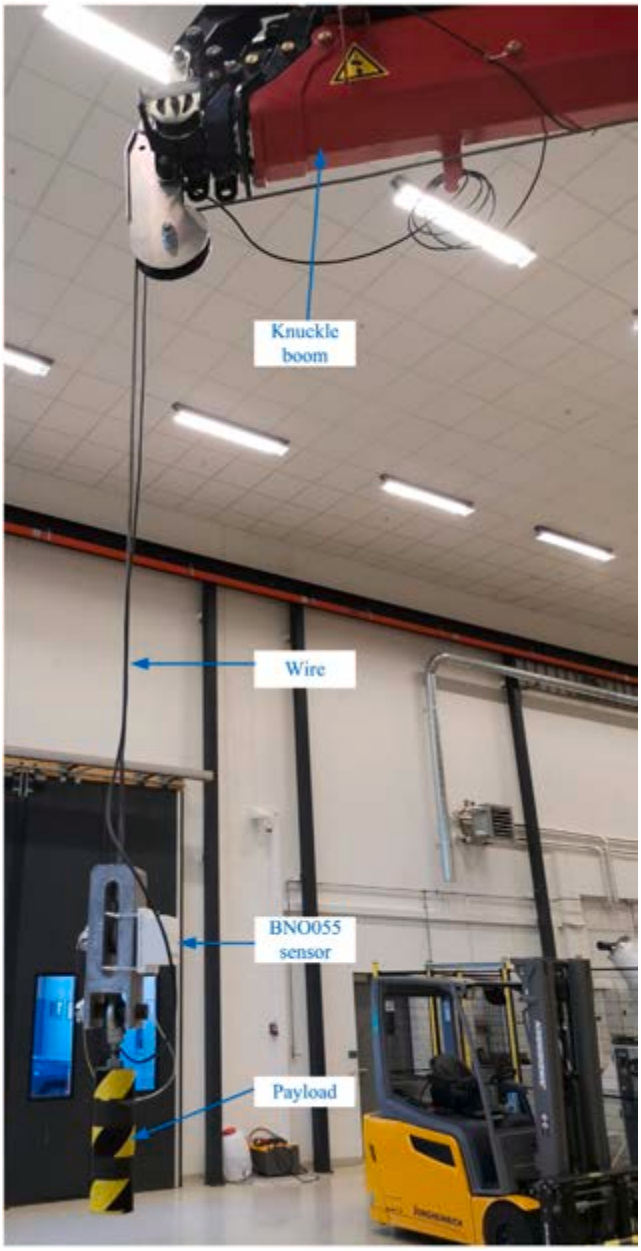

Fig. 22. HMF 2020K4 crane in laboratory.

Table 6
Identified deadband for each actuator.

Actuator	Out, u^+	In, u^-
Main	0.24	−0.22
Knuckle	0.20	−0.31

There is some deadband in the valves on the HMF 2020K4 loader crane, and therefore deadband compensation has been implemented for the laboratory experiments. The identified deadbands for the valves are shown in Table 6. The equation for the deadband compensation is shown in Eq. (62). By adding a small deadband $\tilde{u}$, it is ensured that the valve will be able to stay closed when no movement is needed.

$$\hat{u} = \begin{cases} u^+ + (1-u^+)\cdot u & \text{if } u > \tilde{u} \\ u^- + (1+u^-)\cdot u & \text{if } u < -\tilde{u} \\ 0 & \text{otherwise} \end{cases} \tag{62}$$

where;

$\hat{u}$ = compensated control signal
u = control signal
u^+ = out-stroke deadband
u^- = in-stroke deadband
$\tilde{u}$ = desired deadband, 0.001

In the laboratory there was identified some drift in the payload angle sensor. This has been removed with a digital high pass filter, which is shown in Eqs. (63) and (64).

$$y_i = \alpha \cdot y_{i-1} + \alpha \cdot (x_i - x_{i-1}) \tag{63}$$

$$\alpha = \frac{T_f}{T_f + T_s} \tag{64}$$

where;

i = sample number
y = filter output
x = filter input
T_f = filter time constant
T_s = sample time, 0.01 s

To avoid filtering out the motion of the payload, the filter time constant T_f should be larger than the pendulum period T_p. The pendulum period is calculated based on the wire length, shown in Eq. (65).

$$T_p = 2 \cdot \pi \cdot \sqrt{\frac{L_w}{g}} = 2.837 \text{ s} \tag{65}$$

Because of the value of T_p the filter time constant has been set to $T_f = 3$ s. The effects of the drift and the implemented high pass filter is shown in Fig. 23. The payload angle drifted towards an offset of 0.02 rad. With the drift of the payload angle, the position error for the main cylinder converged to a large value. With the high pass filter the drift of the payload angle has been removed, and the position error converges to zero as expected.

In the laboratory experiments two different paths are used. The first path is equal to the path in the simulations shown in Fig. 15, while the second path is used to show experimental results and performance in another configuration. An illustration of the crane and the crane tip motion in the xz-plane for the two paths is shown in Fig. 24. The first path is shown in blue, and the second path is shown in red. The circles denote the starting position of the crane tip for each path and then the crane moves back and forth along the path.

As in the simulations, the payload angle has been plotted for different gains using the first path. This is shown in Fig. 25. Larger gains yielded better suppression and removed the constant oscillations. However, the system became unstable with anti-swing gain $k_a \geq 7$ m/s and the experiment was stopped.

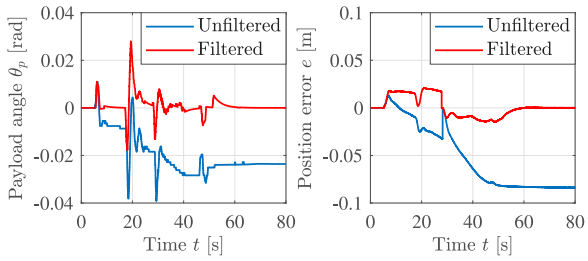

(a) Drift of payload angle. (b) Main cylinder position error.

Fig. 23. Payload angle drift and its effect on the position error for the main cylinder.

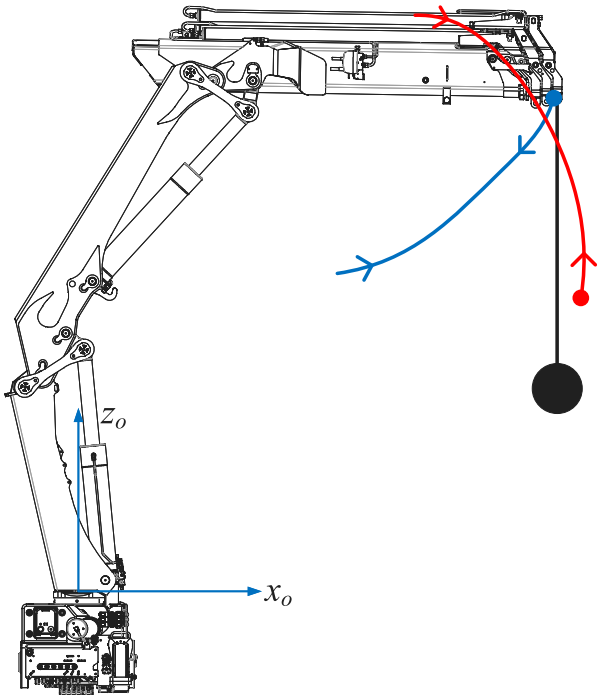

Fig. 24. Crane tip motion in the xz-plane for the first path (blue) and second path (red) in the laboratory. (For interpretation of the references to color in this figure legend, the reader is referred to the web version of this article.)

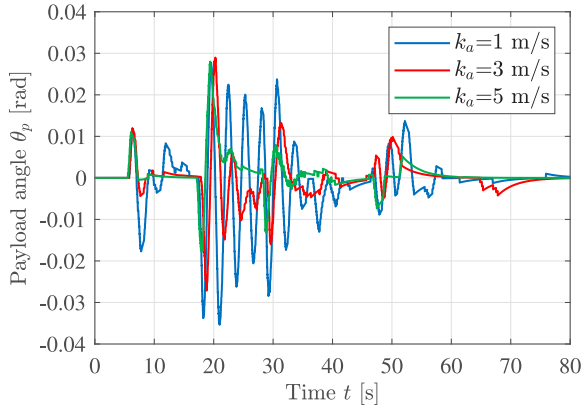

Fig. 25. Payload angle θ_p for different anti-swing gains k_a.

A plot of the payload angle with and without anti-swing is shown in Fig. 26. The payload experiences large oscillations without the anti-swing controller. With the controller, the payload angle is significantly reduced.

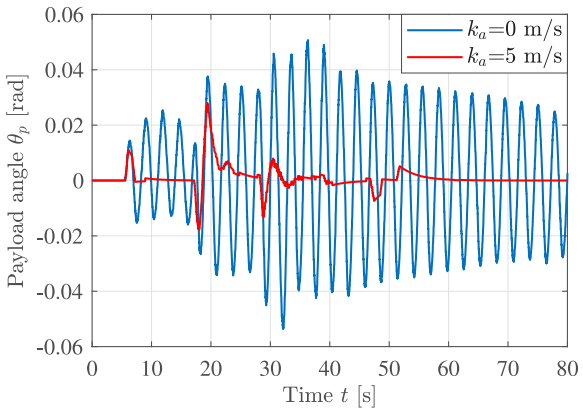

Fig. 26. Payload angle θ_p with (red line) and without (blue line) anti-swing control during the first path. (For interpretation of the references to color in this figure legend, the reader is referred to the web version of this article.)

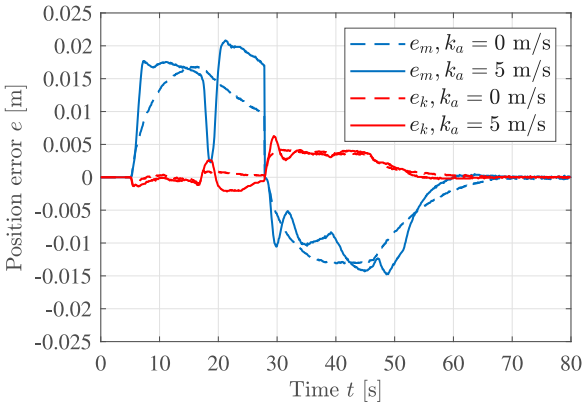

Fig. 27. Cylinder position error with (solid line) and without (dashed line) anti-swing control.

The position error with and without anti-swing is shown in Fig. 27. The position error with anti-swing control is kept close to the position error without control, showing that the anti-swing controller is able to suppress the payload angle without a large impact on the position error. The position error without anti-swing control is larger compared to the ideal system in the simulations.

The payload angle θ_p during the motion along the second path is shown in Fig. 28. The control system yields good suppression of the payload angle for this configuration also. Due to the vertical crane tip motion during the first few seconds of the second path, the payload barely oscillates in this segment.

7. Conclusion

In this paper a novel anti-swing controller for hydraulic cranes is designed utilizing load independent velocity control. The anti-swing controller is simulated, evaluated, and experimentally verified on a hydraulic loader crane. Relevant kinematic functions are derived to enable control of the payload angle. The motion control system operates in actuator space, and controls the two hydraulic cylinders in order to suppress the payload angle during motion. The kinematic functions are used to transform the feedback of the payload angle θ_p into a command signal for the valves.

In the simulations, the feedback gain k_a is evaluated in order to suppress the payload angle θ_p during motion. Simulation results show significant reduction in the payload angle and elimination of oscillations during a motion with constant cylinder velocity. This is achieved

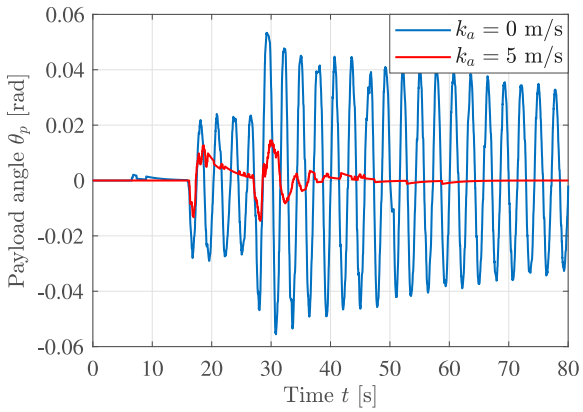

Fig. 28. Payload angle θ_p with (red line) and without (blue line) anti-swing control during the second path. (For interpretation of the references to color in this figure legend, the reader is referred to the web version of this article.)

Table 7
Lengths of the knuckle linkage.

Name	Length [m]
l_h	1.626
l_i	1.650
l_j	0.168
l_k	0.490
l_m	0.220
l_n	0.280

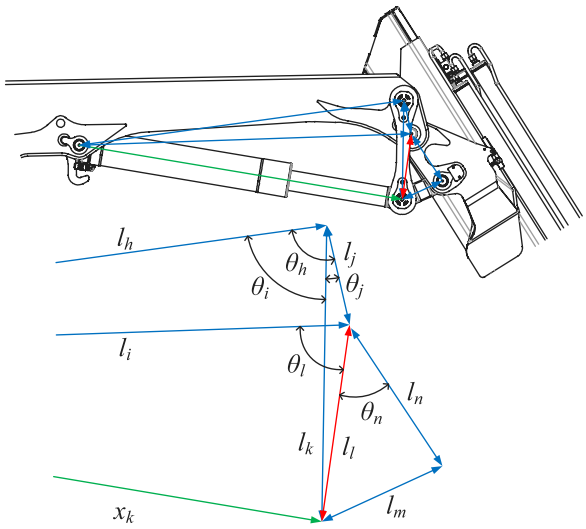

Fig. 29. Geometry of the linkage system for the knuckle joint.

without larger cylinder position errors or oscillations in the control signal. Simulation results verify the performance of the anti-swing controller.

In the laboratory, a high pass filter is added to eliminate sensor drift. A deadband compensator is used to compensate for the deadband in the valves. The feedback gain k_a is also evaluated, and the experimental verification shows that the anti-swing controller successfully suppresses the payload angle, with similar results as in the simulations. Results in the laboratory showcase the feasibility of the novel anti-swing controller for hydraulic cranes in a practical application.

Future work may include extending the anti-swing controller to include the slewing motion of the crane, which will include deriving the necessary kinematic functions. Actively controlling the wire length with a winch can also be added, and may include gain scheduling based on the wire length. Modeling of the flexibility of the crane may also be included to analyze how this interacts with the payload dynamics, and how this affects the performance of the anti-swing control system.

CRediT authorship contribution statement

Konrad Johan Jensen: Conceptualization, Methodology, Software, Validation, Formal analysis, Investigation, Resources, Data curation, Writing - original draft, Writing - review & editing. **Morten Kjeld Ebbesen:** Conceptualization, Methodology, Resources, Writing - review & editing, Supervision. **Michael Rygaard Hansen:** Conceptualization, Methodology, Resources, Writing - review & editing, Supervision.

Declaration of competing interest

The authors declare that they have no known competing financial interests or personal relationships that could have appeared to influence the work reported in this paper.

Funding

This work was supported by the Norwegian Ministry of Education and Research grant number 155597.

Appendix A. Jacobian matrix and inverse Jacobian

Recalling the transformation matrix $\mathbf{A}_{DH}$ and the crane tip positions x_t and z_t as:

$$\mathbf{A}_{DH} = \begin{bmatrix} c_{\theta_m+\theta_k} & 0 & -s_{\theta_m+\theta_k} & x_t \\ 0 & 1 & 0 & 0 \\ s_{\theta_m+\theta_k} & 0 & c_{\theta_m+\theta_k} & z_t \\ 0 & 0 & 0 & 1 \end{bmatrix} \tag{A.1}$$

$$x_t = -l_{1x} + l_{2x}\cdot c_{\theta_m} - l_{2z}\cdot s_{\theta_m} + l_{3x}\cdot c_{\theta_m+\theta_k} + l_{3z}\cdot s_{\theta_m+\theta_k} \tag{A.2}$$

$$z_t = l_{1z} + l_{2x}\cdot s_{\theta_m} + l_{2z}\cdot c_{\theta_m} + l_{3x}\cdot s_{\theta_m+\theta_k} - l_{3z}\cdot c_{\theta_m+\theta_k} \tag{A.3}$$

The Jacobian matrix is defined as the partial derivative of the crane tip position with respect to the joint angles, shown in Eqs. (A.4)–(A.8).

$$\mathbf{J} = \begin{bmatrix} \frac{\partial}{\partial\theta_m}(x_t) & \frac{\partial}{\partial\theta_k}(x_t) \\ \frac{\partial}{\partial\theta_m}(z_t) & \frac{\partial}{\partial\theta_k}(z_t) \end{bmatrix} \tag{A.4}$$

$$\frac{\partial}{\partial\theta_m}(x_t) = -l_{2x}\cdot s_{\theta_m} - l_{2z}\cdot c_{\theta_m} - l_{3x}\cdot s_{\theta_m+\theta_k} + l_{3z}\cdot c_{\theta_m+\theta_k} \tag{A.5}$$

$$\frac{\partial}{\partial\theta_k}(x_t) = l_{3x}\cdot s_{\theta_m+\theta_k} - l_{3z}\cdot c_{\theta_m+\theta_k} \tag{A.6}$$

$$\frac{\partial}{\partial\theta_m}(z_t) = l_{2x}\cdot c_{\theta_m} - l_{2z}\cdot s_{\theta_m} + l_{3x}\cdot c_{\theta_m+\theta_k} + l_{3z}\cdot s_{\theta_m+\theta_k} \tag{A.7}$$

$$\frac{\partial}{\partial\theta_k}(z_t) = -l_{3x}\cdot c_{\theta_m+\theta_k} - l_{3z}\cdot s_{\theta_m+\theta_k} \tag{A.8}$$

Inverting the Jacobian matrix yields the solution for the joint velocities, shown in Eqs. (A.9)–(A.15).

$$\mathbf{J}^\dagger \triangleq \mathbf{J}^{-1} = \begin{bmatrix} J_{11}^\dagger & J_{12}^\dagger \\ J_{21}^\dagger & J_{22}^\dagger \end{bmatrix} \tag{A.9}$$

$$\dot{\theta}_m = J_{11}^\dagger\cdot\dot{x}_t + J_{12}^\dagger\cdot\dot{z}_t \tag{A.10}$$

$$\dot{\theta}_k = J_{21}^\dagger\cdot\dot{x}_t + J_{22}^\dagger\cdot\dot{z}_t \tag{A.11}$$

$$J_{11}^\dagger = \frac{-l_{3x}\cdot c_{\theta_m+\theta_k} - l_{3z}\cdot s_{\theta_m+\theta_k}}{l_{2x}\cdot l_{3z}\cdot c_{\theta_k} + l_{3x}\cdot l_{2z}\cdot c_{\theta_k} - l_{2x}\cdot l_{3x}\cdot s_{\theta_k} + l_{2z}\cdot l_{3z}\cdot s_{\theta_k}} \tag{A.12}$$

$$J_{12}^{\dagger} = \frac{-l_{3x}\cdot s_{\theta_m+\theta_k}+l_{3z}\cdot c_{\theta_m+\theta_k}}{l_{2x}\cdot l_{3z}\cdot c_{\theta_k}+l_{3x}\cdot l_{2z}\cdot c_{\theta_k}-l_{2x}\cdot l_{3x}\cdot s_{\theta_k}+l_{2z}\cdot l_{3z}\cdot s_{\theta_k}} \tag{A.13}$$

$$J_{21}^{\dagger} = \frac{-l_{2x}\cdot c_{\theta_m}+l_{2z}\cdot s_{\theta_m}-l_{3x}\cdot c_{\theta_m+\theta_k}-l_{3z}\cdot s_{\theta_m+\theta_k}}{l_{2x}\cdot l_{3z}\cdot c_{\theta_k}+l_{3x}\cdot l_{2z}\cdot c_{\theta_k}-l_{2x}\cdot l_{3x}\cdot s_{\theta_k}+l_{2z}\cdot l_{3z}\cdot s_{\theta_k}} \tag{A.14}$$

$$J_{22}^{\dagger} = \frac{-l_{2x}\cdot s_{\theta_m}-l_{2z}\cdot c_{\theta_m}-l_{3x}\cdot s_{\theta_m+\theta_k}+l_{3z}\cdot c_{\theta_m+\theta_k}}{l_{2x}\cdot l_{3z}\cdot c_{\theta_k}+l_{3x}\cdot l_{2z}\cdot c_{\theta_k}-l_{2x}\cdot l_{3x}\cdot s_{\theta_k}+l_{2z}\cdot l_{3z}\cdot s_{\theta_k}} \tag{A.15}$$

Appendix B. Actuator space kinematics

To calculate the actuator space kinematics for the knuckle joint, the same procedure is followed as with the main joint. The geometry for the knuckle linkage is shown in Fig. 29. The coordinate x_k is the length of the hydraulic cylinder, and the length l_l is the intermediate length. The lengths of the knuckle linkage system are shown in Table 7.

As with the main joint, an offset angle $\tilde{\theta}_k = 3.1086$ rad is subtracted from the joint angle θ_k to ensure that the knuckle boom is horizontal when $\theta_m + \theta_k = 0$. The calculations are shown in Eqs. (B.1)–(B.6), and the knuckle joint angle θ_k is defined in Eq. (B.7).

$$\theta_h = \arccos\left(\frac{l_h^2+l_j^2-l_i^2}{2\cdot l_h\cdot l_j}\right) \tag{B.1}$$

$$\theta_i = \arccos\left(\frac{l_h^2+l_k^2-x_k^2}{2\cdot l_h\cdot l_k}\right) \tag{B.2}$$

$$\theta_j = \theta_h - \theta_i \tag{B.3}$$

$$l_l = \sqrt{l_j^2+l_k^2-2\cdot l_j\cdot l_k\cdot c_{\theta_j}} \tag{B.4}$$

$$\theta_n = \arccos\left(\frac{l_l^2+l_n^2-l_m^2}{2\cdot l_l\cdot l_n}\right) \tag{B.5}$$

$$\theta_l = \arccos\left(\frac{l_i^2+l_l^2-x_k^2}{2\cdot l_i\cdot l_l}\right) \tag{B.6}$$

$$\theta_k = \theta_n + \theta_l - \tilde{\theta}_k \tag{B.7}$$

Appendix C. Time derivative of actuator space kinematics

By taking the time derivative of the actuator space kinematics, expressions for the cylinder velocities $\dot{x}_m$ and $\dot{x}_k$ can be made. The equations for the knuckle joint are given below, but the procedure is the same for the main joint. Taking the time derivative of Eqs. (B.1)–(B.7) from Appendix B yields:

$$\dot{\theta}_h = 0 \tag{C.1}$$

$$\dot{\theta}_i = \frac{x_k}{l_h\cdot l_k\cdot\sqrt{1-\left(\frac{l_h^2+l_k^2-x_k^2}{2\cdot l_h\cdot l_k}\right)^2}}\cdot\dot{x}_k \tag{C.2}$$

$$\dot{\theta}_j = -\frac{x_k}{l_h\cdot l_k\cdot\sqrt{1-\left(\frac{l_h^2+l_k^2-x_k^2}{2\cdot l_h\cdot l_k}\right)^2}}\cdot\dot{x}_k \tag{C.3}$$

$$\begin{aligned}\dot{l}_l &= \left(l_j^2+l_k^2-2\cdot l_j\cdot l_k\cdot c_{\theta_j}\right)^{-\frac{1}{2}}\cdot l_j\cdot l_k\cdot s_{\theta_j}\cdot\dot{\theta}_j \\ &= -\frac{\left(l_j^2+l_k^2-2\cdot l_j\cdot l_k\cdot c_{\theta_j}\right)^{-\frac{1}{2}}\cdot l_j\cdot s_{\theta_j}\cdot x_k}{l_h\cdot\sqrt{1-\left(\frac{l_h^2+l_k^2-x_k^2}{2\cdot l_h\cdot l_k}\right)^2}}\cdot\dot{x}_k\end{aligned} \tag{C.4}$$

$$\begin{aligned}\dot{\theta}_n &= -\frac{l_l^2-l_n^2+l_m^2}{2\cdot l_l^2\cdot l_n\cdot\sqrt{1-\left(\frac{l_l^2+l_n^2-l_m^2}{2\cdot l_l\cdot l_n}\right)^2}}\cdot\dot{l}_l \\ &= \frac{\left(l_l^2-l_n^2+l_m^2\right)\cdot\left(l_j^2+l_k^2-2\cdot l_j\cdot l_k\cdot c_{\theta_j}\right)^{-\frac{1}{2}}\cdot l_j\cdot s_{\theta_j}\cdot x_k}{2\cdot l_l^2\cdot l_n\cdot l_h\cdot\sqrt{1-\left(\frac{l_l^2+l_n^2-l_m^2}{2\cdot l_l\cdot l_n}\right)^2}\cdot\sqrt{1-\left(\frac{l_h^2+l_k^2-x_k^2}{2\cdot l_h\cdot l_k}\right)^2}}\cdot\dot{x}_k\end{aligned} \tag{C.5}$$

$$\begin{aligned}\dot{\theta}_l &= \frac{-1}{\sqrt{1-\left(\frac{l_i^2+l_l^2-x_k^2}{2\cdot l_i\cdot l_l}\right)^2}}\cdot\frac{\dot{l}_l\cdot\left(l_l^2+x_k^2-l_i^2\right)-2\cdot l_l\cdot x_k\cdot\dot{x}_k}{2\cdot l_i\cdot l_l^2} \\ &= \frac{x_k}{l_i\cdot l_l\cdot\sqrt{1-\left(\frac{l_i^2+l_l^2-x_k^2}{2\cdot l_i\cdot l_l}\right)^2}}\cdot\dot{x}_k - \frac{l_l^2+x_k^2-l_i^2}{2\cdot l_i\cdot l_l^2\cdot\sqrt{1-\left(\frac{l_i^2+l_l^2-x_k^2}{2\cdot l_i\cdot l_l}\right)^2}}\cdot\dot{l}_l \\ &= \frac{x_k}{l_i\cdot l_l\cdot\sqrt{1-\left(\frac{l_i^2+l_l^2-x_k^2}{2\cdot l_i\cdot l_l}\right)^2}}\cdot\dot{x}_k \\ &\quad + \frac{\left(l_l^2+x_k^2-l_i^2\right)\cdot\left(l_j^2+l_k^2-2\cdot l_j\cdot l_k\cdot c_{\theta_j}\right)^{-\frac{1}{2}}\cdot l_j\cdot s_{\theta_j}\cdot x_k}{2\cdot l_i\cdot l_l^2\cdot l_h\cdot\sqrt{1-\left(\frac{l_i^2+l_l^2-x_k^2}{2\cdot l_i\cdot l_l}\right)^2}\cdot\sqrt{1-\left(\frac{l_h^2+l_k^2-x_k^2}{2\cdot l_h\cdot l_k}\right)^2}}\cdot\dot{x}_k\end{aligned} \tag{C.6}$$

$$\begin{aligned}\dot{\theta}_k &= \dot{\theta}_n + \dot{\theta}_l \\ &= \left(\frac{\left(l_l^2-l_n^2+l_m^2\right)\cdot\left(l_j^2+l_k^2-2\cdot l_j\cdot l_k\cdot c_{\theta_j}\right)^{-\frac{1}{2}}\cdot l_j\cdot s_{\theta_j}\cdot x_k}{2\cdot l_l^2\cdot l_n\cdot l_h\cdot\sqrt{1-\left(\frac{l_l^2+l_n^2-l_m^2}{2\cdot l_l\cdot l_n}\right)^2}\cdot\sqrt{1-\left(\frac{l_h^2+l_k^2-x_k^2}{2\cdot l_h\cdot l_k}\right)^2}} + \frac{x_k}{l_i\cdot l_l\cdot\sqrt{1-\left(\frac{l_i^2+l_l^2-x_k^2}{2\cdot l_i\cdot l_l}\right)^2}}\right. \\ &\quad \left. + \frac{\left(l_l^2+x_k^2-l_i^2\right)\cdot\left(l_j^2+l_k^2-2\cdot l_j\cdot l_k\cdot c_{\theta_j}\right)^{-\frac{1}{2}}\cdot l_j\cdot s_{\theta_j}\cdot x_k}{2\cdot l_i\cdot l_l^2\cdot l_h\cdot\sqrt{1-\left(\frac{l_i^2+l_l^2-x_k^2}{2\cdot l_i\cdot l_l}\right)^2}\cdot\sqrt{1-\left(\frac{l_h^2+l_k^2-x_k^2}{2\cdot l_h\cdot l_k}\right)^2}}\right)\cdot\dot{x}_k\end{aligned} \tag{C.7}$$

Solving Eq. (C.7) with respect to $\dot{x}_k$ yields:

$$\begin{aligned}\dot{x}_k &= \left(\frac{\left(l_l^2-l_n^2+l_m^2\right)\cdot\left(l_j^2+l_k^2-2\cdot l_j\cdot l_k\cdot c_{\theta_j}\right)^{-\frac{1}{2}}\cdot l_j\cdot s_{\theta_j}\cdot x_k}{2\cdot l_l^2\cdot l_n\cdot l_h\cdot\sqrt{1-\left(\frac{l_l^2+l_n^2-l_m^2}{2\cdot l_l\cdot l_n}\right)^2}\cdot\sqrt{1-\left(\frac{l_h^2+l_k^2-x_k^2}{2\cdot l_h\cdot l_k}\right)^2}} + \frac{x_k}{l_i\cdot l_l\cdot\sqrt{1-\left(\frac{l_i^2+l_l^2-x_k^2}{2\cdot l_i\cdot l_l}\right)^2}}\right. \\ &\quad \left. + \frac{\left(l_l^2+x_k^2-l_i^2\right)\cdot\left(l_j^2+l_k^2-2\cdot l_j\cdot l_k\cdot c_{\theta_j}\right)^{-\frac{1}{2}}\cdot l_j\cdot s_{\theta_j}\cdot x_k}{2\cdot l_i\cdot l_l^2\cdot l_h\cdot\sqrt{1-\left(\frac{l_i^2+l_l^2-x_k^2}{2\cdot l_i\cdot l_l}\right)^2}\cdot\sqrt{1-\left(\frac{l_h^2+l_k^2-x_k^2}{2\cdot l_h\cdot l_k}\right)^2}}\right)^{-1}\cdot\dot{\theta}_k\end{aligned} \tag{C.8}$$

References

[1] Lee Ho-Hoon, Cho Sung-Kun, Cho Jae-Sung. A new anti-swing control of overhead cranes. IFAC Proc Vol 1997;30(13):115–20, IFAC Workshop on Automation in the Steel Industry: Current Practice and Future Developments (ASI'97), Kyongju, Korea, 16–18 July 1997.

[2] Lee Ho-Hoon. Modeling and control of a three-dimensional overhead crane. J Dyn Syst Meas Control 1998;120(4):471–6.

[3] Cho Sung-Kun, Lee Ho-Hoon. An anti-swing control of a 3-dimensional overhead crane. In: Proceedings of the 2000 American control conference. (IEEE Cat. No. 00CH36334), vol. 2. 2000. p. 1037–41.

[4] Lee Ho-Hoon, Choi Seung-Gap. A model-based anti-swing control of overhead cranes with high hoisting speeds. In: Proceedings 2001 ICRA. IEEE international conference on robotics and automation (Cat. No. 01CH37164), vol. 3. 2001. p. 2547–52.

[5] Lee Ho-Hoon, Cho Sung-Kun. A new fuzzy-logic anti-swing control for industrial three-dimensional overhead cranes. In: Proceedings 2001 ICRA. IEEE international conference on robotics and automation (Cat. No. 01CH37164), vol. 3. 2001. p. 2956–61.

[6] Cho Sung-Kun, Lee Ho-Hoon. A fuzzy-logic antiswing controller for three-dimensional overhead cranes. ISA Trans 2002;41(2):235–43.

[7] Lee Ho-Hoon. A new approach for the anti-swing control of overhead cranes with high-speed load hoisting. Internat J Control 2003;76(15):1493–9.

[8] Fang Y, Dixon WE, Dawson DM, Zergeroglu E. Nonlinear coupling control laws for an underactuated overhead crane system. IEEE/ASME Trans Mechatronics 2003;8(3):418–23.

[9] Lee Ho-Hoon. A new design approach for the anti-swing trajectory control of overhead cranes with high-speed hoisting. Internat J Control 2004;77(10):931–40.

[10] Lee Ho-Hoon, Liang Yi, Segura Del. A sliding-mode antiswing trajectory control for overhead cranes with high-speed load hoisting. J Dyn Syst Meas Control 2006;128(4):842–5.

[11] Park Hahn, Chwa Dongkyoung, Hong Keum-Shik. A feedback linearization control of container cranes: Varying rope length. Int J Control Autom Syst 2007;5.

[12] Park M, Chwa D, Hong S. Antisway tracking control of overhead cranes with system uncertainty and actuator nonlinearity using an adaptive fuzzy sliding-mode control. IEEE Trans Ind Electron 2008;55(11):3972–84.
[13] Schindele D, Menn I, Aschemann H. Nonlinear optimal control of an overhead travelling crane. In: 2009 IEEE control applications, intelligent control. 2009. p. 1045–50.
[14] Lee Ho-Hoon, Liang Yi. A robust anti-swing trajectory control of overhead cranes with high-speed load hoisting: experimental study. In: ASME international mechanical engineering congress and exposition, vol. 8: dynamic systems and control, parts A and B. 2010. p. 711–6.
[15] Ngo QH, Hong K. Sliding-mode antisway control of an offshore container crane. IEEE/ASME Trans Mechatronics 2012;17(2):201–9.
[16] Ambrosino Michele, Dawans Arnaud, Thierens Brent, Garone Emanuele. Oscillation reduction for knuckle cranes. In: Proceedings of the 37th international symposium on automation and robotics in construction. Kitakyushu, Japan: International Association for Automation and Robotics in Construction (IAARC); 2020, p. 1590–7.
[17] Singhose WE, Seering Warren, Singer M. Input shaping for vibration reduction with specified insensitivity to modeling errors. In: Proc. Japan-USA symp. flexible automation, vol. 1. 1996.
[18] Sorensen Khalid L, Singhose William, Dickerson Stephen. A controller enabling precise positioning and sway reduction in bridge and gantry cranes. Control Eng Pract 2007;15(7):825–37, Special Issue on Award Winning Applications.
[19] Kjelland Magnus B, Hansen Michael R. Using input shaping and pressure feedback to suppress oscillations in slewing motion of lightweight flexible hydraulic crane. Int J Fluid Power 2015;16(3):141–8.
[20] Boschetti G, Richiedei D, Trevisani A. Delayed reference control for multi-degree-of-freedom elastic systems: Theory and experimentation. Control Eng Pract 2011;19(9):1044–55.
[21] Boschetti G, Caracciolo R, Richiedei D, Trevisani A. A non-time based controller for load swing damping and path-tracking in robotic cranes. J Intell Robot Syst 2014;76(2):201–17.
[22] Kjelland MB, Hansen MR, Tyapin I, Hovland G. Tool-point control of a planar hydraulically actuated manipulator with compensation of non-actuated degree of freedom. In: 2012 12th international conference on control, automation and systems. 2012. p. 672–7.
[23] Bak Morten Kollerup, Hansen Michael Rygaard. Analysis of offshore knuckle boom crane — Part two: Motion control. Model Identif Control 2013;34(4):175–81.
[24] Jensen Konrad Johan, Ebbesen Morten Kjeld, Hansen Michael Rygaard. Adaptive feedforward control of a pressure compensated differential cylinder. Appl Sci 2020;10(21):7847.
[25] Jensen Konrad Johan, Kjeld Ebbesen Morten, Rygaard Hansen Michael. Development of point-to-point path control in actuator space for hydraulic knuckle boom crane. Actuators 2020;9(2):27.
[26] Kjelland Magnus B, Tyapin Ilya, Hovland Geir, Hansen Michael R. Tool-point control for a redundant heave compensated hydraulic manipulator. In: Proceedings of the 2012 IFAC workshop on automatic control in offshore oil and gas production. Trondheim, Norway: Norwegian University of Science and Technology; 2012.

Konrad Johan Jensen received the M.Sc. degree in Mechatronics from the University of Agder, Norway, in 2015. His master's thesis focused on path control of hydraulic cranes. He is currently pursuing a doctorate degree in Mechatronics at the Department of Engineering Sciences at the University of Agder. His main research interests include hydraulic systems, robotics, optimization, and control systems.

Morten Kjeld Ebbesen is affiliated with the Department of Engineering Sciences, University of Agder, Norway, as an associate professor in the Mechatronics group. He received his M.Sc. (2003) and Ph.D. (2008) in mechanical engineering from the University of Aalborg, Denmark. His interests are dynamics, flexible multi-body systems, time-domain simulation, fluid power, and optimization.

Michael Rygaard Hansen received the M.Sc. in Mechanical Engineering, Aalborg University, 1989. Ph.D. in Computer-Aided Analysis and Design of Mechanical Mechanisms, Institute of Mechanical Engineering, Aalborg University, 1992. Main interests lie within the use of numerical methods for modeling, design and optimization of dynamic mechatronic systems. Teaching and supervision experience at B.Sc., M.Sc. and Ph.D. level since 1990. The courses have mainly been devoted to education within mechanical engineering.

Paper D

Novel Concept for Electro-Hydrostatic Actuators for Motion Control of Hydraulic Manipulator

This paper has been published as:

Jensen, K.J.; Kjeld Ebbesen, M.; Rygaard Hansen, M. Novel Concept for Electro-Hydrostatic Actuators for Motion Control of Hydraulic Manipulators.
Energies **2021**, *14(20)*, 6566. doi:10.3390/en14206566

energies

MDPI

Article

Novel Concept for Electro-Hydrostatic Actuators for Motion Control of Hydraulic Manipulators

Konrad Johan Jensen *, Morten Kjeld Ebbesen and Michael Rygaard Hansen

Department of Engineering Sciences, University of Agder, 4879 Grimstad, Norway; morten.k.ebbesen@uia.no (M.K.E.); michael.r.hansen@uia.no (M.R.H.)
* Correspondence: konrad.j.jensen@uia.no

Abstract: Self-contained hydraulic cylinders have gained popularity in the recent years but have not been implemented for high power articulated hydraulic manipulators. This paper presents a novel concept for an electro-hydrostatic actuator applicable to large hydraulic manipulators. The actuator is designed and analyzed to comply with requirements such as load holding, overload handling, and differential flow compensation. The system is analyzed during four quadrant operation to investigate energy efficiency and regenerative capabilities. Numerical simulation is carried out using path control and 2DOF anti-swing of a hydraulic crane as a load case to illustrate a real world scenario. A comparison with traditional valve-controlled actuators is conducted, showing significantly improved efficiency and with similar dynamic response, as well as the possibility for regenerating energy.

Keywords: electro-hydrostatic actuator; pump-controlled cylinder; four-quadrant operation; passive load-holding; servomotor

check for updates

Citation: Jensen, K.J.; Ebbesen, M.K.; Hansen, M.R. Novel Concept for Electro-Hydrostatic Actuators for Motion Control of Hydraulic Manipulators. *Energies* **2021**, *14*, 6566. https://doi.org/10.3390/en14206566

Academic Editor: Per Johansen

Received: 31 August 2021
Accepted: 4 October 2021
Published: 12 October 2021

Publisher's Note: MDPI stays neutral with regard to jurisdictional claims in published maps and institutional affiliations.

Copyright: © 2021 by the authors. Licensee MDPI, Basel, Switzerland. This article is an open access article distributed under the terms and conditions of the Creative Commons Attribution (CC BY) license (https://creativecommons.org/licenses/by/4.0/).

1. Introduction

There has been a trend in the recent years of replacing hydraulic drives with electric drive systems. This more-electric approach expects to deliver higher efficiencies with similar or better dynamic performance, and it has been driven by the decreasing cost of variable frequency drives (VFDs), development of high torque permanent magnet synchronous motors (PMSMs), and advanced motor control. Some systems still retain some hydraulic components, such as electric actuation systems on more-electric aircrafts [1–5] and electric winches on cranes [6,7], while others have successfully been made fully electric, for example battery-powered crawler cranes [8].

Traditional hydraulic systems are often driven by a constant speed induction motor and use hydraulic valves to control the motion of the system. While some of the performance gain of electro-hydrostatic actuators (EHAs) comes from simply replacing the large size, high inertia, direct-on-line induction motor with an inverter driven high performance PMSM, the elimination of hydraulic proportional control valves reduces the power losses in the hydraulic circuit. Some systems which are typically hydraulically actuated may instead be driven by electric motors, for example winches, slewing motors, and traction motors. As with electric motors, the EHAs require electric power and are applicable in the following use cases:

- Grid-connected machines in docks, shipyards, and factories.
- Machines on ships connected to electric generators.
- Battery powered mobile machines.

With the increasing popularity of electric cars in the recent years, the development of electric heavy duty trucks and construction machinery is also receiving research interest. The use of a DC-bus in the form of a battery pack or capacitor bank facilitates the use of EHAs. While the hydraulic slewing motor on mobile machines may be replaced by an electric motor, the need for cylinders in cranes, excavators, front loaders, and other

mobile equipment still remain. For these machines the hydraulic cylinder is a critical component which still has no viable electric counterpart in high power applications [9], and it is known for high force capability, power density, ruggedness, and ability to handle impact loads. This has led to increasing interest in EHAs where, typically, a hydraulic cylinder is driven by a high performance electric motor with accompanying electric and hydraulic components. This hybrid drive approach attempts to give the system the best of both worlds in terms of efficiency, dynamic performance, and force capability.

Some commercial products of electro-hydrostatic systems exist, including servopumps from Baumüller [10], servohydraulic actuators from Bosch Rexroth [11], and variable speed pump drives from Bosch Rexroth [12] and Parker Hannifin [13]. While some systems extend traditional induction motor driven open loop circuits by adding VFDs, other systems use high performance servomotors along with closed loop hydraulic circuits. Typical applications for the commercial products include presses, injection molding machines, and die casting machines. The EHAs may be fully self-contained, or partially centralized with pipes or hoses connecting the cylinder to the motor/pump unit.

Commercial self-contained EHAs often use double rod cylinders which allow for small accumulators. Traditional heavy-duty hydraulic mobile machinery most often uses single rod cylinders to maximize force capability and reduce the complexity and size of the mechanical design. When using single rod cylinders with EHAs, the accumulator must be larger to compensate for the volume difference.

Other concepts of EHAs is included in [14–16] which investigates a self-contained cylinder with passive load holding. The cylinder is connected to a large boom with payload and operates in two quadrants. In [17] an excavator is used as a study case to compare a traditional load sensing circuit with separate closed loop circuits, each driven by an electric motor connected to two fixed displacement pumps. A study of a differential cylinder connected to two pumps is conducted in [18], studying the effect of pump displacement ratio and cylinder area ratio on energy recovery. Other topics of pump-controlled cylinders and EHAs include: load-holding topolgies [19,20], analysis of EHAs [21–23], energy regeneration in EHAs [24], optimization of EHAs [25], and EHAs for more-electric aircraft [26].

The purpose of this paper is to present a novel concept for an EHA as an alternative design to what is found in the provided references. The goal is to show the feasibility of EHAs in applications where traditional hydraulic systems are currently being used, for example hydraulic cranes. In addition, similar performance and better efficiency compared to traditional hydraulic systems are some of the reasons EHAs are of research interest for this paper.

2. Novel Concept

In this paper a novel concept for an EHA is presented. The concept is a closed loop controlled electric-hydraulic-mechanical system that controls a single degree of freedom. The closed-loop system is similar to the self-contained electro-hydrostatic systems which have gained popularity in the recent years. The concept of the EHA is designed to comply with the following requirements, shown in Table 1.

Table 1. Requirements for the EHA.

Functional Requirement	Typical Solution
Passive load holding	Counterbalance valves, POCVs, locking valves
Overload handling	Shock valves, relief valves
Differential flow compensation	Mode switching valves, accumulator, multiple pumps
Four-quadrant operation	Closed circuit with bidirectional pump

Passive load holding and overload handling are typical requirements for most hydraulic systems. Differential flow compensation is used to compensate for the different

areas of a single rod cylinder, while four-quadrant operation allows for regenerative braking sending power back to the electric grid or battery.

The hydraulic circuit of the EHA contains 2/2 poppet valves for load holding, relief valves for overload handling, accumulator and POCVs for differential flow compensation, and a bidirectional pump connected to a servomotor for four-quadrant operation. The proposed novel concept is shown in Figure 1.

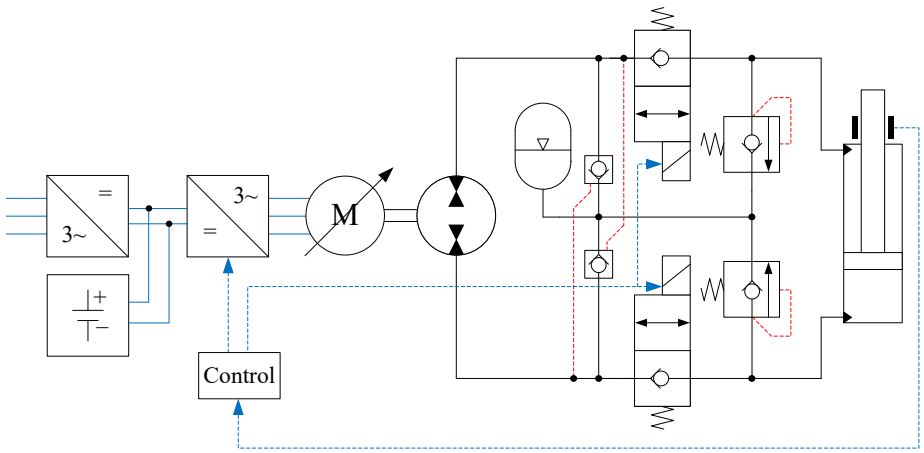

Figure 1. Proposed concept for the EHA.

Using electrically actuated 2/2 poppet valves for passive load holding allows for regenerative braking when they are opened. Typically, counterbalance valves are used and offer load holding and safe handling of overrunning loads. However, when operating the system with assistive loads in quadrants 2 and 4, they function as hydraulic brakes and dissipate the excess energy as heat. In addition, they require moderate pressure on the opposing line to open. By design, they cannot be used with regenerative braking systems. Another approach is to use an external pilot pressure to force the valve fully open when the system needs to move the load. This way the system retains the passive load holding and overload handling and is, in theory, capable of regenerating energy. The disadvantage is the requirement of an external pilot pressure of typically 50–150 bar, which may require an additional small pump when used in an EHA since the servomotor does not idle when no motion is needed. Illustrations of topologies for load holding and overload handling are shown in Figure 2.

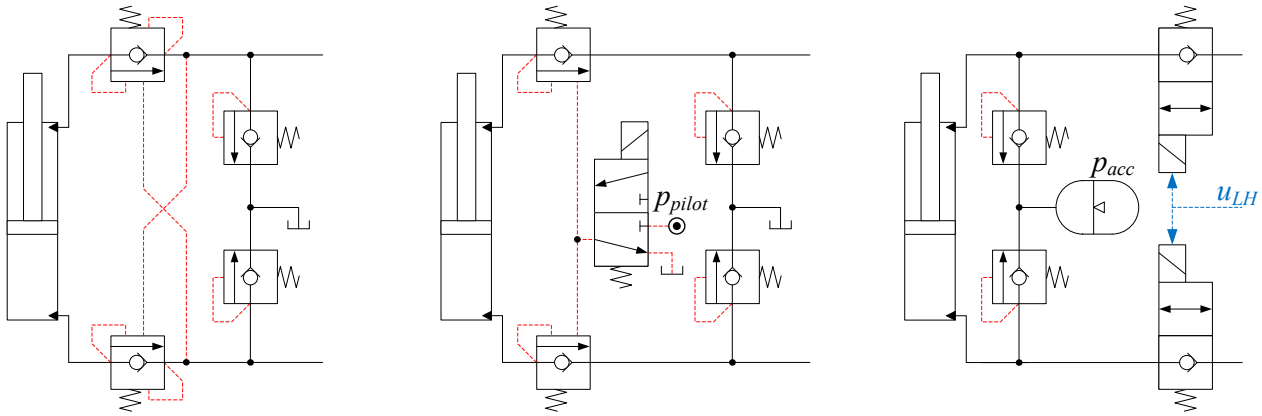

Figure 2. Examples of topologies for load holding and overload handling. (**a**) Traditional counterbalance valves and shock valves for a single rod cylinder; (**b**) Counterbalance valves opened by 3/2-valve and external pilot pressure; (**c**) Load holding design for EHA. Counterbalance valves are used in (**a**,**b**), while (**c**) uses poppet valves.

Four-quadrant operation is a crucial requirement for the EHA. An illustration of the load force, cylinder velocity, and hydraulic flows for each quadrant is shown in Figure 3. Red lines and blue lines denote high pressure and low pressure, respectively. The accumulator is always connected to the low pressure, and the flow in and out of the POCVs change depending on the quadrant.

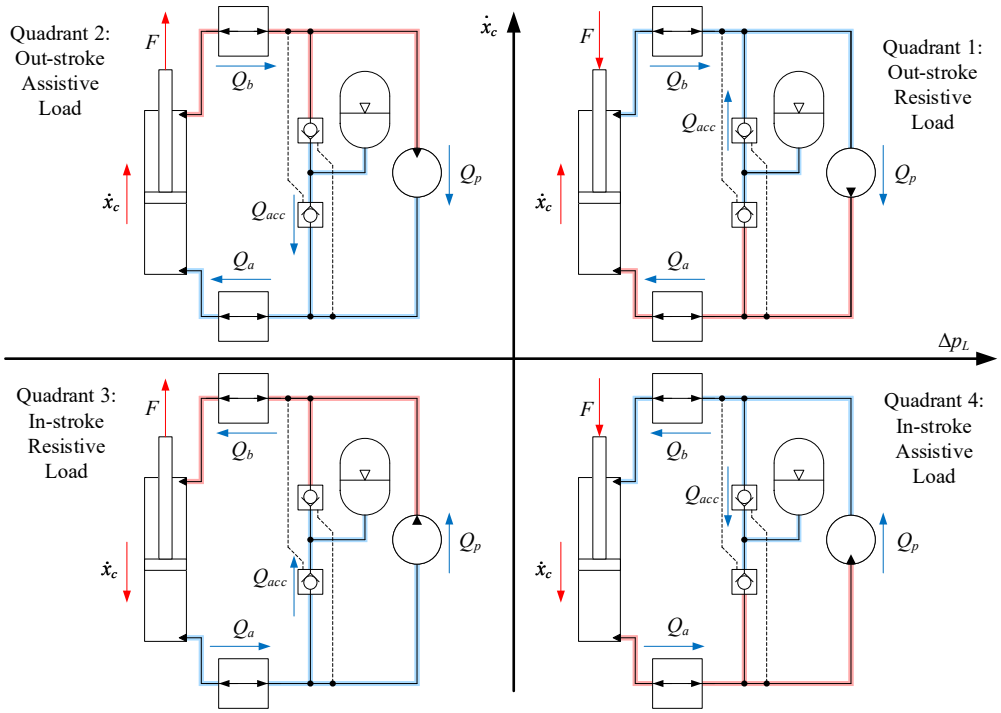

Figure 3. Four-quadrant operation of the simplified circuit with load holding valves energized.

3. Considered System

In this paper an HMF 2020K4 loader crane has been used as a basis for the detailed design and simulation of the EHA, shown in Figure 4. The novel concept is investigated by applying it to two degrees of freedom on a hydraulic loader crane; the main cylinder and the knuckle cylinder. Hence, components and control parameters are quantified and the concept is evaluated via time-domain simulations. The simulations are performed using an outer path control loop with anti-swing which have been developed earlier in [27,28]. The novel concept has also been compared with a traditional design with a single pump driven by an induction motor and proportional valves to control each actuator. The cylinder data are shown in Table 2.

Table 2. Cylinder data.

Name	Parameter	Value
Main cylinder piston diameter	$D_{p,m}$	0.160 m
Main cylinder rod diameter	$D_{r,m}$	0.100 m
Main cylinder stroke	h_m	0.75 m
Knuckle cylinder piston diameter	$D_{p,k}$	0.150 m
Knuckle cylinder rod diameter	$D_{r,k}$	0.100 m
Knuckle cylinder stroke	h_k	0.85 m

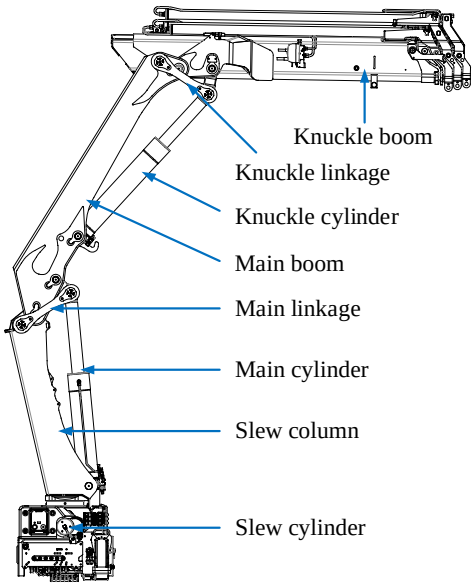

Figure 4. Illustration of the HMF 2020K4 loader crane.

4. Electro-Hydrostatic Actuator Design

The prime mover of the EHA is a servomotor which is driving a fixed displacement pump. The motor is connected to a servo drive modeled as a self-contained unit similar to commercial products and consists of a DC-bus, inverter, current controller, and speed controller.

4.1. Electric Servo System

The servomotor and controller are modeled in the dq-frame, using the Park transformation $\mathbf{P}$, defined in Equations (1) and (2).

$$\begin{bmatrix} u_d \\ u_q \end{bmatrix} = \mathbf{P} \begin{bmatrix} u_a \\ u_b \\ u_c \end{bmatrix} \tag{1}$$

$$\mathbf{P} = \begin{bmatrix} \cos(\theta_e) & \cos(\theta_e - \frac{2\pi}{3}) & \cos(\theta_e + \frac{2\pi}{3}) \\ -\sin(\theta_e) & -\sin(\theta_e - \frac{2\pi}{3}) & -\sin(\theta_e + \frac{2\pi}{3}) \end{bmatrix} \tag{2}$$

where

u_d = d-axis voltage;
u_q = q-axis voltage;
u_a = a-phase voltage;
u_b = b-phase voltage;
u_c = c-phase voltage;
θ_e = electrical rotor angle;

The governing equations for the PMSM in the dq-frame are given in Equations (3)–(5).

$$u_d = R_s i_d + L_d \frac{di_d}{dt} - N_p \omega i_q L_q \tag{3}$$

$$u_q = R_s i_q + L_q \frac{di_q}{dt} + N_p \omega (i_d L_d + \lambda_m) \tag{4}$$

$$T = \frac{3}{2} N_p (i_q (i_d L_d + \lambda_m) - i_d i_q L_q) \tag{5}$$

where

R_s = stator resistance;
L_d = d-axis inductance;

L_q = q-axis inductance;
N_p = number of pole pairs;
ω = motor speed;
λ_m = permanent magnet flux linkage;
T = rotor torque;

The controller uses Field Oriented Control (FOC) and operates in the dq-frame, shown in Figure 5. It uses the motor currents, rotor speed, and electrical rotor angle as feedback. The inner current PI-controller regulates the q-axis current i_q to generate the required torque, while the d-axis current reference $i_{d,ref}$ is kept at zero since the motor is not operated in the field weakening range. The outer speed PI-controller takes a speed reference as input from the user. Space vector modulation (SVM) is used to generate the signals to the inverter. Parameters for the controller are given in Table 3.

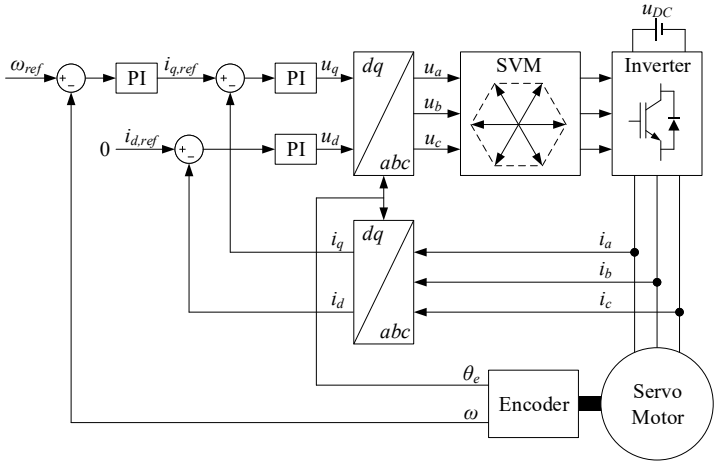

Figure 5. Illustration of the servo drive using FOC.

Table 3. Servo drive parameters.

Name	Parameter	Value
Proportional gain, speed loop	$k_{p,\omega}$	10 As/rad
Integral gain, speed loop	$k_{i,\omega}$	10 A/rad
Proportional gain, current loop	$k_{p,i}$	10 V/A
Integral gain, current loop	$k_{i,i}$	100 V/(A·s)
Controller sampling frequency	f_c	20 kHz
Inverter switching frequency	f_{sw}	2 kHz
DC-bus voltage	u_{DC}	565 V

The selected servomotor is a Beckhoff AM8064R, with its data shown in Table 4. The characteristic curves of speed-torque and speed-power are shown in Figure 6. Based on the maximum speed-torque curve shown in Figure 6a and the torque constant k_T, a torque limiter is made inside the speed PI-controller by limiting the current reference $i_{q,ref}$ using the measured motor speed.

The closed loop response of the servomotor and servo drive using FOC is shown in Figure 7. It shows excellent performance with a low rise time, no overshoot at the speed step, and minimal undershoot at the load step.

Table 4. Servomotor data Beckhoff AM8064R at 400 VAC (565 VDC).

Name	Parameter	Value
Standstill torque	T_0	49.6 Nm
Standstill current	I_0	30.8 A
Max torque	T_{max}	148 Nm
Max current	I_{max}	108 A
Rated torque	T_{rated}	36.5 Nm
Rated current	I_{rated}	24.4 A
Rated speed	n_{rated}	3000 rpm
Rated power	P_{rated}	11.5 kW
Torque constant	k_T	1.61 Nm/A
Line resistance	R_L	0.35 Ω
Line inductance	L_L	3.40 mH
Friction torque	T_{fric}	0.2 Nm
Rotor inertia	J	38.6 kgcm^2
Pole pairs	N_p	5
Thermal time constant	t_{th}	44 min

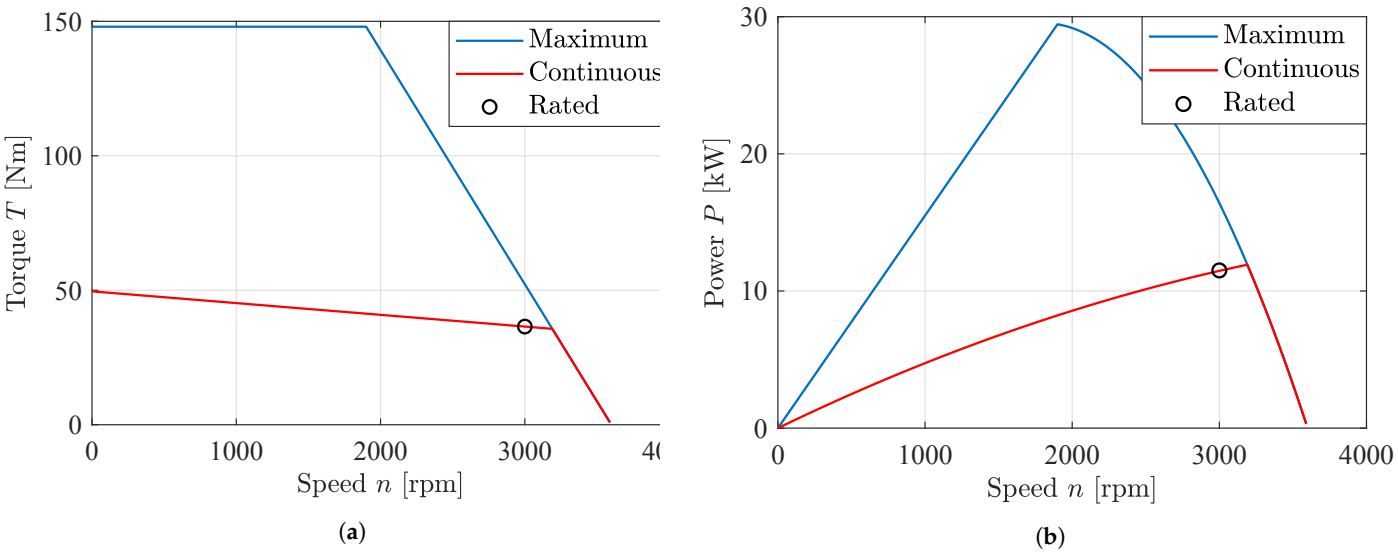

Figure 6. Torque and power curves for the selected motor with maximum, continuous, and rated operation. (**a**) Speed-torque curve; (**b**) Speed-power curve.

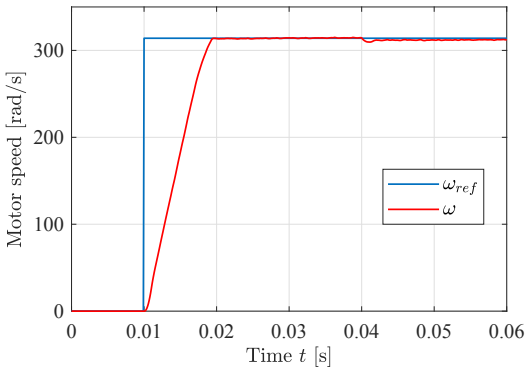

Figure 7. Servomotor closed loop dynamic response using FOC. Rated speed step at $t = 0.01$ s and rated load step at $t = 0.04$ s.

4.2. Hydraulic System

For this system a pressure level of 300 bar and a required flow of 40 L/min is selected yielding a peak power of 20 kW. The detailed design of the hydraulic circuit with, pump, valves, and pressure sensors is shown in Figure 8. The valve sizes can be chosen based on the selected pressure level and the rated flow of each valve, given in the datasheet. Optional oversizing to reduce the pressure drop may also improve system efficiency. The selected components are listed in Table 5.

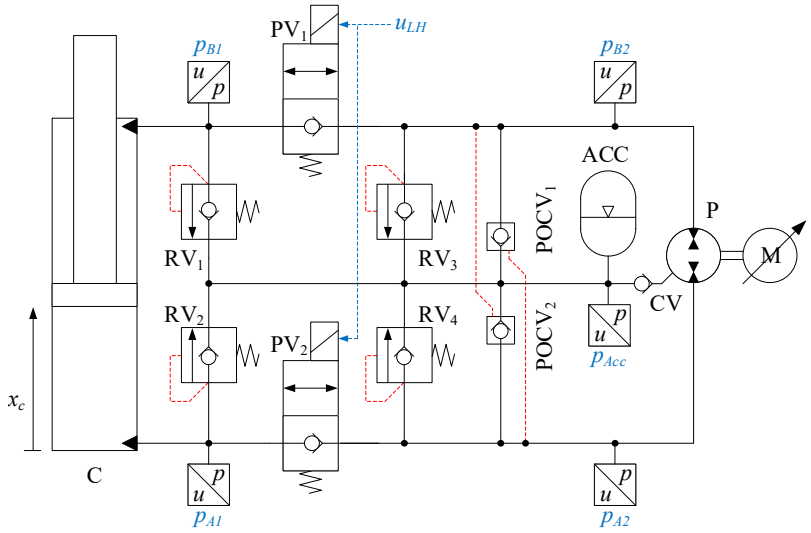

Figure 8. Novel closed-loop electro-hydrostatic actuator circuit.

Table 5. Components of the hydraulic system shown in Figure 8.

Component	Manufacturer	Model Number	Data
Servomotor (M)	Beckhoff [1]	AM8064R	11.5 kW
Hydraulic pump (P)	Bosch Rexroth [2]	A10FZG018	18 cm^3/rev
Accumulator (ACC)	Bosch Rexroth	HAB20	18.1 L
Check valve (CV)	Sun Hydraulics [3]	CXADXCN	28 L/min
Pilot-operated check valve (POCV)	Sun Hydraulics	CKCBXCN	57 L/min
Relief valve (RV)	Sun Hydraulics	RDDALCN	95 L/min
2/2 poppet valve (PV)	Parker Hannifin [4]	DSH121CR	90 L/min

[1] Verl, Germany; [2] Lohr, Germany; [3] Sarasota, USA; [4] Cleveland, USA.

Selecting the pump displacement in a traditional system primarily depends on the required flow if a standard constant speed induction motor is used. On the other hand servomotors are inherently variable speed devices and are typically offered with rated speeds from approximately 500 rpm to 10,000 rpm. Design considerations for the pump and motor include the selected pressure level, required flow, peak power, and maximum pump speed. For a given pump-motor combination a flow-pressure curve can be made showing the operating region of the system. This is shown for the selected pump and motor in Figure 9. The maximum pump speed and maximum pump pressure limits the operating region compared to the speed-torque curve shown in Figure 6a. Note that the design point is closer to the maximum rating than the continuous rating, as the servomotor is not expected to run continuously when used for position control.

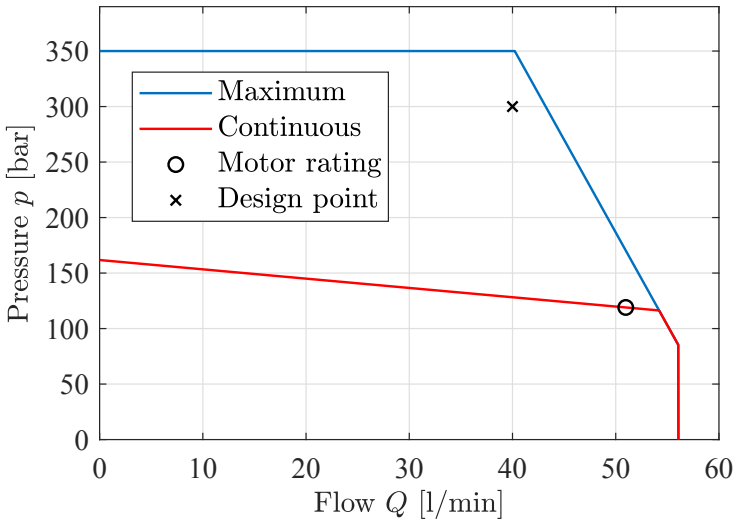

Figure 9. Flow-pressure curve with selected motor and pump.

Sufficient information for the hydraulic pump was not available in the datasheet, therefore the pump is modeled with the same efficiencies at nominal operating conditions as the pump in Section 7, with a volumetric, hydraulic-mechanical, and total efficiency at nominal operating conditions of $\eta_v = 0.94$, $\eta_{hm} = 0.93$, and $\eta = 0.88$. This yields a leakage coefficient of $k_{leak} = 0.0096$ l/min/bar and viscous damping coefficient of $b_{fric} = 0.02$ Nms/rad.

4.3. Control System for EHA

The control system for the EHA is shown in Figure 10 and is a feedback proportional position controller that utilizes a velocity feedforward line. The constant k_ω is the ratio from cylinder velocity to motor speed, defined in Equation (7). It depends on the load pressure difference Δp_L, cylinder areas A_a and A_b, and pump displacement D. In addition, pressure feedback is used based on the load pressure difference, which is going into a high pass filter, shown in Equation (8). This is to dampen oscillations in the cylinder motion. The EHA controller sends the motor speed reference ω_{ref} to the servo drive.

$$\omega_{ref} = k_\omega (k_p e_c + \dot{x}_{ref} - u_{PF}) \tag{6}$$

$$k_\omega = \begin{cases} \dfrac{A_a}{D}, & \Delta p_L > 0 \\ \dfrac{A_b}{D}, & \text{otherwise} \end{cases} \tag{7}$$

$$u_{PF} = \frac{k_{pf} s}{s + \omega_{pf}} \Delta p_L \tag{8}$$

$$\Delta p_L = p_{A1} - \frac{A_b}{A_a} p_{B1} \tag{9}$$

The load holding signal u_{LH} which opens the 2/2 poppet valves is defined in Equation (10). It is based on the cylinder position error e_c and cylinder velocity reference $\dot{x}_{c,ref}$.

$$u_{LH} = \begin{cases} 1, & |e_c| > 0.1 \text{ mm or } |\dot{x}_{c,ref}| > 0 \text{ m/s} \\ 0, & \text{otherwise} \end{cases} \tag{10}$$

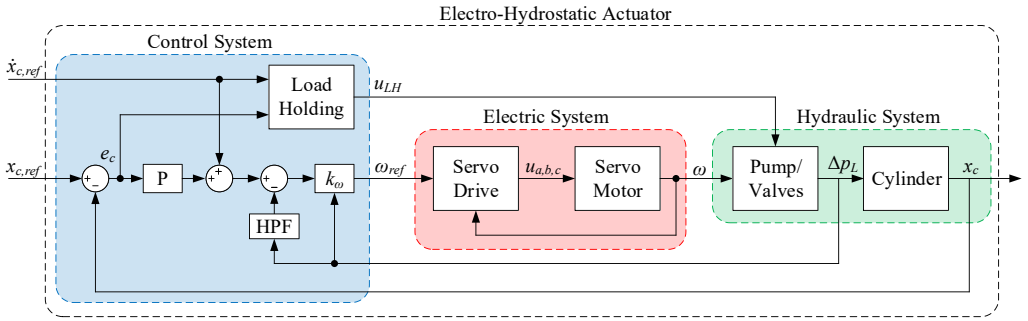

Figure 10. Overview of the EHA with control system, electric system, and hydraulic system.

5. Numerical Analysis of Four Quadrant Operation

A numerical analysis is conducted with the system connected to a constant load mass. The load mass m is 30,000 kg, and the accumulator pre-charge gauge pressure p_0 is 5 bar. The cylinder is moving the mass vertically. The force acting on the cylinder can be considered to consist of three parts; the hydraulic force, the gravitational force, and the friction force. The friction force is modeled with the viscous friction coefficient b_c and Coulomb friction force F_c as a function of the cylinder velocity $\dot{x}_c$. The parameter $\dot{x}_0$ is used to smooth the friction around zero velocity. The forces in quadrant 1 is shown in Equations (11) and (12). An illustration of the cylinder velocity and load mass in four quadrants is shown in Figure 11. The simulation model from MATLAB/Simulink is shown in Figure 12.

$$m\ddot{x}_c = \Delta p_L A_a - mg - F_{fric} \tag{11}$$

$$F_{fric} = b_c\dot{x}_c + F_c \tanh\left(\frac{\dot{x}_c}{\dot{x}_0}\right) \tag{12}$$

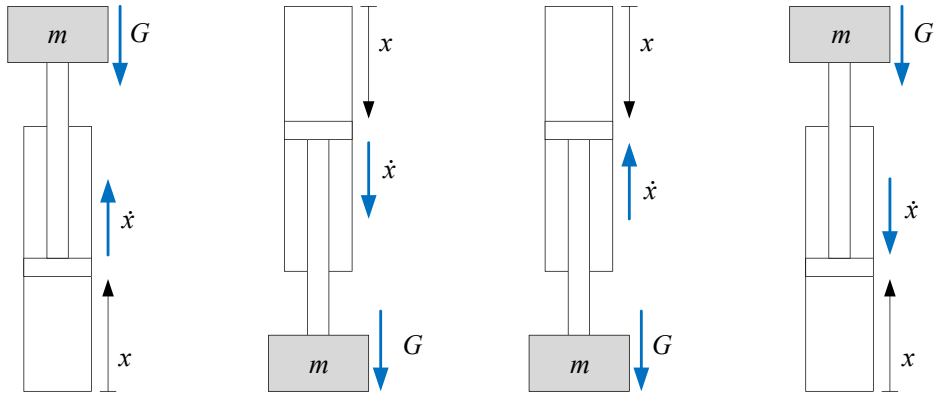

Figure 11. Illustration of four quadrant cylinder velocity and load mass with vertical motion.

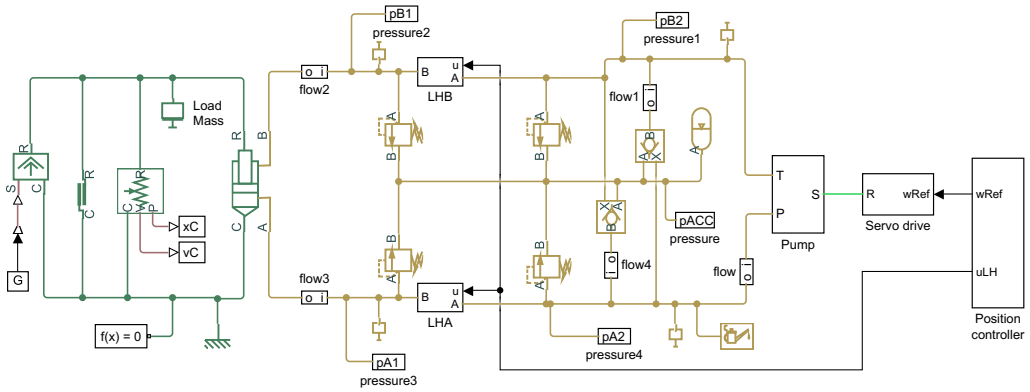

Figure 12. Simscape model of the EHA.

5.1. Tuning of Controller Parameters

The pressure feedback bandwidth ω_{pf} should be less than the minimum eigenfrequency of the hydraulic system $\omega_{hyd,min}$. This is to avoid filtering out the motion of interest. The minimum eigenfrequency is calculated based on the minimum hydraulic stiffness $k_{hyd,min}$, given below for a differential cylinder:

$$k_{hyd,min} = \frac{\beta(\sqrt{A_a} + \sqrt{A_b})^2}{h_m} \tag{13}$$

$$\omega_{hyd,min} = \sqrt{\frac{k_{hyd,min}}{m}} \tag{14}$$

For the cylinder in the Simscape model the minimum eigenfrequency is $\omega_{hyd,min} = 53.2$ rad/s, and the pressure feedback bandwidth is set one decade below at $\omega_{pf} = 5.32$ rad/s. The control parameters k_p and k_{pf} can easily be tuned manually or iteratively using the nonlinear Simscape model to achieve a balance between setpoint tracking and minimal oscillations. Another approach is to linearize the system and tune the controllers using linear control theory. A few assumptions and simplifications are made. Firstly, the load holding valves are ignored, meaning the pump is pushing fluid directly into the cylinder. The system is assumed to operate in Quadrant 1 meaning there is a high pressure on the piston-side of the cylinder and a low pressure on the rod-side, set to $p_{B1} = p_{B2} = p_{Acc} = 0$ bar. The cylinder is also assumed to be fully extended, $x_c = h_m$. A block diagram of the linearized model is shown in Figure 13.

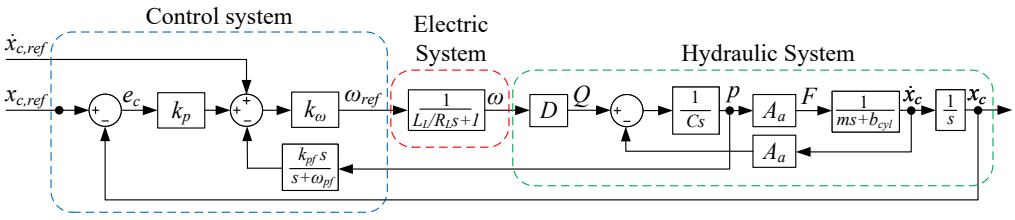

Figure 13. Closed-loop linear model of the EHA.

The electric system could in theory be linearized as a DC-equivalent motor with the servo drive containing PI-controllers for the motor current and motor speed. However, simplifications can be made where the transfer function from speed reference to motor speed has a time constant which approximates to the motor time constant $t_{motor} = \frac{L_L}{R_L}$. This assumes that the motor and drive are properly configured as a closed-loop system. The selected motor has a time constant of 9.7 ms, and it can be seen from the closed loop response in Figure 7 that this approximation is a good fit. A similar approach was also used in [15]. The linearized parameters used in the model are the hydraulic capacitance C,

and viscous damping for the cylinder and motor, given in Equations (15)–(17). A nominal cylinder speed of $\dot{x}_{c,nom} = 0.04$ m/s is used, and $\beta = 10^9$ Pa is used for the bulk modulus of the hydraulic oil.

$$C = \frac{A_a h_m}{\beta} \tag{15}$$

$$b_{cyl} = b_c + \frac{F_c}{\dot{x}_{c,nom}} \tag{16}$$

$$b_{motor} = \frac{T_{fric}}{\omega_{rated}} \tag{17}$$

Tuning of the two parameters k_p and k_{pf} can be done separately by rearranging the transfer functions for the control system, electric system, and hydraulic system, shown in Figure 14.

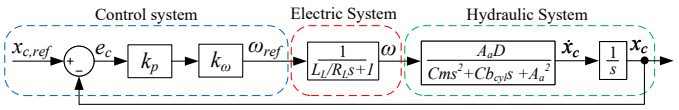

(**a**)

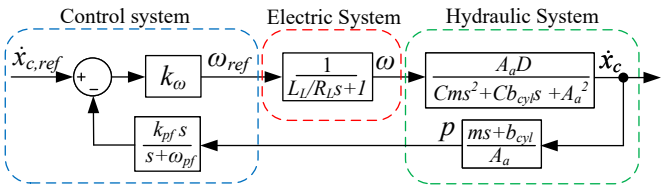

(**b**)

Figure 14. Simplified linear models used for tuning. (**a**) Linear model for tuning k_p; (**b**) Linear model for tuning k_{pf}.

Tuning these two models are straightforward, and can be done using for example bode plots, step responses, or MATLABs PID Tuner. The feedback gain k_p should provide fast setpoint tracking without excessive oscillations, and the pressure feedback gain k_{pf} should dampen the oscillations without slowing the system down. The step responses are

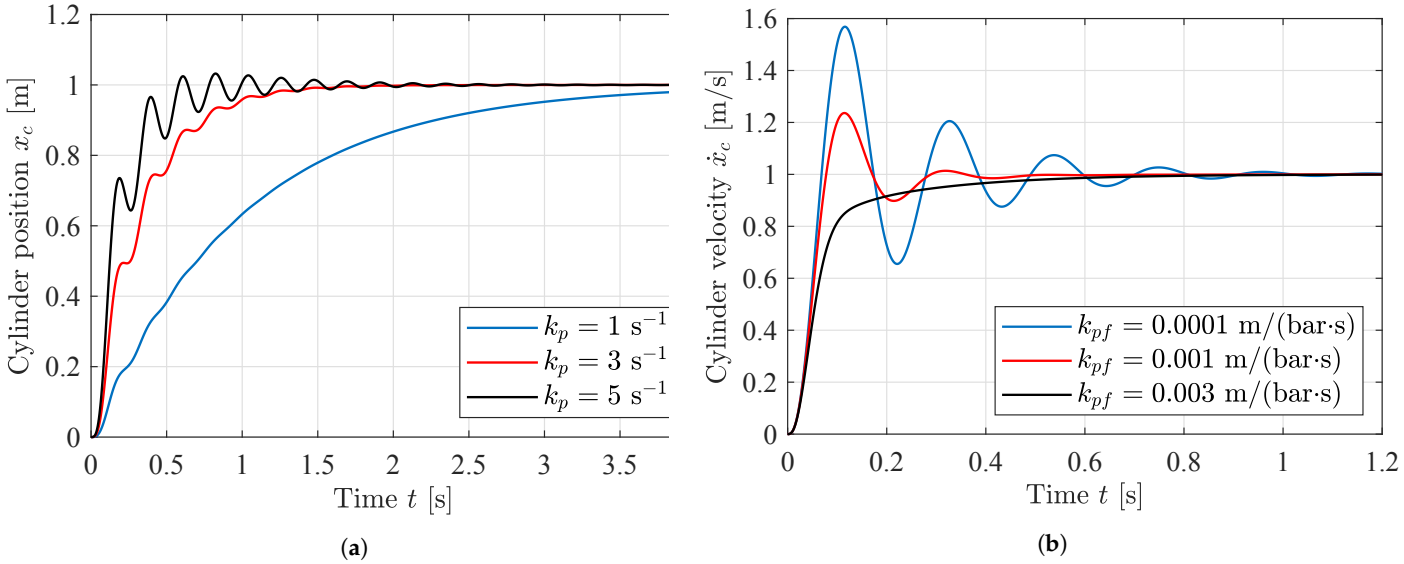

(**a**) (**b**)

Figure 15. Step responses from the linear models. (**a**) Tuned step responses of k_p from Figure 14a; (**b**) Tuned step responses of k_{pf} from Figure 14b.

5.2. Simulation Results From Simscape Model

While the linearized models can provide some insight to appropriate controller parameters, the non-linear Simscape model is used to verify the performance of the EHA and its control system. The controller parameters have been selected based on both the linear and nonlinear model. The friction parameters have been estimated from the HMF 2020K4 crane in the laboratory. Simulation parameters are shown in Table 6.

Table 6. Simulation parameters.

Name	Parameter	Value
Proportional gain	k_p	5 s^{-1}
Pressure feedback gain	k_{pf}	0.001 m/(bar·s)
Pressure feedback bandwidth	ω_{pf}	5.32 rad/s
Load mass	m	30,000 kg
Viscous friction	b_c	150 kNs/m
Coulomb friction	F_c	4 kN
Smoothing parameter	$\dot{x}_0$	0.001 m/s

Position and position error during the simulation are shown in Figure 16. The system shows excellent position tracking in all four quadrants. The cylinder is following a trapezoidal velocity profile from 0.5 m and traveling 0.2 m.

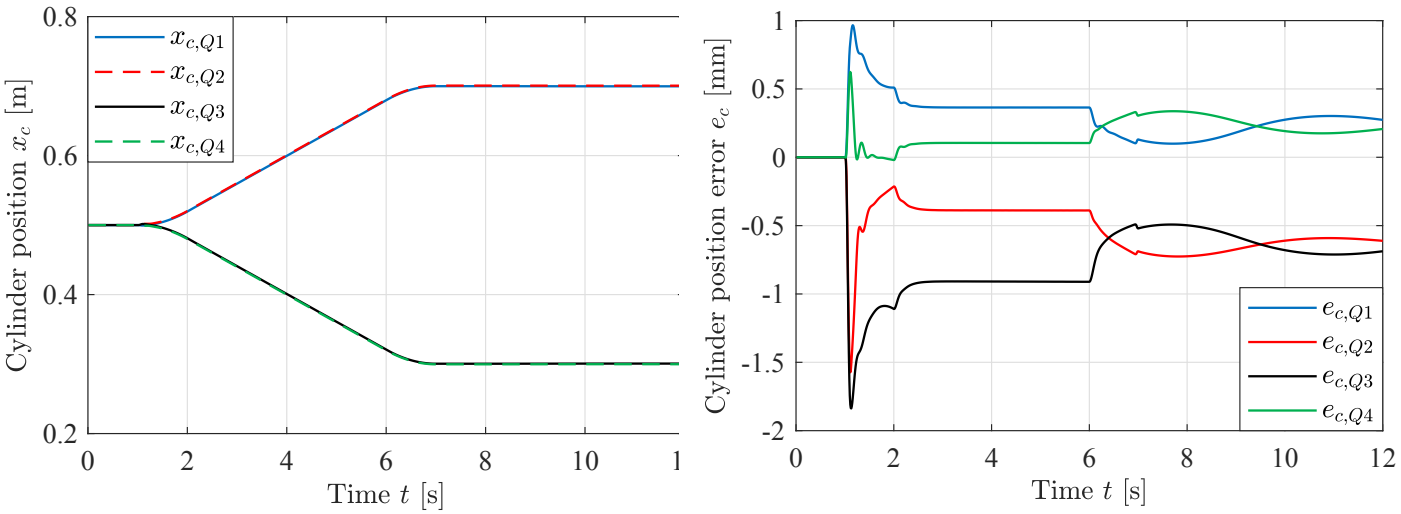

(**a**) (**b**)

Figure 16. Cylinder position and position error for all four quadrants. (**a**) Cylinder position x_c; (**b**) Cylinder position error e_c.

The cylinder velocity and motor speed are shown in Figure 17. The cylinder velocity reference is a trapezoid, while the motor speed reference is generated by the EHA controller. Both the cylinder and the motor follow the reference during motion with minimal overshoot.

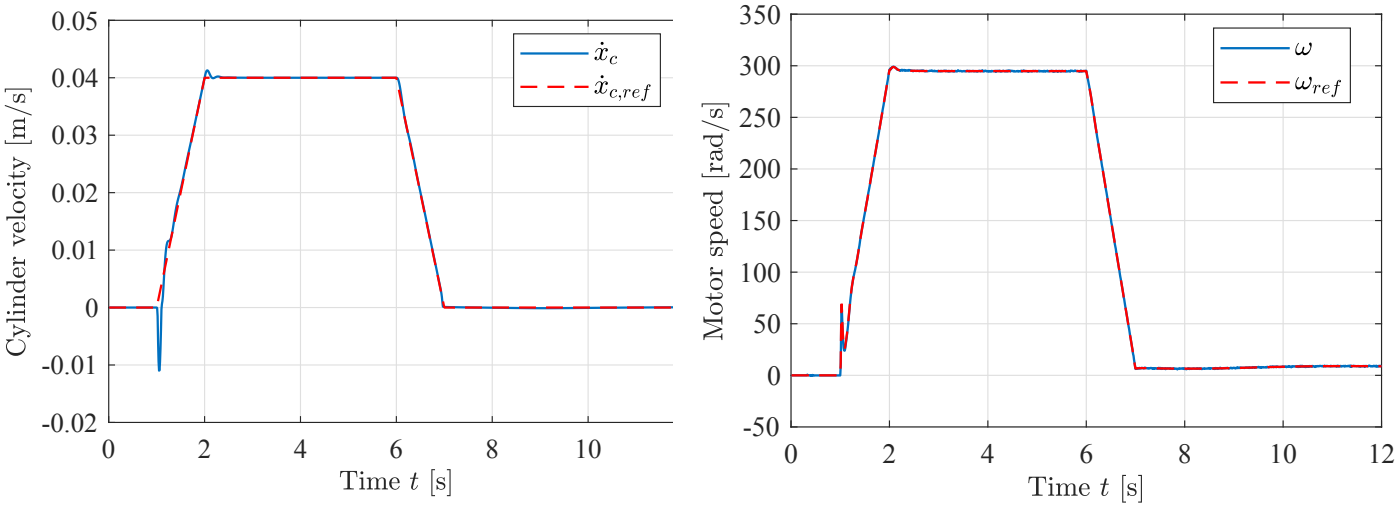

(**a**) (**b**)

Figure 17. Cylinder velocity and motor speed for operation in quadrant 1. (**a**) Cylinder velocity $\dot{x}_c$; (**b**) Motor speed ω.

Plots of the system pressures are shown in Figure 18. The pressures are not oscillating, showcasing stability during motion. The cylinder pressures are higher in quadrant 2 and 3 since the gravitational force is acting on the smaller rod-side area. The system pressures are lowest in quadrant 2, but the system is not experiencing cavitation.

The system efficiency is of significant interest for the EHA. To calculate the efficiency of the system, the power coming from/going into the DC-bus, accumulator, and cylinder must be considered. While the contribution from the accumulator is rather small, depending on the quadrant, the accumulator can receive or deliver power to either the cylinder or back to the DC-bus. The system consumes approximately 15 kW when pumping, and delivers approximately 10 kW when motoring. The efficiency during motion is between 0.78 and 0.85, shown in Figure 19.

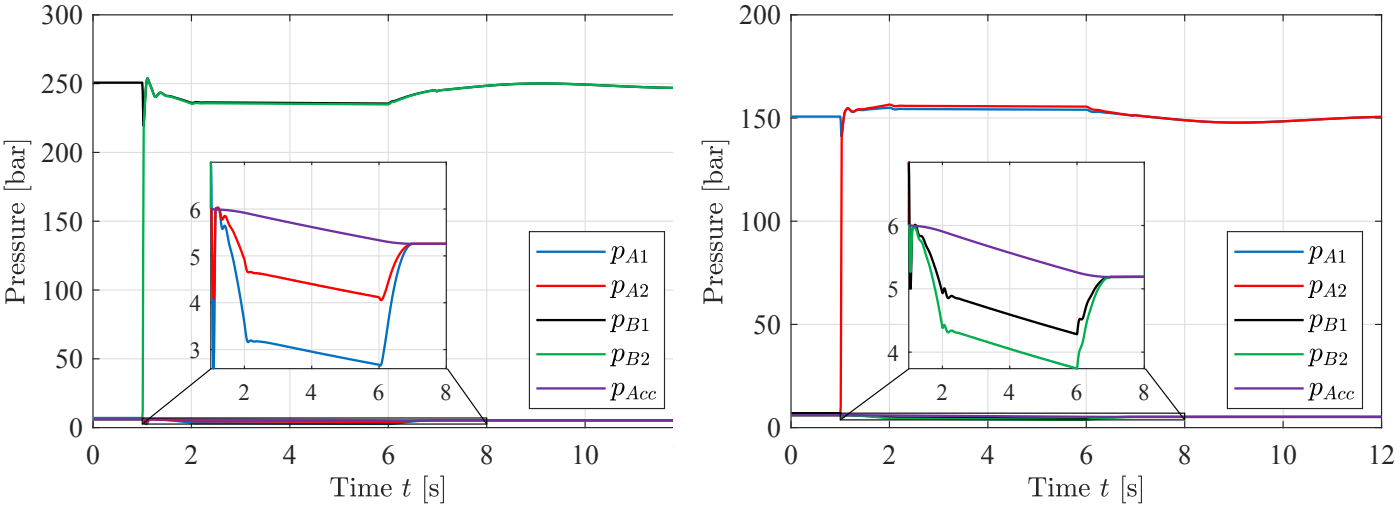

(**a**) (**b**)

Figure 18. *Cont.*

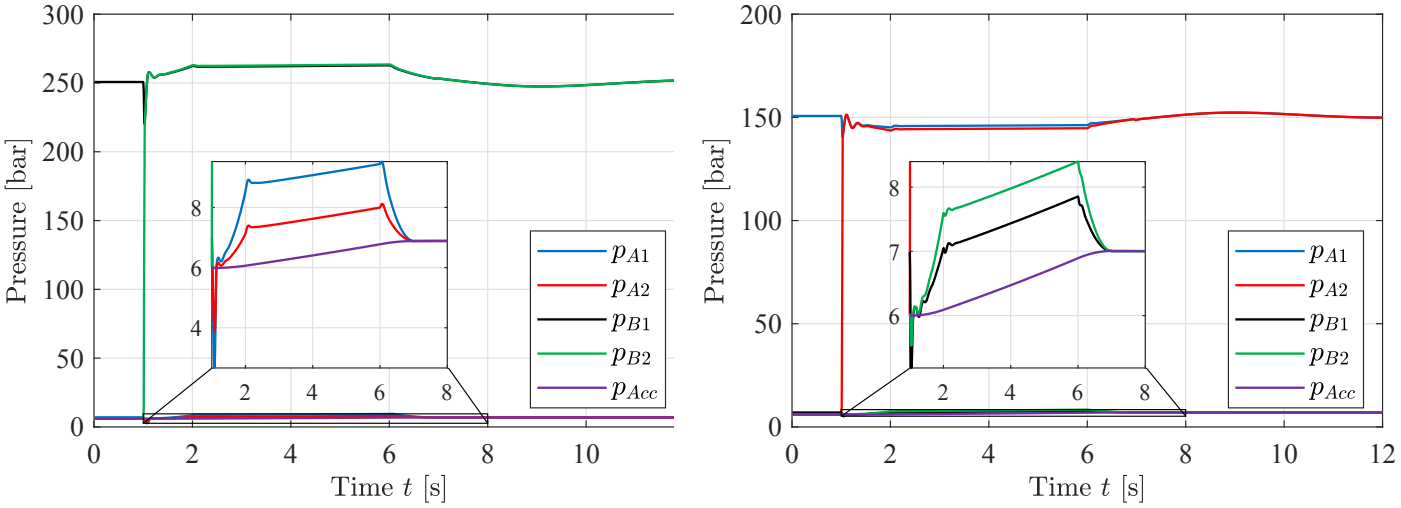

(**c**) (**d**)

Figure 18. System pressures for all four quadrants during motion. (**a**) Quadrant 2; (**b**) Quadrant 1; (**c**) Quadrant 3; (**d**) Quadrant 4.

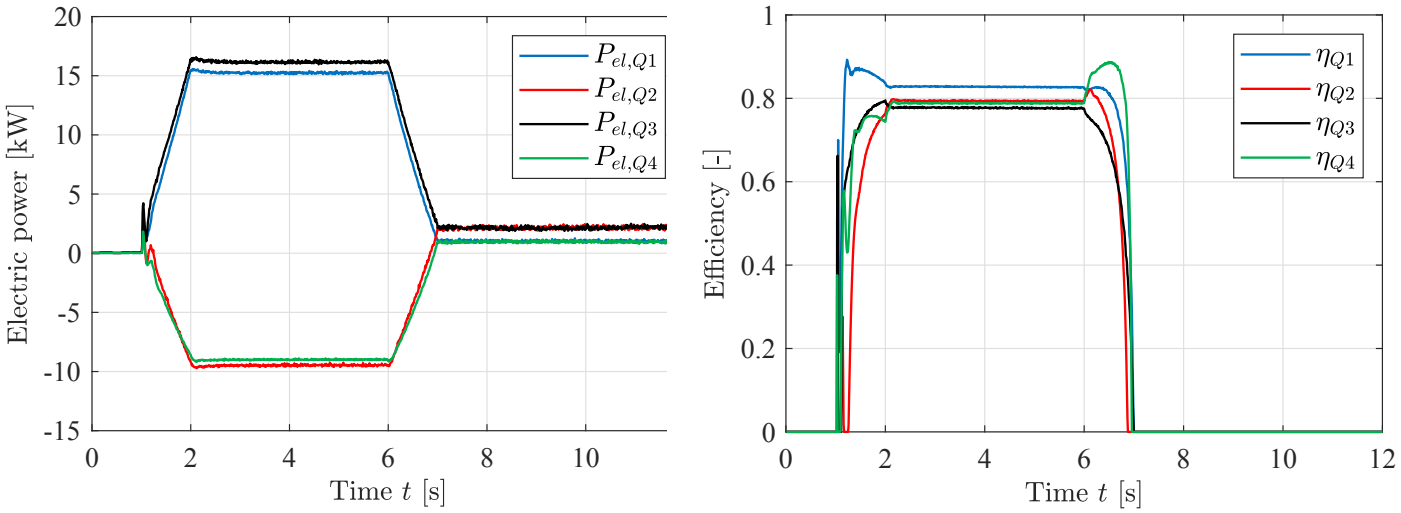

(**a**) (**b**)

Figure 19. Electric power and efficiency for all four quadrants. Operation in quadrants 1 and 3 consume power, while operation in quadrants 2 and 4 regenerate power. (**a**) Electric power P_{el} from/to the DC-bus; (**b**) Efficiency η of the system.

6. Thermal Considerations

To model the thermal behavior of the servomotor a first order transfer function is used. The input is the power dissipated in the motor and the output is the motor temperature above ambient. The thermal time constant $t_{th} = 44$ min is given in Table 4 and the steady state gain can be calculated from rated operation. The motor is rated thermal class F which allows a temperature rise of 105 °C above ambient. The calculations are shown in Equations (18)–(20). Figure 20 shows the allowable continuous current to stay below

105 °C as a function of the motor speed ω. The thermal model is very close to the data interpolated from the datasheet.

$$t_{motor} = \frac{k_{th}}{t_{th}s + 1} P_{diss} \tag{18}$$

$$P_{diss} = I^2 R + |\omega| T_{fric} \tag{19}$$

$$k_{th} = \frac{105°\text{C}}{I_{rated}^2 R + |\omega_{rated}| T_{fric}} = 0.6287°\text{C/W} \tag{20}$$

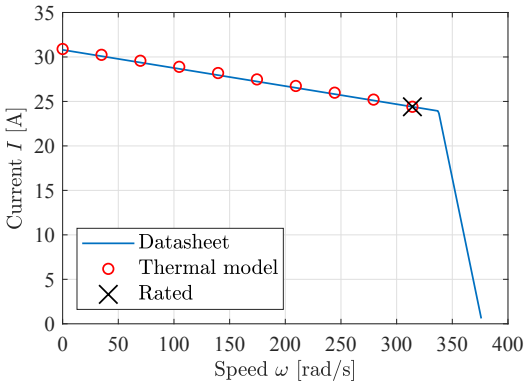

Figure 20. Allowable continuous current to stay below 105 °C.

To simulate the dynamic thermal behavior of the motor a load cycle similar to the one used in Section 5 is used. The system operates in quadrant 1 and 4. The motor current and motor speed are then passed into the thermal model which runs this load cycle for 5 h. The system is tested with different payloads to analyze the temperature response. Plots of the load cycle and temperature are shown in Figure 21. These results show that the system is able to operate indefinitely with the load mass used in Section 5 of 30,000 kg (30 Ton).

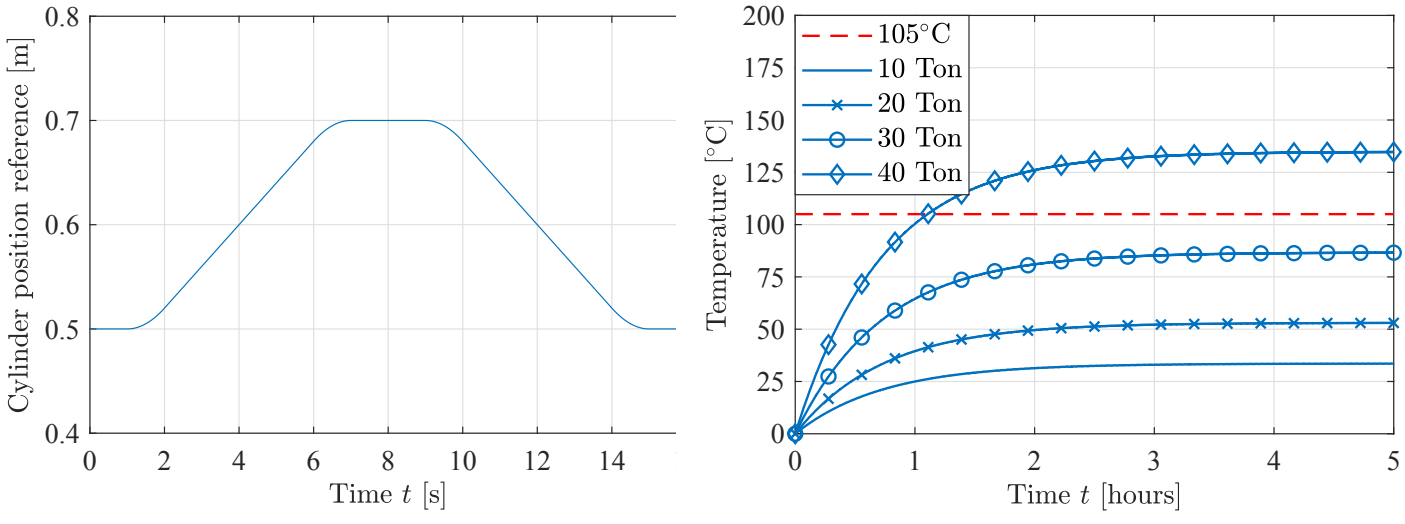

(**a**) (**b**)

Figure 21. Position reference and temperature for the load cycle running repeatedly for 5 h. (**a**) Position reference; (**b**) Temperatures with different loads.

7. Valve-Controlled System

In the valve-controlled system the two cylinders are driven by a single variable displacement load sensing pump. A pressure compensator, directional control valve, and counterbalance valves control the motion of each cylinder. This is a state-of-the-art

load sensing design which is commonly used in industrial applications such as offshore hydraulic cranes, as well as the HMF 2020K4 crane in the laboratory. An illustration of the hydraulic circuit is shown in Figure 22.

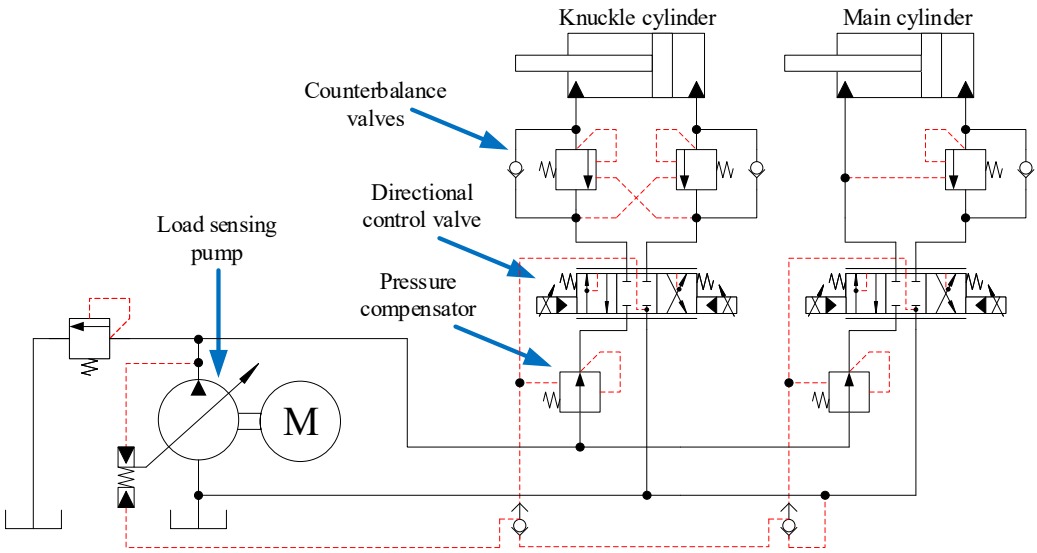

Figure 22. Hydraulic circuit for the valve-controlled system.

The pressure compensator throttles the flow to ensure that there is a constant pressure drop over the directional control valve. This in turn gives a load independent flow. The governing equations of the pressure compensator in steady state are given in Equations (21) and (22).

$$p_{load} = \begin{cases} p_a & \text{if } u_{spool} \geq 0 \\ p_b & \text{otherwise} \end{cases} \tag{21}$$

$$p_p = p_{load} + p_{set} \tag{22}$$

where

p_p = compensated pressure at port p;
p_a = pressure at port a;
p_b = pressure at port b;
p_{set} = spring pressure setting;
p_{load} = load pressure;
u_{spool} = position of the main spool, $-1 \leq u_{spool} \leq 1$;

Double counterbalance valves are used on the knuckle cylinder, and throttle the flow to assist in load holding and load lowering. The unitless openings of the counterbalance valves are calculated in Equations (23) and (24).

$$u_a = \frac{p_{a2} + \psi p_{b1} - p_{crack,a}}{\Delta p} \tag{23}$$

$$u_b = \frac{p_{b2} + \psi p_{a1} - p_{crack,b}}{\Delta p} \tag{24}$$

where

u_a = opening of valve a, $0 \leq u_a \leq 1$;
u_b = opening of valve b, $0 \leq u_b \leq 1$;
p_{a1} = pressure at valve a input side;
p_{a2} = pressure at valve a actuator side;
p_{b1} = pressure at valve b input side;
p_{b2} = pressure at valve b actuator side;

$p_{crack,a}$ = crack pressure of valve a;
$p_{crack,b}$ = crack pressure of valve b;
ψ = pilot area ratio;
Δp = pressure difference for full opening;

The pump is a Bosch Rexroth A4VSO with a displacement of 71 cm^3/rev. The datasheet for the pump yields a laminar leakage model, with a leakage coefficient of $k_{leak} = 0.02$ L/min/bar. The friction model has been interpolated to be viscous friction with a damping coefficient of $b_{fric} = 0.14$ Nms/rad. This gives a volumetric, hydraulic-mechanical, and total efficiency at nominal operating conditions of $\eta_v = 0.94$, $\eta_{hm} = 0.93$, and $\eta = 0.88$, respectively. Based on the estimated parameters a contour plot of the pump total efficiency as a function of pressure and flow is shown in Figure 23, showing poor efficiency when operating with either low flow or low pressure.

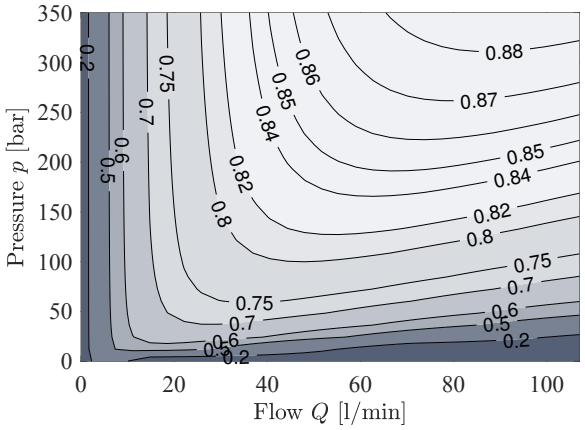

Figure 23. Pump total efficiency η as a function of pressure and flow with estimated parameters.

During operation the pump pressure and pump flow are functions of the load sensing pressures and actuator flows, given in Equations (25) and (26). A margin pressure p_{margin} is added to the pump pressure setting. This is to ensure the pressure compensator has some headroom to adjust the pressure drop over the directional control valve. A consequence of this margin pressure is the poor efficiency seen when the load pressures are low. The margin pressure typically ranges from 10 bar to 30 bar, and $p_{margin} = 20$ bar is used in this simulation.

$$p_{pump} = \max(p_{LS,m}, p_{LS,k}) + p_{margin} \tag{25}$$

$$Q_{pump} = Q_m + Q_k \tag{26}$$

The hydraulic pump is driven by a constant speed induction motor. The motor is selected to be an IE3 4-pole 30 kW induction motor from ABB [29]. The motor data given in the datasheet is shown in Table 7, and the dynamic motor model is shown in Figure 24.

Table 7. Induction motor data ABB 3GBP202410 at 400 VAC 50 Hz.

Name	Parameter	Value
Nominal power	P_n	30 kW
Nominal torque	T_n	193 Nm
Nominal speed	n_n	1483 rpm
Nominal current	I_n	54.8 A
Rotor inertia	J	0.385 kgm^2
Power factor	$\cos(\phi)$	0.84
Efficiency	η	0.936
Pole pairs	N_p	2

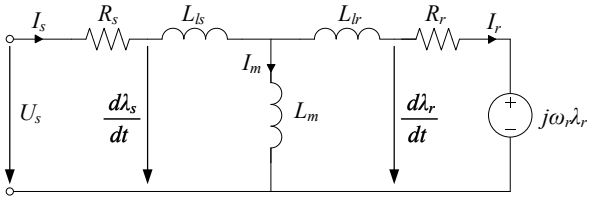

Figure 24. Dynamic induction motor model.

The motor parameters have been estimated based on the motor data with the following estimations and assumptions:

- Leakage inductances L_{ls} and L_{lr} are 5% of the magnetizing inductance L_m. The nominal stator flux λ_s, magnetizing current I_m, and inductances L_s and L_r can then be calculated as

$$\lambda_s = \frac{400\text{ V}}{2\pi 50\text{ Hz}} = 1.2732\text{ Wb} \tag{27}$$
$$I_m = jI_n \sin(\phi) = j29.73\text{ A} \tag{28}$$
$$L_m = \frac{\lambda_s}{|I_m|} = 42.8\text{ mH} \tag{29}$$
$$L_{ls} = 0.05L_m = 2.2\text{ mH} \tag{30}$$
$$L_{lr} = 0.05L_m = 2.2\text{ mH} \tag{31}$$
$$L_s = L_{ls} + L_m = 45\text{ mH} \tag{32}$$
$$L_r = L_{lr} + L_m = 45\text{ mH} \tag{33}$$

- Stator conduction losses contribute to 40 % of the losses. The stator resistance R_s is then calculated as

$$R_s = \frac{0.4P_n(1-\eta)}{3I_n^2} = 0.0852\ \Omega \tag{34}$$

- Rotor conduction losses contribute to 40 % of the losses. The rotor current I_r and rotor resistance R_r are calculated as

$$I_s = I_n \cos(\phi) + jI_n \sin(\phi) \tag{35}$$
$$I_r = I_s - I_m = I_n \cos(\phi) \tag{36}$$
$$R_r = \frac{0.4P_n(1-\eta)}{3I_r^2} = 0.1208\ \Omega \tag{37}$$

- The last 20 % of the losses are modeled as Coulomb friction losses. The friction torque T_{fric} is calculated as

$$T_{fric} = 0.2T_{rated}(1-\eta) = 2.47\text{ Nm} \tag{38}$$

As the efficiency of the motor model is crucial to determine the efficiency of the system, a numerical simulation with constant load is used as verification. The dynamic response and efficiency of the motor is shown in Figure 25, with startup at 1 second, and full load at 3 s. The efficiency of the motor matches the motor data, shown with a dash-dotted line.

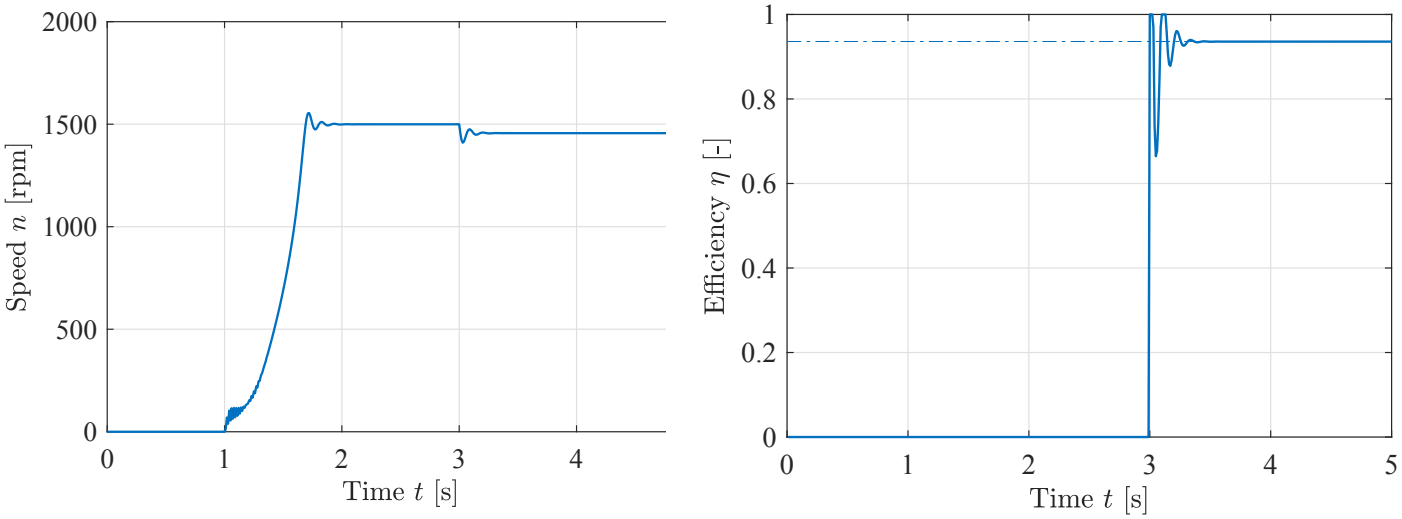

(**a**) (**b**)

Figure 25. Motor speed and efficiency during startup and full load. (**a**) Motor speed using the estimated parameters; (**b**) Motor efficiency using the estimated parameters (solid line) and motor data (dash-dotted).

8. Load Case: Path Control and Anti-Swing for Hydraulic Crane

To test the performance of the developed system, numerical simulations are carried out with path control and anti-swing as a load case. Path control and 2-DOF anti-swing have previously been developed in [27,28]. An illustration of the HMF 2020K4 crane with hanging load is shown in Figure 26. A block diagram of the path control, anti-swing control, and the crane is shown in Figure 27. The green blocks have been developed earlier, the red blocks represents the mechanical system, and the blue blocks represents either the valve-controlled system or the EHA developed in this paper. The cylinder position reference used in the path controller is shown in Figure 28. The path is designed such that the knuckle cylinder operates in all four quadrants during motion. Two simulations are carried out running the same path, one with a traditional valve-controlled system, and one with the new EHA.

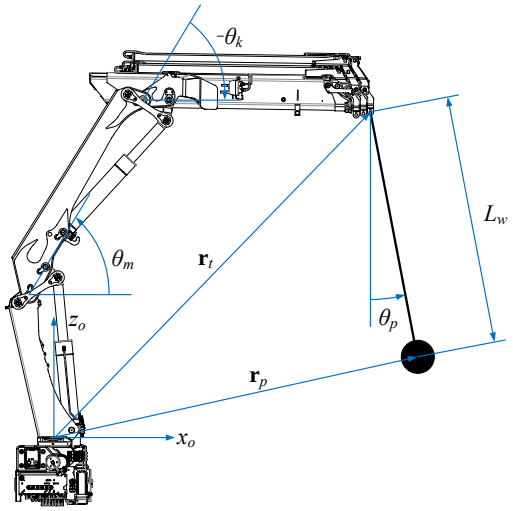

Figure 26. Illustration of the HMF crane with hanging load.

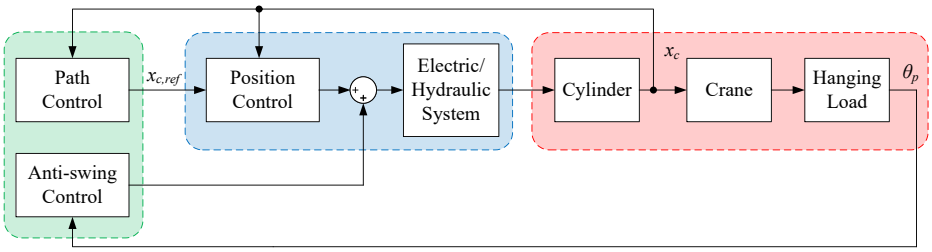

Figure 27. Block diagram of the path control, anti-swing control, and crane.

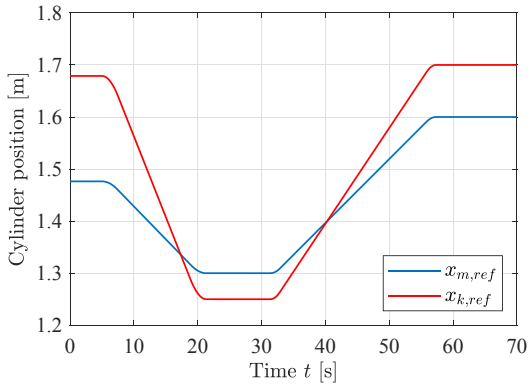

Figure 28. Cylinder position reference during load case.

8.1. Simulation with Valve-Controlled Actuators

The first test is the original valve-controlled system running path control and 2D anti-swing. Compare energy efficiency etc. The simulation is carried out with the same controller parameters used in [28].

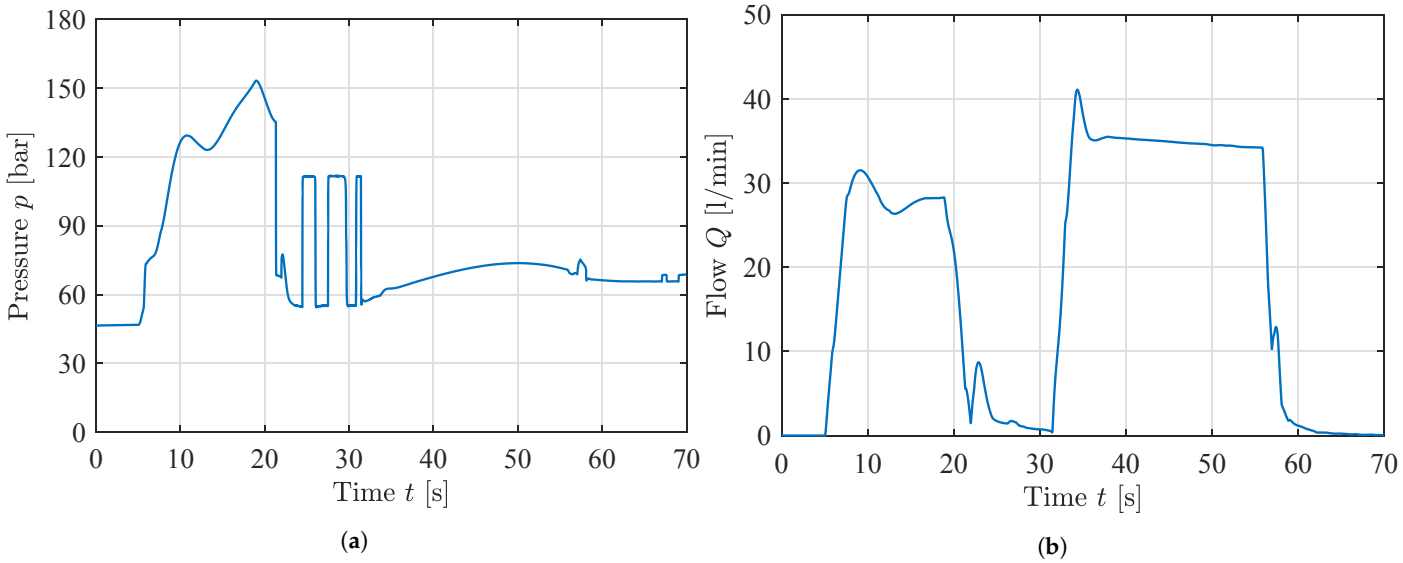

(**a**) (**b**)

Figure 29. Pump pressure and flow during motion with valve-controlled actuators. (**a**) Pump pressure; (**b**) Pump flow.

A plot of the power and consumed energy is shown in Figure 30. During motion 46 kJ was delivered to the cylinders while 505 kJ was consumed from the grid. This yields an overall efficiency of less than 0.1.

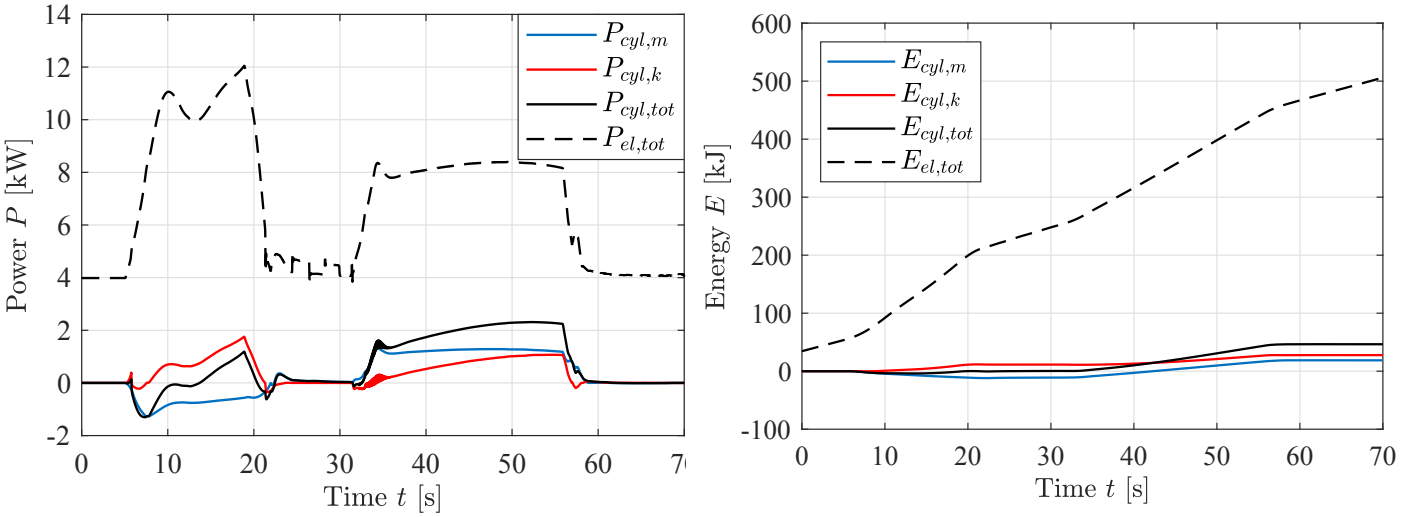

(**a**) (**b**)

Figure 30. Power and energy during motion with valve-controlled actuators. (**a**) Power from the grid and to the cylinders; (**b**) Consumed energy with valve-controlled actuators.

The cylinder position error and swing angle are shown in Figure 31 to evaluate the performance of the control system. The RMS value of the position errors and swing angle are calculated to be RMS(e_m) = 5.8 mm, RMS(e_k) = 3.6 mm, and RMS(θ_p) = 4.3 mrad.

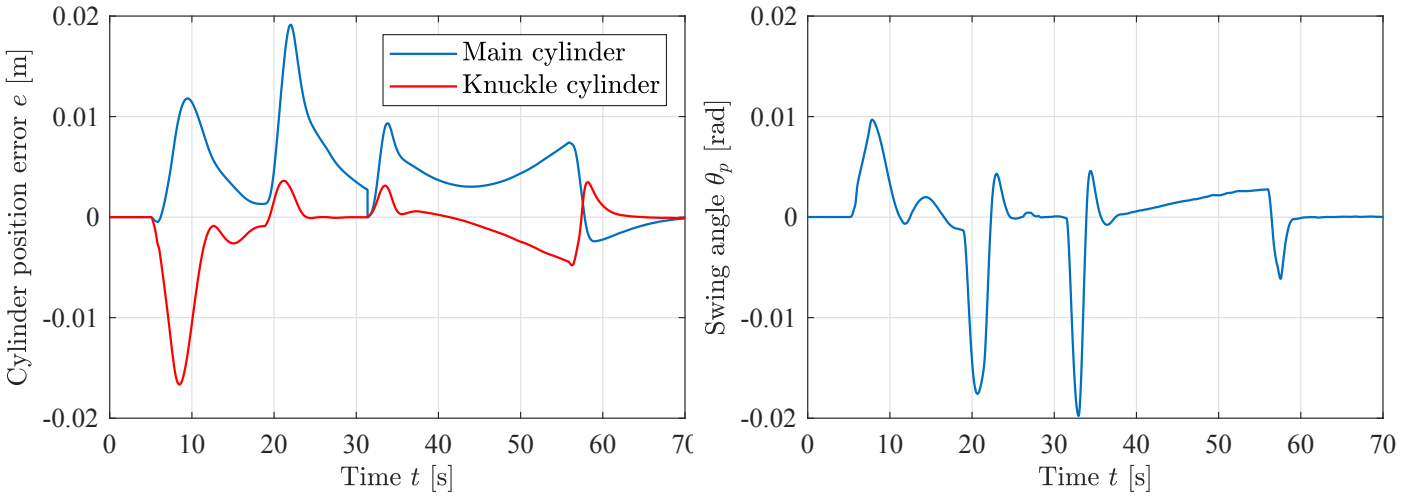

(**a**) (**b**)

Figure 31. Cylinder position error and swing angle during motion with valve-controlled actuators. (**a**) Cylinder position error; (**b**) Swing angle.

8.2. Simulation with Electro-Hydrostatic Actuators

The second test is when two separate EHAs are mounted on the HMF 2020K4 and running path control and 2D anti-swing.

Plots of the pressures and flows in the knuckle circuit are shown in Figure 32. Some oscillations can be seen as the system compensates for the swing angle during motion.

A plot of the electric power P_{el} from the grid and the power to the cylinders P_{cyl} is shown in Figure 33. Negative power indicate that the system is regenerating power. The total power is the sum of the main EHA and knuckle EHA.

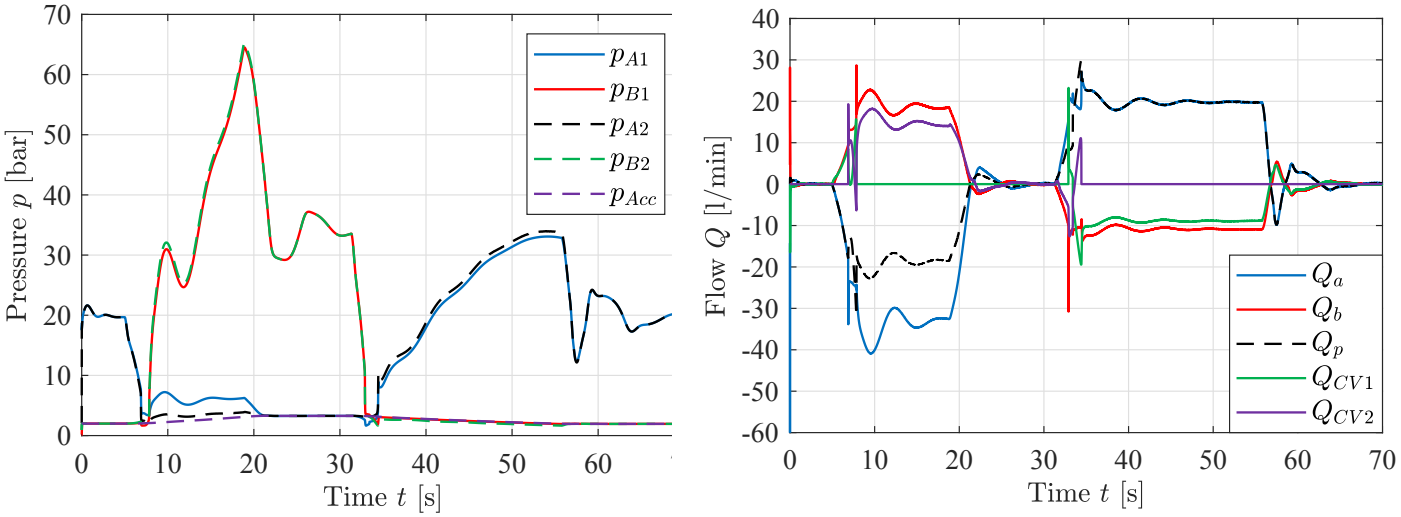

(**a**) (**b**)

Figure 32. Press

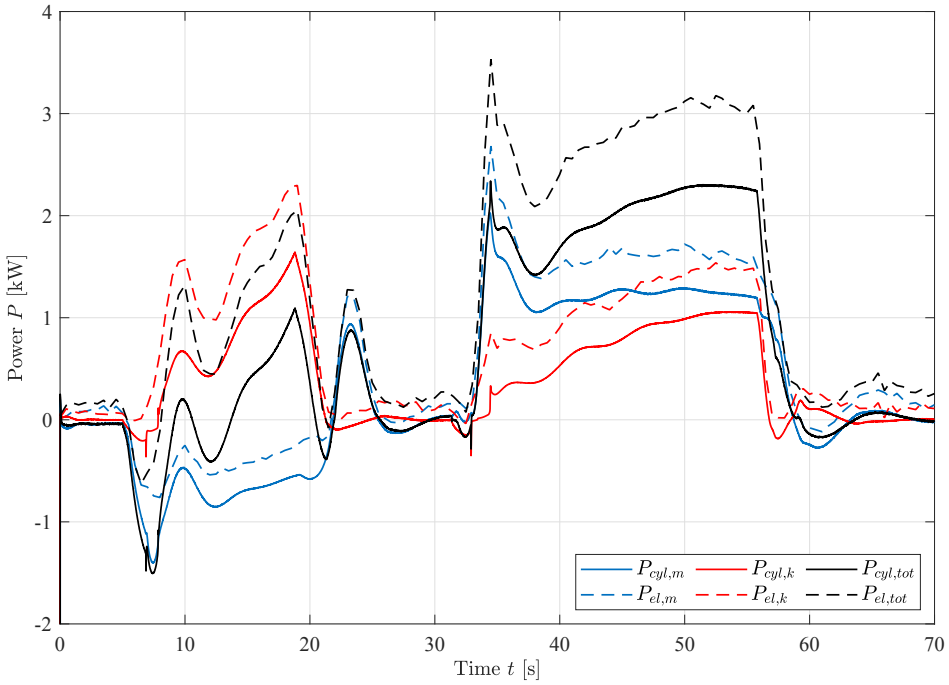

Figure 33. Power from the grid (dashed) and power to the cylinders (solid) with EHAs.

A plot of the consumed energy is shown in Figure 34. After completing the motion 47 kJ was delivered to the cylinders while 88 kJ was consumed from the grid.

Cylinder position error and swing angle are shown in Figure 35 to verify the performance of the novel concept. The RMS value of the position errors and swing angle are calculated to be RMS(e_m) = 5.4 mm, RMS(e_k) = 3.3 mm, and RMS(θ_p) = 4.4 mrad, virtually identical to the valve-controlled system.

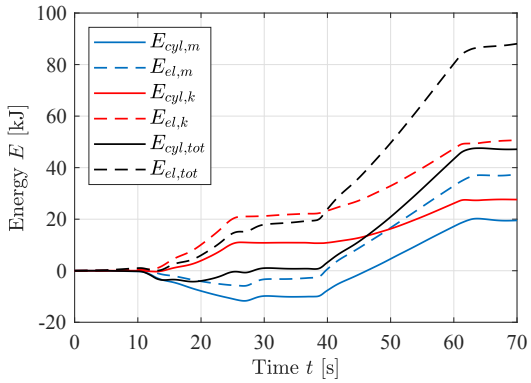

Figure 34. Energy consumed during motion

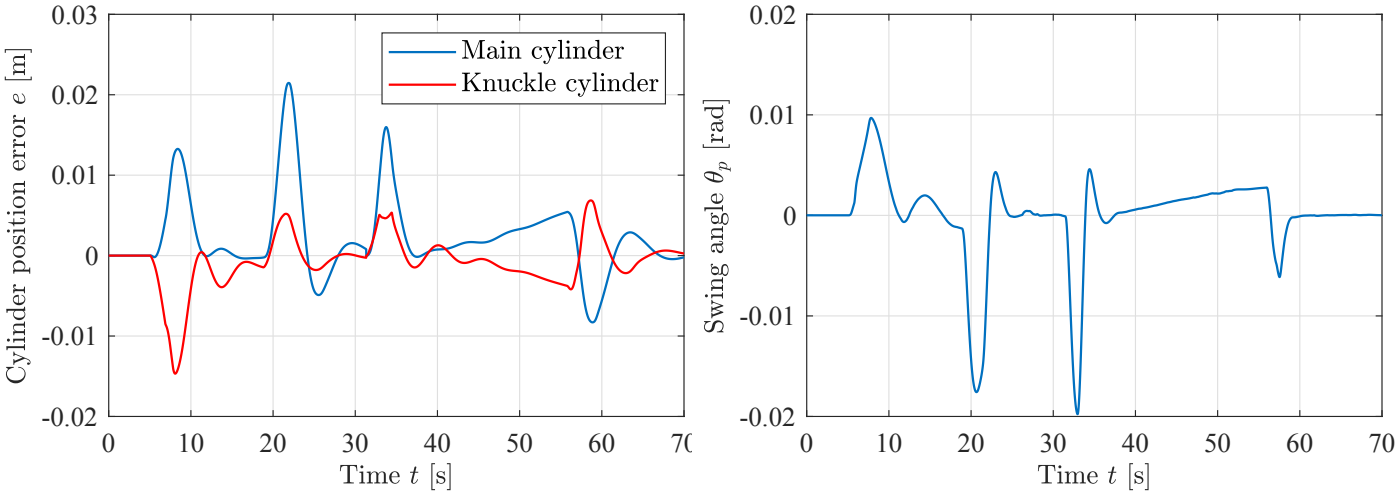

(**a**) (**b**)

Figure 35. Cylinder position error and swing angle during motion with EHAs. (**a**) Cylinder position error; (**b**) Swing angle.

9. Discussion

There are many advantages to EHAs, but also some disadvantages which will be discussed in this chapter. Today the use of EHAs allows for self-contained hydraulic systems, typically with electric power cables coming from a centrally located servo drive. The use of EHAs will often reduce the number of hydraulic hoses in a system, minimizing the risk and environmental impact of spilling hydraulic fluids in case of hose rupture. While EHAs require a battery pack or capacitor bank to effectively store the regenerated energy, traditional valve-controlled systems often require cooling to handle the generated heat from the hydraulic system. While not exclusive to EHAs, the use of one servomotor per actuator eliminates the problem of flow sharing typically found in valve-controlled systems, meaning each actuator can run at full power at all times. This also eliminates the problem of flow and pressure mismatch in load sensing hydraulic systems, where the pump must deliver a high pressure to all actuators even if only a single actuator has a high load pressure.

By using the high fidelity models in Simscape the EHA is tested under various loading conditions. The system is able to lift the payload of 30,000 kg with good position tracking and high efficiency. Even though the design point of the system is above the rated conditions, a thermal analysis shows that the system is able to operate indefinitely using the prescribed position reference. This is due to the inherently low duty cycle of position control for the servo system.

During the load case with anti-swing the performance of the valve-controlled system and the EHA are almost identical. The main difference is the energy consumption which is greatly reduced by using the novel system, shown in Table 8.

Table 8. Performance comparison between valve-controlled system and electro-hydrostatic system.

Parameter	Valve-Controlled	Electro-Hydrostatic
Main cylinder error	5.8 mm	5.8 mm
Knuckle cylinder error	5.4 mm	3.3 mm
Swing angle	4.3 mrad	4.4 mrad
Energy consumed	505 kJ	88 kJ

These results equate to a reduction in energy consumption of 82%, and an increase in overall efficiency from 9% to 53%. This showcases the excellent energy efficiency of the novel EHA. The reduced energy consumption is closely related to the ability to regenerate electrical power. The higher initial cost of the EHA, especially for the servomotor, servo drive, and battery pack, will be offset by the greatly reduced energy consumption.

10. Conclusions

This paper investigates electro-hydrostatic actuators applicable to large multi-axis hydraulic manipulators. The novel system is designed and analyzed to comply with requirements such as load holding, overload handling, and differential flow compensation. The electric servo system is modeled in the dq-frame and uses Field Oriented Control to regulate the motor current and motor speed. The hydraulic system has been designed and modeled using commercially available components and includes 2/2 poppet valves for load holding and pilot-operated check valves for differential flow compensation. The control system uses feedforward control for cylinder velocity and feedback for cylinder position, in addition to pressure feedback to reduce oscillations. Control logic for energizing the load holding valves is also presented.

A numerical analysis of four quadrant operation with constant load is first conducted. The cylinder follows a trapezoidal velocity profile during motion. The results show good tracking performance for both the servomotor and cylinder, with minimal oscillations. High energy efficiency is achieved in all four quadrants with a peak efficiency of 0.85. These results also showcase the excellent ability to regenerate energy.

A thermal model of the motor is made based on the datasheet, and thermal simulations show that the system can operate indefinitely with a load cycle based on the position reference used in Section 5 and load mass of 30,000 kg.

A load case with path control and anti-swing for a hydraulic crane is conducted to compare the performance and energy efficiency of the novel system with a typical valve-controlled system. A high fidelity model of the valve-controlled system is made to accurately model the energy efficiency in all components. The model consists of a grid-connected induction motor, variable displacement pressure compensated pump, pressure compensated directional control valves, and counterbalance valves. The valve-controlled system and electro-hydrostatic system are actuating two of the cylinders on the crane to follow a prescribed path with a hanging load. Results from the simulations show virtually identical performance regarding the position control of the cylinders and the anti-swing control of the hanging load. The main difference is the significant reduction of energy consumption by 82%, showcasing the superior efficiency of the novel EHA.

Future work may include investigating potential improvements to the design of the EHA, specifically for higher power applications. This may also include building a prototype of the EHA to verify the performance of the system.

Author Contributions: Conceptualization, K.J.J, M.K.E. and M.R.H; methodology, K.J.J; software, K.J.J; validation, K.J.J; formal analysis, K.J.J; investigation, K.J.J; data curation, K.J.J; writing–original draft preparation, K.J.J; writing–review and editing, K.J.J., M.K.E and M.R.H.; visualization, K.J.J.; supervision, M.K.E. and M.R.H. All authors have read and agreed to the published version of the manuscript.

Funding: This research was funded by the Norwegian Ministry of Education and Research grant number 155597. The APC was funded by the University of Agder.

Data Availability Statement: Not applicable.

Conflicts of Interest: The authors declare no conflict of interest.

References

1. Bozhko, S.; Hill, C.; Yang, T. *More-Electric Aircraft: Systems and Modeling*; Wiley: Hoboken, NJ, USA, 2018; pp. 1–31. [CrossRef]
2. Wheeler, P.; Bozhko, S. The More Electric Aircraft: Technology and challenges. *IEEE Electrif. Mag.* **2014**, *2*, 6–12. [CrossRef]
3. Wang, X.; Liao, R.; Shi, C.; Wang, S. Linear Extended State Observer-Based Motion Synchronization Control for Hybrid Actuation System of More Electric Aircraft. *Sensors* **2017**, *17*, 2444. [CrossRef] [PubMed]
4. Henke, M.; Narjes, G.; Hoffmann, J.; Wohlers, C.; Urbanek, S.; Heister, C.; Steinbrink, J.; Canders, W.R.; Ponick, B. Challenges and Opportunities of Very Light High-Performance Electric Drives for Aviation. *Energies* **2018**, *11*, 344. [CrossRef]
5. Wheeler, P. Technology for the more and all electric aircraft of the future. In Proceedings of the 2016 IEEE International Conference on Automatica (ICA-ACCA), Curico, Chile, 19–21 October 2016; pp. 1–5. [CrossRef]
6. Semi-Electric AHC Cranes. Available online: https://www.macgregor.com/Products/products/offshore-and-subsea-load-handling/semi-electric-ahc-cranes/ (accessed on 26 January 2021).
7. Wu, X.; Lai, X.; Zhu, J.; Huang, H.; Chen, L.; Du, S.; Wu, M. Intelligent Control System Design for Electric-drive Rig in Complex Geological Drilling Process. In Proceedings of the 2019 Chinese Control Conference (CCC), Guangzhou, China, 27–30 July 2019; pp. 7079–7082. [CrossRef]
8. LR 1250.1 Unplugged - The First Battery-Powered Crawler Crane in the World. Available online: https://www.liebherr.com/en/aus/products/construction-machines/deep-foundation/product-launch/lr-1250-unplugged.html (accessed on 26 January 2021).
9. Hagen, D.; Pawlus, W.; Ebbesen, M.K.; Andersen, T.O. Feasibility Study of Electromechanical Cylinder Drivetrain for Offshore Mechatronic Systems. *Model. Identif. Control.* **2017**, *38*, 59–77. [CrossRef]
10. The Best of Both Worlds: Combine Hydraulic and Servo Technology and Save up to 80% of Energy Costs. Available online: https://www.baumueller.com/en/insights/drive-technology/change-to-servo-hydraulic (accessed on 26 January 2021).
11. Self-contained Hydraulic Actuators–Intelligent Hybrid Power for Extreme Force Control. https://www.boschrexroth.com/en/xc/products/product-groups/industrial-hydraulics/topics/self-contained-hydraulic-actuators/ (accessed on 26 January 2021).
12. Sytronix – Variable-speed Pump Drives for Hydraulic Applications. Available online: https://www.boschrexroth.com/en/us/products/systems-and-modules/sytronix-variable-speed-pump-drives/index (accessed on 26 January 2021).
13. How Variable Speed Drives Become Simpler and More Efficient. Available online: http://blog.parker.com/how-variable-speed-drives-become-simpler-and-more-efficient (accessed on 26 January 2021).
14. Padovani, D.; Ketelsen, S.; Hagen, D.; Schmidt, L. A Self-Contained Electro-Hydraulic Cylinder with Passive Load-Holding Capability. *Energies* **2019**, *12*, 292. [CrossRef]
15. Hagen, D.; Padovani, D.; Choux, M. A Comparison Study of a Novel Self-Contained Electro-Hydraulic Cylinder versus a Conventional Valve-Controlled Actuator—Part 1: Motion Control. *Actuators* **2019**, *8*, 79. [CrossRef]
16. Hagen, D.; Padovani, D.; Choux, M. A Comparison Study of a Novel Self-Contained Electro-Hydraulic Cylinder versus a Conventional Valve-Controlled Actuator—Part 2: Energy Efficiency. *Actuators* **2019**, *8*, 78. [CrossRef]
17. Casoli, P.; Scolari, F.; Minav, T.; Rundo, M. Comparative Energy Analysis of a Load Sensing System and a Zonal Hydraulics for a 9-Tonne Excavator. *Actuators* **2020**, *9*, 39. [CrossRef]
18. Agostini, T.; De Negri, V.; Minav, T.; Pietola, M. Effect of Energy Recovery on Efficiency in Electro-Hydrostatic Closed System for Differential Actuator. *Actuators* **2020**, *9*, 12. [CrossRef]
19. Hagen, D.; Padovani, D.; Choux, M. Enabling Energy Savings in Offshore Mechatronic Systems by using Self-Contained Cylinders. *Model. Identif. Control.* **2019**, *40*, 89–108. [CrossRef]
20. Ketelsen, S.; Andersen, T.O.; Ebbesen, M.K.; Schmidt, L. A Self-Contained Cylinder Drive with Indirectly Controlled Hydraulic Lock. *Model. Identif. Control.* **2020**, *41*, 185–205. [CrossRef]
21. Zhang, S.; Li, S.; Minav, T. Control and Performance Analysis of Variable Speed Pump-Controlled Asymmetric Cylinder Systems under Four-Quadrant Operation. *Actuators* **2020**, *9*, 123. [CrossRef]
22. Gøytil, P.H.; Padovani, D.; Hansen, M.R. A Novel Solution for the Elimination of Mode Switching in Pump-Controlled Single-Rod Cylinders. *Actuators* **2020**, *9*, 20. [CrossRef]
23. Ketelsen, S.; Padovani, D.; Andersen, T.O.; Ebbesen, M.K.; Schmidt, L. Classification and Review of Pump-Controlled Differential Cylinder Drives. *Energies* **2019**, *12*, 1293. [CrossRef]
24. Qu, S.; Fassbender, D.; Vacca, A.; Busquets, E. A high-efficient solution for electro-hydraulic actuators with energy regeneration capability. *Energy* **2021**, *216*, 119291. [CrossRef]
25. Xue, L.; Wu, S.; Xu, Y.; Ma, D. A Simulation-Based Multi-Objective Optimization Design Method for Pump-Driven Electro-Hydrostatic Actuators. *Processes* **2019**, *7*, 274. [CrossRef]
26. Huang, L.; Yu, T.; Jiao, Z.; Li, Y. Active Load-Sensitive Electro-Hydrostatic Actuator for More Electric Aircraft. *Appl. Sci.* **2020**, *10*, 6978. [CrossRef]

27. Jensen, K.J.; Kjeld Ebbesen, M.; Rygaard Hansen, M. Development of Point-to-Point Path Control in Actuator Space for Hydraulic Knuckle Boom Crane. *Actuators* **2020**, *9*, 27. [CrossRef]
28. Jensen, K.J.; Ebbesen, M.K.; Hansen, M.R. Anti-swing control of a hydraulic loader crane with a hanging load. *Mechatronics* **2021**, *77*, 102599. [CrossRef]
29. Low Voltage Process Performance Motors. Available online: https://library.e.abb.com/public/8b08bf36a95844a8a275e5883223736b/PPM_catalog_13042016.pdf (accessed on 27 January 2021).

Paper E

Development of 3D Anti-Swing Control for Hydraulic Knuckle Boom Crane

This paper has been published as:

Jensen, K.J.; Kjeld Ebbesen, M.; Rygaard Hansen, M. Development of 3D Anti-Swing Control for Hydraulic Knuckle Boom Crane. *Modeling, Identification and Control* 42(3):113–129, 2021. doi:10.4173/mic.2021.3.2

Modeling, Identification and Control, Vol. 42, No. 3, 2021, pp. 113–129, ISSN 1890–1328

Development of 3D Anti-Swing Control for Hydraulic Knuckle Boom Crane

K. J. Jensen [1] M. K. Ebbesen [1] M. R. Hansen [1]

[1] *Department of Engineering Sciences, University of Agder, 4879 Grimstad, Norway.*
E-mail: {konrad.j.jensen,morten.k.ebbesen,michael.r.hansen}@uia.no

Abstract

In this paper, 3D anti-swing control for a hydraulic loader crane is presented. The difference between hydraulic and electric cranes are discussed to show the challenges associated with hydraulic actuation. The hanging load dynamics and relevant kinematics of the crane are derived to model the system and create the 3D anti-swing controller. The anti-swing controller generates a set of tool point velocities which are added to the electro-hydraulic motion controller via feedforward. A dynamic simulation model of the crane is made, and the control system is evaluated in simulations with a path controller in actuator space. Simulation results show significant reduction in the load swing angles during motion using the proposed anti-swing controller in addition to pressure feedback. Experiments are carried out to verify the performance of the anti-swing controller. Results show that the implemented pressure feedback is crucial for reaching stability, and with it the control system yields good suppression of the swing angles in practice.

Keywords: Loader crane; Anti-swing; Hydraulics; Kinematics; Feedforward; Pressure feedback

1 Introduction

Anti-swing control of cranes and hoists is a topic which has received extensive research in the past decades. Applications include lifting equipment in factories, shipyards, and warehouses etc. One of the challenges associated with these machines is the undesirable load swing of the hanging load when moving. The load swing can reduce efficiency, increase cycle times, and potentially lead to safety hazards and accidents. Different techniques have been implemented to dampen this load swing. Anti-swing control is a difficult task, as systems with hanging loads are underactuated, meaning the degrees of freedom are greater than the number of controlled actuators.

A typical application of anti-swing control is electric overhead cranes, where the translational motion is controlled by one or more electric servomotors. The controller often consists of two parts, one feedback controller for regulating the position of the crane, and a second controller to suppress the load swing of the hanging load. Earlier work on anti-swing control of electric overhead cranes include Lee et al. (1997); Lee (1998); Sung-Kun Cho and Ho-Hoon Lee (2000); Ho-Hoon Lee and Seung-Gap Choi (2001), utilizing linear system models. More advanced and nonlinear anti-swing control systems including sliding mode control, robust control, and fuzzy logic are found in Ho-Hoon Lee and Sung-Kun Cho (2001); Cho and Lee (2002); Lee (2003); Fang et al. (2003); Lee (2004); Lee et al. (2006); Park et al. (2007); Park et al. (2008); Schindele et al. (2009); Lee and Liang (2010); Ngo and Hong (2012); Ambrosino et al. (2020).

A method which has been tested for anti-swing and vibration reduction in flexible systems is called input shaping. The input signal to the system is designed to be self-canceling, using the bandwidth and damping ratio of a dynamic system model Singhose et al. (1996);

doi:10.4173/mic.2021.3.2
© 2021 Norwegian Society of Automatic Control

Sorensen et al. (2007); Kjelland and Hansen (2015).

Delayed reference control is a similar method which has been used on cranes. In this case the reference generator is time shifted based on the measured payload angle, see Boschetti et al. (2011, 2014).

Anti-swing control for hydraulic cranes is not an extensively studied area, but references include Kjelland et al. (2012) which investigates tool-point control and anti-swing for a planar hydraulic crane.

For this paper, a hydraulic loader crane is considered, see Figure 2. In this case the load is hanging from the crane tip, instead of the trolley of an overhead crane. The hydraulic loader crane uses pressure compensated valves, which give a load independent velocity control for each actuator. For closed loop control systems, the load independent velocity control can be utilized in a control system using feedforward Bak and Hansen (2013); Jensen et al. (2020a). In this case, both a position reference and a velocity reference are generated in the control system. An example of a typical closed loop electro-hydraulic motion control system with feedforward (FF) and feedback (FB) is shown in Figure 1.

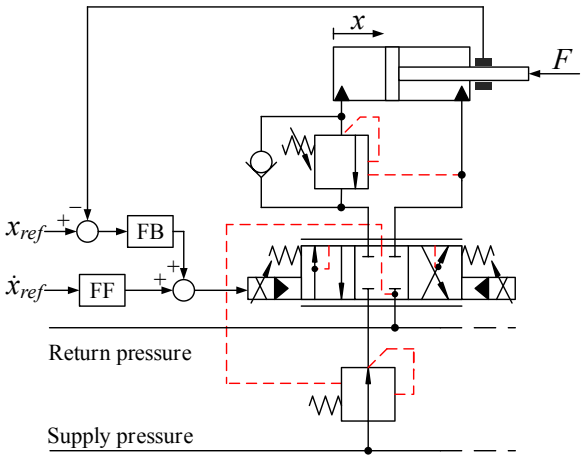

Figure 1: Electro-hydraulic motion control system with feedforward.

This paper is based on the previous work in Jensen et al. (2021), which focus on 2D anti-swing, and extends the relevant kinematics and dynamics in order to create a 3D anti-swing control system.

2 Considered System

In this paper an HMF 2020K4 loader crane is used as a case study for modeling, simulation, and experiments. Figure 2 shows the main components of the HMF 2020K4 loader crane. The relevant data for the cylinders are shown in Table 1. Each actuator is controlled via a pressure compensated proportional directional valve which ensures load independent flow control of the actuators. Counterbalance valves are also used for load holding, assisting in lowering of the booms, and pressure relief of pressure surges. An illustration of the hydraulic system for the knuckle cylinder is shown in Figure 3. Figure 4 shows the hanging load definitions along with the main boom angle θ_m, knuckle boom angle θ_k, and swing angles α (in-plane angle) and β (out-of-plane angle).

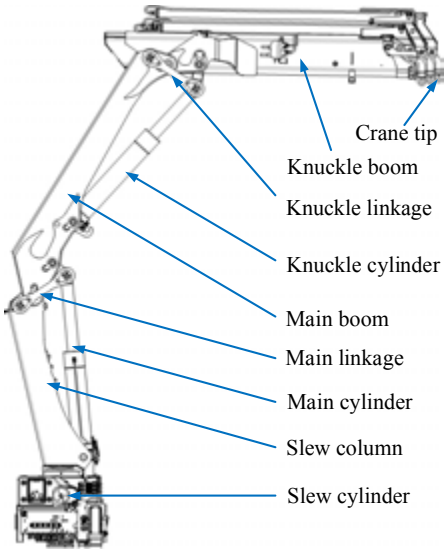

Figure 2: Main components of the considered crane.

Table 1: Data for the cylinders.

Description	Name	Value
Slew piston diameter	D_s	0.125 m
Slew piston area	A_s	0.0123 m^2
Slew piston area ratio	ϕ_s	1
Slew rack and pinion radius	r_s	0.105 m
Slew valve maximum flow	$Q_{max,s}$	25 l/min
Main piston diameter	$D_{p,m}$	0.16 m
Main piston area	A_m	0.0201 m^2
Main rod diameter	$D_{r,m}$	0.1 m
Main annulus area	$A_{a,m}$	0.0123 m^2
Main piston area ratio	$\phi_m = \frac{A_{a,m}}{A_m}$	0.6094
Main valve maximum flow	$Q_{max,m}$	40 l/min
Knuckle piston diameter	$D_{p,k}$	0.15 m
Knuckle piston area	A_k	0.0177 m^2
Knuckle rod diameter	$D_{r,k}$	0.1 m
Knuckle annulus area	$A_{a,k}$	0.0098 m^2
Knuckle piston area ratio	$\phi_k = \frac{A_{a,k}}{A_k}$	0.5556
Knuckle valve maximum flow	$Q_{max,k}$	40 l/min

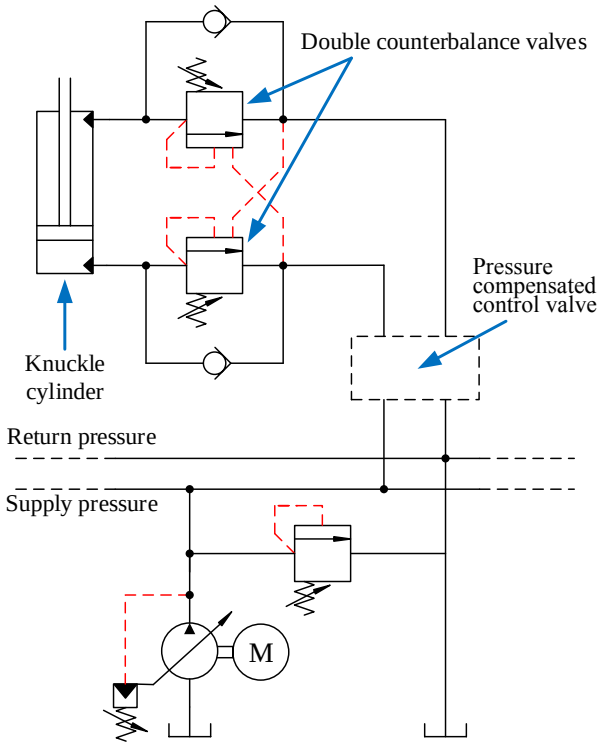

Figure 3: Hydraulic circuit for the knuckle cylinder.

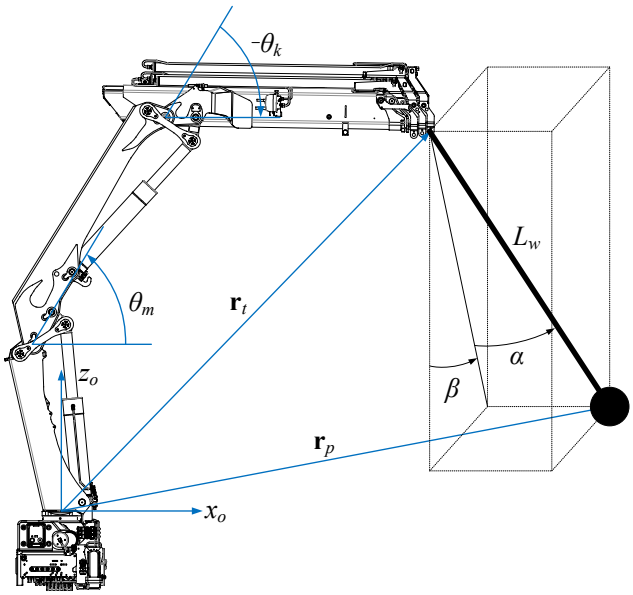

Figure 4: Definitions of crane tip and hanging load geometries.

2.1 Difference from electric overhead cranes

Since anti-swing control, primarily of electric overhead cranes, is an extensively studied subject, a short discussion about the differences between electric and hydraulic cranes is presented in this section.

Regarding actuation, the electric motor produces a torque based on the motor current, while hydraulic cylinders produce a force based on the hydraulic pressure. Pressure compensated directional valves are often used on hydraulic cranes, which enable load independent velocity control of the cylinder. On electric cranes, the motor current is controlled to provide a force acting on the system through a rack and pinion. This difference in velocity control and force control also affects the anti-swing control system for the crane.

A typical overhead crane is illustrated in Figure 5. The hanging load is connected to the trolley, and the trolley is able to move in the x-direction. An electric motor exerts a force F_{motor} on the trolley through the wheels, which affects both the trolley motion and payload motion.

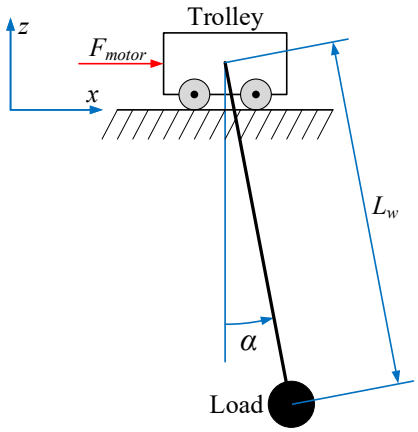

Figure 5: Typical overhead crane with hanging load.

2.2 Control strategy

The control strategy suggested in this paper is shown in Figure 6. This control strategy is useful for any hydraulically actuated manipulator with a tool point and a number of joint angles controlled by means of hydraulic cylinders. This constitutes a wide variety of load handling machinery. The main task is position control of the tool point and, classically, this may be combined with a velocity feedforward term. Feedback control is most easily implemented in actuator space Jensen et al. (2020b). Therefore, inverse kinematics is used to transform from tool point coordinates via joint coordinates to actuator coordinates. The anti-swing

controller is introduced in parallel with the feedforward term, and is used to counteract the continuously measured swing angles by adjusting the tool point velocities. Therefore, the anti-swing controller also requires a kinematic transformation into actuator space.

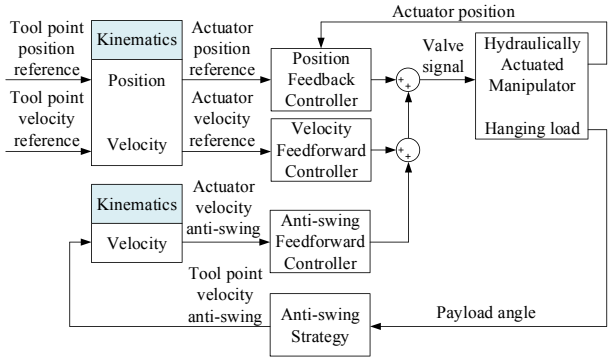

Figure 6: Anti-swing control strategy.

The proposed control strategy is implemented for a 3-dimensional case using three actuators. Howerever, more actuators may be used in combination with redundancy optimization, see Kjelland et al. (2012).

3 System Modeling

A dynamic model of the crane has been made in MATLAB Simscape™. 3D CAD models have been imported into the model using the Multibody library, and the hydraulic system has been modeled using the hydraulic library. A side view of the crane in the simulation model is shown in Figure 7.

Figure 7: 2D view of the crane model in MATLAB Simscape™.

3.1 Hanging Load Dynamics

To derive the equations of motion for the hanging load, the Euler-Lagrange equations are used. For the following equations, the notation $s_\alpha = \sin(\alpha)$, $c_\alpha = \cos(\alpha)$ is used. With the boom tip position defined as $\mathbf{r}_t = [x_t\ y_t\ z_t]^T$, the payload position is calculated as follows.

$$\mathbf{r}_p = \mathbf{r}_t + L_w \begin{bmatrix} s_\alpha \\ c_\alpha s_\beta \\ -c_\alpha c_\beta \end{bmatrix} \tag{1}$$

The payload velocity is calculated by taking the time derivative of the payload position.

$$\dot{\mathbf{r}}_p = \dot{\mathbf{r}}_t + L_w \begin{bmatrix} \dot{\alpha} c_\alpha \\ \dot{\beta} c_\alpha c_\beta - \dot{\alpha} s_\alpha s_\beta \\ \dot{\alpha} s_\alpha c_\beta + \dot{\beta} c_\alpha s_\beta \end{bmatrix} + \dot{L}_w \begin{bmatrix} s_\alpha \\ c_\alpha s_\beta \\ -c_\alpha c_\beta \end{bmatrix} \tag{2}$$

The Lagrangian $\mathcal{L}$ of the system is defined as the kinetic energy $\mathcal{K}$ minus the potential energy $\mathcal{P}$, and is shown in Equation (3).

$$\mathcal{L} = \mathcal{K} - \mathcal{P} \tag{3}$$

The kinetic energy of the payload is:

$$\mathcal{K} = \frac{1}{2} m_p \dot{\mathbf{r}}_p^T \dot{\mathbf{r}}_p \tag{4}$$

The potential energy of the payload is:

$$\mathcal{P} = m_p g \left(z_t - L_w c_\alpha c_\beta\right) \tag{5}$$

Selecting the coordinate $q = [\alpha\ \beta]^T$, the Euler-Lagrange equation is defined in Equation 6.

$$\frac{d}{dt}\frac{\partial \mathcal{L}}{\partial \dot{q}} - \frac{\partial \mathcal{L}}{\partial q} = 0 \tag{6}$$

Solving Equation (6) gives two coupled second order differential equations, shown in Equation (7) and (8). The full calculations are given in Appendix A in Equations (A.1)-(A.13).

$$\begin{aligned} \ddot{\alpha} = \frac{1}{L_w} \Big(& -c_\alpha \ddot{x}_t + s_\alpha s_\beta \ddot{y}_t - s_\alpha c_\beta \ddot{z}_t - 2\dot{\alpha}\dot{L}_w \\ & - s_\alpha c_\alpha \dot{\beta}^2 L_w - g s_\alpha c_\beta \Big) \end{aligned} \tag{7}$$

$$\begin{aligned} \ddot{\beta} = \frac{1}{c_\alpha L_w} \Big(& -c_\beta \ddot{y}_t - s_\beta \ddot{z}_t + 2 s_\alpha \dot{\alpha}\dot{\beta} L_w \\ & - 2\dot{\beta}\dot{L}_w - g s_\beta \Big) \end{aligned} \tag{8}$$

3.2 Joint Space Kinematics

The joint space kinematics describes the relation between the joint angles and Cartesian coordinates of

the crane tip. Figure 8 shows the geometry which is used with the Denavit-Hartenberg parameters, where both booms are horizontal. The distances between consecutive joints are shown in Table 2. The Denavit-Hartenberg parameters are shown in Table 3, where $\mathbf{R}$ and $\mathbf{T}$ are rotational and translational matrices, respectively. The angles θ_s, θ_m ,and θ_k denote the rotation about the slew joint, main joint, and knuckle joint, respectively.

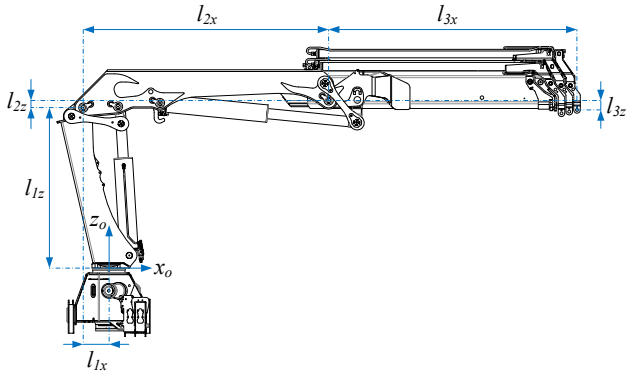

Figure 8: Crane geometry used with Denavit-Hartenberg parameters.

Table 2: Coordinates shown in Figure 8.

Name	Length [m]
l_{1x}	0.250
l_{1z}	1.569
l_{2x}	2.400
l_{2z}	0.070
l_{3x}	2.429
l_{3z}	0.093

Table 3: Denavit-Hartenberg parameters.

$\mathbf{R}_z$	$\mathbf{T}_z$	$\mathbf{T}_x$	$\mathbf{R}_x$
θ_s	l_{1z}	$-l_{1x}$	$90°$
θ_m	0	0	$-90°$
0	l_{2z}	l_{2x}	$90°$
θ_k	0	0	$-90°$
0	$-l_{3z}$	l_{3x}	0

The transformation matrix $\mathbf{A}_{DH}$ from the base of the crane to the tip of the crane can be established as a sequence of transformations based on the Denavit-Hartenberg parameters, shown in Equation (9).

$$\begin{aligned}\mathbf{A}_{DH} = {} & \mathbf{R}_z(\theta_s)\mathbf{T}_z(l_{1z})\mathbf{T}_x(-l_{1x})\mathbf{R}_x(90°)\mathbf{R}_z(\theta_m) \\ & \mathbf{R}_x(-90°)\mathbf{T}_z(l_{2z})\mathbf{T}_x(l_{2x})\mathbf{R}_x(90°) \\ & \mathbf{R}_z(\theta_k)\mathbf{R}_x(-90°)\mathbf{T}_z(-l_{3z})\mathbf{T}_x(l_{3x}) \end{aligned} \tag{9}$$

The final matrix $\mathbf{A}_{DH}$ is shown in Equation (10). The joint kinematics from the crane base to the crane tip is now contained in x_t, y_t, and z_t.

$$\mathbf{A}_{DH} = \begin{bmatrix} c_{\theta_s}c_{\theta_m+\theta_k} & -s_{\theta_s} & -c_{\theta_s}s_{\theta_m+\theta_k} & x_t \\ s_{\theta_s}c_{\theta_m+\theta_k} & c_{\theta_s} & -s_{\theta_s}s_{\theta_m+\theta_k} & y_t \\ s_{\theta_m+\theta_k} & 0 & c_{\theta_m+\theta_k} & z_t \\ 0 & 0 & 0 & 1 \end{bmatrix} \tag{10}$$

$$\begin{aligned} x_t = {} & c_{\theta_s}(-l_{1x} + l_{2x}c_{\theta_m} - l_{2z}s_{\theta_m} \\ & + l_{3x}c_{\theta_m+\theta_k} + l_{3z}s_{\theta_m+\theta_k}) \end{aligned} \tag{11}$$

$$\begin{aligned} y_t = {} & s_{\theta_s}(-l_{1x} + l_{2x}c_{\theta_m} - l_{2z}s_{\theta_m} \\ & + l_{3x}c_{\theta_m+\theta_k} + l_{3z}s_{\theta_m+\theta_k}) \end{aligned} \tag{12}$$

$$\begin{aligned} z_t = {} & l_{1z} + l_{2x}s_{\theta_m} + l_{2z}c_{\theta_m} \\ & + l_{3x}s_{\theta_m+\theta_k} - l_{3z}c_{\theta_m+\theta_k} \end{aligned} \tag{13}$$

To find the correlation between the desired crane tip velocities and the joint velocities, the inverse Jacobian matrix must be defined. The correlation between crane tip velocities and joint velocities is shown in Equations (14) and (15).

$$\begin{bmatrix} \dot{x}_t \\ \dot{y}_t \\ \dot{z}_t \end{bmatrix} = \mathbf{J} \begin{bmatrix} \dot{\theta}_s \\ \dot{\theta}_m \\ \dot{\theta}_k \end{bmatrix} \tag{14}$$

$$\begin{bmatrix} \dot{\theta}_s \\ \dot{\theta}_m \\ \dot{\theta}_k \end{bmatrix} = \mathbf{J}^{-1} \begin{bmatrix} \dot{x}_t \\ \dot{y}_t \\ \dot{z}_t \end{bmatrix} \tag{15}$$

First, the Jacobian matrix is defined as the partial derivative of the crane tip position with respect to the joint angles, shown in Equation (16).

$$\mathbf{J} = \begin{bmatrix} \frac{\partial}{\partial\theta_s}(x_t) & \frac{\partial}{\partial\theta_m}(x_t) & \frac{\partial}{\partial\theta_k}(x_t) \\ \frac{\partial}{\partial\theta_s}(y_t) & \frac{\partial}{\partial\theta_m}(y_t) & \frac{\partial}{\partial\theta_k}(y_t) \\ \frac{\partial}{\partial\theta_s}(z_t) & \frac{\partial}{\partial\theta_m}(z_t) & \frac{\partial}{\partial\theta_k}(z_t) \end{bmatrix} \tag{16}$$

$$\frac{\partial}{\partial \theta_s}(x_t) = -s_{\theta_s}(-l_{1x} + l_{2x}c_{\theta_m} - l_{2z}s_{\theta_m} + l_{3x}c_{\theta_m+\theta_k} + l_{3z}s_{\theta_m+\theta_k}) \quad (17)$$

$$\frac{\partial}{\partial \theta_m}(x_t) = c_{\theta_s}(-l_{2x}s_{\theta_m} - l_{2z}c_{\theta_m} - l_{3x}s_{\theta_m+\theta_k} + l_{3z}c_{\theta_m+\theta_k}) \quad (18)$$

$$\frac{\partial}{\partial \theta_k}(x_t) = c_{\theta_s}(-l_{3x}s_{\theta_m+\theta_k} + l_{3z}c_{\theta_m+\theta_k}) \quad (19)$$

$$\frac{\partial}{\partial \theta_s}(y_t) = c_{\theta_s}(-l_{1x} + l_{2x}c_{\theta_m} - l_{2z}s_{\theta_m} + l_{3x}c_{\theta_m+\theta_k} + l_{3z}s_{\theta_m+\theta_k}) \quad (20)$$

$$\frac{\partial}{\partial \theta_m}(y_t) = s_{\theta_s}(-l_{2x}s_{\theta_m} - l_{2z}c_{\theta_m} - l_{3x}s_{\theta_m+\theta_k} + l_{3z}c_{\theta_m+\theta_k}) \quad (21)$$

$$\frac{\partial}{\partial \theta_k}(y_t) = s_{\theta_s}(-l_{3x}s_{\theta_m+\theta_k} + l_{3z}c_{\theta_m+\theta_k}) \quad (22)$$

$$\frac{\partial}{\partial \theta_s}(z_t) = 0 \quad (23)$$

$$\frac{\partial}{\partial \theta_m}(z_t) = l_{2x}c_{\theta_m} - l_{2z}s_{\theta_m} + l_{3x}c_{\theta_m+\theta_k} + l_{3z}s_{\theta_m+\theta_k} \quad (24)$$

$$\frac{\partial}{\partial \theta_k}(z_t) = -l_{3x}c_{\theta_m+\theta_k} - l_{3z}s_{\theta_m+\theta_k} \quad (25)$$

The inverse Jacobian matrix is used to generate the joint velocities, shown in Equations (26)-(38).

$$\mathbf{J}^\dagger \triangleq \mathbf{J}^{-1} = \begin{bmatrix} J_{11}^\dagger & J_{12}^\dagger & J_{13}^\dagger \\ J_{21}^\dagger & J_{22}^\dagger & J_{23}^\dagger \\ J_{31}^\dagger & J_{32}^\dagger & J_{33}^\dagger \end{bmatrix} \quad (26)$$

$$\dot{\theta}_s = J_{11}^\dagger \dot{x}_t + J_{12}^\dagger \dot{y}_t + J_{13}^\dagger \dot{z}_t \quad (27)$$

$$\dot{\theta}_m = J_{21}^\dagger \dot{x}_t + J_{22}^\dagger \dot{y}_t + J_{23}^\dagger \dot{z}_t \quad (28)$$

$$\dot{\theta}_k = J_{31}^\dagger \dot{x}_t + J_{32}^\dagger \dot{y}_t + J_{33}^\dagger \dot{z}_t \quad (29)$$

$$J_{11}^\dagger = \frac{-s_{\theta_s}}{-l_{1x}+l_{2x}c_{\theta_m}-l_{2z}s_{\theta_m}+l_{3x}c_{\theta_m+\theta_k}+l_{3z}s_{\theta_m+\theta_k}} \quad (30)$$

$$J_{12}^\dagger = \frac{c_{\theta_s}}{-l_{1x}+l_{2x}c_{\theta_m}-l_{2z}s_{\theta_m}+l_{3x}c_{\theta_m+\theta_k}+l_{3z}s_{\theta_m+\theta_k}} \quad (31)$$

$$J_{13}^\dagger = 0 \quad (32)$$

$$J_{21}^\dagger = \frac{-c_{\theta_s}(l_{3x}c_{\theta_m+\theta_k}+l_{3z}s_{\theta_m+\theta_k})}{-l_{2x}l_{3x}s_{\theta_k}+l_{2x}l_{3z}c_{\theta_k}+l_{2z}l_{3x}c_{\theta_k}+l_{2z}l_{3z}s_{\theta_k}} \quad (33)$$

$$J_{22}^\dagger = \frac{-s_{\theta_s}(l_{3x}c_{\theta_m+\theta_k}+l_{3z}s_{\theta_m+\theta_k})}{-l_{2x}l_{3x}s_{\theta_k}+l_{2x}l_{3z}c_{\theta_k}+l_{2z}l_{3x}c_{\theta_k}+l_{2z}l_{3z}s_{\theta_k}} \quad (34)$$

$$J_{23}^\dagger = \frac{-l_{3x}s_{\theta_m+\theta_k}+l_{3z}c_{\theta_m+\theta_k}}{-l_{2x}l_{3x}s_{\theta_k}+l_{2x}l_{3z}c_{\theta_k}+l_{2z}l_{3x}c_{\theta_k}+l_{2z}l_{3z}s_{\theta_k}} \quad (35)$$

$$J_{31}^\dagger = \frac{c_{\theta_s}(l_{2x}c_{\theta_m}-l_{2z}s_{\theta_m}+l_{3x}c_{\theta_m+\theta_m}+l_{3z}s_{\theta_m+\theta_k})}{-l_{2x}l_{3x}s_{\theta_k}+l_{2x}l_{3z}c_{\theta_k}+l_{2z}l_{3x}c_{\theta_k}+l_{2z}l_{3z}s_{\theta_k}} \quad (36)$$

$$J_{32}^\dagger = \frac{s_{\theta_s}(l_{2x}c_{\theta_m}-l_{2z}s_{\theta_m}+l_{3x}c_{\theta_m+\theta_m}+l_{3z}s_{\theta_m+\theta_k})}{-l_{2x}l_{3x}s_{\theta_k}+l_{2x}l_{3z}c_{\theta_k}+l_{2z}l_{3x}c_{\theta_k}+l_{2z}l_{3z}s_{\theta_k}} \quad (37)$$

$$J_{33}^\dagger = \frac{l_{2x}s_{\theta_m}+l_{2z}c_{\theta_m}+l_{3x}s_{\theta_m+\theta_k}-l_{3z}c_{\theta_m+\theta_k}}{-l_{2x}l_{3x}s_{\theta_k}+l_{2x}l_{3z}c_{\theta_k}+l_{2z}l_{3x}c_{\theta_k}+l_{2z}l_{3z}s_{\theta_k}} \quad (38)$$

3.3 Actuator Space Kinematics

The actuator space kinematics describes the relation between the cylinder lengths, cylinder velocities, joint angles, and joint angular velocities. They have previously been developed in Jensen et al. (2021). The shorthand kinematic expressions are shown in Equations (39)-(47). Figure 9 and Figure 10 show the geometry of the linkage system for the main joint and knuckle joint, respectively.

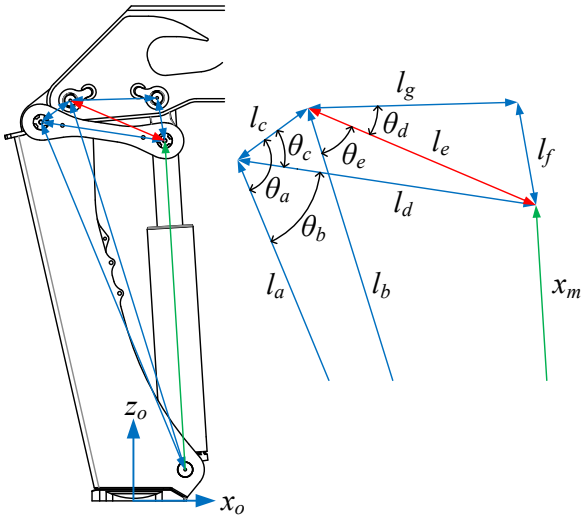

Figure 9: Geometry of the linkage system for the main joint.

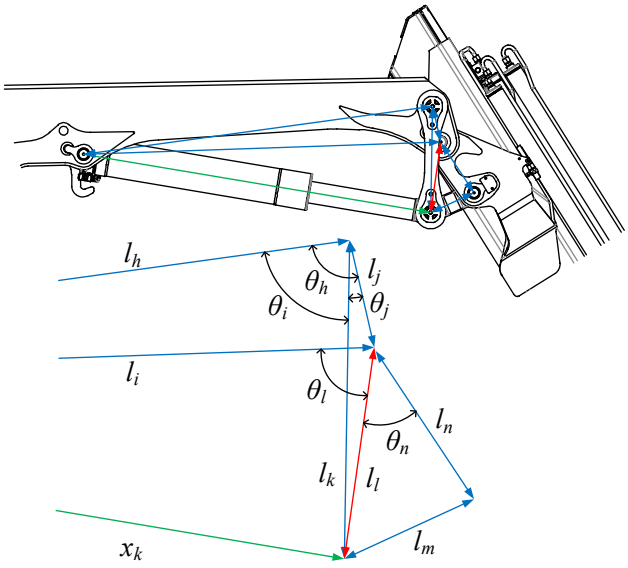

Figure 10: Geometry of the linkage system for the knuckle joint.

$$\theta_s = \frac{x_s}{r_s} \tag{39}$$
$$\theta_m = \theta_m(x_m) \tag{40}$$
$$\theta_k = \theta_k(x_k) \tag{41}$$
$$\dot{\theta}_s = \frac{\dot{x}_s}{r_s} \tag{42}$$
$$\dot{\theta}_m = \frac{\partial \theta_m(x_m)}{\partial x_m}\dot{x}_m \tag{43}$$
$$\dot{\theta}_k = \frac{\partial \theta_k(x_k)}{\partial x_k}\dot{x}_k \tag{44}$$
$$\dot{x}_s = \dot{\theta}_s r_s \tag{45}$$
$$\dot{x}_m = \left(\frac{\partial \theta_m(x_m)}{\partial x_m}\right)^{-1}\dot{\theta}_m = \theta^{\dagger}_{x_m}\dot{\theta}_m \tag{46}$$
$$\dot{x}_k = \left(\frac{\partial \theta_k(x_k)}{\partial x_k}\right)^{-1}\dot{\theta}_k = \theta^{\dagger}_{x_k}\dot{\theta}_k \tag{47}$$

3.4 Hydraulic Modeling

All three cylinders are controlled by pressure compensated directional valves. An illustration of the valve is shown in Figure 11. The pressure compensator senses the load pressure to keep the pressure drop over the directional valve constant, thus ensuring a load independent flow. The governing equations of the pressure compensator are given in Equations (48)-(50).

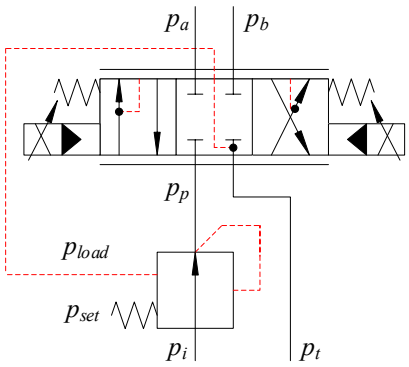

Figure 11: Pressure compensated directional valve.

$$u_{pc} = \frac{p_{set} + p_{load} - p_p}{\Delta p_c} \tag{48}$$
$$p_{load} = \begin{cases} p_a & \text{if } u_{spool} \geq 0 \\ p_b & \text{otherwise} \end{cases} \tag{49}$$
$$Q_{pc} = k_{pc} u_{pc} \sqrt{p_i - p_p} \tag{50}$$

where;

u_{pc}	=	opening of compensator, $0 \leq u_{pc} \leq 1$
p_p	=	compensated pressure at port p
Δp_c	=	pressure difference when fully opened
p_a	=	pressure at port a
p_b	=	pressure at port b
p_t	=	tank pressure
p_{set}	=	spring pressure setting
p_{load}	=	load pressure
u_{spool}	=	main spool position, $-1 \leq u_{spool} \leq 1$
Q_{pc}	=	flow in pressure compensator
k_{pc}	=	flow gain of compensator
p_i	=	compensator inlet pressure

The steady state of p_p is then given by Equation (51).

$$p_p = p_{load} + p_{set} \tag{51}$$

The sensing of the load pressures p_a and p_b ensures that the pressure drop over the directional control valve always equals p_{set}, and that the flow is load independent. This is shown in Equation (52).

$$Q = k_v u_{spool}\sqrt{p_p - p_{load}} = k_v u_{spool}\sqrt{p_{set}} = Q_{max} u_{spool} \tag{52}$$

where;

k_v	=	flow gain of the directional valve
Q_{max}	=	maximum valve flow

To assist with load holding, lowering of the load, and protection against pressure surges, counterbalance valves are used between the directional valve and the hydraulic cylinder. Figure 12 shows an illustration of double counterbalance valves, as used on the slew cylinder and knuckle cylinder. The main cylinder uses a single counterbalance valve.

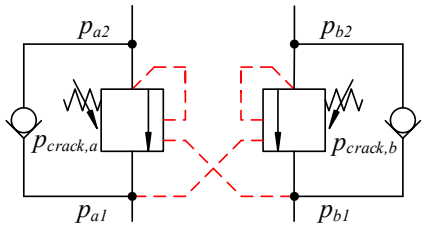

Figure 12: Double counterbalance valves.

The governing equations of the counterbalance valves are shown in Equations (53) and (54).

$$u_a = \frac{p_{a2} + \psi p_{b1} - p_{crack,a}}{\Delta p_{CBV}} \tag{53}$$
$$u_b = \frac{p_{b2} + \psi p_{a1} - p_{crack,b}}{\Delta p_{CBV}} \tag{54}$$

where;

u_a	=	opening of valve a, $0 \leq u_a \leq 1$
u_b	=	opening of valve b, $0 \leq u_b \leq 1$
p_{a1}	=	pressure at valve a input side
p_{a2}	=	pressure at valve a actuator side
p_{b1}	=	pressure at valve b input side
p_{b2}	=	pressure at valve b actuator side
$p_{crack,a}$	=	crack pressure of valve a
$p_{crack,b}$	=	crack pressure of valve b
ψ	=	pilot area ratio
Δp_{CBV}	=	pressure difference when fully opened

4 Control System Design

The control of the hydraulic cylinders uses feedback of the position error, and feedforward based on the velocity reference. Since the hydraulic system yields load independent velocity control, feedforward is an effective control method, as stated in Bak and Hansen (2013) and Jensen et al. (2020b). The anti-swing gain k_a and the payload angles α and β are used to generate two anti-swing crane tip velocities, $\dot{x}_{t,a}$ and $\dot{y}_{t,a}$ in order to suppress the payload angles. These velocities are transformed into joint space and then into actuator space, to yield the anti-swing slew velocity $\dot{\theta}_{s,a}$ and cylinder velocities $\dot{x}_{m,a}$ and $\dot{x}_{k,a}$. This is shown in Equations (55)-(58).

The full control system is shown in Figure 13, outlining the feedback controller (blue), feedforward controller (red), and anti-swing controller (green). It should be noted that the slew angle is used instead of the slew cylinder length since it is connected to a sensor on the crane. The anti-swing controller uses actuator kinematics (Act. Kin.), inverse Jacobian (Inv. Jac.), and inverse actuator kinematics (Inv. Act.). Both the feedforward controller and anti-swing controller use the gain k_{ff} to calculate the valve opening from actuator velocity.

$$\begin{bmatrix} \dot{x}_{t,a} \\ \dot{y}_{t,a} \\ \dot{z}_{t,a} \end{bmatrix} = k_a \begin{bmatrix} \alpha \\ \beta \\ 0 \end{bmatrix} \tag{55}$$

$$\begin{bmatrix} \dot{\theta}_{s,a} \\ \dot{\theta}_{m,a} \\ \dot{\theta}_{k,a} \end{bmatrix} = J^{\dagger} \begin{bmatrix} \dot{x}_{t,a} \\ \dot{y}_{t,a} \\ \dot{z}_{t,a} \end{bmatrix} \tag{56}$$

$$\dot{x}_{m,a} = \theta^{\dagger}_{x_m} \dot{\theta}_{m,a} \tag{57}$$

$$\dot{x}_{k,a} = \theta^{\dagger}_{x_k} \dot{\theta}_{k,a} \tag{58}$$

The anti-swing cylinder velocities $\dot{x}_{m,a}$ and $\dot{x}_{k,a}$ are then multiplied by k_{ff} to generate the valve opening. The control outputs for the control system are shown in Equations (59)-(61).

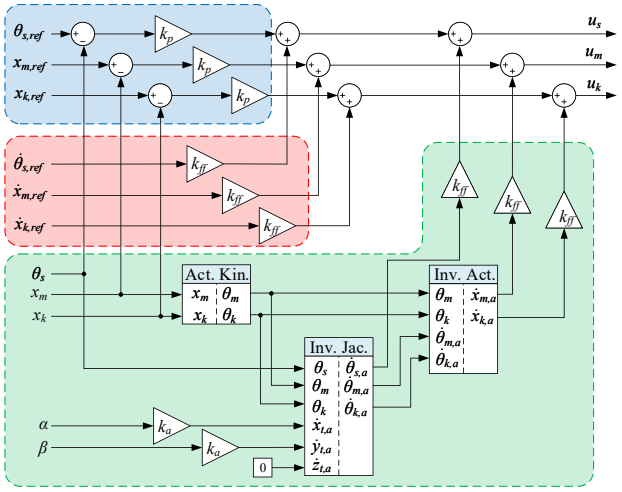

Figure 13: Illustration of the 3D anti-swing control system, with feedback controller (blue), feedforward controller (red), and anti-swing controller (green).

$$u_s = (\theta_{s,ref} - \theta_s)k_{p,s} + (\dot{\theta}_{s,ref} + \dot{\theta}_{s,a})k_{ff,s} \tag{59}$$

$$u_m = (x_{m,ref} - x_m)k_{p,m} + (\dot{x}_{m,ref} + \dot{x}_{m,a})k_{ff,m} \tag{60}$$

$$u_k = (x_{k,ref} - x_k)k_{p,k} + (\dot{x}_{k,ref} + \dot{x}_{k,a})k_{ff,k} \tag{61}$$

4.1 Theoretical closed loop analysis

An analysis of the closed loop hanging load dynamics can be conducted based on the open loop hanging load dynamics and the selected control law. The control law controls the velocity of the crane tip. Recalling from earlier sections, the open loop dynamics and control law are given as:

$$\ddot{\alpha} = \frac{1}{L_w}\Big(-c_\alpha \ddot{x}_t + s_\alpha s_\beta \ddot{y}_t - s_\alpha c_\beta \ddot{z}_t - 2\dot{\alpha}\dot{L}_w - s_\alpha c_\alpha \dot{\beta}^2 L_w - g s_\alpha c_\beta\Big) \tag{62}$$

$$\ddot{\beta} = \frac{1}{c_\alpha L_w}\Big(-c_\beta \ddot{y}_t - s_\beta \ddot{z}_t + 2 s_\alpha \dot{\alpha}\dot{\beta} L_w - 2\dot{\beta}\dot{L}_w - g s_\beta\Big) \tag{63}$$

$$\dot{x}_t = \alpha k_a \tag{64}$$

$$\dot{y}_t = \beta k_a \tag{65}$$

$$\dot{z}_t = 0 \tag{66}$$

The expressions for $\ddot{x}_t$, $\ddot{y}_t$ and $\ddot{z}_t$ can be made by taking the time derivative of the crane tip velocities:

$$\ddot{x}_t = \dot{\alpha} k_a \tag{67}$$

$$\ddot{y}_t = \dot{\beta} k_a \tag{68}$$

$$\ddot{z}_t = 0 \tag{69}$$

The closed loop hanging load dynamics can now be described as:

$$\ddot{\alpha} = \frac{1}{L_w}\Big(-c_\alpha \dot{\alpha} k_a + s_\alpha s_\beta \dot{\beta} k_a - 2\dot{\alpha}\dot{L}_w - s_\alpha c_\alpha \dot{\beta}^2 L_w - g s_\alpha c_\beta\Big) \tag{70}$$

$$\ddot{\beta} = \frac{1}{c_\alpha L_w}\Big(-c_\beta \dot{\beta} k_a + 2 s_\alpha \dot{\alpha}\dot{\beta} L_w - 2\dot{\beta}\dot{L}_w - g s_\beta\Big) \tag{71}$$

Linearization is conducted to analyze the damping that the control law provides. Linearizing around $\alpha \approx \beta \approx 0$ and $\dot{L}_w \approx 0$ yields two decoupled equations of motion:

$$\ddot{\alpha} = -\frac{\dot{\alpha} k_a}{L_w} - \frac{g\alpha}{L_w} \tag{72}$$

$$\ddot{\beta} = -\frac{\dot{\beta} k_a}{L_w} - \frac{g\beta}{L_w} \tag{73}$$

A Laplace transform is performed on the linearized and decoupled equations of motion, yielding:

$$s^2\alpha = -\frac{s\alpha k_a}{L_w} - \frac{g\alpha}{L_w} \tag{74}$$

$$s^2\beta = -\frac{s\beta k_a}{L_w} - \frac{g\beta}{L_w} \tag{75}$$

The two equations yield the same second order transfer function, given as:

$$s^2 + \frac{s k_a}{L_w} + \frac{g}{L_w} = 0 \tag{76}$$

$$s^2 + 2s\zeta\omega + \omega^2 = 0 \tag{77}$$

The bandwidth and damping ratio are calculated as:

$$\omega = \sqrt{\frac{g}{L_w}} \tag{78}$$

$$\zeta = \frac{k_a}{2\sqrt{L_w g}} \tag{79}$$

It can be seen that the damping ratio ζ increases as the anti-swing gain k_a increases, and that the system is stable with $k_a > 0$, yielding poles in the left half-plane. An analytical expression for the anti-swing gain can now be calculated based on desired damping ratio and wire length by rearranging Equation (79).

$$k_a = 2\zeta\sqrt{L_w g} \tag{80}$$

Equation (80) can be used to achieve the desired damping of the hanging payload and for the purpose of gain scheduling for systems with a variable wire length L_w.

5 System Simulation

For the simulation, a path controller based on a trapezoidal velocity reference is used, as described in Jensen et al. (2020b). The path controller operates in actuator space, and uses segments of constant cylinder velocity. The position reference for each actuator is shown in Figure 14. The relevant parameters for the simulation are shown in Table 4.

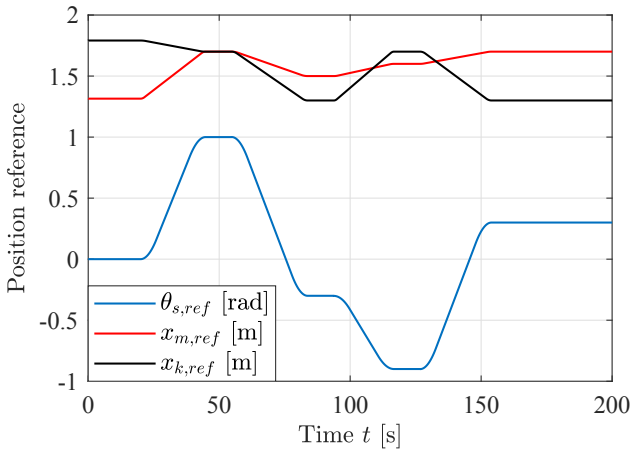

Figure 14: Position reference for each actuator.

Table 4: Simulation parameters.

Description	Name	Value
Slew feedback	$k_{p,s}$	1 rad^{-1}
Slew feedforward	$k_{ff,s}$	8.84 s/rad
Main feedback	$k_{p,m}$	5 m^{-1}
Main out-stroke feedforward	$k^+_{ff,m}$	30.16 s/m
Main in-stroke feedforward	$k^-_{ff,m}$	18.37 s/m
Knuckle feedback	$k_{p,k}$	20 m^{-1}
Knuckle out-stroke feedforward	$k^+_{ff,k}$	26.51 s/m
Knuckle in-stroke feedforward	$k^-_{ff,k}$	14.72 s/m
Wire length	L_w	2 m
Anti-swing gain	k_a	5 m/s

A plot of the swing angles α and β without control is shown in Figure 15. The pendulum is oscillating heavily as expected. A plot of the same angles with anti-swing control is shown in Figure 16. Although both angles are lower, the angle β experiences high frequency oscillations. The source of the oscillations are identified as the slewing motion itself. Looking at the slew position error, the high frequency oscillations occur both with and without anti-swing control, shown in Figure 17.

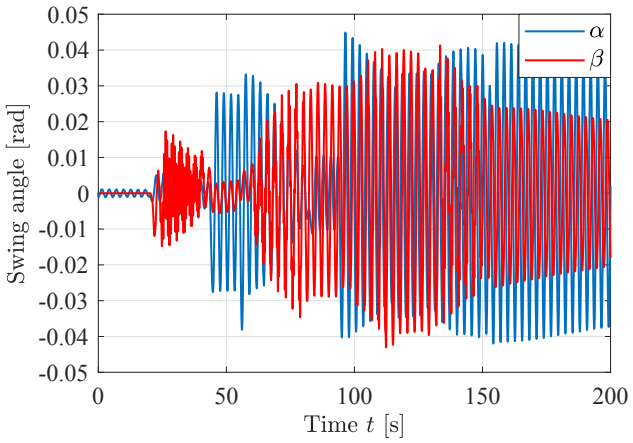

Figure 15: Swing angles without anti-swing control.

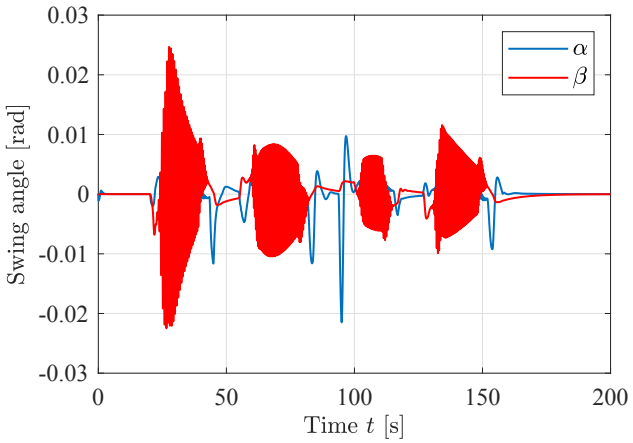

Figure 16: Swing angles with anti-swing control.

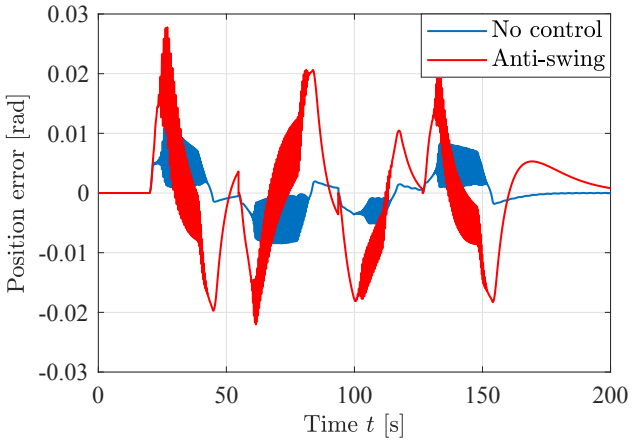

Figure 17: Slew position error with and without anti-swing control.

To compensate for the oscillations in the slewing motion, pressure feedback is implemented. By measuring the load pressure, the control signal is modified by subtracting the high-pass filtered load pressure. Pressure feedback has previously been used to dampen oscillations of hydraulic systems, see Pedersen et al. (2016), Pedersen and Andersen (2018) and Hagen et al. (2019). The implementation is shown in Equation (81), using the filter gain k_{pf}, filter frequency ω_{pf}, and load pressure p_L. Figure 18 shows the swing angles with anti-swing and pressure feedback, with $k_{pf} = 0.02$ bar^{-1} and $\omega_{pf} = 15$ rad/s. The high frequency oscillations in the swing angle β are successfully suppressed, and both angles are significantly dampened compared to the system without anti-swing control. The position error with anti-swing and pressure feedback is shown in Figure 19, showing no oscillations.

$$\hat{u}_s = u_s - \frac{k_{pf} s}{s + \omega_{pf}} p_L \tag{81}$$

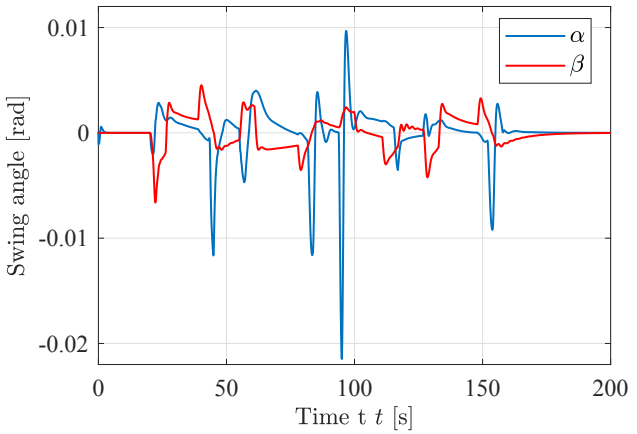

Figure 18: Swing angles with anti-swing and pressure feedback.

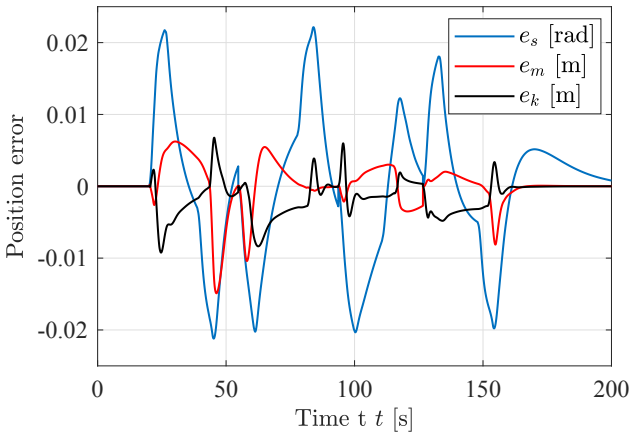

Figure 19: Position error with anti-swing and pressure feedback.

To evaluate the performance of the anti-swing controller and pressure feedback, a quantitative analysis is performed comparing the RMS value of the three position errors and two swing angles. Table 5 shows the RMS values when the system is simulated without anti-swing control, with anti-swing control (AS), and with both anti-swing control and pressure feedback (AS+PF). Due to the increase in the three position errors, it is clear that the anti-swing controller has a negative impact. This is expected and tolerated, since the primary focus of the control system is to suppress the swing angles. The pressure feedback also gives a negative impact on the position error. However, looking at the slew position error e_s from Figure 17 and 19, the elimination of the high frequency oscillations is a big advantage. For the hanging payload, both the anti-swing control and the pressure feedback give a large reduction in the swing angles, with a decrease in the RMS value of approximately 90 %. The introduction of the pressure feedback yields a significant improvement for the angle β, which is also seen in Figure 16 and 18.

Table 5: Quantitative simulation results.

Variable	No control	AS	AS+PF
RMS(α) [mrad]	21.21	2.55	2.52
RMS(β) [mrad]	16.97	4.25	1.47
RMS(e_s) [mrad]	3.17	9.03	9.73
RMS(e_m) [mm]	0.35	3.21	3.27
RMS(e_k) [mm]	1.54	2.79	2.78

6 Experimental Results

The anti-swing controller is implemented on a CompactRIO connected to the HMF 2020K4 loader crane. A picture of the test setup is shown in Figure 20. The sensor used in the experiments is the BNO055 Absolute Orientation Sensor from Bosch Sensortec. It outputs three Euler angles and they are all used to calculate the payload angles α and β.

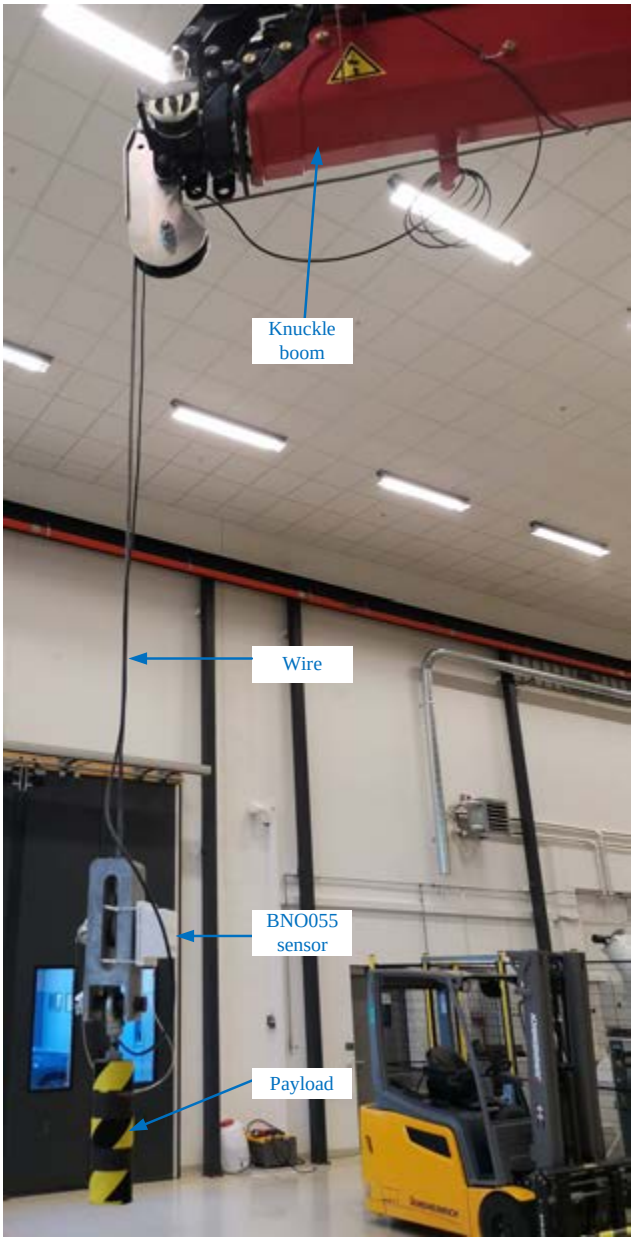

Figure 20: HMF 2020K4 crane in the laboratory.

There is some deadband in the valves on the HMF 2020K4 loader crane, and therefore deadband compensation has been implemented for the laboratory experiments. The identified deadbands for the valves are shown in Table 6. The equation for the deadband compensation is shown in Equation (82). By introducing a small transition region $\tilde{u}$, the compensated control

signal will be continuous which avoids unnecessary oscillations of the spool, while ensuring that the valve will be able to stay closed when no movement is needed.

Table 6: Identified deadband for the actuators.

Actuator	Out, u^+	In, u^-
Slew	0.22	-0.26
Main	0.24	-0.22
Knuckle	0.20	-0.31

$$\hat{u} = \begin{cases} \min\left(u^+ + (1-u^+)u, \dfrac{u^+}{\tilde{u}}u\right) & \text{if } u > 0 \\ \max\left(u^- + (1+u^-)u, -\dfrac{u^-}{\tilde{u}}u\right) & \text{else} \end{cases} \quad (82)$$

where;

$\hat{u}$	=	compensated control signal
u	=	control signal
u^+	=	out-stroke deadband
u^-	=	in-stroke deadband
$\tilde{u}$	=	transition region, 0.01

In the laboratory there was identified some drift in the payload angle sensor. This has been removed with a digital high pass filter, which is shown in Equations (83) and (84). This implementation was also used for the pressure feedback filter.

$$y_i = k_f y_{i-1} + k_f(x_i - x_{i-1}) \quad (83)$$

$$k_f = \frac{T_f}{T_f + T_s} \quad (84)$$

where;

i	=	sample number
y	=	filter output
x	=	filter input
T_f	=	filter time constant
T_s	=	sample time, 0.01 s

To avoid filtering out the motion of the payload, the filter time constant T_f should be larger than the pendulum period T_p. The pendulum period is calculated based on the wire length, shown in Equation (85). Because of the value of T_p the filter time constant has been set to $T_f = 3$ s.

$$T_p = 2\pi\sqrt{\frac{L_w}{g}} = 2.837 \text{ s} \quad (85)$$

Due to limited space, a path shorter than the one used in the simulations is used in the laboratory. The position reference used in the laboratory is shown in Figure 21. The parameters used in the laboratory are shown in Table 7. The slew feedback, slew feedforward, and main feedback have been adjusted to improve position tracking.

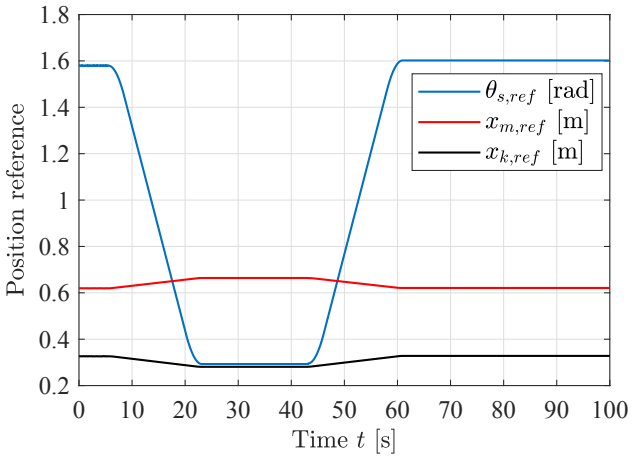

Figure 21: Position reference used in laboratory.

Table 7: Parameters used in laboratory.

Description	Name	Value
Slew feedback	$k_{p,s}$	3 rad^{-1}
Slew feedforward	$k_{ff,s}$	5.67 s/rad
Main feedback	$k_{p,m}$	15 m^{-1}
Main out-stroke feedforward	$k^+_{ff,m}$	30.16 s/m
Main in-stroke feedforward	$k^-_{ff,m}$	18.37 s/m
Knuckle feedback	$k_{p,k}$	20 m^{-1}
Knuckle out-stroke feedforward	$k^+_{ff,k}$	26.51 s/m
Knuckle in-stroke feedforward	$k^-_{ff,k}$	14.72 s/m
Wire length	L_w	2 m
Anti-swing gain	k_a	5 m/s

A plot of the swing angles without anti-swing control is shown in Figure 22, showing oscillations of the payload as expected. A plot of the position error without control is shown in Figure 23, showing good tracking except for the start of the slew actuator motion.

The influence of the pressure feedback turned out to be significant. The system became unstable without it, and proper tuning was needed to reach stability. The parameters used in the simulations, $k_{pf} = 0.02$ bar^{-1} and $\omega_{pf} = 15$ rad/s resulted in an unstable system. Different values were tested in the laboratory, and a plot of different filter configurations is shown in Figure 24. High gain and low bandwidth yielded a stable system, and $k_{pf} = 0.04$ bar^{-1} and $\omega_{pf} = 1$ rad/s were selected.

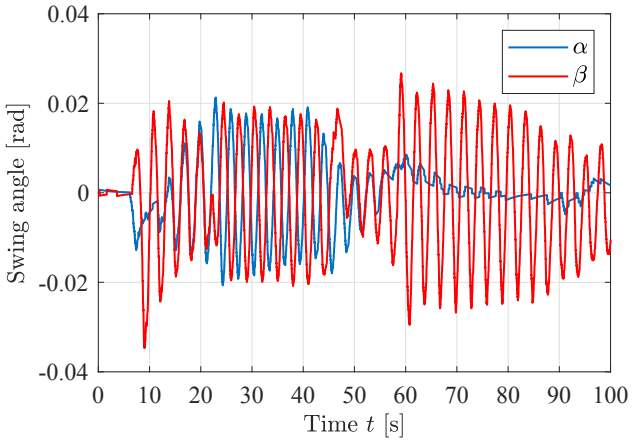

Figure 22: Swing angles without anti-swing control.

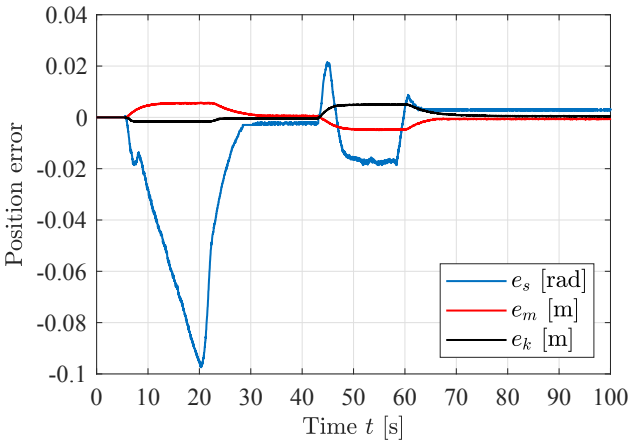

Figure 23: Position error without anti-swing control.

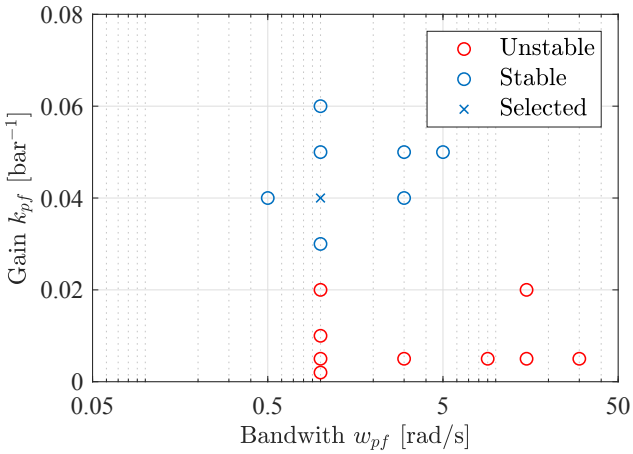

Figure 24: Stable and unstable pressure feedback configurations in the laboratory.

A plot of the swing angles without control is shown in Figure 25, showing good suppression of the oscillations, especially of α. The angle β still has some oscillations, which can be attributed to the fact that this angle is affected the most by the slewing motion and the instability issues mentioned. A plot of the position error with control is shown in Figure 26, again showcasing some difficulty to control the slewing motion. The control signal from the pressure feedback, before deadband compensation, is shown in Figure 27. It gives a large contribution, and even saturates at t=60 s.

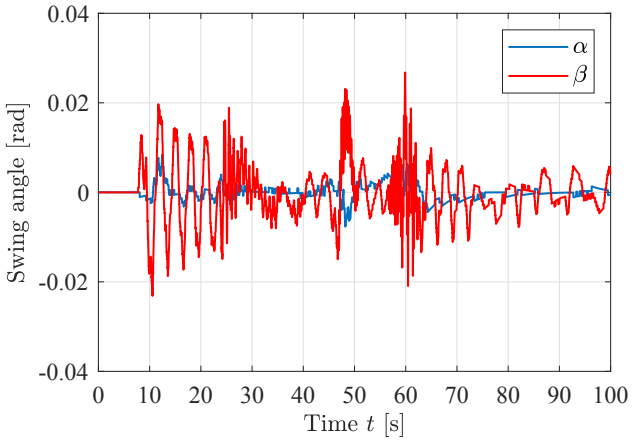

Figure 25: Swing angles with anti-swing control.

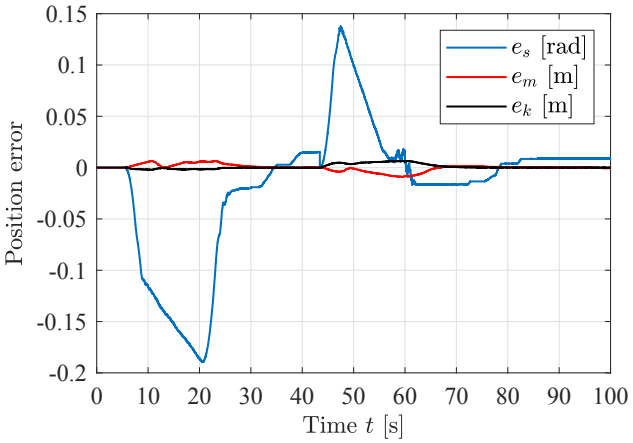

Figure 26: Position error with anti-swing control.

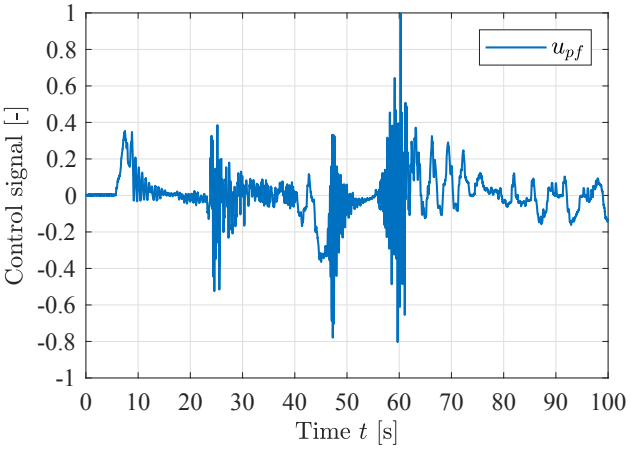

Figure 27: Control signal from pressure feedback.

The RMS values of the swing angles and position errors with and without anti-swing control is shown in Table 8. The angle α is reduced by 75 %, with a slight impact on position error on the main and knuckle cylinder. The angle β is reduced by 51 %, but has a large impact on the slew position error, quantifying the challenges faced with the slewing motion.

Table 8: Quantitative laboratory results.

Variable	No control	Anti-swing
RMS(α) [mrad]	7.19	1.75
RMS(β) [mrad]	12.94	6.29
RMS(e_s) [mrad]	26.12	66.88
RMS(e_m) [mm]	2.91	3.26
RMS(e_k) [mm]	2.19	2.36

7 Conclusion

In this paper a 3D anti-swing controller for a hydraulic loader crane is designed, simulated, evaluated, and experimentally verified on a hydraulic loader crane. Relevant kinematic functions are derived to enable control of the swing angles. The motion control system operates in actuator space, and controls the three hydraulic cylinders in order to suppress the swing angles during motion. The kinematic functions are used to transform the feedback of the swing angles α and β into command signals for the valves.

Simulation results show a large reduction in the swing angles using the anti-swing controller. Additionally, oscillations in the slewing motion were identified and suppressed by the introduction of pressure feedback. Quantitative analysis shows a slight increase in position error, but a 90 % decrease in swing angles with the proposed controller. The increase in position error is expected as the suppression of the swing angles takes a higher priority.

Laboratory experiments show stability issues with the slewing motion when using anti-swing control, and pressure feedback was required to reach stability. Results show a large reduction of 75 % for the in-plane angle α, with a small impact on position error for the main and knuckle cylinders. The slewing motion proved more difficult to control, with a larger impact on the slew position error, but still a 51 % reduction for the out-of-plane angle β was obtained.

Acknowledgments

This work was supported by the Norwegian Ministry of Education and Research grant number 155597.

Appendix A. Solving the Euler-Lagrange Equations for Hanging Load Dynamics

Selecting the coordinate $q = [\alpha\ \beta]^T$, the Euler-Lagrange equation is recalled as defined in Equation 6.

$$\frac{d}{dt}\frac{\partial \mathcal{L}}{\partial \dot{q}} - \frac{\partial \mathcal{L}}{\partial q} = 0 \tag{A.1}$$

Expanding the Lagrangian $\mathcal{L} = \mathcal{K} - \mathcal{P}$ yields:

$$\begin{aligned}\mathcal{L} = \frac{1}{2}m_p\Big(&\dot{x}_t^2 + \dot{y}_t^2 + \dot{z}_t^2 + \dot{\alpha}^2 L_w^2 + c_\alpha^2\dot{\beta}^2 L_w^2 + \dot{L}_w^2 + 2c_\alpha \dot{x}_t\dot{\alpha}L_w + 2s_\alpha\dot{x}_t\dot{L}_w - 2s_\alpha s_\beta\dot{y}_t\dot{\alpha}L_w \\ &+ 2c_\alpha c_\beta\dot{y}_t\dot{\beta}L_w + 2c_\alpha s_\beta\dot{y}_t\dot{L}_w + 2s_\alpha c_\beta\dot{z}_t\dot{\alpha}L_w + 2c_\alpha s_\beta\dot{z}_t\dot{\beta}L_w - 2c_\alpha c_\beta\dot{z}_t\dot{L}_w\Big) - m_p g\left(z_t - c_\alpha c_\beta L_w\right)\end{aligned} \tag{A.2}$$

Solving the Euler-Lagrange equation using the coordinate α yields:

$$\begin{aligned}\frac{\partial \mathcal{L}}{\partial \alpha} = m_p\Big(&-s_\alpha c_\alpha\dot{\beta}^2 L_w^2 - s_\alpha\dot{x}_t\dot{\alpha}L_w + c_\alpha\dot{x}_t\dot{L}_w - c_\alpha s_\beta\dot{y}_t\dot{\alpha}L_w - s_\alpha c_\beta\dot{y}_t\dot{\beta}L_w - s_\alpha s_\beta\dot{y}_t\dot{L}_w + c_\alpha c_\beta\dot{z}_t\dot{\alpha}L_w \qquad (A.3)\\ &- s_\alpha s_\beta\dot{z}_t\dot{\beta}L_w + s_\alpha c_\beta\dot{z}_t\dot{L}_w - g s_\alpha c_\beta L_w\Big) \qquad (A.4)\end{aligned}$$

$$\frac{\partial \mathcal{L}}{\partial \dot{\alpha}} = m_p\left(\dot{\alpha}L_w^2 + c_\alpha\dot{x}_t L_w - s_\alpha s_\beta\dot{y}_t L_w + s_\alpha c_\beta\dot{z}_t L_w\right) \tag{A.5}$$

$$\begin{aligned}\frac{d}{dt}\frac{\partial \mathcal{L}}{\partial \dot{\alpha}} = m_p\Big(&\ddot{\alpha}L_w^2 + 2\dot{\alpha}L_w\dot{L}_w - s_\alpha\dot{x}_t\dot{\alpha}L_w + c_\alpha\ddot{x}_t L_w + c_\alpha\dot{x}_t\dot{L}_w \\ &- c_\alpha s_\beta\dot{y}_t\dot{\alpha}L_w - s_\alpha c_\beta\dot{y}_t\dot{\beta}L_w - s_\alpha s_\beta\ddot{y}_t L_w - s_\alpha s_\beta\dot{y}_t\dot{L}_w \\ &+ c_\alpha c_\beta\dot{z}_t\dot{\alpha}L_w - s_\alpha s_\beta\dot{z}_t\dot{\beta}L_w + s_\alpha c_\beta\ddot{z}_t L_w + s_\alpha c_\beta\dot{z}_t\dot{L}_w\Big)\end{aligned} \tag{A.6}$$

$$\frac{d}{dt}\frac{\partial \mathcal{L}}{\partial \dot{\alpha}} - \frac{\partial \mathcal{L}}{\partial \alpha} = m_p\Big(c_\alpha\ddot{x}_t L_w - s_\alpha s_\beta\ddot{y}_t L_w + s_\alpha c_\beta\ddot{z}_t L_w + \ddot{\alpha}L_w^2 + 2\dot{\alpha}L_w\dot{L}_w + s_\alpha c_\alpha\dot{\beta}^2 L_w^2 + g s_\alpha c_\beta L_w\Big) = 0 \tag{A.7}$$

Solving for $\ddot{\alpha}$ yields:

$$\ddot{\alpha} = \frac{1}{L_w}\Big(-c_\alpha\ddot{x}_t + s_\alpha s_\beta\ddot{y}_t - s_\alpha c_\beta\ddot{z}_t - 2\dot{\alpha}\dot{L}_w - s_\alpha c_\alpha\dot{\beta}^2 L_w - g s_\alpha c_\beta\Big) \tag{A.8}$$

Solving the Euler-Lagrange equation using the coordinate β yields:

$$\frac{\partial \mathcal{L}}{\partial \beta} = m_p\Big(-s_\alpha c_\beta\dot{y}_t\dot{\alpha}L_w - c_\alpha s_\beta\dot{y}_t\dot{\beta}L_w + c_\alpha c_\beta\dot{y}_t\dot{L}_w - s_\alpha s_\beta\dot{z}_t\dot{\alpha}L_w + c_\alpha c_\beta\dot{z}_t\dot{\beta}L_w + c_\alpha s_\beta\dot{z}_t\dot{L}_w - g c_\alpha s_\beta L_w\Big) \tag{A.9}$$

$$\frac{\partial \mathcal{L}}{\partial \dot{\beta}} = m_p\Big(c_\alpha^2\dot{\beta}L_w^2 + c_\alpha c_\beta\dot{y}_t L_w + c_\alpha s_\beta\dot{z}_t L_w\Big) \tag{A.10}$$

$$\begin{aligned}\frac{d}{dt}\frac{\partial \mathcal{L}}{\partial \dot{\beta}} = m_p\Big(&-2s_\alpha c_\alpha\dot{\alpha}\dot{\beta}L_w^2 + c_\alpha^2\ddot{\beta}L_w^2 + 2\dot{\beta}L_w\dot{L}_w \\ &- s_\alpha c_\beta\dot{y}_t\dot{\alpha}L_w - c_\alpha s_\beta\dot{y}_t\dot{\beta}L_w + c_\alpha c_\beta\ddot{y}_t L_w + c_\alpha c_\beta\dot{y}_t\dot{L}_w \\ &- s_\alpha s_\beta\dot{z}_t\dot{\alpha}L_w + c_\alpha c_\beta\dot{z}_t\dot{\beta}L_w + c_\alpha s_\beta\ddot{z}_t L_w + c_\alpha s_\beta\dot{z}_t\dot{L}_w\Big)\end{aligned} \tag{A.11}$$

$$\frac{d}{dt}\frac{\partial \mathcal{L}}{\partial \dot{\beta}} - \frac{\partial \mathcal{L}}{\partial \beta} = m_p \left(c_\alpha c_\beta \ddot{y}_t L_w + c_\alpha s_\beta \ddot{z}_t L_w - 2 s_\alpha c_\alpha \dot{\alpha}\dot{\beta} L_w^2 + 2\dot{\beta} L_w \dot{L}_w + c_\alpha^2 \ddot{\beta} L_w^2 + g c_\alpha s_\beta L_w \right) = 0 \tag{A.12}$$

Solving for $\ddot{\beta}$ yields:

$$\ddot{\beta} = \frac{1}{c_\alpha L_w} \left(-c_\beta \ddot{y}_t - s_\beta \ddot{z}_t + 2 s_\alpha \dot{\alpha}\dot{\beta} L_w - 2\dot{\beta}\dot{L}_w - g s_\beta \right) \tag{A.13}$$

References

Ambrosino, M., Dawans, A., Thierens, B., and Garone, E. Oscillation reduction for knuckle cranes. In *Proceedings of the 37th International Symposium on Automation and Robotics in Construction (ISARC)*. International Association for Automation and Robotics in Construction (IAARC), Kitakyushu, Japan, pages 1590–1597, 2020. doi:10.22260/ISARC2020/0221.

Bak, M. K. and Hansen, M. R. Analysis of offshore knuckle boom crane part two: Motion control. *Modeling, Identification and Control*, 2013. 34(4):175–181. doi:10.4173/mic.2013.4.2.

Boschetti, G., Caracciolo, R., Richiedei, D., and Trevisani, A. A non-time based controller for load swing damping and path-tracking in robotic cranes. *Journal of Intelligent & Robotic Systems*, 2014. 76(2):201–217. doi:10.1007/s10846-014-0036-7.

Boschetti, G., Richiedei, D., and Trevisani, A. Delayed reference control for multi-degree-of-freedom elastic systems: Theory and experimentation. *Control Engineering Practice*, 2011. 19(9):1044 – 1055. doi:10.1016/j.conengprac.2011.05.006.

Cho, S.-K. and Lee, H.-H. A fuzzy-logic antiswing controller for three-dimensional overhead cranes. *ISA Transactions*, 2002. 41(2):235 – 243. doi:10.1016/S0019-0578(07)60083-4.

Fang, Y., Dixon, W. E., Dawson, D. M., and Zergeroglu, E. Nonlinear coupling control laws for an underactuated overhead crane system. *IEEE/ASME Transactions on Mechatronics*, 2003. 8(3):418–423. doi:10.1109/TMECH.2003.816822.

Hagen, D., Padovani, D., and Choux, M. Design and implementation of pressure feedback for loadcarrying applications with position control. In *Proceedings of the Sixteenth Scandinavian International Conference on Fluid Power*. Tampere, Finland, 2019.

Ho-Hoon Lee and Seung-Gap Choi. A model-based anti-swing control of overhead cranes with high hoisting speeds. In *Proceedings 2001 ICRA. IEEE International Conference on Robotics and Automation (Cat. No.01CH37164)*, volume 3. pages 2547–2552 vol.3, 2001. doi:10.1109/ROBOT.2001.933006.

Ho-Hoon Lee and Sung-Kun Cho. A new fuzzy-logic anti-swing control for industrial three-dimensional overhead cranes. In *Proceedings 2001 ICRA. IEEE International Conference on Robotics and Automation (Cat. No.01CH37164)*, volume 3. pages 2956–2961 vol.3, 2001. doi:10.1109/ROBOT.2001.933070.

Jensen, K. J., Ebbesen, M. K., and Hansen, M. R. Adaptive feedforward control of a pressure compensated differential cylinder. *Applied Sciences*, 2020a. 10(21):7847. doi:10.3390/app10217847.

Jensen, K. J., Ebbesen, M. K., and Hansen, M. R. Anti-swing control of a hydraulic loader crane with a hanging load. *Mechatronics*, 2021. 77:102599. doi:10.1016/j.mechatronics.2021.102599.

Jensen, K. J., Kjeld Ebbesen, M., and Rygaard Hansen, M. Development of point-to-point path control in actuator space for hydraulic knuckle boom crane. *Actuators*, 2020b. 9(2):27. doi:10.3390/act9020027.

Kjelland, M. B. and Hansen, M. R. Using input shaping and pressure feedback to suppress oscillations in slewing motion of lightweight flexible hydraulic crane. *International Journal of Fluid Power*, 2015. 16(3):141–148. doi:10.1080/14399776.2015.1089071.

Kjelland, M. B., Hansen, M. R., Tyapin, I., and Hovland, G. Tool-point control of a planar hydraulically actuated manipulator with compensation of non-actuated degree of freedom. In *2012 12th International Conference on Control, Automation and Systems*. pages 672–677, 2012.

Kjelland, M. B., Tyapin, I., Hovland, G., and Hansen, M. R. Tool-point control for a redundant heave compensated hydraulic manipulator. *Proceedings of the 2012 IFAC Workshop on Automatic Control in Offshore Oil and Gas Production, Norwegian University of Science and Technology, Trondheim, Norway*, 2012. doi:10.3182/20120531-2-NO-4020.00034.

Lee, H.-H. Modeling and Control of a Three-Dimensional Overhead Crane. *Journal of Dynamic Systems, Measurement, and Control*, 1998. 120(4):471–476. doi:10.1115/1.2801488.

Lee, H.-H. A new approach for the anti-swing control of overhead cranes with high-speed load hoisting. *International Journal of Control*, 2003. 76(15):1493–1499. doi:10.1080/0020717031000160495 4.

Lee, H.-H. A new design approach for the anti-swing trajectory control of overhead cranes with high-speed hoisting. *International Journal of Control*, 2004. 77(10):931–940. doi:10.1080/00207170412331270550.

Lee, H.-H., Cho, S.-K., and Cho, J.-S. A new anti-swing control of overhead cranes. *IFAC Proceedings Volumes*, 1997. 30(13):115 – 120. doi:10.1016/S1474-6670(17)44380-1. IFAC Workshop on Automation in the Steel Industry: Current Practice and Future Developments (ASI’97), Kyongju, Korea, 16-18 July 1997.

Lee, H.-H. and Liang, Y. A Robust Anti-Swing Trajectory Control of Overhead Cranes With High-Speed Load Hoisting: Experimental Study. 2010. Volume 8: Dynamic Systems and Control, Parts A and B:711–716. doi:10.1115/IMECE2010-39708.

Lee, H.-H., Liang, Y., and Segura, D. A Sliding-Mode Antiswing Trajectory Control for Overhead Cranes With High-Speed Load Hoisting. *Journal of Dynamic Systems, Measurement, and Control*, 2006. 128(4):842–845. doi:10.1115/1.2364010.

Ngo, Q. H. and Hong, K. Sliding-mode antisway control of an offshore container crane. *IEEE/ASME Transactions on Mechatronics*, 2012. 17(2):201–209. doi:10.1109/TMECH.2010.2093907.

Park, H., Chwa, D., and Hong, K.-S. A feedback linearization control of container cranes: Varying rope length. *International Journal of Control, Automation, and Systems*, 2007. 5.

Park, M., Chwa, D., and Hong, S. Antisway tracking control of overhead cranes with system uncertainty and actuator nonlinearity using an adaptive fuzzy sliding-mode control. *IEEE Transactions on Industrial Electronics*, 2008. 55(11):3972–3984. doi:10.1109/TIE.2008.2004385.

Pedersen, H. C. and Andersen, T. O. Pressure feedback in fluid power systemsactive damping explained and exemplified. *IEEE Transactions on Control Systems Technology*, 2018. 26(1):102–113. doi:10.1109/TCST.2017.2650680.

Pedersen, H. C., Andersen, T. O., and Hansen, M. R. Guidelines for properly adjusting pressure feedback in systems with over-centre valves. In *Proceedings of the BATH/ASME 2016 Symposium on Fluid Power and Motion Control*. Bath, UK, 2016. doi:10.1115/FPMC2016-1780.

Schindele, D., Menn, I., and Aschemann, H. Nonlinear optimal control of an overhead travelling crane. In *2009 IEEE Control Applications, (CCA) Intelligent Control, (ISIC)*. pages 1045–1050, 2009. doi:10.1109/CCA.2009.5280705.

Singhose, W., Seering, W., and Singer, M. Input shaping for vibration reduction with specified insensitivity to modeling errors. *Proc. Japan-USA Symp. Flexible Automation*, 1996. 1.

Sorensen, K. L., Singhose, W., and Dickerson, S. A controller enabling precise positioning and sway reduction in bridge and gantry cranes. *Control Engineering Practice*, 2007. 15(7):825 – 837. doi:10.1016/j.conengprac.2006.03.005. Special Issue on Award Winning Applications.

Sung-Kun Cho and Ho-Hoon Lee. An anti-swing control of a 3-dimensional overhead crane. In *Proceedings of the 2000 American Control Conference. ACC (IEEE Cat. No.00CH36334)*, volume 2. pages 1037–1041 vol.2, 2000. doi:10.1109/ACC.2000.876658.

Paper F

Online Deflection Compensation of a Flexible Hydraulic Loader Crane Using Neural Networks and Pressure Feedback

This paper has been published as:

Jensen, K.J.; Kjeld Ebbesen, M.; Rygaard Hansen, M. Online Deflection Compensation of a Flexible Hydraulic Loader Crane Using Neural Networks and Pressure Feedback. *Robotics* **2022**, *11(2)*, 34. doi:10.3390/robotics11020034

robotics

MDPI

Article

Online Deflection Compensation of a Flexible Hydraulic Loader Crane Using Neural Networks and Pressure Feedback

Konrad Johan Jensen *, Morten Kjeld Ebbesen and Michael Rygaard Hansen

Department of Engineering Sciences, University of Agder, 4879 Grimstad, Norway; morten.k.ebbesen@uia.no (M.K.E.); michael.r.hansen@uia.no (M.R.H.)
* Correspondence: konrad.j.jensen@uia.no

Abstract: The deflection compensation of a hydraulically actuated loader crane is presented. Measurement data from the laboratory are used to design a neural network deflection estimator. Kinematic expressions are derived and used with the deflection estimator in a feedforward topology to compensate for the static deflection. A dynamic deflection compensator is implemented, using pressure feedback and an adaptive bandpass filter. Simulations are conducted to verify the performance of the control system. Experimental results showcase the effectiveness of both the static and dynamic deflection compensator while running closed-loop motion control, with a 90% decrease in static deflection.

Keywords: deflection compensation; kinematics; loader crane; hydraulics; neural network

check for updates

Citation: Jensen, K.J.; Ebbesen, M.K.; Hansen, M.R. Online Deflection Compensation of a Flexible Hydraulic Loader Crane Using Neural Networks and Pressure Feedback. *Robotics* **2022**, *11*, 34. https://doi.org/10.3390/robotics11020034

Academic Editor: Ming Xie

Received: 21 February 2022
Accepted: 16 March 2022
Published: 17 March 2022

Publisher's Note: MDPI stays neutral with regard to jurisdictional claims in published maps and institutional affiliations.

Copyright: © 2022 by the authors. Licensee MDPI, Basel, Switzerland. This article is an open access article distributed under the terms and conditions of the Creative Commons Attribution (CC BY) license (https://creativecommons.org/licenses/by/4.0/).

1. Introduction

Flexible manipulators have received extensive research attention in recent years. The use of lightweight though flexible manipulators yields many advantages over rigid structures, including lower mass and inertia, lower energy consumption, higher payload-to-weight ratio, and smaller actuators. However, there are challenges associated with the structural flexibility of these manipulators that must be taken into account. The deflection, oscillations, and potential nonlinearities may lead to issues with steady-state performance, stability, and controllability.

Different approaches of modeling flexible manipulators have previously been considered, such as lumped parameter [1–3], assumed modes [4–6], Lagrangian formulation [7,8] and neural networks [9].

The control of flexible manipulators is typically divided into two groups, model-based control and model-free control. The primary goal of both control techniques is to dampen oscillations and reduce the consequences of static deflection in the flexible manipulator. Model-based control may use the modeling techniques shown earlier, and can be implemented in a feedforward topology. This includes control with linear models [10], nonlinear inverse dynamics [11], and input shaping [12]. In model-free control, the system does not rely on a mathematical model of the system, but rather sensor measurements from the system. Model-free control includes robust control and sliding mode control [13–15].

Another technique that has received research interest for the control of flexible manipulators is neural network control. This can include both feedforward and feedback controllers [16]. Neural networks are often combined with sliding mode control for robust control and the stabilization of nonlinear systems [17–19]. Kinematic control of redundant manipulators was investigated in [20,21].

Large manipulators, such as hydraulic cranes, may experience large static deflections under heavy load. This is especially an issue with weight-optimized structures, such as loader cranes. As a consequence, the calculated crane tip position based on rigid body kinematics may yield significant errors and may be a safety concern that, potentially, can lead to collisions with the surroundings if not compensated for. This is especially

true when using closed-loop motion control and when forward kinematics are used to estimate the crane tip position. For manually operated cranes, the operator may visually identify and compensate for the deflections, effectively closing the loop. This is often called operator in the loop. To reach the same level of automation as industrial robots, deflection compensation may play a critical role in increasing the precision and safety when using closed-loop motion control for large cranes.

In this paper, a new method for closed-loop control of a hydraulic manipulator is presented. The novelty lies in the combination of compensation for both static and dynamic deflection while running path control. This combination of path control and static and dynamic compensation is an answer to the previously mentioned problems for highly flexible manipulators, and is therefore developed and implemented on a commercial hydraulically actuated loader crane.

2. Considered System

In this paper, a HMF 2020K4 loader crane made by HMF Group A/S (Højbjerg, Denmark) is used as a basis for simulations and experiments; see Figure 1. The crane has three degrees of freedom of interest: the rotation of the main boom, the rotation of the knuckle boom and the extension of the telescopic booms. They are controlled by means of the main cylinder, the knuckle cylinder and, working as a single sequential cylinder, the telescopic cylinders. Each cylinder is driven by a pressure-compensated directional control valve, which ensures load-independent flow control. Counterbalance valves are used for load holding, assisting in load lowering, and protection against pressure surges. An illustration of the hydraulic system for the knuckle cylinder is shown in Figure 2.

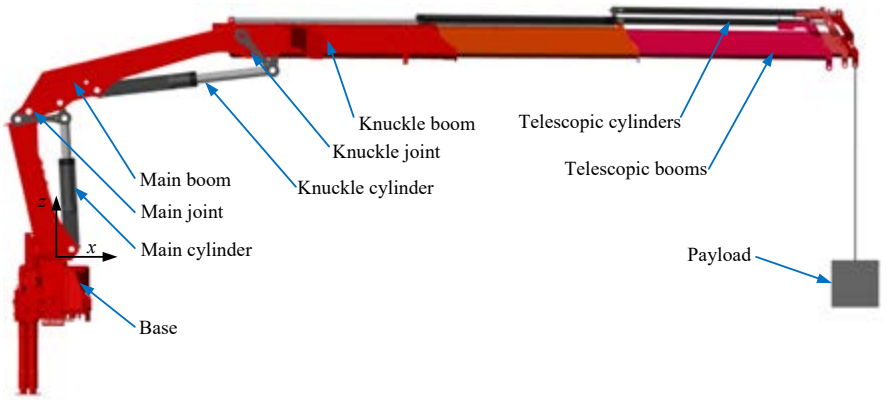

Figure 1. Illustration of the HMF 2020K4 loader crane.

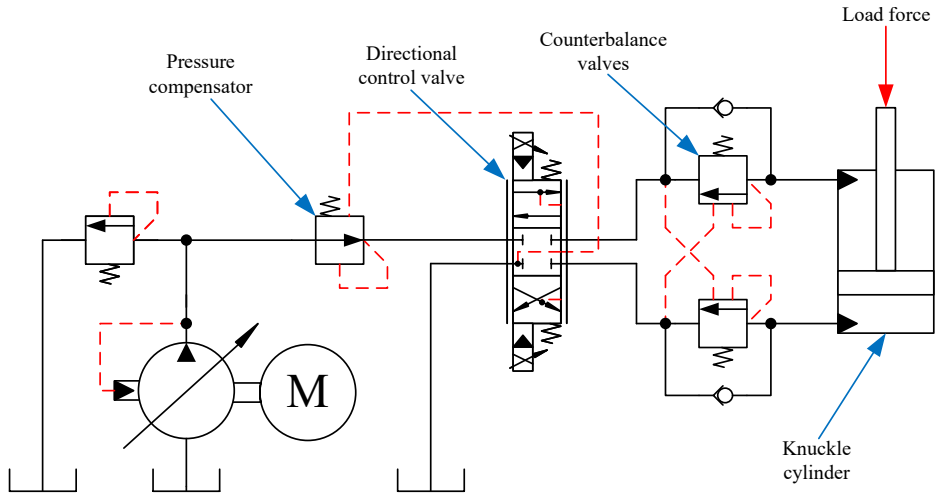

Figure 2. Hydraulic system of the knuckle cylinder.

Control Strategy

The novel approach is shown in Figure 3. The crane is running path control in the actuator space with position feedback and velocity feedforward developed in [22]. The control strategy for the deflection compensation is split into static compensation and dynamic compensation. The static deflection compensator uses feedforward and adjusts the position reference based on an estimated deflection for a given actuator position. The dynamic deflection compensator uses feedback of the load pressure p_L to measure and suppress the oscillations of the crane.

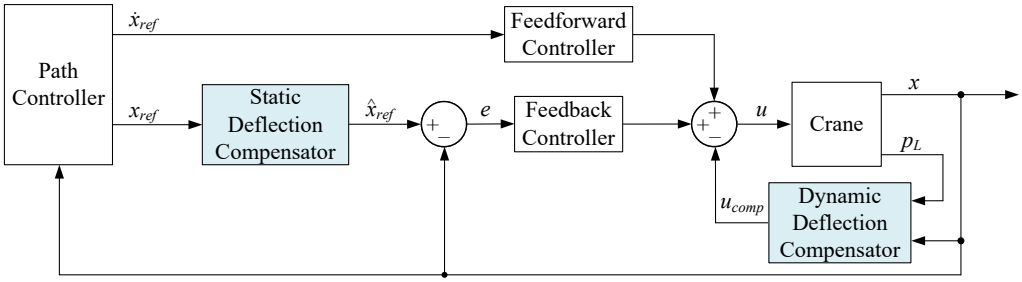

Figure 3. Control strategy with the novel deflection compensators highlighted in light blue.

3. Static Deflection Compensation

The static deflection compensator is a model-based feedforward controller and is based on a deflection estimator and kinematic functions. The estimated deflection of the crane is in Cartesian space, while the motion controller operates in actuator space. The relevant kinematic relations are derived in this section and are then used to generate a modified cylinder position reference.

3.1. Measuring Deflection in Laboratory

Experiments are conducted in the laboratory using a laser tracker, namely a Leica Absolute Tracker AT960. The laser tracker measures the position of a reflector mounted on the crane tip. A 581 kg payload is connected to the winch on the crane, and by measuring the crane tip position with and without the payload, the deflection of the crane tip is effectively measured. The setup in the laboratory is shown in Figure 4. Note that 581 kg was the heaviest payload that the crane could consistently lift at this boom length and pressure level available in the laboratory.

Multiple measurements are conducted with different cylinder positions. The resulting crane tip position in the xz-plane with and without load is shown in Figure 5, with the black lines illustrating the crane position for one of the samples. Deflection is calculated as the difference between the load and no-load tip position.

3.2. Forward Kinematics

Forward kinematics are used to go from joint space to Cartesian space. The forward kinematics are calculated based on Denavit–Hartenberg parameters. Figure 6 shows the joint angles, telescopic length, lifting radius, and tip position. Figure 7 shows the geometry which is used with the Denavit–Hartenberg parameters, where both booms are horizontal. The dimensions between consecutive joints are shown in Table 1. The Denavit–Hartenberg parameters are shown in Table 2, where **R** and **T** are rotational and translational matrices, respectively. The angles θ_m and θ_k denote the rotation about the main joint and knuckle joint, respectively. The forward kinematics are similar to what was developed earlier in [23], with the addition of the telescopic actuator length x_t used in this paper.

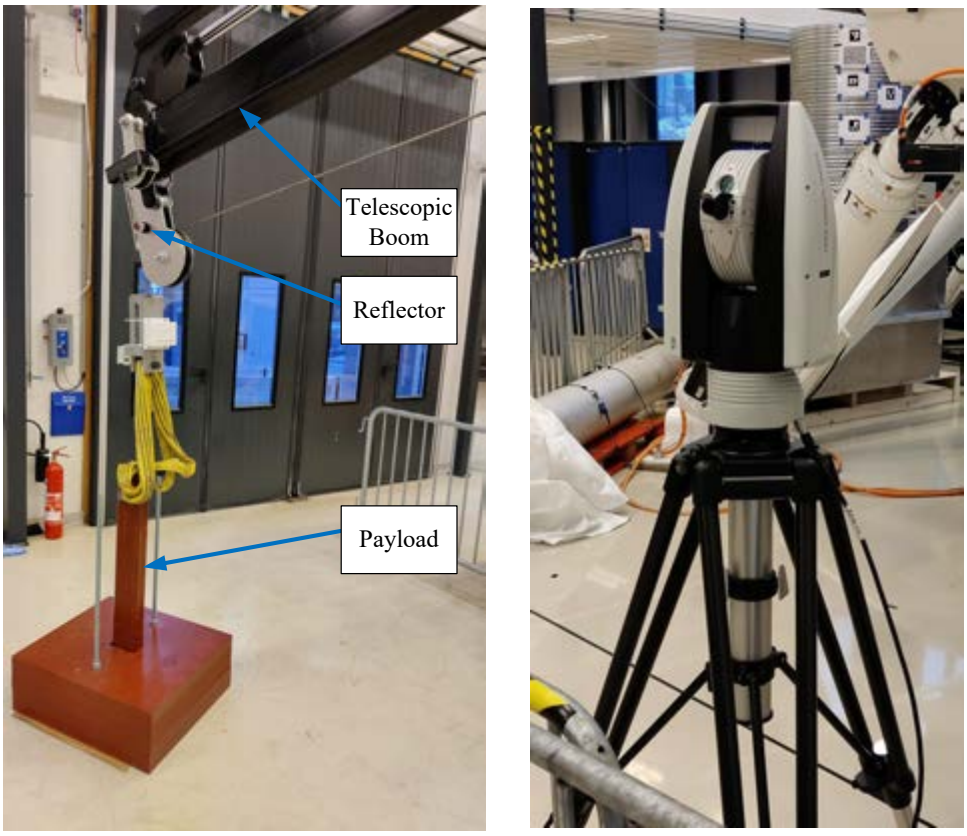

(**a**) (**b**)

Figure 4. Experimental setup in the lab. The laser tracker measures the crane tip position using the attached reflector. (**a**) Crane tip showing the telescopic boom, reflector, and payload, (**b**) Leica Absolute Tracker AT960.

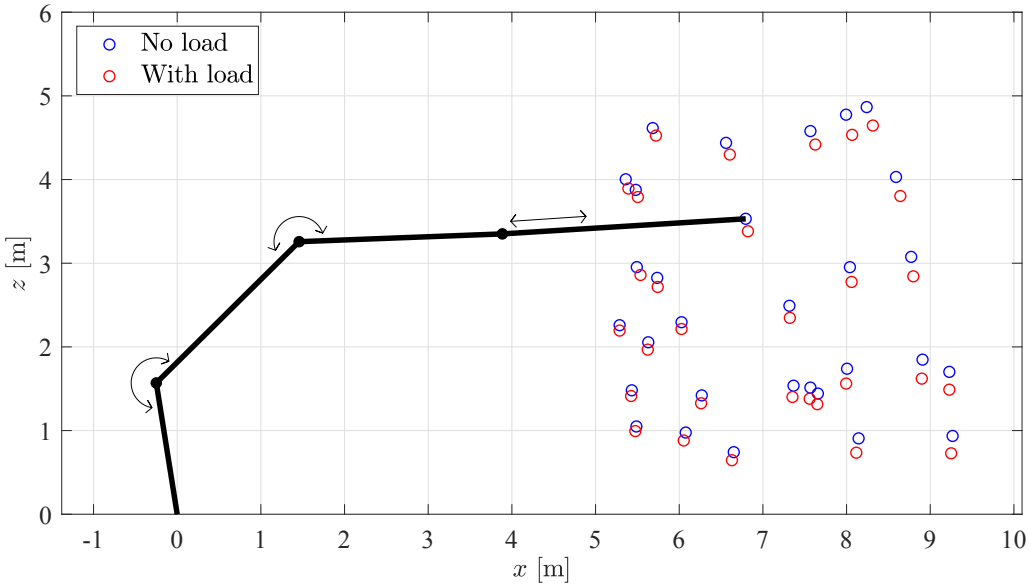

Figure 5. Crane tip position in xz-plane with and without load from laboratory measurements. Crane position illustrated in black with its three degrees of freedom.

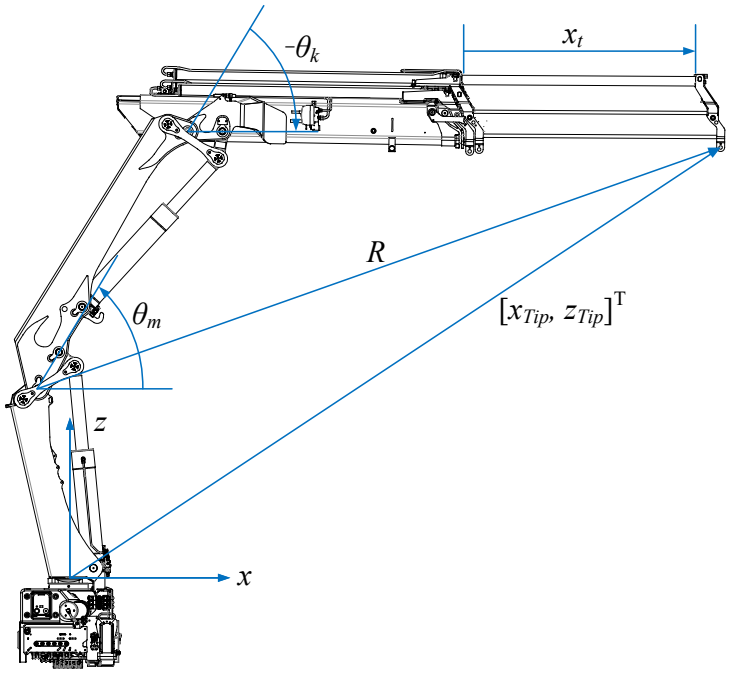

Figure 6. Crane geometry showing joint angles, lifting radius R, telescopic length x_t, and crane tip position.

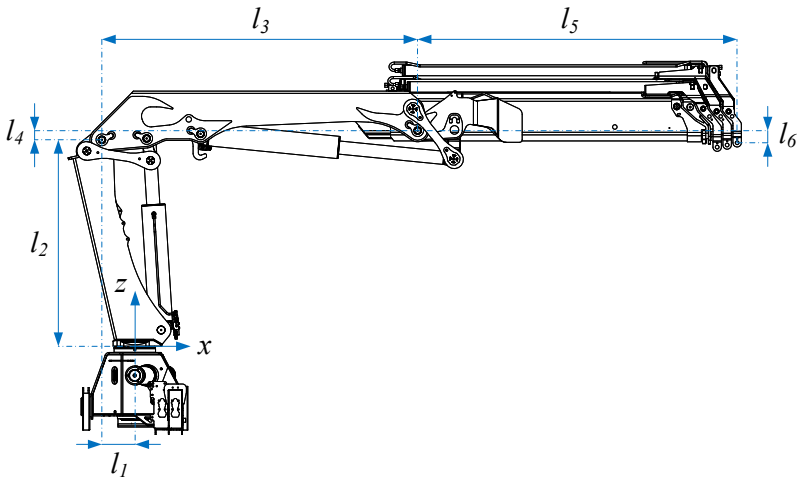

Figure 7. Crane geometry used with Denavit–Hartenberg parameters.

Table 1. Dimensions shown in Figure 7.

Name	Length [m]
l_1	0.250
l_2	1.569
l_3	2.400
l_4	0.070
l_5	2.429
l_6	0.093

Table 2. Denavit–Hartenberg parameters.

$\mathbf{R}_z$	$\mathbf{T}_z$	$\mathbf{T}_x$	$\mathbf{R}_x$
0	l_2	$-l_1$	90°
θ_m	0	0	-90°
0	l_4	l_3	90°
θ_k	0	0	-90°
0	$-l_6$	l_5	0
0	0	x_t	0

The transformation matrix $\mathbf{A}_{DH}$ is given as

$$\begin{aligned}\mathbf{A}_{DH} &= \mathbf{T}_z(l_2)\cdot\mathbf{T}_x(-l_1)\cdot\mathbf{R}_x(90^\circ)\cdot\mathbf{R}_z(\theta_m)\cdot\mathbf{R}_x(-90^\circ)\cdot\mathbf{T}_z(l_4)\cdot\mathbf{T}_x(l_3)\cdot\mathbf{R}_x(90^\circ)\\ &\quad\cdot\mathbf{R}_z(\theta_k)\cdot\mathbf{R}_x(-90^\circ)\cdot\mathbf{T}_z(-l_6)\cdot\mathbf{T}_x(l_5)\cdot\mathbf{T}_x(x_t) \qquad (1)\\ &= \begin{bmatrix} c_{\theta_m+\theta_k} & 0 & -s_{\theta_m+\theta_k} & x_{Tip} \\ 0 & 1 & 0 & 0 \\ s_{\theta_m+\theta_k} & 0 & c_{\theta_m+\theta_k} & z_{Tip} \\ 0 & 0 & 0 & 1 \end{bmatrix} \qquad (2)\end{aligned}$$

The crane tip positions x_{Tip} and z_{Tip} are given in Equations (3) and (4), using the notation $\cos(\theta) = c_\theta$ and $\sin(\theta) = s_\theta$.

$$x_{Tip} = -l_1 + l_3\cdot c_{\theta_m} - l_4\cdot s_{\theta_m} + l_5\cdot c_{\theta_m+\theta_k} + l_6\cdot s_{\theta_m+\theta_k} + x_t\cdot c_{\theta_m+\theta_k} \qquad (3)$$

$$z_{Tip} = l_2 + l_3\cdot s_{\theta_m} + l_4\cdot c_{\theta_m} + l_5\cdot s_{\theta_m+\theta_k} - l_6\cdot c_{\theta_m+\theta_k} + x_t\cdot s_{\theta_m+\theta_k} \qquad (4)$$

3.3. Inverse Kinematics

Inverse kinematics are used to go from Cartesian space to joint space. Solving the inverse kinematics of the crane is similar to a typical two-link manipulator, with the exception that the length of each link is split into an x-component and z-component. In addition, the three actuators give the crane kinematic redundancy in the case of motion in the xz-plane. This is solved by keeping the telescopic actuator length x_t fixed and solving for the main joint angle θ_m and knuckle joint angle θ_k. This is done because the main cylinder and knuckle cylinder are easier to control and have less friction than the telescopic cylinder.

The calculations are based on the lifting radius R, which is the distance from the main joint to the crane tip. The squared lifting radius R^2 is given by

$$R^2 = \left(x_{Tip} + l_1\right)^2 + \left(z_{Tip} - l_2\right)^2 \qquad (5)$$

Some intermediate equations are used to solve for the knuckle boom angle θ_k. Inserting Equations (3) and (4) into (5) yields

$$\begin{aligned}R^2 &= (l_3\cdot c_{\theta_m} - l_4\cdot s_{\theta_m} + l_5\cdot c_{\theta_m+\theta_k} + l_6\cdot s_{\theta_m+\theta_k} + x_t\cdot c_{\theta_m+\theta_k})^2\\ &\quad + (l_3\cdot s_{\theta_m} + l_4\cdot c_{\theta_m} + l_5\cdot s_{\theta_m+\theta_k} - l_6\cdot c_{\theta_m+\theta_k} + x_t\cdot s_{\theta_m+\theta_k})^2\\ &= 2\cdot(l_3\cdot l_5 - l_4\cdot l_6 + l_3\cdot x_t)\cdot c_{\theta_k} + 2\cdot(l_3\cdot l_6 + l_4\cdot l_5 + l_4\cdot x_t)\cdot s_{\theta_k} \qquad (6)\\ &\quad + l_3^2 + l_4^2 + l_5^2 + l_6^2 + 2\cdot l_5\cdot x_t + x_t^2\end{aligned}$$

The equations in a more compact form are given below:

$$R^2 = A\cdot c_{\theta_k} + B\cdot s_{\theta_k} + C \qquad (7)$$

$$A = 2\cdot(l_3\cdot l_5 - l_4\cdot l_6 + l_3\cdot x_t) \qquad (8)$$

$$B = 2\cdot(l_3\cdot l_6 + l_4\cdot l_5 + l_4\cdot x_t) \qquad (9)$$

$$C = l_3^2 + l_4^2 + l_5^2 + l_6^2 + 2\cdot l_5\cdot x_t + x_t^2 \qquad (10)$$

Solving Equation (7) yields two solutions, and by taking the minimum angle, the crane will be in the desired elbow-up configuration. The calculation of θ_k is shown below:

$$\theta_k^* = 2 \cdot \tan^{-1}\left(\frac{B \pm \sqrt{A^2 + B^2 - C^2 + 2 \cdot C \cdot R^2 - R^4}}{A - C + R^2}\right) \tag{11}$$

$$\theta_k = \min(\theta_k^*) \tag{12}$$

To find θ_m, Equations (3) and (4) are expanded, and the terms containing θ_m are factorized out.

$$x_{Tip} = (l_5 \cdot c_{\theta_k} + l_6 \cdot s_{\theta_k} + x_t \cdot c_{\theta_k} + l_3) \cdot c_{\theta_m} - (l_5 \cdot s_{\theta_k} - l_6 \cdot c_{\theta_k} + x_t \cdot s_{\theta_k} + l_4) \cdot s_{\theta_m} - l_1 \tag{13}$$

$$z_{Tip} = (l_5 \cdot s_{\theta_k} - l_6 \cdot c_{\theta_k} + x_t \cdot s_{\theta_k} + l_4) \cdot c_{\theta_m} + (l_5 \cdot c_{\theta_k} + l_6 \cdot s_{\theta_k} + x_t \cdot c_{\theta_k} + l_3) \cdot s_{\theta_m} + l_2 \tag{14}$$

Rearranging gives a more compact form, yielding two equations with two unknowns, namely $\cos(\theta_m)$ and $\sin(\theta_m)$.

$$x_{Tip} = E \cdot c_{\theta_m} - D \cdot s_{\theta_m} - l_1 \tag{15}$$

$$z_{Tip} = D \cdot c_{\theta_m} + E \cdot s_{\theta_m} + l_2 \tag{16}$$

$$D = l_5 \cdot s_{\theta_k} - l_6 \cdot c_{\theta_k} + x_t \cdot s_{\theta_k} + l_4 \tag{17}$$

$$E = l_5 \cdot c_{\theta_k} + l_6 \cdot s_{\theta_k} + x_t \cdot c_{\theta_k} + l_3 \tag{18}$$

These two equations are then solved to find θ_m.

$$c_{\theta_m} = \frac{D \cdot z_{Tip} - D \cdot l_2 + E \cdot x_{Tip} + E \cdot l_1}{D^2 + E^2} \tag{19}$$

$$s_{\theta_m} = \frac{E \cdot z_{Tip} - E \cdot l_2 - D \cdot x_{Tip} - D \cdot l_1}{D^2 + E^2} \tag{20}$$

$$\theta_m = \tan^{-1}\left(\frac{s_{\theta_m}}{c_{\theta_m}}\right) \tag{21}$$

3.4. Actuator Kinematics

Actuator kinematics are used to go from actuator space to joint space. They were developed earlier in [23]. An illustration of the main joint linkage is shown in Figure 8. The associated lengths are given in Table 3.

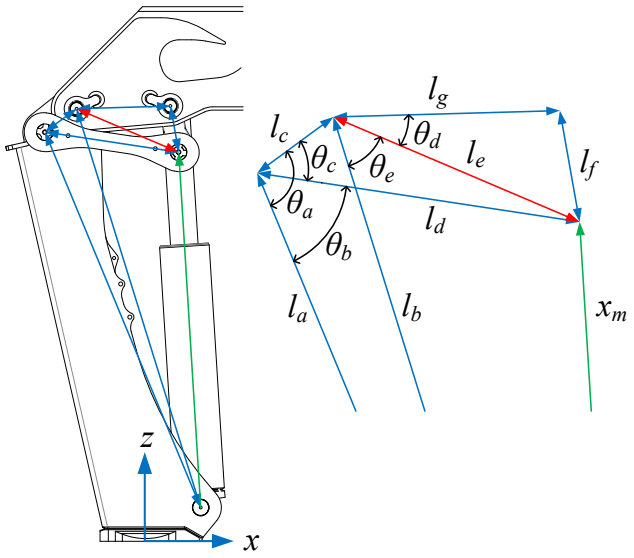

Figure 8. Illustration of the main joint actuator kinematics.

Table 3. Lengths of the parts in the main linkage.

Name	Length [m]
l_a	1.473
l_b	1.514
l_c	0.143
l_d	0.490
l_f	0.170
l_g	0.340

For reference, the calculation of the main joint angle $\theta_m = \theta_m(x_m)$ is given below:

$$\theta_a = \cos^{-1}\left(\frac{l_a^2 + l_c^2 - l_b^2}{2 \cdot l_a \cdot l_c}\right) \tag{22}$$

$$\theta_b = \cos^{-1}\left(\frac{l_a^2 + l_d^2 - x_m^2}{2 \cdot l_a \cdot l_d}\right) \tag{23}$$

$$\theta_c = \theta_a - \theta_b \tag{24}$$

$$l_e = \sqrt{l_c^2 + l_d^2 - 2 \cdot l_c \cdot l_d \cdot c_{\theta_c}} \tag{25}$$

$$\theta_d = \cos^{-1}\left(\frac{l_e^2 + l_g^2 - l_f^2}{2 \cdot l_e \cdot l_g}\right) \tag{26}$$

$$\theta_e = \cos^{-1}\left(\frac{l_b^2 + l_e^2 - x_m^2}{2 \cdot l_b \cdot l_e}\right) \tag{27}$$

$$\theta_m = \theta_d + \theta_e - \tilde{\theta}_m \tag{28}$$

3.5. Inverse Actuator Kinematics

Inverse actuator kinematics are used to go from joint space to actuator space. As taking the inverse of Equation (28) is difficult due to it being such a complex expression, curve fitting is used instead. The 9th order polynomials are used, shown below:

$$x = p_9 \cdot \theta^9 + p_8 \cdot \theta^8 + p_7 \cdot \theta^7 + p_6 \cdot \theta^6 + p_5 \cdot \theta^5 + p_4 \cdot \theta^4 + p_3 \cdot \theta^3 + p_2 \cdot \theta^2 + p_1 \cdot \theta + p_0 \tag{29}$$

While the mapping $\theta_m = \theta_m(x_m)$ given in Equation (28) describes the actuator kinematics for the main cylinder, the inverse kinematics is the mapping $x_m = x_m(\theta_m)$. Iteratively calculating and plotting $\theta_m = \theta_m(x_m)$ and then switching the axis gives a solution on which the curve is fitted. The coefficients for the main cylinder and knuckle cylinder are given in Table 4, and plots of the curve fits are shown in Figure 9, showing that the curve fit yields a close match to the numerical inverse.

Table 4. Curve-fitting coefficients for inverse actuator kinematics.

Coefficient	Main	Knuckle
p_9	-8.324×10^{-5}	-2.044×10^{-5}
p_8	4.068×10^{-4}	-2.996×10^{-4}
p_7	-4.087×10^{-4}	-1.571×10^{-3}
p_6	-1.797×10^{-3}	-4.609×10^{-3}
p_5	2.914×10^{-3}	-1.045×10^{-2}
p_4	1.293×10^{-2}	-1.135×10^{-2}
p_3	-4.794×10^{-2}	3.451×10^{-3}
p_2	2.438×10^{-2}	1.153×10^{-2}
p_1	3.471×10^{-1}	3.042×10^{-1}
p_0	1.291	1.923

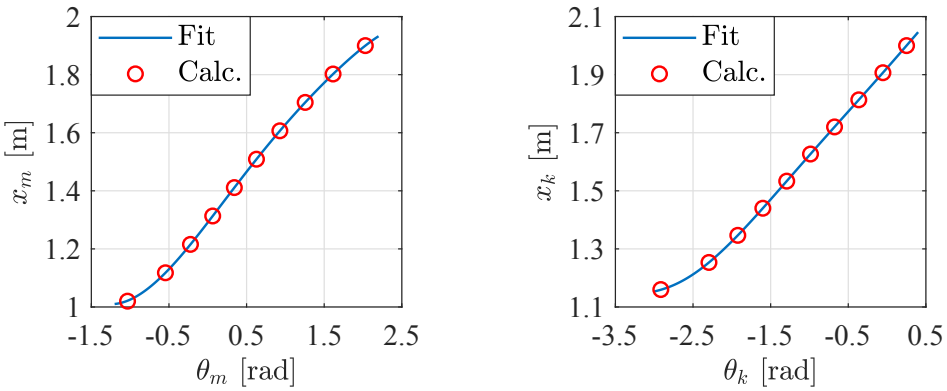

(**a**) (**b**)

Figure 9. Curve fit for inverse actuator kinematics. (**a**) Curve fit for main cylinder, (**b**) Curve fit for knuckle cylinder.

3.6. Neural Network Deflection Estimator

A neural network is used to estimate the deflection of the crane tip. Measurements from the laboratory make up the training data for the network. The network predicts the deflection in the x- and z-directions based on the cylinder positions x_m, x_k, and x_t. The selected topology is a classical multilayer perceptron with a single hidden layer. Each node uses the tanh activation function. Input scaling is employed to normalize the data to the range $[-1, 1]$, in order to stay in the center region of the tanh activation function. Likewise, the output scaling is used to scale the outputs from $[-1, 1]$ to a desired range, set by the measured deflection in the output training data. An illustration of a single node with weights, bias, and activation function is shown in Figure 10. An overview of the neural network with input scaling, output scaling, and ten hidden neurons is shown in Figure 11.

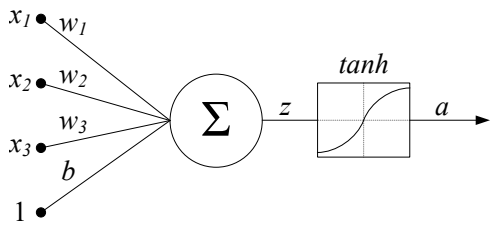

Figure 10. Illustration of a single node.

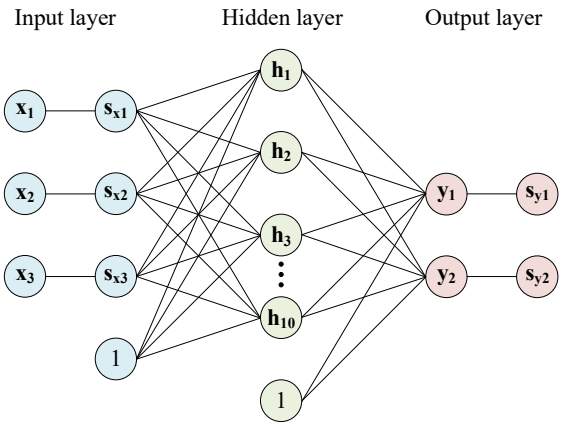

Figure 11. Overview of the neural network.

3.6.1. Forward Propagation

Forward propagation refers to computing the outputs of the network with a given input. The computations are done using vectors and matrices to calculate the output of each layer in a single step. The formula for the input scaling is shown in Equations (30)–(34). The input is scaled to lie between -1 and 1 based on the maximum and minimum value of the input training data $\mathbf{x}_{training}$.

$$\mathbf{s_x} = (\mathbf{x} - \mathbf{x}_{min}) \cdot \frac{\mathbf{s}_{\mathbf{x},max} - \mathbf{s}_{\mathbf{x},min}}{\mathbf{x}_{max} - \mathbf{x}_{min}} + \mathbf{s}_{\mathbf{x},min} \tag{30}$$

$$\mathbf{x}_{min} = \min(\mathbf{x}_{training}) \tag{31}$$

$$\mathbf{x}_{max} = \max(\mathbf{x}_{training}) \tag{32}$$

$$\mathbf{s}_{\mathbf{x},min} = -1 \tag{33}$$

$$\mathbf{s}_{\mathbf{x},max} = 1 \tag{34}$$

Forward propagation for the hidden layer and output layer using tanh as the activation function is shown in Equations (35)–(38).

$$\mathbf{z_h} = \mathbf{W_h} \cdot \mathbf{s_x} + \mathbf{b_h} \tag{35}$$

$$\mathbf{h} = \tanh(\mathbf{z_h}) \tag{36}$$

$$\mathbf{z_y} = \mathbf{W_y} \cdot \mathbf{h} + \mathbf{b_y} \tag{37}$$

$$\mathbf{y} = \tanh(\mathbf{z_y}) \tag{38}$$

where

$\mathbf{W_h}$ = weight matrix of the hidden layer;
$\mathbf{b_h}$ = bias vector of the hidden layer;
$\mathbf{W_y}$ = weight matrix of the output layer;
$\mathbf{b_y}$ = bias vector of the output layer.

The output scaling is similar to the input scaling, and is shown in Equations (39)–(43).

$$\mathbf{s_y} = (\mathbf{y} - \mathbf{y}_{min}) \cdot \frac{\mathbf{s}_{\mathbf{y},max} - \mathbf{s}_{\mathbf{y},min}}{\mathbf{y}_{max} - \mathbf{y}_{min}} + \mathbf{s}_{\mathbf{y},min} \tag{39}$$

$$\mathbf{y}_{min} = -1 \tag{40}$$

$$\mathbf{y}_{max} = 1 \tag{41}$$

$$\mathbf{s}_{\mathbf{y},min} = \min(\mathbf{y}_{training}) \tag{42}$$

$$\mathbf{s}_{\mathbf{y},max} = \max(\mathbf{y}_{training}) \tag{43}$$

3.6.2. Backpropagation

Backpropagation refers to the process of calculating the gradient of the cost function with respect to the weights. This is typically done using the chain rule one layer at the time. The gradient descent is then used to update the weights. The training data are now a matrix, where each column is a single measurement. The cost function is made using the squared Frobenius norm of the scaled output minus the output training data. The cost function is defined as

$$C = \frac{1}{2} \cdot \left\| \mathbf{s_y} - \mathbf{y}_{training} \right\|_F^2 \tag{44}$$

To train the network, the partial derivatives of the cost function must first be calculated. Note that the derivative of the activation function is $\frac{d}{dx}\tanh(x) = 1 - \tanh^2(x)$. The backpropagation for the output layer and the weight $\mathbf{W_h}$ is shown in Equations (45)–(49). Di-

viding by the number of training examples, N is used to average the calculations across the training set.

$$\frac{\partial C}{\partial \mathbf{y}} = \mathbf{s_y} - \mathbf{y}_{training} \tag{45}$$

$$\frac{\partial \mathbf{y}}{\partial \mathbf{z_y}} = 1 - \tanh^2(\mathbf{z_y}) \tag{46}$$

$$\frac{\partial C}{\partial \mathbf{z_y}} = \frac{\partial C}{\partial \mathbf{y}} \cdot \frac{\partial \mathbf{y}}{\partial \mathbf{z_y}} \tag{47}$$

$$\frac{\partial \mathbf{z_y}}{\partial \mathbf{W_y}} = \mathbf{h}^T \tag{48}$$

$$\frac{\partial C}{\partial \mathbf{W_y}} = \frac{1}{N} \cdot \frac{\partial C}{\partial \mathbf{z_y}} \cdot \frac{\partial \mathbf{z_y}}{\partial \mathbf{W_y}} \tag{49}$$

The partial derivatives are then used to update the weights. L2 regularization is used to avoid overfitting. This limits the value of the weights in the network to achieve better generalization. Updating the weights with L2 regularization only requires one additional parameter λ, in addition to the learning rate η. The adjusted cost function and the updates to the weight $\mathbf{W_h}$ are shown in Equations (50)–(51).

$$C^* = C + \frac{\lambda}{2 \cdot N} \cdot \|\mathbf{W_h}\|_F^2 \tag{50}$$

$$\mathbf{W_h} \leftarrow \mathbf{W_h} - \eta \cdot \left(\frac{\partial C}{\partial \mathbf{W_h}} + \lambda \cdot \mathbf{W_h} \right) \tag{51}$$

3.6.3. Training Results

The measured deflection from the laboratory is used to train the network. The network is trained using $\eta = 1$ and $\lambda = 10^{-4}$ and converged after 3×10^5 iterations. Surface plots of the estimated deflection for some cylinder lengths are shown in Figures 12 and 13. It can be seen that the telescope length x_t does not significantly impact the deflection in x-direction, but it has a major contribution to the deflection in the z-direction.

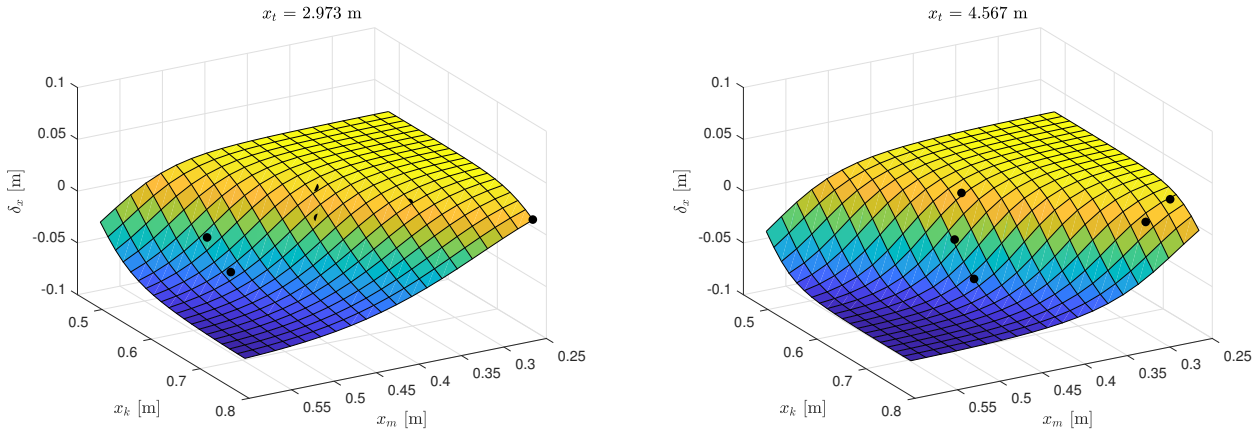

(**a**) (**b**)

Figure 12. Predicted deflection in x-direction δ_x. Black dots show measured data from the laboratory. (**a**) Predicted δ_x with x_t = 2.973 m. (**b**) Predicted δ_x with x_t = 4.567 m.

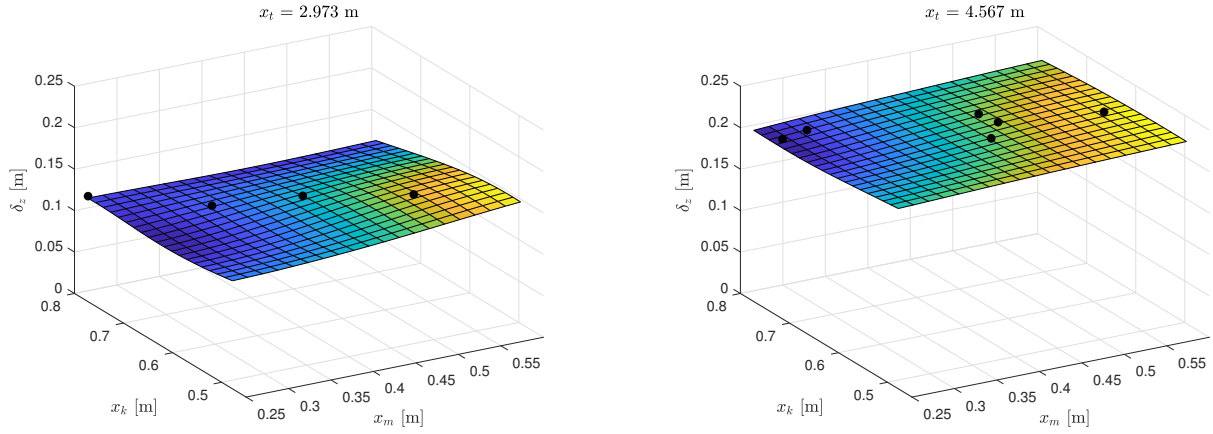

(**a**) (**b**)

Figure 13. Predicted deflection in z-direction δ_z. Black dots show measured data from the laboratory. (**a**) Predicted δ_z with x_t = 2.973 m. (**b**) Predicted δ_z with x_t = 4.567 m.

3.7. Control System

The block diagram for the static deflection compensator is shown in Figure 14. The system uses actuator kinematics (Act. Kin.) and forward kinematics (For. Kin.) to transform the cylinder position references into Cartesian space. The output of the deflection estimator (Def. Est.) is added to the Cartesian position reference. Inverse kinematics (Inv. Kin.) and inverse actuator kinematics (Inv. Act.) are then used to generate the modified cylinder position references $\hat{x}_{ref}$. It should be noted that while the telescopic position reference is used in the calculations, it is not modified since only the main cylinder and knuckle cylinder compensate for the deflection.

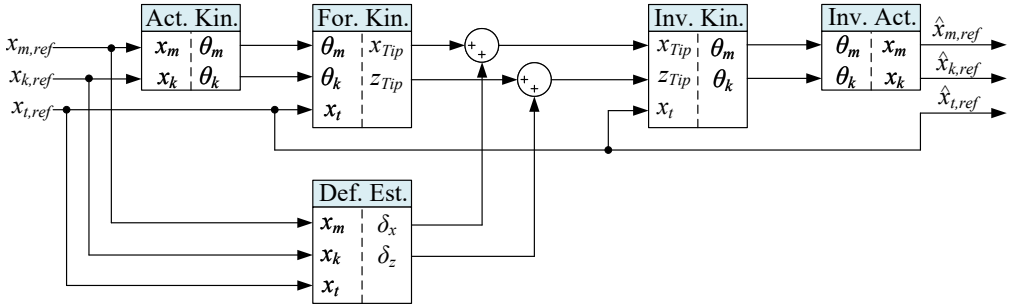

Figure 14. Block diagram of the static deflection compensator.

4. Dynamic Deflection Compensation

The dynamic deflection compensator is based on the feedback of the load pressure on the main cylinder. Pressure feedback has previously shown its effectiveness in [24], where it was used to suppress oscillations for the slewing motion of the HMF 2020K4 loader crane. The load pressure is defined as the effective pressure acting on a cylinder—see Equation (52)—and is derived from the a-side and b-side pressures, respectively. By measuring these pressures, the load pressure can be calculated. Further, by measuring the position and velocity of the cylinder, the gravitational term $G(x)$ and the friction term F_{fric} can be estimated. Using proper filtering, the acceleration $\ddot{x}$ can be estimated based on Equation (53). The inertia term $M(x)$ represents the effective mass of the cylinder.

$$p_L = p_a - \frac{A_b}{A_a} \cdot p_b \tag{52}$$

$$M(x) \cdot \ddot{x} = p_L \cdot A_a - G(x) - F_{fric}(\dot{x}) \tag{53}$$

4.1. Crane Natural Frequency

In the laboratory, the oscillations of the crane tip are measured using the Leica Absolute Tracker AT960. The hanging load is rapidly lifted for a short distance to induce oscillations in the crane, similar to an impulse response. Figure 15 shows the crane tip z-position in the laboratory with two load impulses for $x_t = 3.288$ m at $t = 2$ s and $x_t = 2.906$ m at $t = 32$ s.

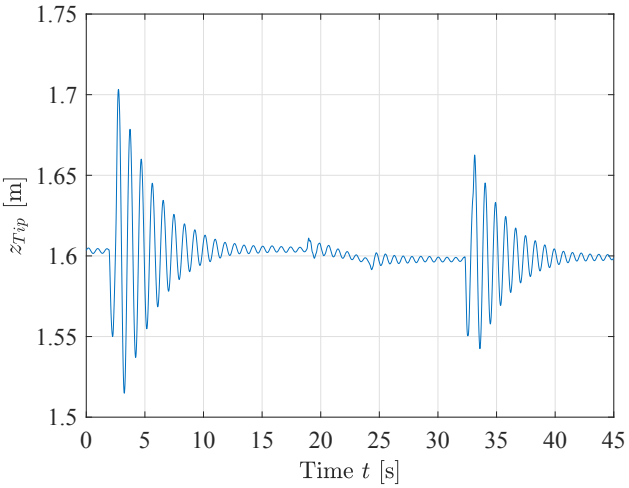

Figure 15. Crane tip oscillations from laboratory.

The natural frequency is extracted from the time series data, and by taking multiple measurements with varying telescopic lengths, the natural frequency of the crane tip is estimated using curve fitting. The measured and estimated crane tip natural frequency is shown in Figure 16. The formula for the estimate is given as

$$\hat{\omega}_{Tip} = 0.11 \frac{\text{rad/s}}{\text{m}^2} \cdot x_t^2 - 1.716 \frac{\text{rad/s}}{\text{m}} \cdot x_t + 11.63 \text{ rad/s} \tag{54}$$

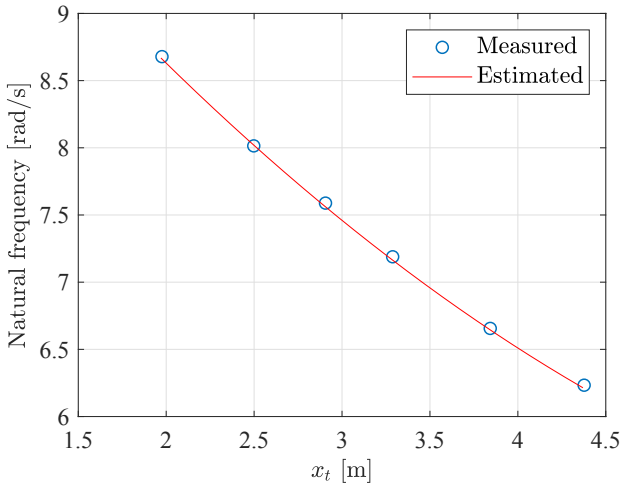

Figure 16. Estimated crane natural frequency.

4.2. Adaptive Bandpass Filter

An adaptive bandpass filter is used to extract the crane tip oscillations from the main cylinder load pressure. A critically damped bandpass filter is selected, which has the following transfer function:

$$G_{BP}(s) = \frac{2 \cdot s \cdot \omega_f}{s^2 + 2 \cdot s \cdot \omega_f + \omega_f^2} \tag{55}$$

$$= 2 \cdot \frac{\omega_f}{s + \omega_f} \cdot \frac{s}{s + \omega_f} \tag{56}$$

The bandpass filter is used in a feedback loop to suppress the oscillations. The control signal from the dynamic compensator with feedback gain k_{pL} is then given as

$$u_{comp} = k_{pL} \cdot p_L \cdot G_{BP}(s) \tag{57}$$

A digital implementation with variable bandpass frequency is made by separating the bandpass filter into a lowpass filter and a highpass filter, shown in Equations (58)–(62). The estimated eigenfrequency of the crane is used as the center frequency of the filter. y_{HP}, y_{LP}, and y_{BP} denote the output of the highpass, lowpass, and bandpass filters, respectively.

$$\omega_f = \hat{\omega}_{Tip}(x_t) \tag{58}$$

$$\alpha = \frac{1}{1 + \omega_f \cdot T_s} \tag{59}$$

$$y_{HP,i} = \alpha \cdot y_{HP,i-1} + \alpha \cdot (x_i - x_{i-1}) \tag{60}$$

$$y_{LP,i} = \alpha \cdot y_{LP,i-1} + (1 - \alpha) \cdot y_{HP,i} \tag{61}$$

$$y_{BP,i} = 2 \cdot y_{LP,i} \tag{62}$$

where

i = sample number;
x = filter input;
y = filter output(s);
T_s = sample time, 0.01 s;
$\hat{\omega}_{Tip}$ = estimated tip eigenfrequency.

5. Modeling of Telescopic Actuation System

A model of the crane containing the hydraulic system, main boom, and knuckle boom was previously created using Simscape™ components; see [23–25]. For this paper, the telescopic actuation system is modeled and added to the Simscape model. A section view from the CAD model is given in Figure 17, showing how the telescopic booms are packed inside each other, as well as showing the unique telescopic cylinders. An illustration of a telescopic cylinder is given in Figure 18, showing how the three tubes are used to transport the fluid through the telescopic system. The associated diameters D and stroke length h are given in Table 5. Note that $D_{i,m}$ refers to the inner diameter of the middle tube, etc.

Table 5. Telescopic cylinder data, in [mm].

	$D_{o,o}$	$D_{i,o}$	$D_{o,m}$	$D_{i,m}$	$D_{o,i}$	$D_{i,i}$	h
Cylinder 1	80	70	55	35	20	15	1885
Cylinder 2	80	70	55	35	20	15	1950
Cylinder 3	80	70	50	34	20	15	2000
Cylinder 4	80	70	50	34	20	15	2100

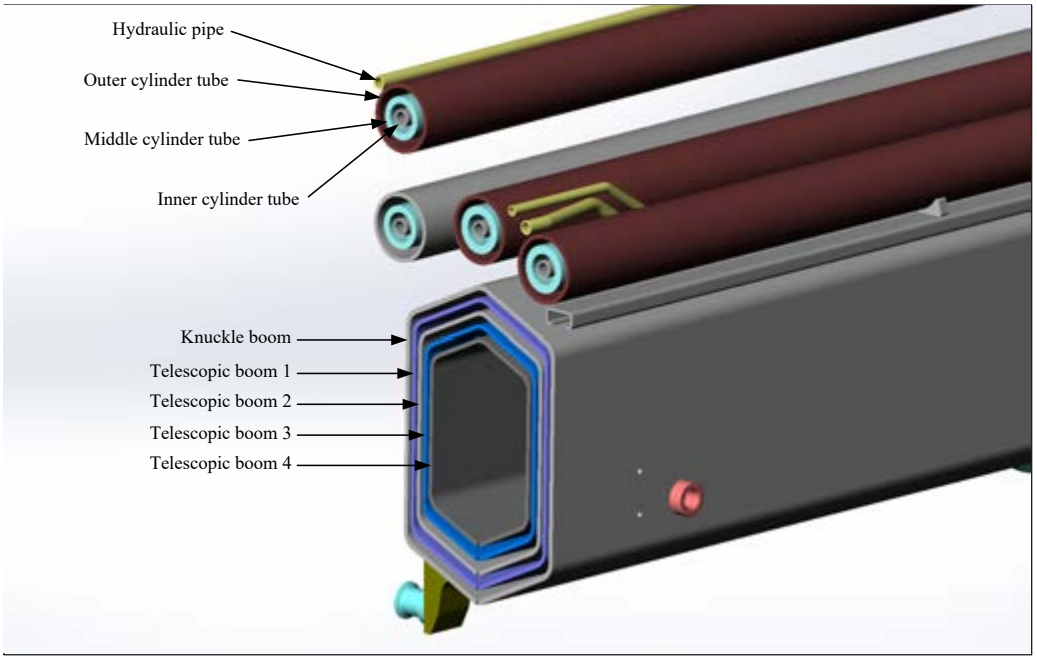

Figure 17. Section view of the telescopic system, from CAD model.

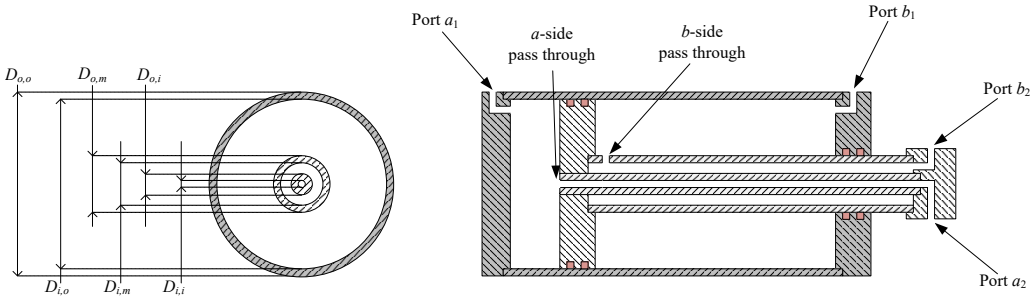

Figure 18. Illustration of a telescopic cylinder.

The inner tube allows for the a-side of all cylinders to be connected together, effectively making the cylinders connected in parallel, hydraulically. Mechanically, the booms are connected in series. The effective area and area ratio ϕ of the cylinders are given by

$$A_a = \frac{\pi}{4} \cdot D_{i,o}^2 \tag{63}$$

$$A_b = \frac{\pi}{4} \cdot D_{i,o}^2 - \frac{\pi}{4} \cdot D_{o,m}^2 \tag{64}$$

$$\phi = \frac{A_b}{A_a} \tag{65}$$

The hydraulic system for the telescopic cylinders is shown in Figure 19. The counterbalance valve is a special recirculating type, which effectively connects the a-side and b-side to the same pressure during the out-stroke motion. The workings of the telescopic circuit are shown in detail in Figure 20. Since the outer diameter of the middle tube is larger for cylinders 1 and 2, they have a smaller b-side area and will start moving first. The counterbalance valve has a rated flow of 70 L/min, and a pilot area ratio of 4. The directional control valve has a rated flow of 40 L/min.

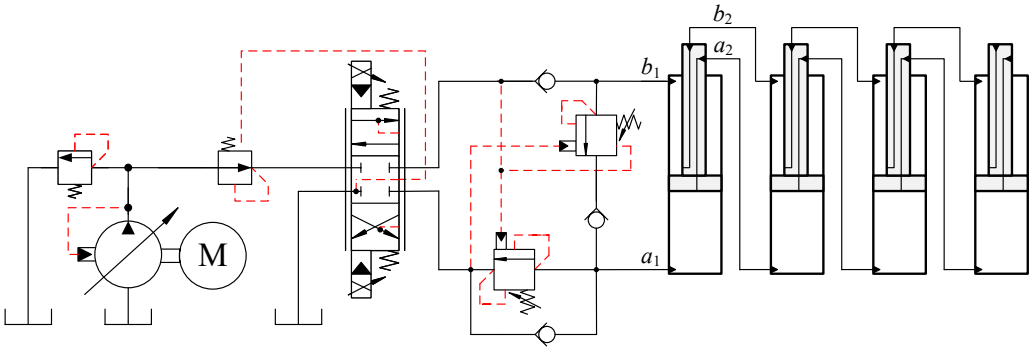

Figure 19. Hydraulic system for the telescopic cylinders.

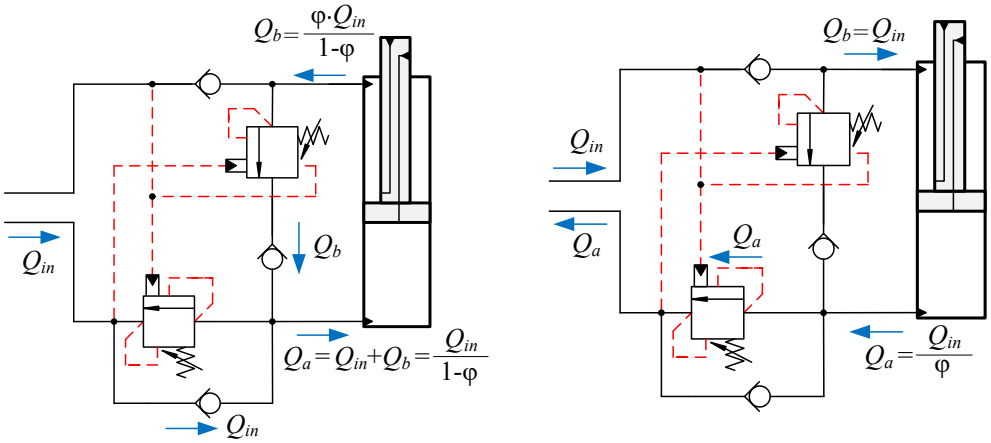

(**a**) (**b**)

Figure 20. Flows in the telescopic circuit. (**a**) Flows in the telescopic circuit during out-stroke motion. (**b**) Flows in the telescopic circuit during in-stroke motion.

To obtain the proper motion sequence of the telescopic cylinders as observed on the physical crane, the friction in each is adjusted such that the outer cylinders have slightly more friction. The inner cylinder has an estimated Coulomb friction of 10 kN and viscous friction of 2 kN· s/m. The outer cylinders have an adjusted viscous friction of 2.1, 2.2, and 2.3 kN· s/m, respectively. Figure 21 shows that the inner cylinder moves first, as is desired. It can also be seen that the velocities of cylinders 3 and 4 are slightly higher since they have a larger area ratio ϕ, which results in a higher Q_a during the out-stroke motion.

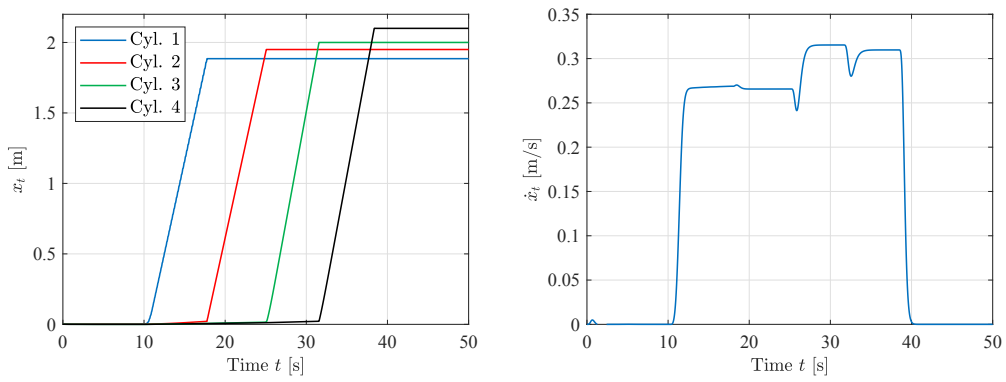

(**a**) (**b**)

Figure 21. Motion sequence and velocity of the telescopic cylinders. (**a**) Position of each telescopic cylinder. (**b**) Velocity of the full telescopic system.

6. Simulation Results

To verify the performance and feasibility of the static and dynamic deflection compensator, simulations are performed in the MATLAB Simulink® environment. A simplification of the flexibility is made by placing a rotational spring between the knuckle boom and first telescopic boom, illustrated in Figure 22. A similar approach was used in [26]. The deflection on the physical crane is due to many factors, such as structural flexibility, deformation of the sliding blocks between the booms, slack between the booms, and compression of the liquid in the cylinders. As such, an accurate model corresponding to the measured data is difficult to create, which is why a neural network is used to estimate the deflection in the first place. The purpose of the simplified model is to give the crane model an approximate static and dynamic deflection on which the developed compensator will be tested. Note that the neural network is simply re-trained to fit the measurements from the Simscape model in this section.

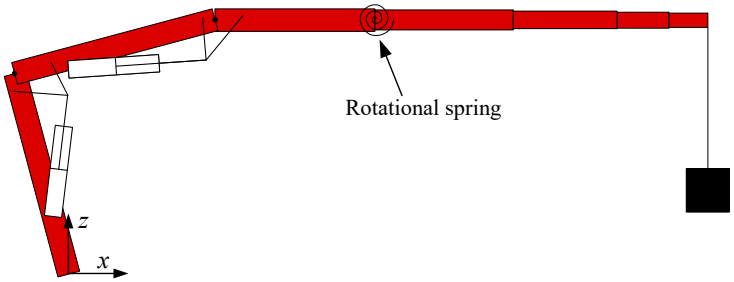

Figure 22. Illustration of the simplified flexible model.

In the simulations, the crane is running path control, developed earlier in [22]. Three simulations are performed, one without load, one with load, and one with load and deflection compensation. A load impulse is done at $t = 20$ s. The crane is moving from $[x_m, x_k, x_t]^T = [1.38\text{ m}, 1.8\text{ m}, 4\text{ m}]^T$ to $[1.43\text{ m}, 1.85\text{ m}, 2\text{ m}]^T$. Figure 23 shows the vertical position z_{Tip} during simulations, as the deflection is largest in the z-direction. It can be seen that the static deflection is compensated for after 6 s. The dynamic deflection compensator quickly dampens the oscillations induced by the load impulse.

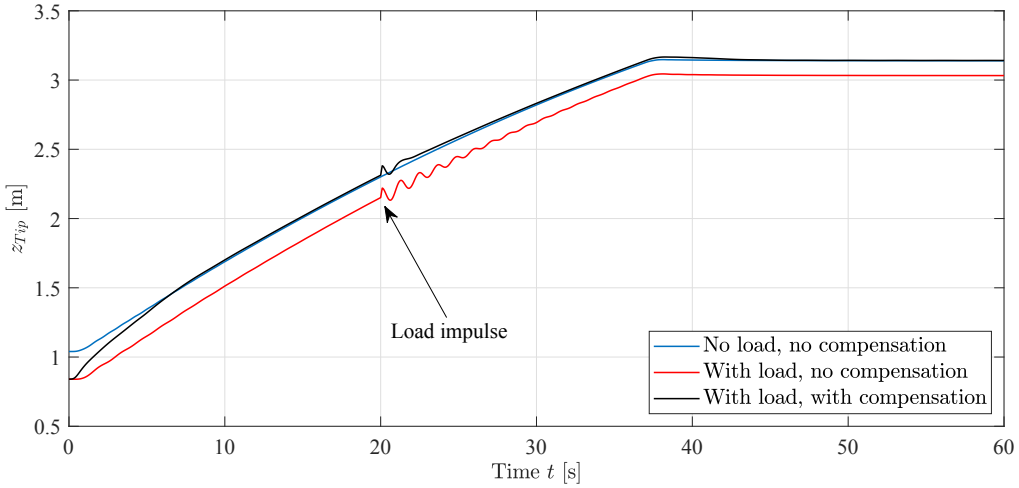

Figure 23. The vertical coordinate of the crane tip, z_{Tip}, is plotted as a function of time for three different conditions.

To investigate the effects of the deflection compensator, the change in cylinder position reference $\Delta x_{ref} = \hat{x}_{ref} - x_{ref}$ from the static compensator and the control signal u_{comp} from the dynamic compensator is shown in Figure 24. The static deflection compensator modifies

the cylinder position reference by a few centimeters, varying smoothly with the cylinder positions. The effect of the dynamic deflection compensator is most prominent at the load impulse at $t = 20$ s, giving a rapid correction to dampen the oscillations.

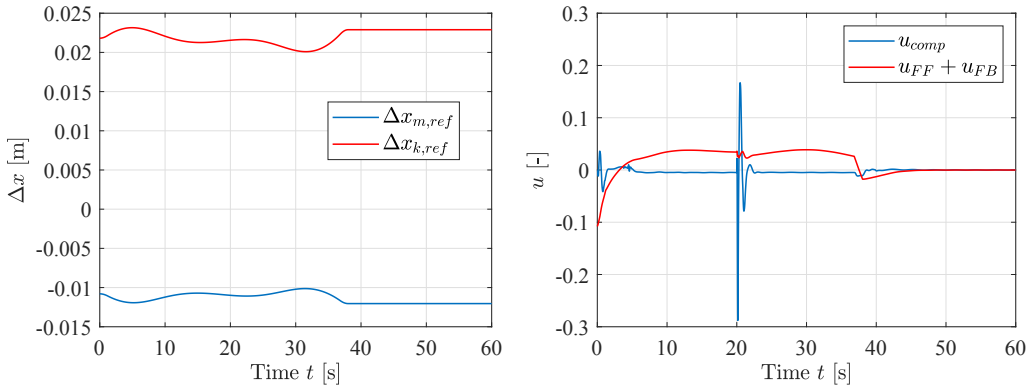

(**a**) (**b**)

Figure 24. Effects of the static and dynamic deflection compensator. (**a**) Change in cylinder position reference from the static deflection compensator, (**b**) control signal from the dynamic deflection compensator u_{comp}, and motion controller $u_{FF} + u_{FB}$.

7. Experimental Verification

Experiments are conducted on the HMF 2020K4 loader crane in the laboratory. The deflection compensator is implemented on a CompactRIO connected to the crane. A picture of the test setup is shown in Figure 25.

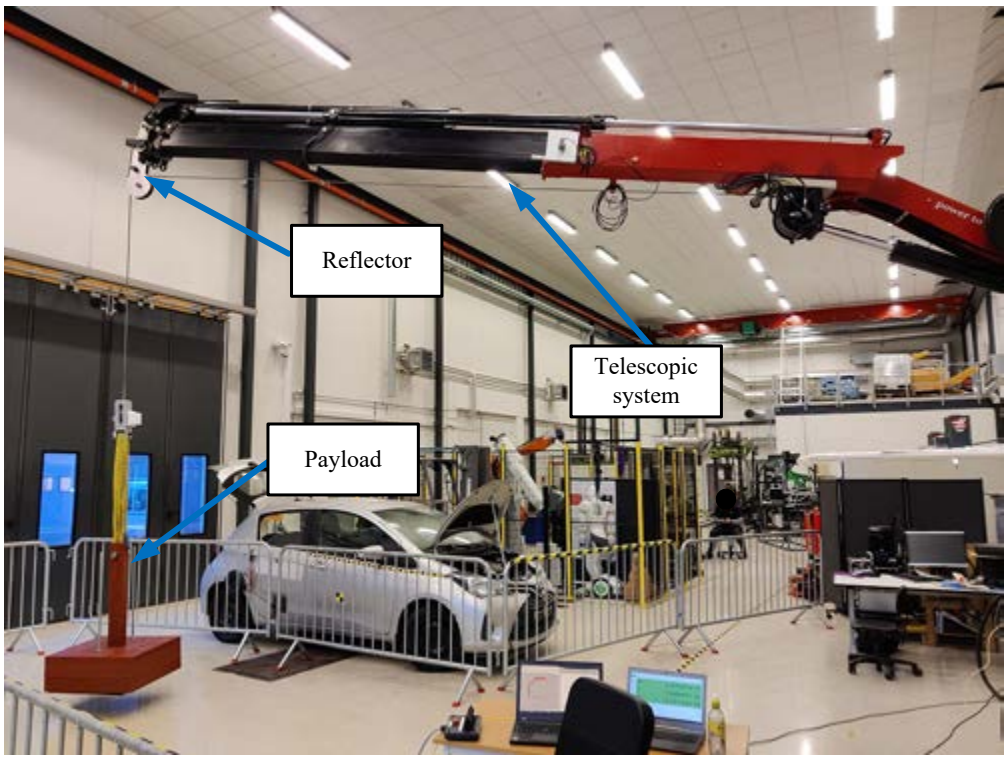

Figure 25. Experimental setup in the laboratory, showing the crane with a hanging load.

There is some deadband in the valves on the loader crane. Deadband compensation is implemented for the laboratory experiments. The deadbands are identified from the test and are shown in Table 6. The equation for the deadband compensator is shown

in Equation (66). A small transition region $\tilde{u}$ is introduced to keep the control signal continuous, which reduces unnecessary oscillations, and ensures that the valve will be able to stay closed when no movement is needed. Parameters used in the experiments are shown in Table 7.

Table 6. Identified deadband for the actuators.

Actuator	Out, u^+	In, u^-
Main	0.24	−0.22
Knuckle	0.20	−0.31
Telescope	0.33	−0.33

$$\hat{u} = \begin{cases} \min\left(u^+ + (1-u^+)u, \dfrac{u^+}{\tilde{u}}u\right) & \text{if } u > 0 \\ \max\left(u^- + (1+u^-)u, -\dfrac{u^-}{\tilde{u}}u\right) & \text{else} \end{cases} \tag{66}$$

where

$\hat{u}$ = compensated control signal
u = control signal
u^+ = out-stroke deadband
u^- = in-stroke deadband
$\tilde{u}$ = transition region, 0.01.

Table 7. Parameters used in laboratory.

Description	Name	Value
Main feedback	$k_{p,m}$	15 m^{-1}
Main out-stroke feedforward	$k^+_{ff,m}$	30.16 s/m
Main in-stroke feedforward	$k^-_{ff,m}$	18.37 s/m
Knuckle feedback	$k_{p,k}$	20 m^{-1}
Knuckle out-stroke feedforward	$k^+_{ff,k}$	26.51 s/m
Knuckle in-stroke feedforward	$k^-_{ff,k}$	14.72 s/m
Telescope feedback	$k_{p,t}$	2 m^{-1}
Telescope out-stroke feedforward	$k^+_{ff,t}$	3.33 s/m
Telescope in-stroke feedforward	$k^-_{ff,t}$	3.7 s/m
Pressure feedback gain	k_{pL}	0.02 bar^{-1}

The crane moves from $[x_m, x_k, x_t]^T = [0.395\text{ m}, 0.6151\text{ m}, 4.168\text{ m}]^T$ to $[0.4869\text{ m}, 0.6161\text{ m}, 2.015\text{ m}]^T$ while using the path controller. The path is run three times, one without load, one with load, and one with load and deflection compensation. A plot of the tip position in the xz-plane is shown in Figure 26, while the z-position versus time is shown in Figure 27. It can be seen that the compensator is able to compensate for the static deflection almost completely, in addition to removing the oscillations at the start and end of the motion. At the end of the path, the static deflection of the vertical coordinate of the crane tip, z_{Tip}, is reduced from 56.8 mm to 5.7 mm, a 90% decrease.

To showcase the effects of the deflection compensator, the change in cylinder position reference $\Delta x_{ref} = \hat{x}_{ref} - x_{ref}$ from the static compensator and the control signal u_{comp} from the dynamic compensator is shown in Figure 28. The static deflection compensator modifies the cylinder position reference smoothly. The effect of the dynamic deflection compensator can be seen throughout the whole motion, actively suppressing oscillations.

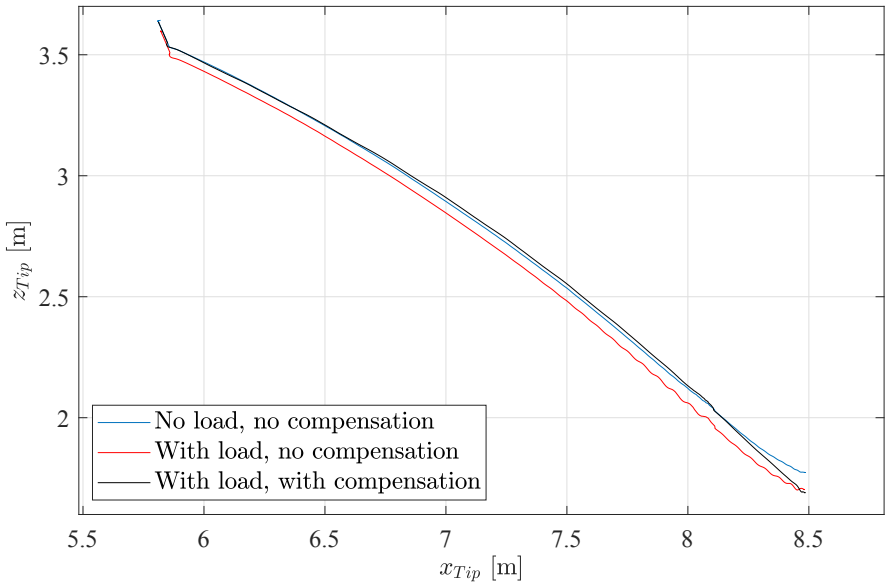

Figure 26. Crane tip position in the xz-plane during motion in laboratory.

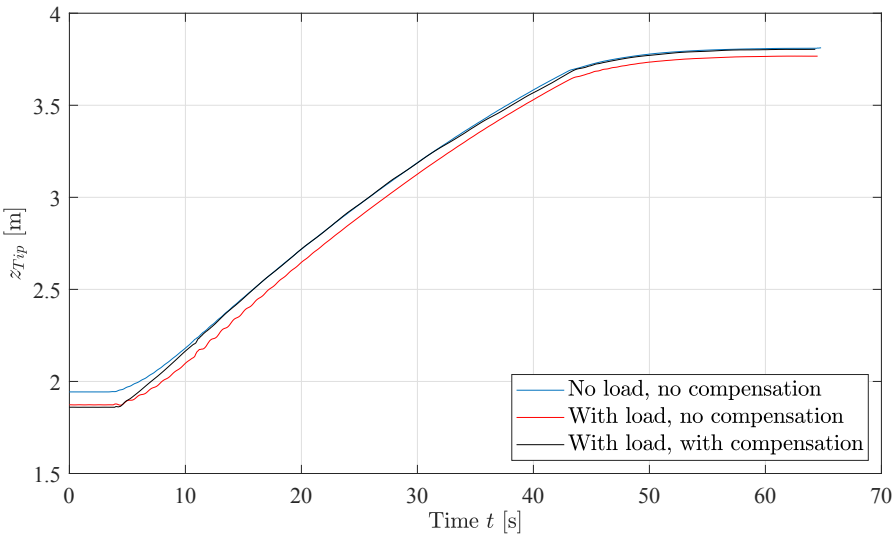

Figure 27. The vertical coordinate of the crane tip, z_{Tip}, plotted as a function of time during motion in laboratory.

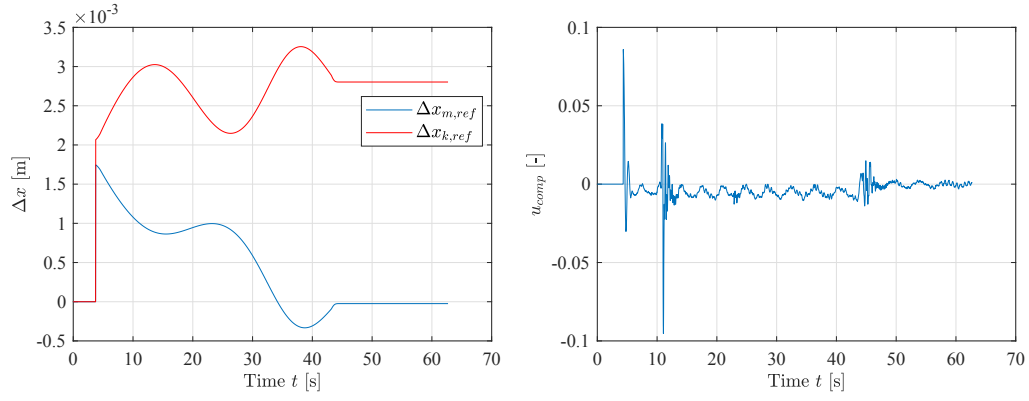

(**a**) (**b**)

Figure 28. Effects of the static and dynamic deflection compensator in laboratory. (**a**) Change in cylinder position reference from the static deflection compensator. (**b**) Control signal from the dynamic deflection compensator.

To demonstrate the capabilities of the dynamic deflection compensator more clearly, a load impulse test is performed similar to the simulations. In this case, the position controller is disabled and only the dynamic compensator is activated. It can be seen in Figure 29 that the dynamic deflection compensator quickly dampens the oscillations. The slight drift at the end occurs simply because the position controller is deactivated during this test.

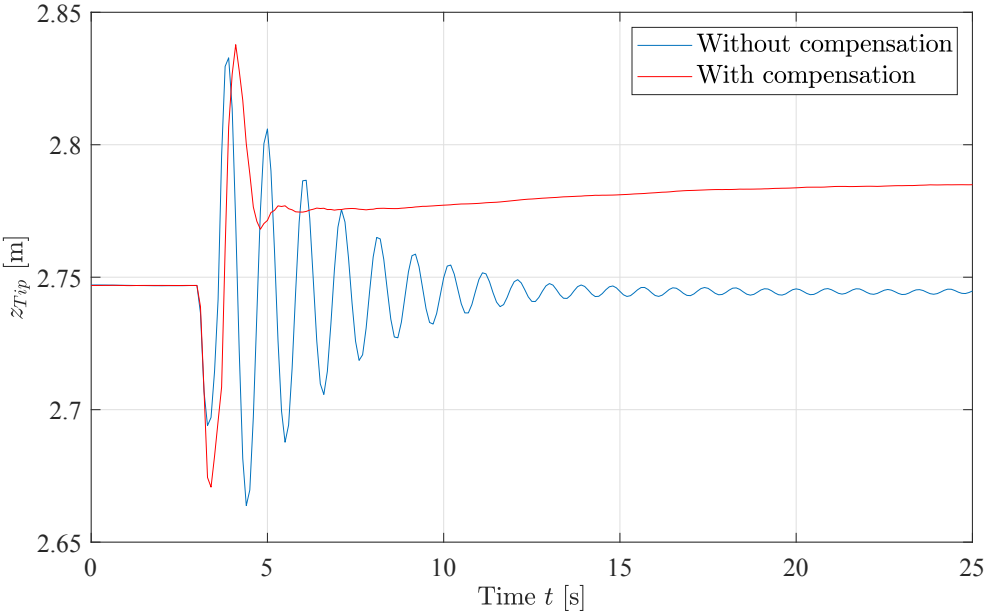

Figure 29. Load impulse test with only dynamic compensator activated.

8. Conclusions

In this paper, a novel method for stable deflection compensation is introduced and implemented on a commercially available loader crane. The new method is verified both numerically via simulations and experimentally by conducting several path-following tasks that all clearly demonstrate the simultaneous effect of compensating for crane tip deflections while suppressing oscillations in the system. The deflection of the crane tip is first measured in the laboratory using a laser tracker. A neural network deflection estimator is designed and trained using backpropagation with training data from laboratory measurements. The relevant kinematic functions are derived for the static compensator and are used to transform the cylinder position reference from the actuator space to Cartesian coordinates. The estimated tip deflection is added to the reference, and inverse kinematics are then used to transform the modified reference from Cartesian space into actuator space. The dynamic compensator uses pressure feedback with an adaptive bandpass filter to extract the crane tip oscillations while allowing for steady-state variations. This signal is then used in a feedback loop to compensate for these oscillations.

Simulation results show that the static compensator is able to minimize the effects of the deflection and move the crane tip to a similar position as in the no-load case. The dynamic compensator is able to suppress the oscillations in both general path traveling as well as load impulse situations.

Laboratory experiments are conducted to evaluate the control system on the hydraulic loader crane in practice. Experimental results are similar to the simulations in that both the static and dynamic compensators are able to minimize the effects of the deflection and oscillations. The crane tip is able to follow the same position as in the no-load case with a 90% decrease in static deflection. In the laboratory, the control signal from the dynamic compensator successfully suppresses the oscillations during the entire motion.

Further work may include stability analysis of the neural network deflection estimator and adaptive bandpass filter. Since the system was tested with a heavy payload, the ef-

fects of lighter loads may also be investigated, for example, by adding another input to the deflection estimator representing the measured or estimated weight of the payload. Different types of neural networks may also be investigated, for example, dynamic neural networks. In addition, the novel method requires a mapping of the deflection and an estimate of the natural frequency of the crane. While the best results are obtained by physical measurements as presented in this paper, it is expected that simpler and less time consuming estimates can still yield significant improvement in accuracy and stability when implemented using the presented method.

Author Contributions: Conceptualization, K.J.J., M.K.E. and M.R.H.; methodology, K.J.J.; software, K.J.J.; validation, K.J.J.; formal analysis, K.J.J.; investigation, K.J.J.; data curation, K.J.J.; writing—original draft preparation, K.J.J.; writing—review and editing, K.J.J., M.K.E. and M.R.H.; visualization, K.J.J.; supervision, M.K.E. and M.R.H. All authors have read and agreed to the published version of the manuscript.

Funding: This research was funded by the Norwegian Ministry of Education and Research grant number 155597. The APC was funded by the University of Agder.

Conflicts of Interest: The authors declare no conflict of interest.

References

1. Giorgio, I.; Del Vescovo, D. Non-Linear Lumped-Parameter Modeling of Planar Multi-Link Manipulators with Highly Flexible Arms. *Robotics* **2018**, *7*, 60. [CrossRef]
2. Wanner, J.; Sawodny, O. A lumped parameter model of the boom of a mobile concrete pump. In Proceedings of the 2019 18th European Control Conference (ECC), Naples, Italy, 25–28 June 2019; pp. 2808–2813. [CrossRef]
3. Sun, C.; He, W.; Hong, J. Neural Network Control of a Flexible Robotic Manipulator Using the Lumped Spring-Mass Model. *IEEE Trans. Syst. Man Cybern. Syst.* **2017**, *47*, 1863–1874. [CrossRef]
4. Rahimi, H.; Nazemizadeh, M. Dynamic analysis and intelligent control techniques for flexible manipulators: A review. *Adv. Robot.* **2014**, *28*, 63–76. [CrossRef]
5. Lochan, K.; Roy, B.; Subudhi, B. A review on two-link flexible manipulators. *Annu. Rev. Control* **2016**, *42*, 346–367. [CrossRef]
6. Subedi, D.; Tyapin, I.; Hovland, G. Dynamic Modeling of Planar Multi-Link Flexible Manipulators. *Robotics* **2021**, *10*, 70. [CrossRef]
7. Lochan, K.; Roy, B.; Subudhi, B. Recursive Lagrangian dynamic modeling and simulation of multi-link spatial flexible manipulator arms. *Appl. Math. Mech.-Engl. Ed.* **2009**, *30*, 1283–1294. [CrossRef]
8. Beres, W.; Sasiadek, J.; Vukovich, G. Control and dynamic analysis of multilink flexible manipulator. In Proceedings of the IEEE International Conference on Robotics and Automation, Atlanta, GA, USA, 2–6 May 1993; Volume 3, pp. 478–483. [CrossRef]
9. Talebi, H.; Patel, R.; Asmer, H. Dynamic modeling of flexible-link manipulators using neural networks with application to the SSRMS. In Proceedings of the 1998 IEEE/RSJ International Conference on Intelligent Robots and Systems. Innovations in Theory, Practice and Applications (Cat. No. 98CH36190), Victoria, BC, Canada, 17 October 1998; Volume 1, pp. 673–678. [CrossRef]
10. Comi, F.; Miguel, A.O.; Cavenago, F.; Ferretti, G.; Magnani, G.; Rusconi, A. Modelling, Validation and Control of DELIAN Flexible Manipulator. *IFAC-PapersOnLine* **2019**, *52*, 364–369. [CrossRef]
11. Lozano, R.; Valera, A.; Albertos, P.; Arimoto, S. PD control of robot manipulators considering joint flexibility, actuators dynamics and friction. In Proceedings of the 1997 American Control Conference (Cat. No. 97CH36041), Albuquerque, NM, USA, 6 June 1997; Volume 5, pp. 2638–2641. [CrossRef]
12. Newman, D.; Vaughan, J. Concurrent Design of Linear Control with Input Shaping for a Two-Link Flexible Manipulator Arm. In Proceedings of the 14th IFAC Workshop on Time Delay Systems TDS 2018, Budapest, Hungary, 28–30 June 2018; Volume 51, pp. 66–71. [CrossRef]
13. Mohamed, Z.; Khairudin, M.; Husain, A.R.; Subudhi, B. Linear matrix inequality-based robust proportional derivative control of a two-link flexible manipulator. *J. Vib. Control* **2016**, *22*, 1244–1256. [CrossRef]
14. Xu, Q.; Wang, W.; Xia, H.; Wang, Y.; Feng, Y. Second-Order Non-Singular Terminal Sliding Mode Optimal Control of Uncertain Flexible Manipulator. In Proceedings of the 2018 IEEE 8th Annual International Conference on CYBER Technology in Automation, Control, and Intelligent Systems (CYBER), Tianjin, China, 19–23 July 2018; pp. 1376–1381. [CrossRef]
15. Lochan, K.; Roy, B.; Subudhi, B. SMC Controlled Chaotic Trajectory Tracking of Two-Link Flexible Manipulator with PID Sliding Surface. *IFAC-PapersOnLine* **2016**, *49*, 219–224. [CrossRef]
16. Talebi, H.; Patel, R.; Khorasani, K. Inverse dynamics control of flexible-link manipulators using neural networks. In Proceedings of the 1998 IEEE International Conference on Robotics and Automation (Cat. No. 98CH36146), Leuven, Belgium, 20 May 1998; Volume 1, pp. 806–811. [CrossRef]
17. Tang, Y.G.; Sun, F.C.; Sun, F.; Hu, T.L. Tip Position Control of a Flexible-Link Manipulator with Neural Networks. *Int. J. Control. Autom. Syst.* **2006**, *4*, 308–317.

18. Tang, Y.; Sun, F.; Sun, Z. Neural network control of flexible-link manipulators using sliding mode. *Neurocomputing* **2006**, *70*, 288–295. [CrossRef]
19. Zhang, Y.; Yang, T.; Sun, Z. Neuro-sliding-mode control of flexible-link manipulators based on singularly perturbed model. *Tsinghua Sci. Technol.* **2009**, *14*, 444–451. [CrossRef]
20. Li, S.; Wang, H.; Rafique, M.U. A Novel Recurrent Neural Network for Manipulator Control With Improved Noise Tolerance. *IEEE Trans. Neural Netw. Learn. Syst.* **2018**, *29*, 1908–1918. [CrossRef] [PubMed]
21. Li, S.; Zhang, Y.; Jin, L. Kinematic Control of Redundant Manipulators Using Neural Networks. *IEEE Trans. Neural Netw. Learn. Syst.* **2017**, *28*, 2243–2254. [CrossRef] [PubMed]
22. Jensen, K.J.; Kjeld Ebbesen, M.; Rygaard Hansen, M. Development of Point-to-Point Path Control in Actuator Space for Hydraulic Knuckle Boom Crane. *Actuators* **2020**, *9*, 27. [CrossRef]
23. Jensen, K.J.; Ebbesen, M.K.; Hansen, M.R. Anti-swing control of a hydraulic loader crane with a hanging load. *Mechatronics* **2021**, *77*, 102599. [CrossRef]
24. Jensen, K.J.; Ebbesen, M.K.; Hansen, M.R. Development of 3D Anti-Swing Control for Hydraulic Knuckle Boom Crane. *Model. Identif. Control* **2021**, *42*, 113–129. [CrossRef]
25. Jensen, K.J.; Kjeld Ebbesen, M.; Rygaard Hansen, M. Adaptive Feedforward Control of a Pressure Compensated Differential Cylinder. *Appl. Sci.* **2020**, *10*, 7847. [CrossRef]
26. Pedersen, M.M.; Hansen, M.R.; Ballebye, M. Developing a Tool Point Control Scheme for a Hydraulic Crane Using Interactive Real-time Dynamic Simulation. *Model. Identif. Control* **2010**, *31*, 133–143. [CrossRef]